Muriel Rovira Esteva

SHORT RANGE ORDER in DISORDERED PHASES using NEUTRON DIFFRACTION

Muriel Rovira Esteva

SHORT RANGE ORDER using NEUTRON DIFFRACTION

Short-range order in disordered phases using neutron diffraction

by Muriel Rovira Esteva

Supervised by
Luis Carlos Pardo
Josep Lluís Tamarit

The research in this PhD thesis has been carried out within the doctoral programme of Computational and Applied Physics of the Department of Physics and Nuclear Engineering of the Technical University of Catalonia. It has been mainly supported by a FPI (Research Personnel Training) fellowship from the Spanish Ministry of Science and Innovation (FIS2008-00837) and partly by the European Commission under the 7th Framework Programme through the 'Research Infrastructures' action of the 'Capacities' Programme, NMI3-II Grant number 283883.

Physics is like sex

Sure, it may give some practical results...

but that's not why we do it.*

*Probably not by Richard Feynman.

Thanks...

To family, friends, and other animals, who have unconditionally supported me and helped me keep my sanity (or insanity) from start to finish. I've missed you a lot.

And to my supervisors, for always being true to scientific quality and ethics, creativity, openness, but, especially, for their friendship. I couldn't have been luckier.

Barcelona, July 2014

Short-range order in disordered phases using neutron diffraction

Resum

La difracció de neutrons és una tècnica molt potent que permet sondar l'estructura de fases desordenades en un ventall d'escales de longitud. Tanmateix, degut a la complexitat inherent d'aquestes fases desordenades, l'anàlisi de la informació que es desprèn de les dades experimentals no és evident.

En aquest treball es presenten diversos mètodes alternatius que permeten treure el màxim profit de les mesures de difracció de neutrons, així com de les configuracions moleculars obtingudes en simulacions de dinàmica molecular o del modelatge de les dades. Aquests mètodes consisteixen principalment en un enfocament bayesià en l'ajust de les estructures moleculars mesurades amb difracció de neutrons, i en una anàlisi multidimensional de les funcions de distribució de probabilitat de l'estructura molecular obtingudes en simulacions o tècniques de modelatge de dades, en comptes del mitjanat estàndard de diverses variables.

Aquestes metodologies s'apliquen a la investigació de diversos sistemes desordenats per tal de resoldre una sèrie de qüestions obertes: l'origen de la transició líquid-líquid en el trans-1,2-dicloroetà ($C_2Cl_2H_2$), l'extrema fragilitat del vidre orientacional del 1,1,2,2-tetracloro-1,2-difluoroetà (F-112, $C_2Cl_2F_2$), la paradoxa de la densitat local en el tetraclorur de carboni (CCl_4), i els rols de les interaccions estèrica i electrostàtica en l'ordre de curt abast de líquids de molècules quasitetraèdriques, en particular el triclorobromometà ($CBrCl_3$) i el dibromodiclorometà (CBr_2Cl_2).

Addicionalment, també s'hi inclou un breu repàs del marc teòric de la difracció de neutrons en sistemes desordenats, així com dels aspectes pràctics de l'equip experimental i del tractament de dades necessari, per tal que els investigadors interessats disposin d'una visió general completa sobre tema.

Abstract

Neutron diffraction is a powerful technique that allows to probe the structure of disordered phases across a variety of length scales. However, due to the inherent complexity of these disordered phases, the analysis of the information contained in the experimental data is not obvious.

In this work, a few alternative methods are presented that allow to make the most of the neutron diffraction measurements as well as the molecular configurations obtained from molecular dynamics simulations or data modelling. They mainly consist in a Bayesian approach to fit the molecular structures measured with neutron diffraction, and a multidimensional analysis of the molecular structure probability distribution functions obtained from simulations or data modelling techniques, instead of the standard averaging over many variables.

These methodologies are then applied to the structural investigation of several disordered systems in order to answer a series of open questions: the origin of the liquid-liquid transition in trans-1,2-dichloroethene ($C_2Cl_2H_2$), the extreme fragility of 1,1,2,2-tetrachloro-1,2-difluoroethane's orientational glass (F-112, $C_2Cl_2F_2$), the local density paradox in carbon tetrachloride (CCl_4), and the roles of steric and electrostatic interactions in the short range order of the liquids of quasitetrahedral molecules, particularly trichlorobromomethane ($CBrCl_3$) and dibromodichloromethane (CBr_2Cl_2).

Additionally, a concise summary of the theoretical framework for neutron diffraction of disordered systems, as well as the practicalities of the experimental setup and the necessary data treatment, are also included to provide interested researchers with a self-contained overview on the topic.

Contents

Chapter 1

Introduction

Condensed matter is not continuous, it is made of atoms which concentrate certain properties in very small regions, such as mass and electron density. However, order or disorder is normally determined by the small variations in charge distribution throughout the volume. The reason why amorphous materials, such as liquids and structural glasses, appear as generally homogeneous and isotropic, is because they are microscopically disordered at atomic scales. They do not only display a positional and orientational disorder of their atoms or molecules, but they also often have defects such as dangling bonds, vacancies, and intersticial elements [1–4].

1.1 Order and disorder

The atoms or molecules of a gas do not interact with each other because the density is too low, therefore, their positions and orientations are completely uncorrelated. The fact that the molecules in an ideal gas are distributed independently and randomly throughout the whole available volume makes it the ideal limit of perfect disorder [1].

On the opposite side, the ideal limit of order is a perfect crystal, where the density is large enough to allow the interactions between atoms or molecules to fully determine all their positions and orientations. Because of this, the whole crystal can be reproduced simply by knowing its ordering rules, normally described by the kind of crystal symmetry and the arrangement of the atoms or molecules within the unit cell.

Most crystals have translational symmetry, that is, their atomic or molecular pattern is repeated periodically along the three spatial dimensions. However, some systems have interactions that are strong enough to completely determine the arrangement of its elements, thus being perfectly ordered, but at the same time lacking any translational symmetry. These systems are called quasicrystals and often display symmetries not possible in regular crystals, such as five-fold.

Most materials lie somewhere between the ordered and disordered

ideal limits. In them, a competition takes place between an ordering drive, due to interactions between atoms or molecules favouring certain positions or orientations, and a disordering drive, often due to randomness induced by thermal agitation [3]. In practice, since there is always some kind of physical restriction, completely disordered structures such as ideal gases never occur in nature. Neither do completely ordered structures such as perfect crystals, due to particle vibrations at finite temperatures and even at zero-point, where the uncertainty principle does not allow particles to stay simultaneously localized and completely still [5]. However, they are both good approximations for many substances.

When the system is composed out of elements with spherical symmetry, only the positional degrees of freedom can show some level of disorder. But elements with a certain internal structure, such as irregularly shaped molecules, have the additional possibility of having those internal degrees of freedom correlated with the rest of the molecules through diverse kinds of interactions (steric, dipolar, magnetic...). Whether this correlation affects only the nearest neighbours, displaying a certain short range order, or extends throughout the whole material, displaying long range order, is determined by the span and strength of each type of interaction in the particular conditions of the system [1, 2].

Depending on the complexity of the material and the dominant interactions at play, it may happen that the disorder is only expressed in some, or even just one, of the degrees of freedom (such as orientation of the molecules, position of their centres of mass, intramolecular geometry, or dipole orientation), while keeping the rest perfectly ordered. Each kind of short or long range order will have to be studied with a diversity of techniques and strategies.

Disordered phases are more abundant than the crystalline ones and as interesting from a scientific and technological point of view. In particular, from the point of view of basic science, many fascinating solid state problems are connected with disorder, and two of the fundamental states of matter, gas and liquid, are disordered as well. Remarkably, a significant amount of the environmental phenomena that affect human life takes place in the gaseous atmosphere that

surrounds the earth, and about 70% of the surface of the earth is covered by liquid water.

Besides, apart from the human body being made of about two thirds of water, most biological materials are conglomerates composed of ordered structures mixed with a certain amount of amorphous ones (bone, muscle, connective tissue, wood, silk, etc.) [6]. And there is an endless list of technological applications based on disordered materials: solar cells, liquid-crystal displays (LCDs), transistors, food manufacture and processing, pharmaceuticals, cosmetics, soaps, lubricants, construction, implants, and many more [3, 7–10].

1.2 Disordered materials

1.2.1 Liquids

A liquid is a material where the interactions between its atoms or molecules allow them to freely diffuse among the other atoms or molecules of the material but that, at the same time, are also loosely held together, so they do not tend to separate from each other as it happens in gaseous phases.

Macroscopically, this is reflected in liquids being able to flow under an arbitrarily small shear stress; and since pressure applied to a particular region is transmitted to the rest of the liquid, they tend to keep a constant volume [2, 4].

However, dynamics play an important role in the description of the properties of fluids, such as elasticity or viscosity, and often their response to stimuli strongly depends on the application rate of the forces. For instance, liquids have an elastic response to shear at short time scales, that is, they do not flow. This is particularly apparent in very viscous liquids where atoms or molecules have less mobility and forces from a wider time range induce this kind of response [11, 12].

Liquids exist in a very small range of possible temperature and pressure values, but they are very important for physics, chemistry, technology, and life [2].

Due to the high mobility of its constituents, liquids are normally

homogeneous and isotropic and do not display translational nor orientational long range order. After gases, they exhibit the most disordered structures. However, their atoms or molecules are affected by interactions with their neighbours, which causes a certain short range order. That means that the relative positions and orientations between the closest atoms or molecules are correlated even though this correlation does not persist over long distances [2].

If the packing is high and the elements are very close to each other, their repulsive interactions of mutual impenetrability become the dominant influence, which has an effect in the probability distribution of preferred structures. This is reflected by the fact that substances that have an amorphous and a crystalline phase with the same density usually display many resemblances in their short range order [1].

Both, crystals and liquids, arrange in rather tight packings, which results in liquids being almost as incompressible as crystals. In fact, in most substances the volume occupied by each atom of the liquid is very similar to that of its crystal [1].

This means that the structure of most simple liquids is determined by its packing and that, in general, if we look at the arrangement of the closest elements in the liquid, it is not so different from their arrangement in the crystal. For instance, the number of covalent bonds per atom may be the same on average (although in amorphous materials dangling bonds can often be found). Consequently, the liquid can be considered sometimes as simply a deformation from the ordered structure of the crystal (see Figure 1.1) [1, 3, 13].

If we take a look at the packing of crystals made of identical hard spheres, a good approximation for many atoms, we see that molecules that arrange in face centred cubic (fcc) and hexagonal lattices, both with a coordination number of 12, yield the maximum packing that can be achieved. In these lattices, if neighbouring spheres are in contact with each other, 74% of space is occupied. And other lattices, such as the simple cubic, with a coordination number of 6, and the body centred cubic, with a coordination number of 8, have packings of only 52% and 68%, respectively. The larger the number of first neighbours, the larger the packing.

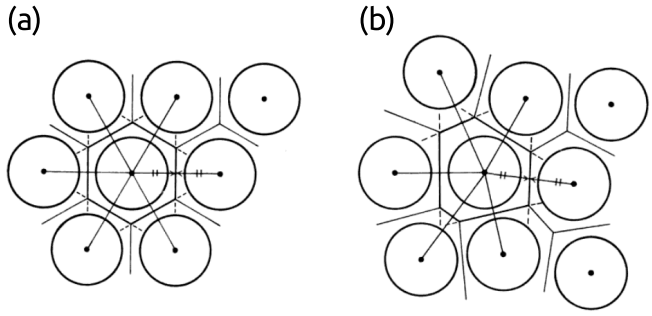

Figure 1.1: (a) A 2D example of the perfect translational order found in crystals, and (b) an example of the kind of deviation from the crystalline structure that can be found in liquids and structural glasses. *Modified from Ref. [1].*

Higher packings can be achieved when crystals with spheres of different sizes are considered, because the smaller ones can fill the interstitial spaces left by the larger ones, similarly to what happens in ionic crystals. They can also be achieved in crystals with non-spherical elements, although most tightly packed molecular crystals have values ranging between 68 and 74% of occupancy [1, 3, 14].

Organising the elements randomly causes dilatation because the disorder generates empty spaces that decrease the density. Empirically, the maximum occupation reached with random packing of hard spheres is about 64%. That is why most liquids are less dense than their respective crystals (although of course there are exceptions). The packing in most molecular liquids around the fusion temperature is between 50 and 60%. The shape of their molecules has a significant impact in their arrangement in the liquid, for instance, long rigid molecules cannot be packed without inducing some sort of orientational correlation. [1, 3]

Locally, the greatest difference between liquid and crystal is the large parameter fluctuations such as the coordination number and the atomic volume, but this can not be deduced directly from measurements, that just provide an average of the diverse local structures present in the liquid [1].

There are many different kinds of liquids, and they display a rich variety of characteristics and disparate behaviours. For instance, the typical length scales of atomic liquids are just a few angstroms, but in more complex liquids such as colloidal suspensions, where particles are homogeneously dispersed in a different substance, those particles or colloids normally have a size between a nanometre and a micrometer [15].

1.2.2 Other equilibrium phases

As has been mentioned, the highly correlated relative position and orientation of the molecules in crystals leads to extremely ordered structures that show extensive long range order throughout the whole system, while molecular interactions in liquids are only enough to favour certain positions and orientations of the closest neighbours leading to some short range order.

Depending on the dominant interactions and their range in each system, it can happen that some degrees of freedom are highly correlated yielding long range order, while at the same time others are weakly interacting only showing short range order. This is the case of plastic crystals where molecules can rotate more or less freely but have their centres of mass in a highly ordered crystal lattice: they display translational order but have rotational disorder at the same time (see Figure 1.2) [2].

Liquid crystals also show a combination of ordered and disordered degrees of freedom. For instance, in the nematic phase, molecules show translational disorder such as liquids but with highly correlated orientations. However, liquid crystals can have a variety of complex phases, such as the smectic phase, where the molecules keep the orientational order but organise in layers with inner translational disorder, or the cholesteric phase, where there is translational disorder of the molecular centres of mass but their orientations follow a swirl. The shape of the molecules plays a crucial role on the kind of phases that can form, for instance, long molecules tend to arrange their orientation in the same direction when packed, or flat molecules can have discotic phases where they tend to arrange in layers [1, 2].

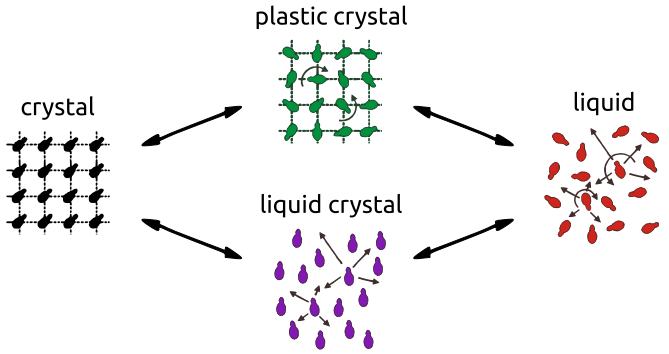

Figure 1.2: Scheme of the degrees of freedom existing in plastic and liquid crystal phases. The position and orientation of molecules are perfectly ordered in a crystal, but both are quite disordered in a liquid. In a plastic crystal the position of the centre of mass of the molecules is perfectly ordered but not their orientation, and in the case of a nematic phase of a liquid crystal what is ordered is their orientation but not their position. More complex phases involving other combinations of ordered or disordered degrees of freedom are possible. *Modified from Ref. [16].*

1.2.3 Glasses

1.2.3.1 Avoiding crystallization

In gases the density is so low that the atoms or molecules do not interact with each other. If the density increases, for instance because the temperature has been decreased, the neighbours are close enough to at least weakly interact with each other and we can obtain a liquid, where some short range order is favoured. But if the density is increased even further, the constituents of the material may be so close that their mutual interactions can perfectly determine all their degrees of freedom. However, whether this lack of freedom results in an ordered or disordered structure is another matter. And since crystal formation is a probabilistic process, attaining the ordered phase is not always guaranteed.

Due to the partially random nature of liquid structure, there is

some probability that a few particles will spontaneously arrange locally in a small crystalline structure at a certain point. If this crystalline nucleus is thermodynamically unstable, because the temperature is too high, for example, it will simply dissolve again within the liquid, otherwise it will start to grow. Below the melting temperature, the crystalline structure is energetically more favourable than the liquid one, but that applies only if the whole system is completely in one of the phases. If the liquid and the crystal have to coexist, as in the case of small crystalline nuclei surrounded by liquid, there is a mismatch at the interface that introduces an additional energetic penalisation, which means that in practice crystallisation will always start well below the melting temperature. Besides, since the crystal and the liquid phases occupy different volumes, a spontaneously generated crystal nucleus within the liquid will induce a non-zero elastic strain upon the rest of the sample, specially on viscous liquids, which will contribute to its thermodynamic instability [12]. Hence, crystal nuclei which get spontaneously generated in the liquid will dissolve again until the thermodynamic conditions allow them to overcome these energy barriers.

Crystal formation has two phases: nucleation and growth. And while the first is dominated by surface tension (with an elastic correction in viscous liquids), the second is dominated by viscosity of the background liquid, which allows or hinders additional particles from moving into place at the boundaries of the already formed crystalline structure [12].

Since nucleation is a statistical process, it is possible through different strategies to avoid crystallization for a long time even for liquids quite below the melting temperature. These metastable phases are called supercooled liquids, and they are equilibrium phases in the sense that, except the system actually undergoing the first order transition and crystallising, the measurement of the system properties yields the same results consistently, so it can not be determined whether they are the most stable phase or not. That is because the structural relaxation time of supercooled liquids is shorter than the available experimental time, so the system can equilibrate, despite their nucleation time becoming larger [12].

The structure of supercooled liquids is essentially the same as their structure above the melting temperature. Still, as the temperature decreases, their short range order can also show some differences due to the change in density. A greater difference can be observed in their dynamic properties, such as lower particle mobility and higher viscosity, which results in a more cooperative dynamics that tends to segregate particles into fast- and slow-moving clusters. When the sample is deeply supercooled, the viscosity becomes so huge that the particles are under kinetic inhibition and unable to rearrange, so nucleation cannot take place. However, if the system is cooled down slowly, it has plenty of time to nucleate the crystal structure during this process. Therefore, to avoid crystallisation, very fast cooling rates are normally used, although other strategies are also possible, such as adding other constituents to favour lattice irregularities [12].

1.2.3.2 Structural glass transition

If crystallization is successfully avoided, the viscosity of the supercooled liquid keeps progressively increasing and slowing down the dynamics, due to the need to rearrange larger highly interacting regions simultaneously, until a point is reached where it effectively traps the system in a disordered structure (see Figure 1.3). The relaxation time also increases, until there is a dynamic glass transition and it takes longer for the system to equilibrate than the available experimental time. When this happens, the supercooled liquid has become a structural glass, and any measurement that we carry out is really performed out of the equilibrium, which may not be of importance for some quantities, but yields crucially different results for others, such as many thermodynamic magnitudes specifically defined only in equilibrated systems [12]. Window glasses, plastics, and caramel are common everyday examples of these kind of materials.

Because the "available experimental time" is a rather arbitrary concept, which depends on the experimental technique, it has been defined as being between 100 and 1000 seconds for the purpose of defining glassy phases, which means that the dynamic glass transition will take place by definition when the relaxation time of the system

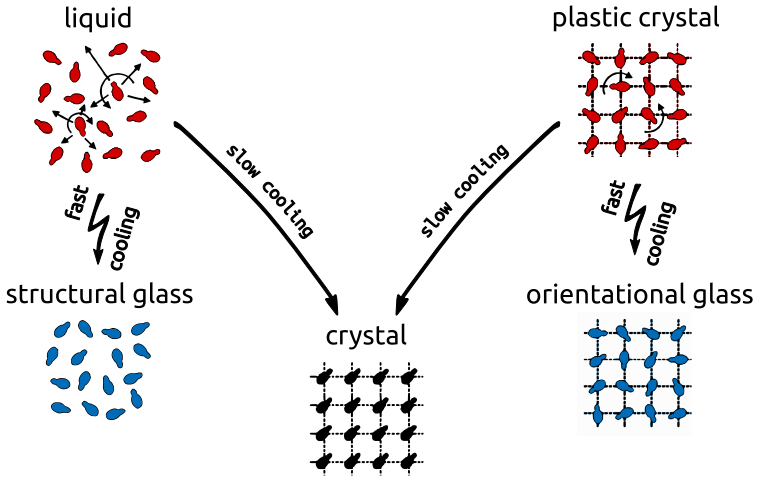

Figure 1.3: Arresting different degrees of freedom results in different kinds of glasses. For example, a structural glass with translational and rotational disorder can be obtained from a liquid, while an orientational glass with translational order and rotational disorder can be obtained from a plastic crystal. *Modified from Ref. [16].*

reaches this value range or, equivalently, when its viscosity reaches 10^{13} Poise. Taking into account that most liquids rarely have more than 0.001 or 0.01 Poise at the melting temperature, is clear that this is a huge viscosity. These quantities are also taken as the empirical values used to differentiate highly viscous liquids from amorphous solids, which means that if the compound displays a larger viscosity or relaxation time than these values it will not be considered a liquid but a solid instead.

Liquids cooled down below the glass transition temperature T_g have a very similar structure than the one they had above it, they lack any long range order and are arrested in a similar short range order than the one they had, although they can show slight changes due to the existing density variation. However, drastic dynamic changes take place at T_g, such as an increase of several orders of magnitude in the relaxation time τ and the viscosity η.

There is no latent heat or discontinuity in the density as in a first

order transition between equilibrium states (such as in the liquid to crystal transition), but there is an abrupt change in several physical properties of the system, such as the thermal expansivity (due to a slope change of the volume) or the heat capacity, which would mark a second order transition between equilibrium states. This justifies the definition of a dynamical transition despite the glass being out of the equilibrium [12, 17].

The glass transition temperature T_g depends on the cooling rate but, since the dependence with temperature of the relaxation time (or the viscosity) is exponential or even faster on cooling, it is in practice very difficult to change T_g significantly, so it is still useful to establish its value.

The glass transition will be more significant for liquids that have a steeper variation of their viscosity η on approaching T_g, than for those that have a milder one. This can be quantified through their fragility m:

$$m = \lim_{T \to T_g} \frac{\mathrm{d} \log \eta}{\mathrm{d} \left(T_g / T \right)} \tag{1.1}$$

which is essentially the slope of the viscosity near T_g on an Arrhenius plot. The relaxation time of a liquid changes together with its viscosity, so both magnitudes can be used interchangeably in the definition of the parameter m. Liquids that display an exponential behaviour on approaching T_g are called "strong" and have small m values, while liquids with super-Arrhenius behaviour, undergoing larger variations, have larger m values and are called "fragile".

Regardless of the meaning of the word "fragile" used in common language, the former classification has nothing to do with the tendency of the material of breaking easily, and it simply indicates how abrupt its glass transition is. Since fragile liquids need a much narrower interval of temperatures to experience huge viscosity or relaxation time changes, they are much better glass formers, easily quenching one or more degrees of freedom even at moderate cooling rates. Far from the glass transition, fragile liquids usually display smaller viscosity and relaxation time variations than strong liquids [12].

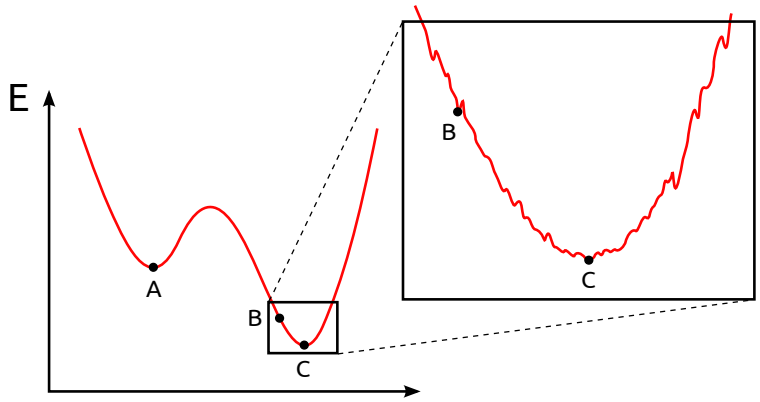

Figure 1.4: Energy landscape of a glass-former material. Point A corresponds to a metastable equilibrium state (local minimum of the energy), point B to an unstable state (out of the equilibrium), and C to a stable equilibrium state (global minimum of the energy).

1.2.3.3 Thermodynamics

Analyses of the energy landscape of the material, that is, the potential energy surface as a function of the particle coordinates, can be very useful to understand the behaviour of supercooled liquids and the formation of glasses [18]. For instance, the roughness of the energy landscape has been linked to good glass formers, that is, fragile ones. An arbitrary energy landscape has been depicted in Figure 1.4.

Supercooled liquids are metastable equilibrium states. Except if they undergo an actual crystallization, measurements over time yield the same properties, because their relaxation time is shorter than their experimental time, so they are able to relax and reach a local equilibrium state where they remain until they crystallize (such as point A in Figure 1.4).

Glasses are out-of-equilibrium states. Their properties depend on the time that has elapsed since they were cooled down below T_g and entered the glassy phase. That is because their relaxation time is larger than the experimental time, so they are in fact being observed during their evolution towards the equilibrium, which means that

they experience ageing (see point B in Figure 1.4 relaxing slowly towards point C due to energy landscape roughness) [1, 12].

For this reason, they are fundamentally disparate states, and structural glasses should not simply be considered highly viscous supercooled liquids [12].

An ergodic system has the same behaviour if averaged over time than if averaged over the phase space, which means that with time the system will explore the different available microstates. At the glass transition a system loses its ergodicity because it is confined to a local minimum of the phase space, and thus is not able to explore a significant portion of the phase space during the available experimental time. This is purely a dynamic effect but nonetheless has measurable consequences.

For instance, the specific heat of supercooled liquids drops to values similar to crystals when they become structural glasses. The explanation is that, in crystals, the only specific heat contribution comes from particle vibrations about the ordered equilibrium positions, because there are no rearrangements, while in structural glasses it mainly comes from particles vibrating as well, because the particles are effectively trapped and there are almost no rearrangements during the experimental time, but in this case the vibration is about the disordered equilibrium positions.

This is a consequence of measuring the specific heat, which is an equilibrium concept, on a glassy system, which is out of equilibrium. Measuring the specific heat on a crystal or a liquid, even if supercooled, does not show this phenomenon because in those systems the experimental time is larger than the relaxation time, so they can readily explore their phase space.

1.2.3.4 Correlation and cooperativity

A correlation function can measure how quickly particle correlations decay with time, such as correlations on their position or orientation. Very often these functions are normalized so that their values lay between one and zero. Where one means that the position or orientation of the particle is perfectly determined by its position or orientation

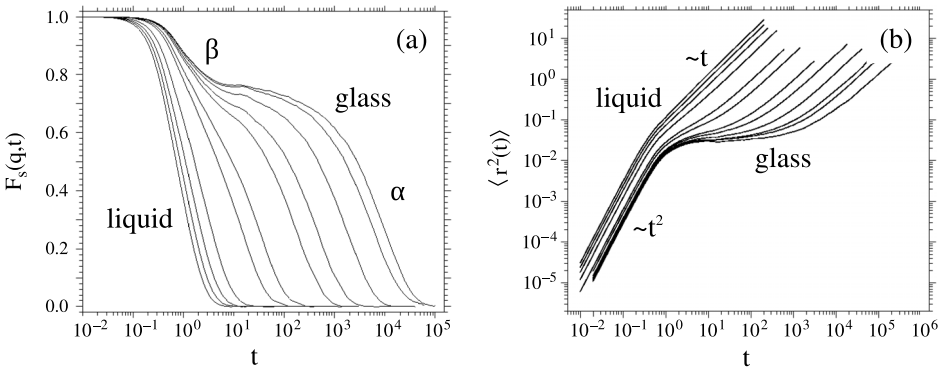

Figure 1.5: (a) In the liquid the correlation function has the short time ballistics regime followed by the diffusive exponential decay. But, when the glass transition is approached, a plateau is formed and a two step relaxation appears. (b) In the liquid the mean square displacement as a function of time shows the crossover from ballistic dynamics to diffusion. However, a plateau interrupting the crossover can be observed as well when the glass transition is approached. *Modified from Refs. [19] and [20].*

at the origin, and zero means that it is completely unrelated to its values at the origin.

At high temperatures, a particle in the liquid will have a ballistic regime for very short times and travelled distances, where it moves freely without interacting. This will be followed by a diffusive regime at longer times and distances, where particle dynamics are determined by the collisions with the rest of the particles, gradually becoming uncorrelated (see Figure 1.5). As the liquid is cooled down, the particles move progressively slower and the correlations last longer until, eventually, a plateau emerges indicating a change in the dynamics near the glass transition, where a two step relaxation takes place. This two step relaxation is a clear signature of any type of glass transition. The fast relaxation process β depends weakly on temperature and does not change much on approaching the glass transition, but the slower relaxation process α does show large variations.

An analysis of the particle mean square displacement in a liquid allows to shed some light on the origin of these two relaxations near the glass transition. At high temperature, the particles move ballistically without encountering any obstacle within very short distances at first (much smaller than interparticle distance), and then they change to diffusive motion at the crossover, where they have to push their way through neighbour particles. As the liquid approaches T_g, the particles keep experiencing the ballistic and diffusive regimes, but a plateau appears in between. This plateau, associated with the distance travelled by the particle in a certain time interval, indicates that the particles get stuck within that distance for a long time before they can actually diffuse.

To understand this behaviour, we can imagine that the neighbours surrounding a particle form a sort of cage. The size of the cage does not change much with the temperature but, as the glass transition temperature is approached, the viscosity increases and the cage becomes very stiff due to the lack of space available to rearrange the particles. Hence, each particle is trapped within this cage, bouncing back and forth, until a great number of neighbours cooperate to 'open' the cage and let the particle go. The β relaxation corresponds to the rattling within the cage, and the α relaxation to the time it requires for the particle to leave the cage, which varies greatly with the temperature because it depends on the mobility of the neighbours. In this picture, all particles are trapped and part of their neighbours cages at the same time.

The relaxation time increases as the liquid is cooled down due to the need of rearranging larger and larger correlated regions, hence, the correlation length increases as the temperature is decreased. Since there is an accentuated cooperative behaviour between the particles, as a consequence, particles tend to cluster together and supercooled liquids near the glass transition show heterogeneous dynamics. Domains of particles with different mobility appear as viscosity increases, segregating themselves in fast or slow clusters [12].

Intramolecular forces are usually much stronger than intermolecular ones. In cooperative systems is normal that very short range interactions propagate up to long distances, even if they are unable

to originate long range order under those conditions [1, 2].

1.2.3.5 Other kinds of glasses

Until now we have been describing glasses as quenched liquids where particles have become positionally and orientationally arrested, and which have thus a similar structure to the original liquid [3]. However, the glass transition is a much more diverse phenomenon than that. In physics, any system that has a disordered degree of freedom that can be dynamically arrested on a non equilibrium state can be a glass, which means that there are a myriad of different kinds of glasses depending on their structure and the degrees of freedom that have been arrested.

Only the three types of glasses with a certain relevance in this work will be mentioned:

Structural glasses These are the standard glasses obtained from liquids which have been extensively described. They maintain their lack of positional and rotational long range order but display certain short range order.

Orientational glasses These glasses are obtained from plastic crystals that have experienced glass transitions. Since the position of molecules in plastic crystals displays long range order, it is their rotational disorder which gets arrested. They yield structures very similar to that of the original plastic crystal (see Figure 1.3).

Conformational glasses These glasses are obtained from materials where the molecules can take more than one possible conformation, and this conformational disorder becomes arrested. Once the conformational glass transition takes place, the time it would take molecules to switch from one conformation to another is longer than the experimental time, so they remain dynamically stuck in the last conformation they had before the glass transition. This can happen regardless of the order or disorder state of other molecular degrees of freedom, such as the

orientational or translational, which may still be able to relax to their equilibrium positions.

If glasses lose all their degrees of freedom as they enter the glass transition, they may be structurally very similar than before becoming a glass, because it will be difficult for particles to rearrange further. However, if not all degrees of freedom are fixed on entering the transition, this will not necessarily be the case any more. For instance, in a conformational glass without rotational arrest, the molecules cannot change their conformation but they can still rotate as a whole, which means that the short range order of such conformational glass can experience large variations as the temperature (or the significant variable) is further decreased.

Regarding the glass transition temperature, although other kinds of glasses may not benefit from the empirical definition using viscosity that was introduced for structural glasses in section 1.2.3.2, they can surely benefit from the more general empirical definition using the relaxation time. Therefore, the glass transition will by definition take place in all kinds of glasses when the dynamical process being arrested reaches a characteristic relaxation time, typically taken between 100 and 1000 seconds.

Although the cage interpretation that was used to understand the two step relaxation in structural glasses is based on the arrangement of the position of the particles, the transition from a one step relaxation to a two step relaxation shows up in all kinds of different systems as the glass transition is approached, which means that the presence of a fast and a slow relaxation is indeed a very fundamental distinctive mark of glassy behaviours, regardless of the degree of freedom that is being arrested [12].

1.3 How to study disordered systems?

To determine the connection between the microscopic molecular interactions and the macroscopic properties of the system has an obvious scientific and technological interest [13].

Gases have been studied since the 19th century, the understanding of crystalline solids experienced an explosion since the middle of the 20th, and scientific efforts during the last 50 years have led to a complete basic understanding of the static and physicochemical properties of liquids. However, no shared theory is able to explain supercooled liquids and the glass transition in a single theoretical framework, although several partial theories have succeeded in explaining some of the features [1, 12, 13, 15, 21].

1.3.1 Statistical description

When a system is perfectly ordered, an ordering rule allows to predict the properties of all its elements, such as the position of all atoms in a crystal from the properties of a single one. This becomes impossible when some randomness is present but, nonetheless, a statistical description of the system can be obtained. A disordered system will show a large deviation from the crystalline structure, hence, it will not be possible to obtain a very detailed description. An order parameter, which quantifies how detailed the structural description can be, might be used to evaluate the degree of disorder [3].

The Wigner-Seitz cell is defined as the smallest volume enclosed by the planes that bisect the lines joining a particle with its neighbours, and is used in crystals as a kind of primitive cell. In disordered structures, the same construction is called Voronoi polyhedron. The number of faces of either of them will equal the coordination number of the atom or molecule. Examples of a Wigner-Seitz cell and a Voronoi polyhedron can be seen in Figure 1.1. Due to the disordered nature of the system, the Voronoi polyhedra will display a range of different geometries. The statistical distributions of volumes, shapes, or first neighbours, provide very useful information to describe the disordered material, but they are hard to link with measurable physical quantities [1, 3].

In practice, the average coordination number and atomic volume of liquid molecules with respect to the crystal are very similar. The greatest difference can be found in the huge local fluctuations of these parameters in the liquid. Unfortunately, this cannot be directly as-

sessed from certain statistical magnitudes that only account for averages [1].

Probability distribution functions are one of the main tools to describe the microscopic structure of disordered materials [3, 4]. The simplest one is the pair correlation function, which can be used to statistically describe the characteristic distances between pairs of elements (atomic nuclei of the same or different species, molecular centres of mass, etc.). The position of the reference element will correspond to the origin, and the probability that another element is found at a certain distance will determine the height of the pair correlation function at that distance. Therefore, the height of the function will depend on the coordination number of that shell [1].

Besides, given that the density of a system is homogeneous, the number of elements at a certain distance of the reference molecule increases as the distance is increased due to purely geometrical reasons, hence, the density of pairs of elements contributing to the pair correlation function will correspondingly increase with the distance.

In perfect ideal crystals, since these distances are precisely defined, their probability distributions in the pair correlation function appear as delta functions (see Figure 1.6(a)). However, the elements of real crystals will always vibrate around their equilibrium positions, which will yield a certain probability distribution about that distance. The area of the probability distribution of each element pair should still be the same that its delta had, but the different peaks may begin to overlap and the analysis become more complicated (see Figure 1.6(b)).

A broadening of the peaks is also obtained if the reason for a distribution of distances is caused by the inherent disorder of the system, such as in a liquid or a structural glass (see Figure 1.6(c)). The difference is that peak broadening about an equilibrium position due to thermal agitation will be similar regardless of how large is the distance to the reference molecule, but variability of the distance between elements due to lack of long range order will gradually increase with the distance. Therefore, as distances become large and the number of peaks in the pair correlation function starts to increase, their overlap in the case of disordered systems quickly leads to a uniform

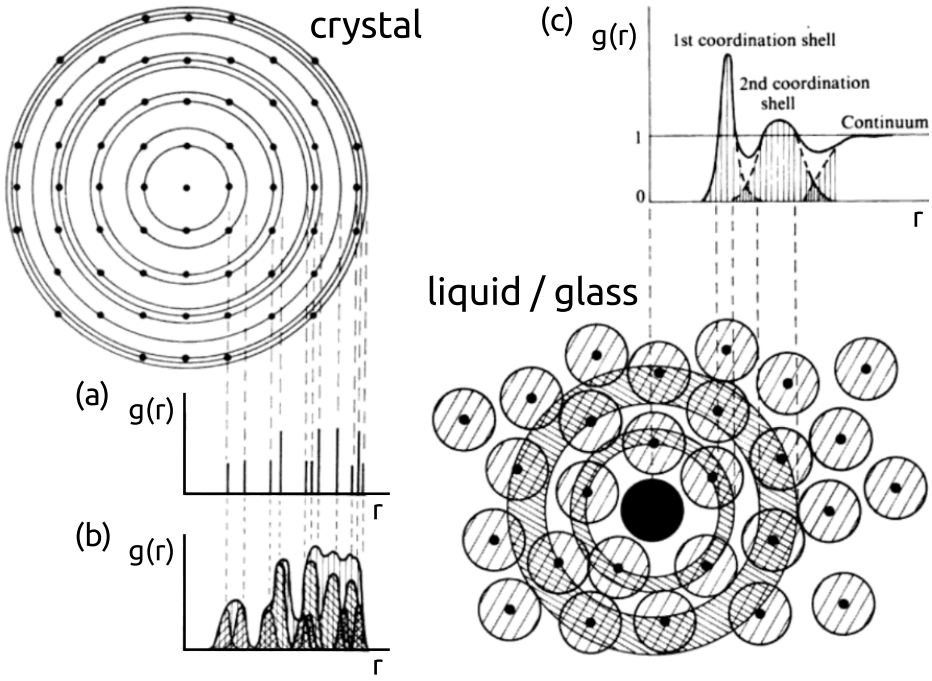

Figure 1.6: Pair correlation function. (a) In the ideal case of a perfect crystal all characteristic distances between the reference particle and the rest of particles are very well determined, so they appear as delta functions. (b) In real crystals the particles vibrate about their equilibrium positions and a certain probability distribution of finding the neighbour particle around each distance is obtained. If the crystal is hot these peak broadenings are larger than if it is cold. (c) In a disordered material, such as a liquid or a structural glass, a distribution of distances is inherent to the variability of possible local arrangements of the system, so the peaks largely overlap, quickly becoming a uniform function at distances where their short range order is lost. *Modified from Ref. [1].*

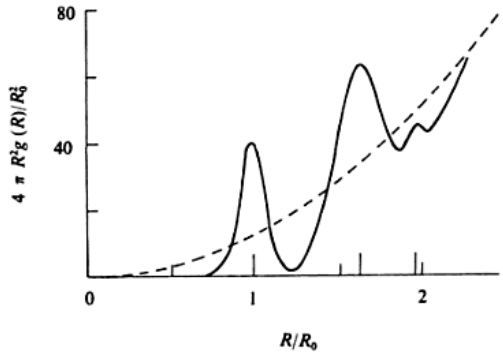

Figure 1.7: Radial distribution function of amorphous Si (solid line) together with the radial distribution function that a continuous medium would yield (dashed line). *Modified from Ref. [1].*

continuum that is conventionally normalised to one.

The radial distribution function contains the same kind of statistical information on the structure of disordered systems (see Figure 1.7). However, the advantage of the radial distribution function is that it is not normalised to the area of the spherical shell at each distance, as the pair correlation function is. For this reason, the fact that the region under consideration is larger and more molecules will be found as the distance to the reference particle increases is reflected on the height of the function. This means that integration of the radial distribution function will directly yield the number of atoms within a coordination shell.

Most theories of simple liquids try to calculate the pair distribution function from the specified intermolecular potential to be able to predict its structural and thermodynamic equilibrium properties. This is so because, if the potential energy can be approximated by pairwise spherically symmetric terms between the atoms or molecules of the liquid, then the thermodynamic properties can be determined only from their pair correlation functions [2, 22].

Besides, the pair correlation function and the radial distribution function can both be obtained, with more or less success, through several scattering techniques. Hence, predictions of theories and models

can be, in principle, directly compared to the experiments.

However, describing the structure of non spherical molecules greatly complicates the problem even if simplified models are used, the relative orientation distribution functions for the different spatial configurations have to be found as well, and they are usually very hard to determine experimentally, if possible at all [1].

1.3.2 Theories and models

For dilute gases, where the constituents are completely disordered, the ideal gas model based on point particles with uncorrelated motion is a good approximation or at least a good basis for the theoretical discussion. There, the thermal motions of particles are explained using random positions and movements, which greatly simplifies the model. Regarding crystalline solids, their highly ordered arrangements introduce many simplifications to describe their structure and construct theories. In particular, application of symmetry principles on the lattice periodicity has allowed huge progress in theory development. The ideal simple model of a perfect crystal with harmonic forces is a good zero order approximation for more refined calculations of most crystals. There, the emphasis is on the structural order which is slightly modified by the particles' thermal motion [3, 11, 15, 23].

Liquids are more complex systems, and neither of these two extreme approximations can be applied. Particles have a significant amount of interaction in a liquid, which results in short range correlations, so they can not be considered to have an uniformly random distribution. But their interaction is not strong enough to neutralise thermal agitation and perfectly determine a regular particle arrangement, which results in symmetry breaking and prevents to use of the same principles that are used in crystals. These short range correlations are very hard to treat analytically, because they do not allow an easy way to reduce the many body dynamics problem to just one or at least a few bodies.

In practice, very few systems have analytical two-body distribution functions available and, if forces are many-body or the potential lacks spherical symmetry, the situation becomes even worse. Ap-

proximate semianalytical methods, such as those based in integral equations or perturbation theories, can be used with varying success for different systems, but computer simulations or modellings, using numerical methods, are nowadays for its adaptability the most extensively used strategies to develop liquid models [13, 24].

The standard statistical physics definition of the correlation function includes a multiple integral of the intermolecular potential for all the particles. For gases, a density expansion can be used that leads to the virial series for thermodynamic functions, but for realistic potentials, only the first terms of the series are known, hence, it can only be used for low density systems. However, the hard spheres model is an exception: several terms of the pressure virial series are available for this potential [22].

Due to the high density of liquids, repulsive forces between atoms or molecules play a dominant role making them almost as incompressible as crystals. The simplest model to take this into account corresponds to mutually impenetrable hard spheres without any other interaction. This is expressed by a potential that is infinite for distances smaller than the radius of the spheres and null for larger values [1].

This ideal model for simple liquids is quite good for most liquids where the constituents are approximately spherical, and is the one most widely used as a first approximation and as the base of further refinements. However, molecules with industrial interest are non spherical and have complex interactions which cannot be characterised by hard spheres or square wells [1, 2, 13, 15, 23].

Integral equations methods consist in using approximations to obtain an integral equation that links the correlation function with a certain potential, and that can be solved analytically or numerically. The two main advantages of these methods are that they can provide with analytic expressions, and that an intermolecular potential can be determined from a known correlation function, which may be very interesting if the latter can be measured. The drawbacks are, on the one hand, that since the obtained correlation function is an approximation, thermodynamic consistency is lost, and, on the other hand, that is not easy in practice to find analytical solutions

to integral equations of correlation functions. The Percus-Yevick and the hypernetted chain methods are two examples of this approach [2, 15, 22, 24].

Perturbative methods consist in establishing a simple well known reference system as the zero order approximation and calculating corrections to that to describe the more realistic problem. The hard spheres system is often used as the reference system in these methods because it is very well known and its analytic expressions are available. The structure of liquids is normally given mainly by packing, which concerns the hard repulsive centre of the intermolecular potential, and attractive interactions can be added as a uniform background potential that does not change the structure. This is the reason that these methods work well in many cases. The disadvantage of these methods is that a suitable reference system which can be used as a first approximation cannot always be found. For instance, the high densities of liquids do not allow normally to use perturbative methods based on non interacting gases. Perturbative methods are used for example by van der Waals, Zwanzig, Carnahan and Starling, or Wertheim theories. This latter perturbative theory allows to build non spherical molecules by joining smaller entities [2, 13, 15].

Computer simulations and modelling are widely used for their adaptability to all kinds of problems and their high accuracy. However, they have the drawbacks that since they are numerical methods they do not provide analytical expressions, and that some techniques only provide solutions compatible to the problem, but which are not unique. Molecular dynamics and reverse Monte Carlo are two popular examples of such methods. The first assumes an interaction potential for the particles and solves the equations of motion of the system averaging over several solutions. The potential can range from very simple models, such as hard spheres or square well, to Lennard-Jones or much more complex ones involving three bodies, non spherical symmetries, or quantum effects. The second modifies an initial structure until its calculated experimental outcome matches the actual experiment [2, 3, 15, 22].

Glasses have additional complications due to being out of equilibrium. On the one hand, it is difficult to take advantage of the

thermodynamic tools that have been conceived to use with equilibrium phases, and on the other hand, thermal history becomes an important player. The reason for this is that, depending on the procedure, different glasses will be obtained, and also that, since glasses are in constant evolution, their properties depend on the time elapsed from the glass transition.

Goldstein's theory of the energy landscape scenario, and mode coupling theory are two examples of theories that try to provide an explanation of the glass transition or the non-equilibrium phases that precede it. The latter, mode coupling theory, tackles relaxations in supercooled liquids. It encompasses a dynamic transition at a certain critical temperature and the two step relaxation at low temperatures. But so far none of the theoretical frameworks provides a complete understanding of the problem [12].

Regarding computational models or simulations, the ample variation of the relaxation times across the glass transition casts an enormous obstacle for these attempts to reach unchallenged realistic solutions, mainly because very demanding computational times are required.

1.3.3 Diffraction experiments

Countless experiments can provide us with information on the structural and dynamic properties of liquids and glasses, however, our emphasis will be on diffraction experiments. It will become apparent, throughout this work, that neutron diffraction has been particularly useful to put to the test computer simulations and models obtained for the systems under study.

This technique allows to measure the differential cross section of our system, which contains averaged structural information of our sample. In monoatomic cases this magnitude is directly related to the pair-correlation function through a Fourier transform and a painstaking series of manipulations of the experimental data. In more complex cases other analogous functions can be obtained from data manipulations and compared to simulations or theoretical models, but interpretation of these functions is less straightforward. Additionally,

since light atoms represent the largest fraction of elements of interest in the compounds studied in this work, and they interact quite weakly with x-rays, neutrons have been chosen as the most suitable diffraction probe [1, 2, 4].

Although other techniques have been used in this work to study the materials of interest, the main stress has been on neutron diffraction, therefore, only this technique will be described in some detail. The following Chapters 2, 3, and 4 will mainly pursue to provide an overview of the main theoretical explanations, experimental procedures, and data treatment used here for this technique.

1.4 Scientific cases in this work

A brief overview is given here to enumerate the various scientific open questions that have been tackled with the methodology presented in this work. An understanding of the short range order of all studied molecular liquids, plastic crystals and glasses is central to explain those scientific problems. All cases have been further explained in more detail in Chapter 6.

1.4.1 Liquid with different high and low temperature behaviours ($C_2Cl_2H_2$)

A number of anomalies between 243 and 257 K have been discovered for this molecular liquid. These are not a consequence of supercooling because its melting temperature is around $T_m = 223$ K. The first to be reported were a tiny density anomaly, manifested as a continuous transition from one straight line to another with the same thermal expansion coefficient, i.e. with the same slope, together with a discontinuity and a minimum in the spin-relaxation time measured by nuclear magnetic resonance (see Figures 1.8(a) and (b), respectively) [28].

Subsequently, a maximum in the specific heat capacity was found through the modulated differential scanning calorimetry technique (see Figure 1.8(c)), which undoubtedly pinpointed the existence of

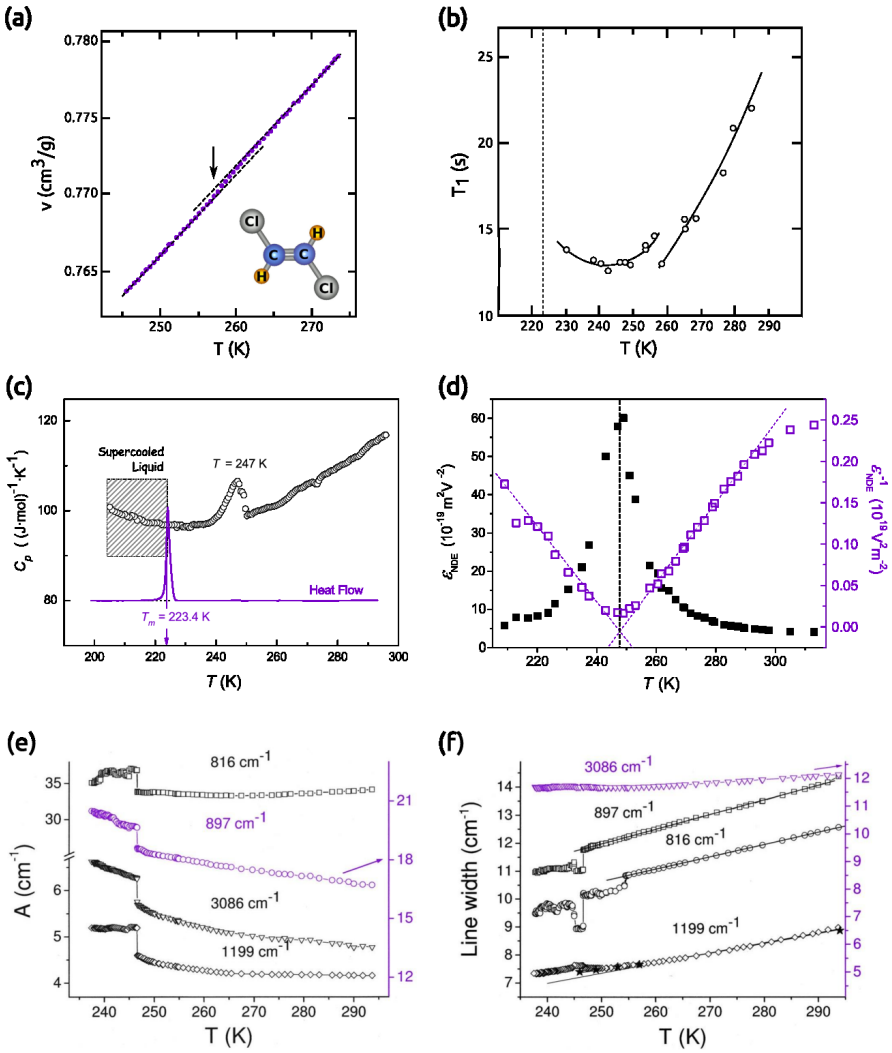

Figure 1.8: Trans-1,2-dichloroethene anomalies between 243 and 257 K. (a) Specific volume, with an inset of the molecular geometry, (b) minimum and discontinuity of the spin-lattice relaxation time, (c) specific heat maximum on cooling with heat flow on heating to show melting point, (d) pretransitional anomaly on the nonlinear dielectric effect, and, lastly, (e) absorbance and (f) linewidth of a few infrared frequency bands. *Modified from Refs. [25–27].*

some sort of transition within the liquid phase and which led some authors to suggest that this was an example of a liquid-liquid phase transition [26]. However, the fingerprints of liquid-liquid phase transitions are still quite unclear and under intense debate, which makes any such classification very polemic. So although it is clear that no first order transition takes place, it has yet to be clarified whether this falls into the liquid-liquid transition scheme or in some other class of transitions yet to be characterised.

Also, nonlinear dielectric effect measurements show a strong pretransitional anomaly, which suggests that, on approaching the transition temperature, fluctuations involving local heterogeneities of several molecules take place (see Figure 1.8(d)) [26]. And infrared spectroscopy measurements exhibit sharp discontinuities in several frequency bands, which denote the transition to a more ordered phase with a locally favoured structure and, thus, enhanced cooperativity (see Figures 1.8(e) and (f)). Besides, the overall temperature dependence of the infrared measurements also suggests that weak hydrogen bonding with chlorine may be playing a role [27].

Therefore, it is very interesting to study this particular behaviour of trans-1,2-dichloroethene and unravel the key differences in the structure and dynamics between the liquid at high and low temperatures. Finding the underlying causes driving its transition could also shed some light on the general mechanisms behind liquid-liquid transitions. The results of these efforts can be found in section 6.1.

1.4.2 Fragile orientational glass ($C_2Cl_2F_2$)

Molecules with the same chemical composition that have their atoms arranged differently are called isomers. Sometimes, a part of a molecule can rotate about a flexible bond between two atoms and change from one geometrical shape to another without breaking any of its bonds. These kind of isomers are called conformations, or rotamers if the molecule needs to overcome a certain energy barrier in order to rotate.

One of such molecules is 1,1,2,2-tetrachloro-1,2-difluoroethane (F-112), that has two different conformations: trans and gauche (see

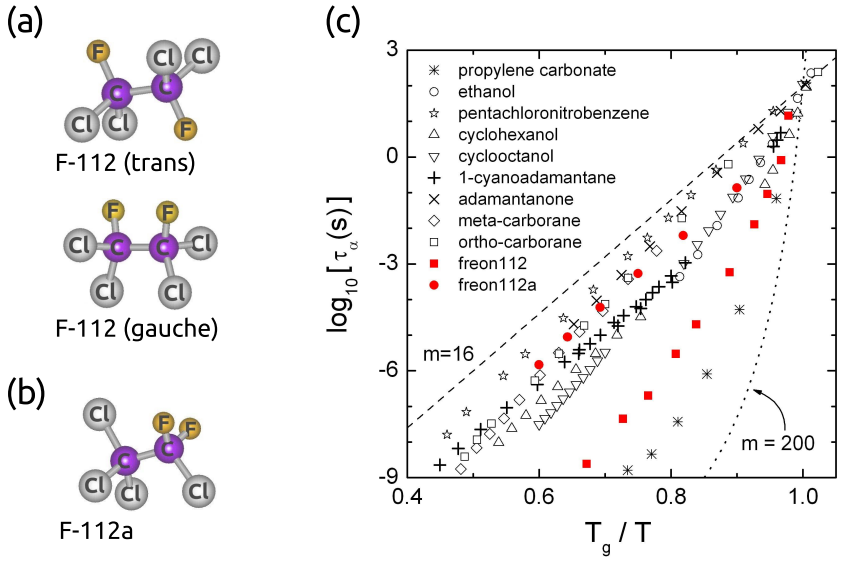

Figure 1.9: (a) The two coexisting conformers of 1,1,2,2-tetrachloro-1,2-difluoroethane (F-112). (b) 1,1,1,2-tetrachloro-2,2-difluoroethane (F-112a). (c) Fragility of compounds F-112 and F-112a compared to other plastic crystals and to propylene carbonate, a typical fragile structural glass former. Strong glasses are closer to an Arrhenius behaviour ($m = 16$) while fragile glasses depart from it. *Figure (c) from Ref. [29].*

Figure 1.9(a)). If the temperature is high and enough energy is freely available, the molecule can easily switch between rotamers and the two coexist in some proportion within the material, which is what happens in its liquid phase.

Below the melting point this compound becomes a plastic crystal, with the centres of mass of its molecules highly ordered in a body centred cubic (bcc) lattice, but with their orientations tumbling about. The rotamers can also switch from one to the other in the higher temperature range of this plastic phase, but at a certain point they stop having enough energy to overcome the rotational barriers and freeze in their last conformation, turning into a conformational glass and leaving only the possibility of reorienting the whole molecule.

If the temperature keeps decreasing and crystallization is avoided, the orientational disorder can become arrested as well, and an orientational glass is formed (see Figure 1.3). Normally, several experimental tricks have to be used to avoid crystallization, but F-112 is a very good glass former and, on the contrary, is very hard to crystallize.

With regards to their behaviour on approaching the glass transition, most orientationally disordered phases are rather strong, showing a moderate temperature dependence. However, F-112 is very fragile, in fact, is the most fragile orientational glass former known so far. This can be assessed in Figure 1.9(c) where the fragility of several plastic crystals, including F-112, is depicted together with that of a typical fragile liquid.

1,1,1,2-tetrachloro-2,2-difluoroethane (F-112a), which is an isomer of F-112 (see Figure 1.9(b)) and displays a plastic phase below the melting temperature that can become an orientational glass as well, is also plotted in this figure and, as can be seen, it is quite strong, as it would be expected of most orientational glass formers. This suggests that the key to F-112 outstanding fragility has to lie on the difference between the two isomers: their molecular geometry.

The glass transition is far from being fully understood but the advantage of investigating these two similar molecules with such different glassy behaviour is that it helps isolate the variables that favour some materials to be better glass formers than others. The results on F-112 and F-112a isomers have been summarised in section 6.2.

1.4.3 Tetrahedral molecules (CCl_4)

Carbon tetrachloride (CCl_4) is a highly symmetric molecule. Since the carbon atom is in the centre of the four chlorine atoms, a perfect tetrahedral intramolecular structure can be assumed, and then only one distance accounting for its size is needed to fully determine its geometry.

This compound has a liquid and a plastic crystal phase which, due to the simple structure of the molecule, have been among the first and most extensively studied disordered phases. In particular, a large number of short range order studies have been carried out to elucidate

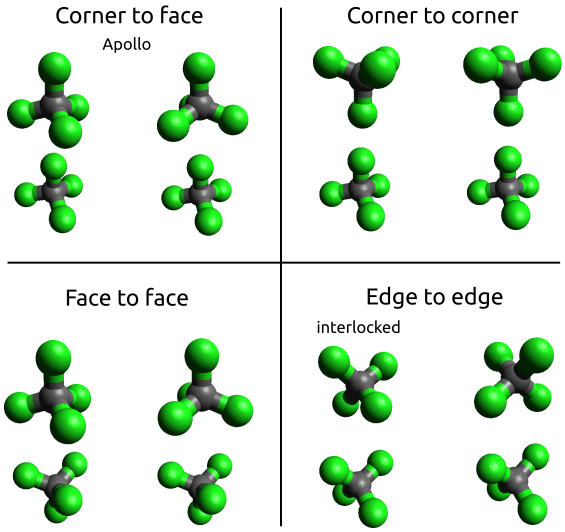

Figure 1.10: A few of the possible relative orientations for pairs of carbon tetrachloride molecules.

the most probable arrangements of the first neighbour. A few possible relative orientations of CCl_4 molecular pairs have been depicted in Figure 1.10. Computer technology advances have allowed better calculations that have challenged widely established CCl_4 structural models, so this compound has still been the object of recent scientific discussions.

One of the open questions that justify further investigations is the so called local density paradox. To introduce this paradox, the pair correlation function between carbon atoms in the liquid and plastic crystal phases is shown in Figure 1.11. Since the carbon atoms correspond more or less to the molecular centres of mass, this corresponds effectively to a pair correlation function of relative positions between the molecules. The profile of the first peak is connected to the probability distribution of distances between a molecule and its first neighbour. As can be seen in this figure, the most likely configuration in the liquid brings the molecules closer than the most likely configuration in the plastic crystal. It would be expected that the phase that allows the molecular pairs to be closer would yield a

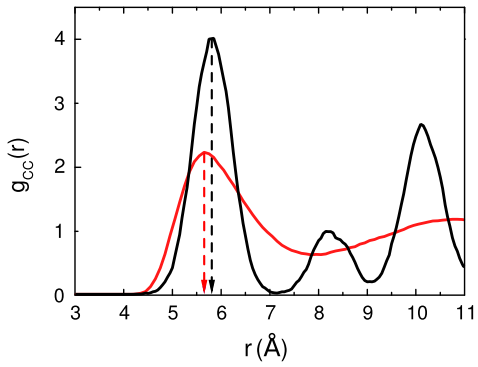

Figure 1.11: Carbon-carbon pair correlation function in the liquid (red) and plastic crystal phases (black) of CCl_4.

higher density, yet this is not the case. On the contrary, the plastic phase of CCl_4 is denser than its liquid.

Although this is not really a paradox due to correlation functions having a statistical nature, which means that the most likely configuration does not necessarily account for the behaviour of the whole system, and that all of them may have to be taken into account to provide a complete picture, these counterintuitive and apparently contradictory results deserve a closer examination of their underlying causes. The solution to this conundrum is explored in Section 6.4.

1.4.4 Quasitetrahedral molecules ($CBrCl_3$ and CBr_2Cl_2)

The intramolecular simplicity of CCl_4 also makes it a perfect candidate to be a model system, which can be used as a reference for other more complex molecules of the tetrahedral family.

Due to its symmetry, the CCl_4 molecule is nonpolar. Consequently, its short range order is essentially determined by steric interactions, which are the repulsive forces preventing two different molecules from occupying the same space. Clearly, when the atomic species of one or more of the molecular sites are substituted, a different contribution to the steric interaction will be obtained for the

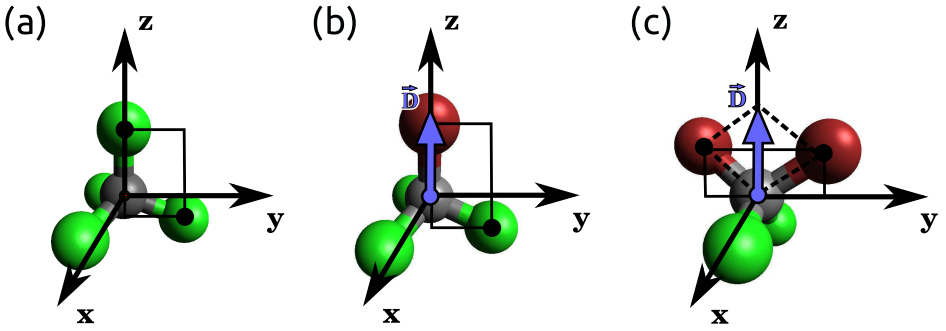

Figure 1.12: (a) CCl_4, highly symmetric and nonpolar, with its four identical and interchangeable carbon-chlorine bonds. (b) $CBrCl_3$, with a rotational symmetry axis that overlaps with one of the CCl_4 axes. (c) CBr_2Cl_2, with the symmetry axis of the dipolar interaction laying in a completely different direction.

new molecule due to the new atom being more or less bulky than the original one. But conveniently enough, many compounds that can be obtained this way, distort their geometry by very little, remaining quite close to the tetrahedral ideal.

However, if for example only some of the four chlorines are replaced, the symmetry of the molecule breaks down and a dipole moment is very likely to appear, which means that the dipolar interaction can potentially become a significant contribution in this other system. For instance, both $CBrCl_3$ and CBr_2Cl_2 show a dipole moment in the direction of the bromine atoms (see Figure 1.12).

To achieve a certain degree of insight on this class of materials, it is necessary to resolve the contributions of the steric and dipolar interactions, and to understand how breaking the symmetry affects the short range order. To determine the influence of each kind of interaction on the short range order of these materials, two strategies can be used: either similar molecules that only differ on the quantities of interest are studied, or computer simulations are performed where the different types of interaction can be suppressed artificially. Both have been undertaken to tackle this problem and are explained in Section 6.5.

1.5 Objectives

The following goals were set for this thesis:

- Development of tools to better systematise the structural analysis of liquids and glasses.
- These tools should ideally be:

  Robust To be sure within reason that the results yielded by the method will not be very far from the real solution or too far from the expected error ranges, regardless of the particular problem.

  Flexible To potentially be able to analyse a wide range of disordered systems.

  Transparent That estimations based on the previous experience of the researcher are always accounted and explicitly quantified, so that they can be subjected to criticism and reproducible analyses are guaranteed.

- Analyse a range of disordered systems using this method in order to explain the microscopic origin, specially of structural features, from certain unexplained properties in these disordered systems:

  TDCE Unravel the microscopic explanation behind its anomalies.

  F-112 Understand the microscopic reasons behind its outstanding fragility.

  CCl_4 Explain the local density paradox.

  $CBrCl_3$ and CBr_2Cl_2 Study the effect on the short range order of quasitetrahedral molecules of the steric and electrostatic interactions.

- Contribute to the general understanding of disordered phases phenomenology through the analysis of these case studies.

Chapter 2

Neutron diffraction theoretical framework

2.1 Why use neutron diffraction?

Scattering techniques consist in measuring how a flux of known characteristics is affected by passing through the sample that is investigated. This flux can be anything that displays interference properties: x-rays, visible light, electrons, neutrons, etc. Typically, the deviation from the impinging trajectory and the energy loss or gain of the probe are measured in these experiments, which allows to determine structural and dynamical characteristics of the sample.

Diffraction is a particular case of these techniques, where the setup allows to assume that the energy exchange of the probes with the sample is negligible compared to the energy of the probes. This means that their velocity does not change its magnitude after interacting with the sample and that only deviations from the initial trajectory have to be measured. This assumption is called static approximation, and is the reason that diffraction experiments can only provide direct information on the structure of the sample but not its dynamics [4, 23].

As has been outlined in Chapter 1, if we intend to study the structure of a disordered material, whose elements organise in a range of different local structures, a statistical description must be used,

so our ultimate goal when studying these materials is to obtain the distribution functions of how the elements arrange within the system.

When measuring these materials with diffraction, every occurring structure contributes with a distinctive scattering and, therefore, the resulting diffractogram reflects an average. Through a series of manipulations of diffraction measurements data, it is possible to obtain, more or less accurately, a few of the distribution functions of the system, which is what makes it one of the most suitable methods to study disordered structures.

In particular, it allows in simple cases to obtain an approximation of the pair correlation function, $g(r)$, which is proportional to the probability of finding a particle at a certain distance of another, but it is possible that other distribution functions are obtained, depending on the complexity of the structure.

The wavelength of the probes used in the diffraction experiment will determine the accessible range of characteristic distances between elements in the sample. Thermal neutrons and x-rays both display a wavelength of the same order of magnitude: about one angstrom, which allows to explore typical interatomic distances.

However, the nature of each probe's interaction with the sample is very different: x-rays interact with the electron cloud of the atom through electromagnetic interaction, while neutrons interact mainly with the nucleus of the atom through the strong interaction [3, 30, 31].

This has a series of practical consequences, such as:

Contrast X-ray scattering cross sections generally increase with the atomic number (with absorption edges providing some of the exceptions). Therefore, the lightest elements are practically invisible, and neighbouring elements in the periodic table are normally indistinguishable due to lack of contrast (see Figure 2.1). However, neutron scattering cross sections vary across the periodic table in a non systematic way, which means that some light atoms are extremely good scatterers, and that two isotopes of the same element can display a huge intensity difference (see Figure 2.2).

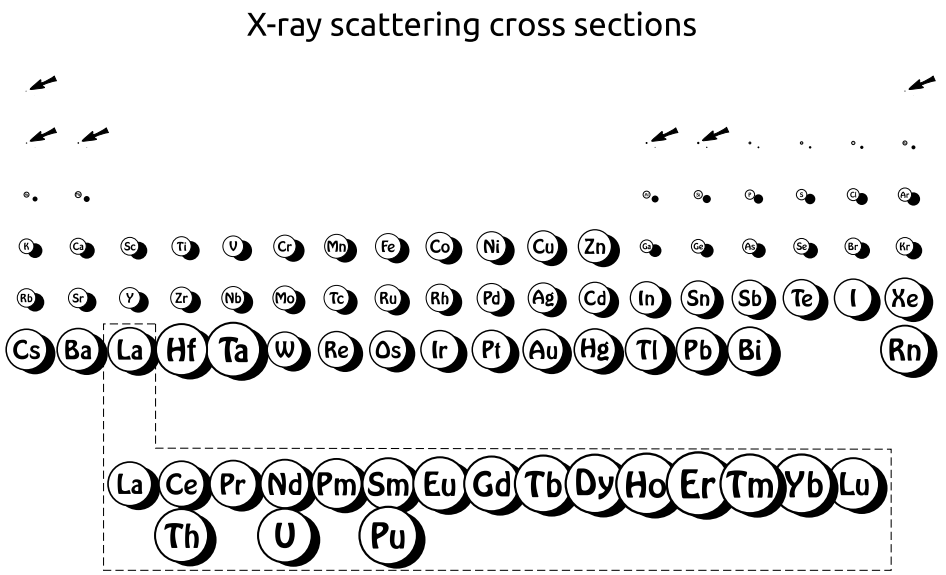

Figure 2.1: X-ray scattering cross sections at 10 keV. As can be observed, diffraction of light atoms (arrows) yields an extremely weak signal with x-ray radiation, if detected at all. *Experimental data to draw the cross sections have been taken from Ref. [32].*

This allows to perform isotopic substitution and enrich the sample with a particular isotope, which has a different scattering cross section, to enhance or diminish the contrast between its components without substantially changing its chemical properties.

Non-destructive bulk technique Neutrons interact with matter much more weakly than x-rays, so the samples do not get damaged during the measurement. This also means that is easier for neutrons to penetrate within the sample and become scattered from the bulk and not the surface but, at the same time, that larger samples are needed to obtain a good measurement.

Simpler analysis In neutron diffraction, nuclei can be considered to be point-like scatterers, hence, neutrons are not sensitive to

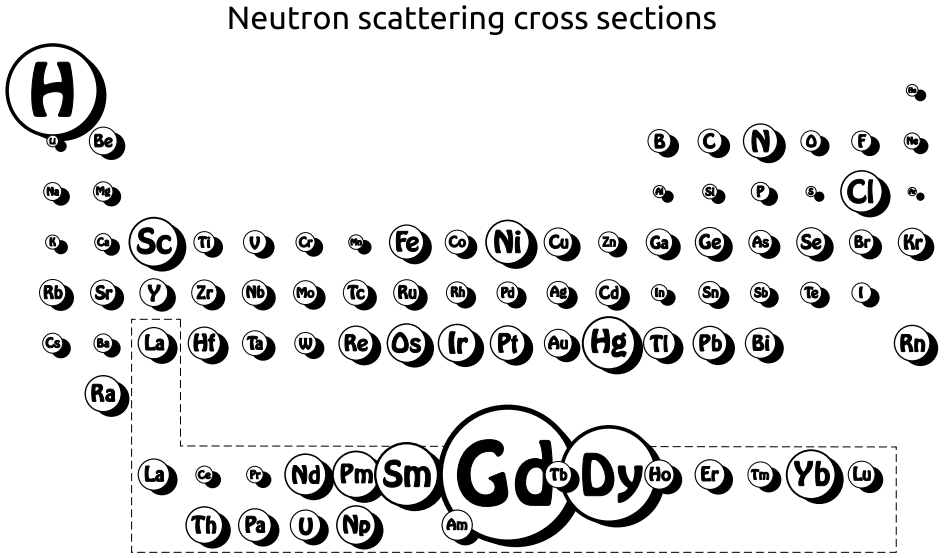

Figure 2.2: Thermal neutron scattering cross sections. As can be seen, scattering intensity using neutron diffraction has an erratic behaviour with respect to the atomic number. Besides, only the averages for the natural abundance of isotopes are shown here, but cross sections can enormously vary between different isotopes of the same element. *Experimental data to draw the cross sections have been taken from Ref. [33].*

their inner structure and scattering of a single atom is isotropic. On the other hand, x-ray scattering intensity is sensitive to the structure of the electron cloud of the atoms (that is, their electron density), so the scattering of a single atom shows an angular dependence. This inner structure of the atom, reflected in the form factor, becomes mixed up with the sample structure and makes the analysis more complex.

Besides, since the rest mass energy of thermal neutrons is much larger than their kinetic energy, they can be considered classical particles and any relativistic effects can be disregarded. X-ray photons, in contrast, with zero rest mass, are always super-relativistic [30].

For these and other reasons, neutron and x-ray scattering are complementary techniques and allow to study different systems, or sometimes, different aspects of the same system. Hence, the particular problem to be studied will determine which is the most appropriate probe to use for the diffraction experiments.

The scientific problems that have been tackled in this work all involve molecules composed fully or in part by light atoms. Since these atoms have small interactions with x-rays, it would be difficult to obtain the complete structure of the molecules under study with them, which supports the choice of neutrons as the diffraction probe.

2.2 Which magnitude is measured?

2.2.1 Cross section

The probability that neutrons in the beam with a certain velocity interact with the sample depends on its composition, that is, what kind of atoms it is made of, and their concentration. Hence, measuring this probability allows to characterize the sample.

This is carried out through the scattering cross section, which is the quotient between I_s, the total intensity scattered by the sample, and Φ_0, the incident flux. The flux provides the number of incident neutrons per unit time that cross a perpendicular unit surface, that is, how many neutrons impinge in the area occupied by the sample. And the total scattering intensity provides the number of scattered neutrons per unit time in all directions, that is, the number of neutrons from the flux that have interacted with the sample. Consequently, the cross section has units of area:

$$\sigma_s \equiv \frac{I_s}{\Phi_0} = \left(\frac{\mathrm{d}n_s}{\mathrm{d}t}\right) \Big/ \left(\frac{\mathrm{d}^2 n_0}{\mathrm{d}t\mathrm{d}s}\right) \tag{2.1}$$

where n_0 and n_s are the incident and scattered neutrons, respectively.

Analogously to the fact that more rain water can be collected if a set of vessels with large cross sections is used than small ones, this effective area is used to characterise the probability that a particular

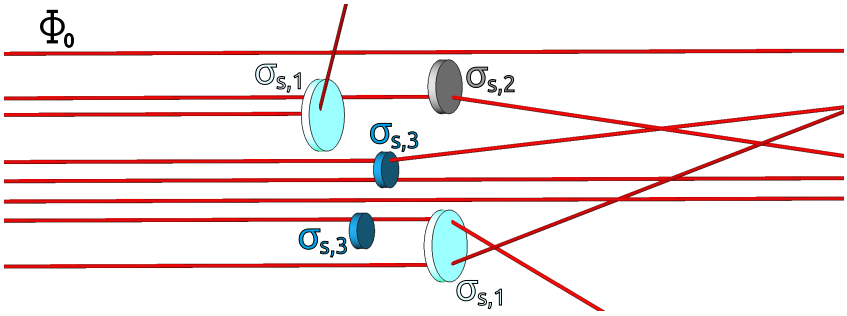

Figure 2.3: Cross section scheme representing three different kinds of atoms under the neutron flux. The scattering cross section σ_s is an effective area used to characterize the probability that each kind of isotope interacts with neutrons of the incoming beam. Nuclei with a higher probability of interacting with neutrons will be simply described by a larger cross section. The same number of neutrons would get scattered if all neutrons impinging in these effective areas were scattered and none of the others were affected.

kind of atom or isotope will be able to influence incoming neutrons (see Figure 2.3). The idea is that this area is the cross section that the atoms would need to have, if 100% of the neutrons impinging in that region interacted with the atom, and none of the others did. Hence, those atoms with higher probabilities of interacting with the neutrons in the beam will be described by larger cross sections and the total cross section of a sample is simply the sum of the individual cross sections of its elements. Figure 2.2 shows the thermal neutron scattering cross sections for each kind of atom, averaged over its natural abundance of isotopes.

The probability that neutrons of the incoming flux will be absorbed by an atom or isotope of the sample can be similarly quantified through a magnitude called absorption cross section.

2.2.2 Differential cross section per atom (DCS)

If the direction of the scattered neutrons is also taken into account, then valuable structural information from the sample, and not only

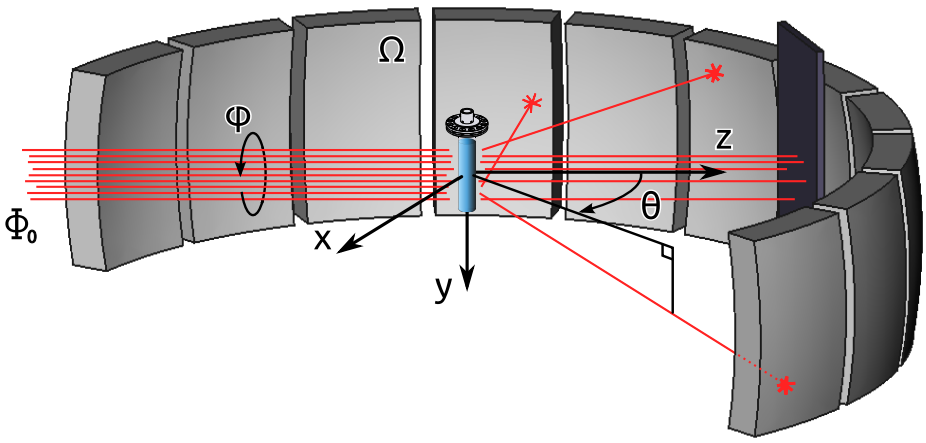

Figure 2.4: Scheme of how the differential cross section is obtained in diffraction measurements. Scattered neutrons are counted by the detector in each direction, and neutrons that did not interact with the sample are absorbed by the beam stopper. For disordered samples such as liquids and glasses, the problem has axial symmetry in the direction of the beam (z axis) and the angle φ does not play a role.

about its composition, can be obtained as well.

In fact, the magnitude that is normally obtained in neutron diffraction experiments is the differential scattering cross section, which is proportional to the probability of finding a scattered particle within a given solid angle. In this case, the number of scattered neutrons per unit time measured in a particular direction $I_s(\theta, \varphi)$, is normalised to the incident neutron flux Φ_0, as well as the solid angle Ω covered by the detector in that position (see Figure 2.4):

$$\frac{\mathrm{d}\sigma_s}{\mathrm{d}\Omega} = \frac{\mathrm{d}}{\mathrm{d}\Omega}\left[\frac{I_s(\theta,\varphi)}{\Phi_0}\right] = \frac{1}{\Phi_0}\left[\frac{\mathrm{d}I_s(\theta,\varphi)}{\mathrm{d}\Omega}\right] \tag{2.2}$$

where the angular dependence of the scattered intensity I_s has been written here explicitly to emphasize it.

For disordered systems such as liquids and glasses, the average structure of the sample is isotropic and the problem can be considered

to have axial symmetry in the direction of the beam, which means that the diffraction patterns consist in circular rings around the z axis (i.e. Debye-Scherrer rings). Since the probability that neutrons get scattered in a certain direction only depends on the angle θ and the angle φ can be disregarded, a bench of detectors spanning across a single semicircle is enough to capture the structural information that can be obtained from the experiment.

Note that the cross section and the differential cross section are extensive magnitudes: they are a sum of all contributions, so the more nuclei in the beam, the more neutrons will be scattered, and more intensity will be measured. This means that if the samples are larger or temperature variations increase their density, these magnitudes will also increase.

In order to be able to compare the structure of different disordered samples regardless of the specificities of each experiment, an intensive magnitude must be used. To this end, a known sample can also be measured, which will allow to normalize the differential cross section measurement of the sample under study and obtain its differential cross section per atom (DCS). However, the density and isotopic composition of both, the sample and the reference material, must be well known.

The ultimate goal of this chapter is to obtain mathematical expressions that connect the experimental DCS measured in diffraction experiments with the probability distributions describing the structure of our systems. Note that, although most concepts are general, the point of view taken here is for diffraction experiments in reactor neutron sources (more details in Chapter 3).

2.3 Scattering by a single nucleus

Before tackling the problem of how to extract sample structures from diffraction measurements, it is good to understand the physical mechanism behind neutron scattering phenomena. To do that, the differential scattering cross section yielded by a fixed single nucleus will be explored in this section.

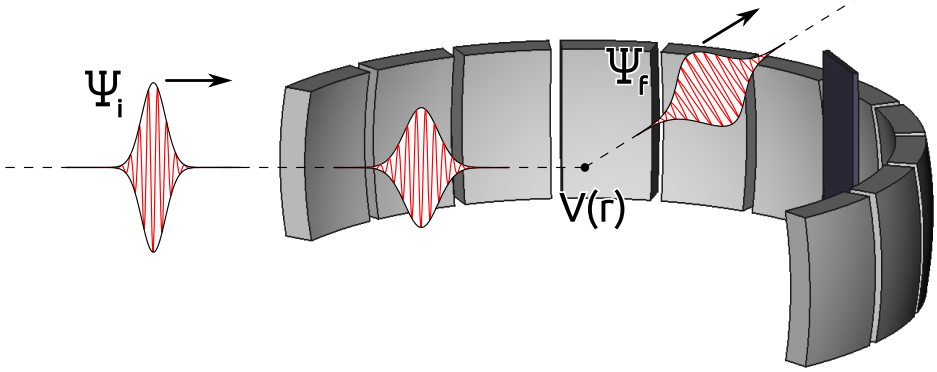

Figure 2.5: Quantum mechanical representation of a neutron scattered by a fixed nucleus when neither the neutron initial position nor momentum are known with absolute certainty. In this case the particle can be represented by a localized wave packet although, even for a free non-interacting particle (far from the nucleus), the position becomes less localized with time due to the uncertainty in its initial velocity.

As shown in Equation 2.2, the differential cross section is obtained from the incident flux Φ_0 and the intensity scattered by the sample I_s, so the next step is to describe these two quantities in terms of the microscopic magnitudes involved in the scattering.

2.3.1 Particle flux

If a beam is homogeneous and perfectly collimated, all particles travel with parallel velocities and the flux is constant along its axis.

In classical mechanics, a uniform collimated flux of particles moving with the same velocity can be easily computed with the expression $\Phi = \rho\, v$, where ρ represents the density of particles, and v their velocity.

In quantum mechanics, particles are represented by wave functions Ψ describing their state and behaviour. However, according to the probabilistic interpretation, wave functions do not carry predicting information about the particular position and velocity of a

particle, but rather they provide information on the distribution of values that would be obtained if these magnitudes were measured for a collection of particles in the same state [34]. For instance, the magnitude $|\Psi(\boldsymbol{r},t)|^2 = \Psi^*(\boldsymbol{r},t)\,\Psi(\boldsymbol{r},t)$ yields the probability density at every specific time and place of finding a particle characterized by the state $\Psi(\boldsymbol{r},t)$. Therefore, the particle flux can be computed instead using the expression $\Phi(t) = |\Psi(\boldsymbol{r},t)|^2 v$, where $\Psi(\boldsymbol{r},t)$ is the wave function describing the state of the particles in the beam, and v is their group velocity [35].

Normally, a heavy particle such as a neutron, characterized by a position and a momentum with their respective uncertainties, can be described by a wave packet, which allows a reasonable localization of the particle. However, even in the simple case of empty space, where the particle does not feel any potential (that is, far from the sample), this uncertainty in its initial velocity translates in an increasing uncertainty on its position at a subsequent time, which means that the wave packet will gradually but inexorably become more delocalised (see Figure 2.5).

In diffraction experiments carried out at reactor sources, the neutron beam wavelength is optimized to the length scale of the structures that are investigated, and only neutrons with that certain wavelength are used. This means that the incoming beam is monochromatic and its neutrons have a well determined initial velocity but that, as a consequence of Heisenberg's Uncertainty Principle, their position is completely unknown.

Far from the sample the particles of the incident beam will not be affected by the interaction potential created by the nucleus, so they will be able to travel freely and the probability of finding a neutron is the same at any point of the incident beam. Therefore, the state of neutrons in the incoming beam can be well described by a plane wave propagating in the direction of the z axis (Figure 2.6):

$$\Psi_0 = \psi_0\, \mathrm{e}^{\mathrm{i}\,(k_0 z - \omega_0 t)} \tag{2.3}$$

where ψ_0 is the amplitude, k_0 the angular wavenumber, and ω_0 the angular frequency of the wave. Plane wave functions represent states with perfectly well defined momenta but complete uncertainty on

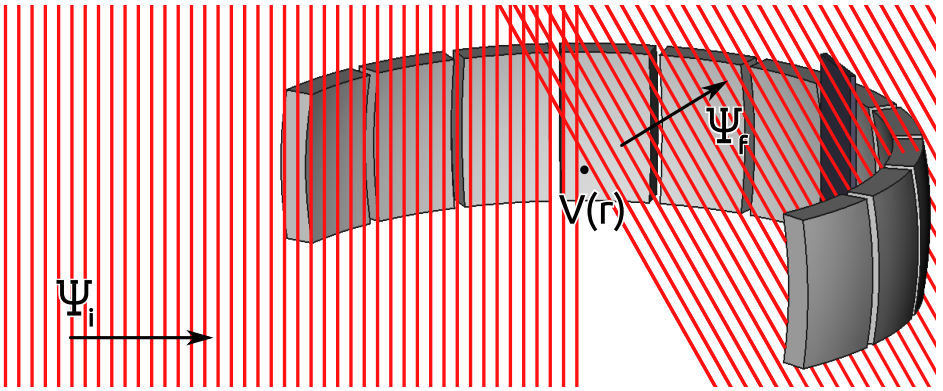

Figure 2.6: Quantum mechanical representation of a particle from an incoming beam scattered by a fixed nucleus when its velocity before and after the event is perfectly known. Since the stationary beam can be characterized by a well defined momentum, but there is no privileged position with a higher probability to find a particle, neutrons can be represented by plane waves.

the position, hence, they will yield the same probability of finding the particle at any point in space. For a neutron beam, the angular wavenumber is $k = (m_n v)/\hbar$ and the frequency $\omega = m_n v^2/2\hbar$, where m_n is the neutron mass, v is its velocity, and $\hbar = h/2\pi$ is the reduced Planck constant.

Within the quantum mechanical formulation, the wave function of any particle must be normalized in order to maintain the physical meaning. This simply means that the amplitude ψ must be chosen so that the probability P of finding the particle somewhere in space is one. However, this is not possible for plane waves because integrating the constant probability density everywhere would yield an infinite probability. A common trick to overcome this problem consists in imagining that the particle is enclosed in a very large box of volume V, and just making sure that the probability of finding the particle inside this box is one:

$$P = \int_V \Psi^* \Psi \, \mathrm{d}v \equiv 1 \tag{2.4}$$

Then, the limit of the solution when this volume tends to infinity can be calculated later on if necessary.

Hence, to normalize the wave function of the neutrons in the incoming beam shown in Equation 2.3, the probability of finding the particle within the box must be set to one:

$$P = \int_V \overbrace{\left[\psi_0 \, \mathrm{e}^{-\mathrm{i}(k_0 z - \omega_0 t)}\right]}^{\Psi^*} \overbrace{\left[\psi_0 \, \mathrm{e}^{\mathrm{i}(k_0 z - \omega_0 t)}\right]}^{\Psi} \mathrm{d}v \tag{2.5}$$

$$= \int_V \psi_0^2 \mathrm{d}v = \psi_0^2 \, V \equiv 1 \tag{2.6}$$

and, therefore, the amplitude of the incoming neutrons wave function must have the value $\psi_0 = 1/\sqrt{V}$. The incoming flux using this wave function is then

$$\Phi_0 = |\Psi_0|^2 \, v_0 = \Psi^* \Psi \, v_0 = \psi_0^2 \, v_0 = \frac{v_0}{V} \quad . \tag{2.7}$$

2.3.2 Determination of the scattering intensity

2.3.2.1 Rate of scattered particles and Fermi's Golden Rule

All particles in the beam begin in the same initial state but, on approaching the nucleus, some will interact with it and get scattered, ending up in a different final state [1]. We are interested in how many particles per unit time will get scattered in a certain direction.

Fermi's Golden Rule (derived by Dirac) allows to compute the transition rate W of particles going from an initial state i to a final state f due to a given interaction potential U:

$$W = \frac{2\pi}{\hbar} |\langle f|U|i\rangle|^2 d_f \tag{2.8}$$

where $\langle f|U|i\rangle$ is called the matrix element, and quantifies the strength of the interaction between the initial and final states, while d_f is the density of final states [23, 36]. The contribution of the density of final states d_f in this expression is expected because statistical physics tells

us that, the more states are available within a certain energy range, the more likely it is that the system will end up in one of the states with that energy (i. e., more particles will get scattered).

However, this expression can only be used when the transition potential U is just a small perturbation to the initial state of the particle. This is because Fermi's Golden Rule is obtained from the more general Lippmann-Schwinger Equation, which describes particle scattering in quantum mechanics, under the condition that the potential is weak and that the resulting state of the neutron beam at every point of the sample can be approximated by its initial state. This assumption is called the first order Born approximation and corresponds to considering that only single scattering events take place during the experiment [1, 23].

Hence, in order to use Fermi's Golden Rule, it is necessary to determine first the character of the potential driving neutron scattering, to ascertain whether it falls within its validity range or not.

2.3.2.2 Character of the nucleus-neutron interaction and Fermi pseudopotential

Even disregarding their electron clouds, bare atomic nuclei are still a very complex ensemble of particles: the strong force compels quarks to stick together in confinement forming protons and neutrons, and an excess of this force is what keeps protons and neutrons together within atomic nuclei. It is also a remnant of this force that affects neutron probes passing by the nucleus in scattering experiments. Consequently, attempting a quantum chromodynamics calculation of the force that nuclei exert upon approaching neutrons would be exceedingly impractical, if not directly unfeasible [30].

Luckily, apart from nuclei being very small, the range of their interaction potential with neutrons is extremely short ranged: it only affects particles about one femtometre away, which is 100.000 times smaller than the wavelengths in the order of the angstrom that characterize thermal neutrons. For this reason, nuclei can be considered to a good approximation to be point-like particles in neutron diffraction experiments and, consequently, their scattering is isotropic (see

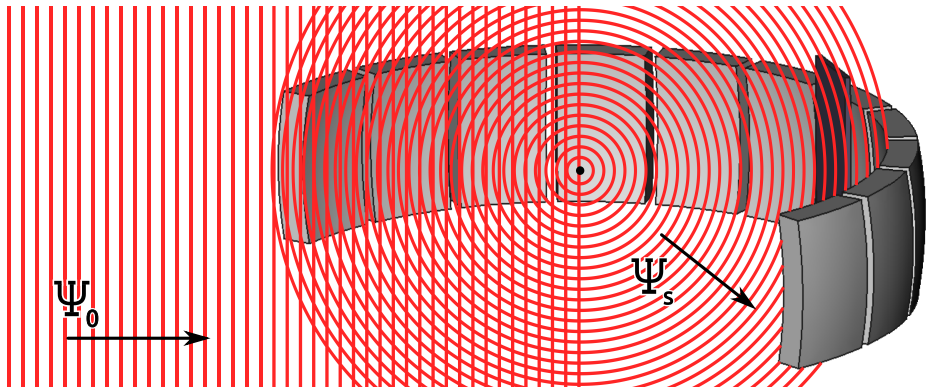

Figure 2.7: Quantum mechanical representation of the scattering of an incoming beam by a single punctual scatterer. Neutrons from the incoming beam can be represented by a plane wave Ψ_0 but, after interacting with a fixed nucleus, they get scattered in all directions and the superposition of their waves becomes a spherical wave Ψ_s. Far from the scatterer the collective spherical wave can also be locally approximated by a plane wave.

Figure 2.7) [30, 36].

The nuclear interaction potential is too strong with respect to the kinetic energy of incident neutrons to be considered a perturbation in Born's approximation, which was described in the previous section. However, a weaker pseudopotential can be constructed that yields the same scattering, as long as this is compensated by an increased interaction range. And since the real potential is so extremely short ranged, this can be done by keeping the extended range of the weaker pseudopotential still small enough to be considered punctual [23, 37, 38].

The Fermi pseudopotential gives an isotropic scattering characterized only by the neutron scattering length b, and can be used for calculation purposes instead of the real potential:

$$U(\boldsymbol{r}) = \frac{2\pi\hbar^2\, b}{m_n}\, \delta(\boldsymbol{r} - \boldsymbol{R}) \tag{2.9}$$

where $\boldsymbol{r}$ and $\boldsymbol{R}$ are the neutron and nucleus positions, respectively,

and b is normally a constant that quantifies the scattering intensity yielded by each kind of isotope. The Dirac delta is used in this effective potential to account for the short range of the interaction between the neutron and the nucleus, which will only take place when both are exactly in the same position.

Since the Fermi pseudopotential is weak enough for the Born approximation to be valid, this means that Fermi's Golden Rule can be used to calculate the rate of scattered particles I_s in a neutron diffraction experiment.

Due to their magnetic moment, neutrons also interact with unpaired electrons in the atomic shell of the atom, but we will disregard these forces because in diamagnetic systems they are much smaller than the nuclear ones [37]. Since any interaction of the neutron with the electron cloud of the atom will hereafter be ignored, the terms atom and nucleus will be used interchangeably from now on.

2.3.2.3 Matrix element for scattered neutrons

After establishing that the Born approximation is valid in most neutron scattering experiments, and that Fermi's Golden Rule can be used to calculate the rate of neutrons that get scattered, the magnitudes appearing in the equation can be computed.

The matrix element appears in Equation 2.8 of Fermi's Golden Rule in bra-ket notation, but it is just a compact denomination for the following integral:

$$\langle f|U|i\rangle = \int \Psi_f^* \, U(\boldsymbol{r}) \, \Psi_i \, \mathrm{d}\boldsymbol{r} \tag{2.10}$$

where Ψ_i is the wave function of the initial state, corresponding to neutrons in the incoming beam, and Ψ_f^* is the complex conjugate of the wave function in the final state, corresponding to neutrons scattered in the direction of one of the detectors.

Both states can be represented by plane waves, because their energy is well defined and the neutron is only affected by the potential U when it is exactly at the same position as the atomic nucleus, so it

can move freely before and after the interaction (see Figure 2.6) [1]:

$$\Psi_i = \frac{1}{\sqrt{V}}\, \mathrm{e}^{\mathrm{i}(\boldsymbol{k_i} \boldsymbol{r} - \omega_i t)} \tag{2.11}$$

$$\Psi_f = \frac{1}{\sqrt{V}}\, \mathrm{e}^{\mathrm{i}(\boldsymbol{k_f} \boldsymbol{r} - \omega_f t)} \tag{2.12}$$

where V is the volume of the imaginary box that contains the scattering experiment, $\boldsymbol{k_i}$ and $\boldsymbol{k_f}$ are the wave vectors, and ω_i and ω_f are the angular frequencies of the initial and final wave functions, respectively.

Note that, since the angular frequency is related to the modulus of its wave vector k through $\omega = \hbar k^2 / 2m_n$, these wave functions can be fully characterized by just their wave vectors.

The spherical symmetry corresponding to isotropic scattering emerges when instead of counting neutrons scattered in a particular direction, all scattered neutrons are taken into account (see Figure 2.7). Such an outgoing spherical wave is observed whenever the wavelength of the probes is significantly larger than the size of the scatterer.

Replacing the initial and final wave functions Ψ_i and Ψ_f in the calculation of the matrix element by the corresponding normalised plane waves:

$$\langle f|U|i\rangle = \int \Psi_f^*\, U(\boldsymbol{r})\, \Psi_i \, \mathrm{d}\boldsymbol{r} \tag{2.13}$$

$$= \int \left[\frac{1}{\sqrt{V}} \mathrm{e}^{-\mathrm{i}(\boldsymbol{k_f} \boldsymbol{r} - \omega_f t)}\right] U(\boldsymbol{r}) \left[\frac{1}{\sqrt{V}} \mathrm{e}^{\mathrm{i}(\boldsymbol{k_i} \boldsymbol{r} - \omega_i t)}\right] \mathrm{d}\boldsymbol{r} \tag{2.14}$$

$$= \frac{1}{V} \int U(\boldsymbol{r})\, \mathrm{e}^{\mathrm{i}(\boldsymbol{k_i} \boldsymbol{r} - \boldsymbol{k_f} \boldsymbol{r} - \omega_i t + \omega_f t)}\, \mathrm{d}\boldsymbol{r} \tag{2.15}$$

where the wave vector is $\boldsymbol{k} = (m_n/\hbar)\, \boldsymbol{v}$, and the angular frequency is $\omega = m_n v^2 / 2\hbar = E/\hbar$, with E being the energy of the neutron in that state.

Since it has been assumed that the nucleus is fixed, no energy from the incoming neutron can be transformed into recoil kinetic energy of the scatterer. Besides, it will be assumed that energy loss due

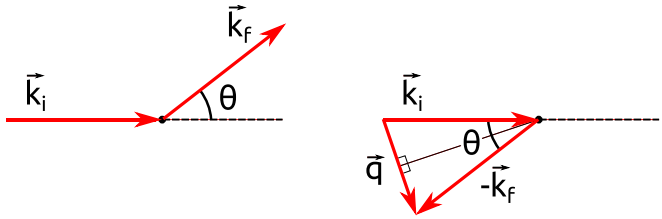

Figure 2.8: Scheme of the relationship between the momentum transfer $\boldsymbol{q}$, the wave vectors $\boldsymbol{k_i}$ and $\boldsymbol{k_f}$, and the scattering angle θ, in the case of elastic scattering.

to an excitation of the nucleus is not possible either, because nuclear excitations are normally in the range of mega electron volts, and neutrons used in scattering techniques are normally at least one million times less energetic than that [23]. Therefore, the scattering will be mainly elastic and the energy of the neutron after being scattered can be approximated by the one it had before the interaction [1].

This means that $\omega_i \simeq \omega_f$, so that the matrix element becomes:

$$\langle f|U|i\rangle = \frac{1}{V}\int U(\boldsymbol{r})\, \mathrm{e}^{\mathrm{i}(\boldsymbol{k_i}-\boldsymbol{k_f})\boldsymbol{r}}\, \cancelto{1}{\mathrm{e}^{-\mathrm{i}(\omega_i-\omega_f)t}}\, \mathrm{d}\boldsymbol{r} \tag{2.16}$$

$$\simeq \frac{1}{V}\int U(\boldsymbol{r})\, \mathrm{e}^{\mathrm{i}\boldsymbol{q}\boldsymbol{r}}\, \mathrm{d}\boldsymbol{r} \tag{2.17}$$

where $\boldsymbol{q} = \boldsymbol{k_i} - \boldsymbol{k_f}$ is the momentum transfer and $\boldsymbol{r}$ is the neutron position.

Figure 2.8 shows that, when the scattering is elastic and, hence, the wave number is the same before and after interacting with the nucleus $|\boldsymbol{k_i}| = |\boldsymbol{k_f}| = k$, the relationship of the momentum transfer with the neutron wave number can be easily computed using simple trigonometric functions:

$$q = 2k \sin\frac{\theta}{2} = \frac{4\pi}{\lambda}\sin\frac{\theta}{2} \tag{2.18}$$

where the identity $k = 2\pi/\lambda$ has been used. From this relationship is also clear that there is a direct correlation between the scattering angle θ and the modulus of the momentum transfer q.

As it can be noted from Equation 2.17, the matrix element under these conditions is proportional to the Fourier transform of the interaction potential.

Fermi's pseudopotential, shown in Equation 2.9, can be introduced in Equation 2.17, and the extremely small range of the potential allows to greatly simplify the calculation of the matrix element:

$$\langle f|U|i\rangle = \frac{1}{V}\left(\frac{2\pi\hbar^2\, b}{m_n}\right)\int \delta(\boldsymbol{r}-\boldsymbol{R})\ \mathrm{e}^{\mathrm{i}\boldsymbol{q}\boldsymbol{r}}\ \mathrm{d}\boldsymbol{r} \tag{2.19}$$

$$= \frac{2\pi\hbar^2\, b}{m_n V}\,\mathrm{e}^{\mathrm{i}\boldsymbol{q}\boldsymbol{R}} \tag{2.20}$$

where $\boldsymbol{R}$ is the nucleus position.

In the particular case of a single nucleus, its position can be simply set as the coordinate origin, and the matrix element is just a constant that depends on the isotope:

$$\langle f|U|i\rangle = \frac{2\pi\hbar^2\, b}{m_n V}\quad . \tag{2.21}$$

2.3.2.4 Density of states

Apart from the matrix element, the density of final states d must also be evaluated to compute the rate of neutrons that are scattered by the sample (see Equation 2.8). This is because a transition is more likely to occur if a particle has a larger amount of available states into which it can resolve [39].

The density of states describes the number of available final energy states per unit volume in an energy interval: $d_f \equiv \mathrm{d}N_E/\mathrm{d}E$. Taking into account that we have assumed purely elastic scattering and that we are measuring the amount of neutrons scattered in a particular direction, only final states where the scattered neutron is travelling in the direction $(\theta,\, \phi)$ with energy $E_f = E_i$ have to be considered.

The scattered neutron states can be described by plane wave functions characterised by their wave vector $\boldsymbol{k} = (k_x, k_y, k_z)$ (see Equation 2.12), which in homogeneous media is also their direction of propagation. However, their energy only depends on the wave number k, the

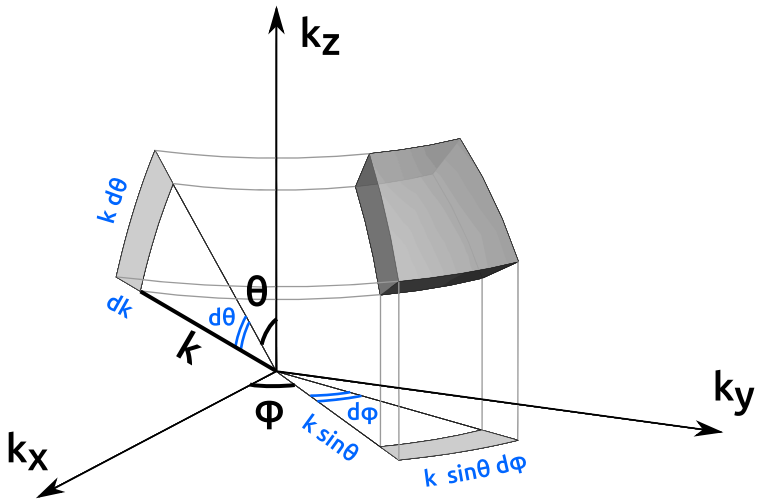

Figure 2.9: Scheme of the calculation of a volume differential in the momentum space in spherical coordinates. The width, height and thickness of the volume are $k \sin\theta \, \mathrm{d}\varphi$, $k \, \mathrm{d}\theta$, and $\mathrm{d}k$, respectively, so the volume in the momentum space occupied by the interval of parameters is $\mathrm{d}V_{\boldsymbol{k}} = k^2 \mathrm{d}k \sin\theta \mathrm{d}\theta \, \mathrm{d}\varphi = k^2 \mathrm{d}k \, \mathrm{d}\Omega$, where $\mathrm{d}\Omega$ is the solid angle occupied by the volume element.

modulus of the wave vector, through the relationship $E = (\hbar^2/2m) \, k^2$. Hence, the number of final states must be evaluated by counting the number of different wave numbers k available with directions between $(\theta, \, \phi)$ and $(\theta + \mathrm{d}\theta, \, \phi + \mathrm{d}\phi)$ and energies E_f and $E_f + \mathrm{d}E$.

A strategy to determine the number of final wave vector states available is to divide the total volume of the interval of interest defined by the aforementioned ranges, $\mathrm{d}V_{\boldsymbol{k}}$, by the volume occupied by a single wave vector state, $v_{\boldsymbol{k}}$:

$$\mathrm{d}N_{\boldsymbol{k}} = \frac{\mathrm{d}V_{\boldsymbol{k}}}{v_{\boldsymbol{k}}} \tag{2.22}$$

Please note that, since the differently scattered neutrons are characterized by their wave vector $\boldsymbol{k}$, these volumes are referring to momentum space volumes, and not real space volumes.

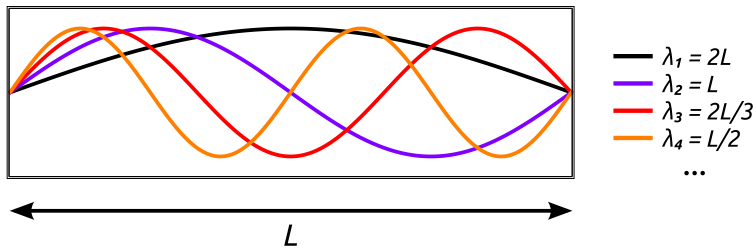

Figure 2.10: Stationary waves allowed in a box of length L must satisfy $\lambda_n = 2L/n$, where $n = 1, 2, 3\ldots$, hence, only certain states are accessible to scattered neutrons. But the direction of propagation (right or left) is not fixed by this restriction, which means that there are two states allowed for each n.

Figure 2.9 shows how the differential volume in the momentum space containing this range of wave vectors can be obtained. The interval with states in the direction $(\theta,\ \phi)$ and energy E_f yields a volume:

$$\mathrm{d}V_{\boldsymbol{k}} = k^2\,\mathrm{d}k\,\mathrm{d}\Omega \tag{2.23}$$

where k is the wave number of the scattered neutron, and $\mathrm{d}\Omega = \sin\theta\,\mathrm{d}\theta\,\mathrm{d}\varphi$ is the solid angle differential in that direction.

Not all wave vectors within the boundaries defined by these energy and direction intervals are really accessible. Recall that we have temporarily adopted the computational artifice of imagining that the whole experiment is enclosed in a large box of volume V, in order to be able to normalise the wave functions. And, due to the fact that a wave can only be stationary within a box when its wavelength value allows it to fit exactly within the boundaries of the box, this trick also prevents the wavelength of the plane wave function from taking arbitrary values, and the system becomes quantized.

For example, in one dimension, if we assume a box of side L, its allowed wavelengths can only be $\lambda_n = 2L/n$, with $n = 1, 2, 3\ldots$ (see Figure 2.10), although the wave can still be travelling in either the positive or negative direction. Since the wavelength and the wave number are related through $k = 2\pi/\lambda$, the only wave numbers allowed will be those conforming to $k = \pm\pi n/L$.

In the case of a scattering experiment contained within the imaginary box of volume V and sides L_x, L_y and L_z, the only wave vectors allowed for scattered neutrons must satisfy:

$$\boldsymbol{k} = \pi \left(\pm \frac{n_x}{L_x}, \pm \frac{n_y}{L_y}, \pm \frac{n_z}{L_z} \right) \tag{2.24}$$

where n_x, n_y and $n_z = 1, 2, 3 \ldots$ Hence, each possible final momentum state is characterized by a combination of three positive or negative integer values: $\pm n_x$, $\pm n_y$, and $\pm n_z$.

This realisation allows us to compute the volume in the momentum space occupied by a single state. The momentum separation between neighbouring states is for each component $\Delta k_x = \pi / L_x$, $\Delta k_y = \pi / L_y$, and $\Delta k_z = \pi / L_z$, which means that each state will occupy a volume of $v_{\boldsymbol{k}} = \pi^3 / (L_x L_y L_z) = \pi^3 / V$ in momentum space (see Figure 2.11).

With the volume occupied in momentum space by our interval of interest $\mathrm{d}V_{\boldsymbol{k}}$, and the volume occupied by a single state $v_{\boldsymbol{k}}$, Equation 2.22 can be used to find the number of final wave vector states available within the interval of interest (see Figure 2.12):

$$\mathrm{d}N_{\boldsymbol{k}} = \frac{\mathrm{d}V_{\boldsymbol{k}}}{v_{\boldsymbol{k}}} = \frac{k^2 \mathrm{d}k \, \mathrm{d}\Omega}{(\pi^3 / V)} = \left(\frac{V}{\pi^3} \right) k^2 \mathrm{d}k \, \mathrm{d}\Omega \tag{2.25}$$

However, although the neutron states are characterised by their wave vector $\boldsymbol{k}$, the density of states is only concerned with the number of energy states, and the energy of each state only depends on its wave number k. Therefore, the combinations of signs in the wave vector components in Equation 2.24 are lost and only the combinations of n_x, n_y, and n_z natural numbers remain:

$$E = \frac{\hbar^2}{2m} k^2 = \frac{\hbar^2}{2m} \left[\left(\frac{n_x}{L_x} \right)^2 + \left(\frac{n_y}{L_y} \right)^2 + \left(\frac{n_z}{L_z} \right)^2 \right] \tag{2.26}$$

This means that there are 8 different wave vectors for each single combination of n_x, n_y, and n_z that give the same energy. This degeneracy has to be taken into account in the calculation of the number of energy states, as a multiplicative factor: $\mathrm{d}N_E = \frac{1}{8} \mathrm{d}N_{\boldsymbol{k}}$.

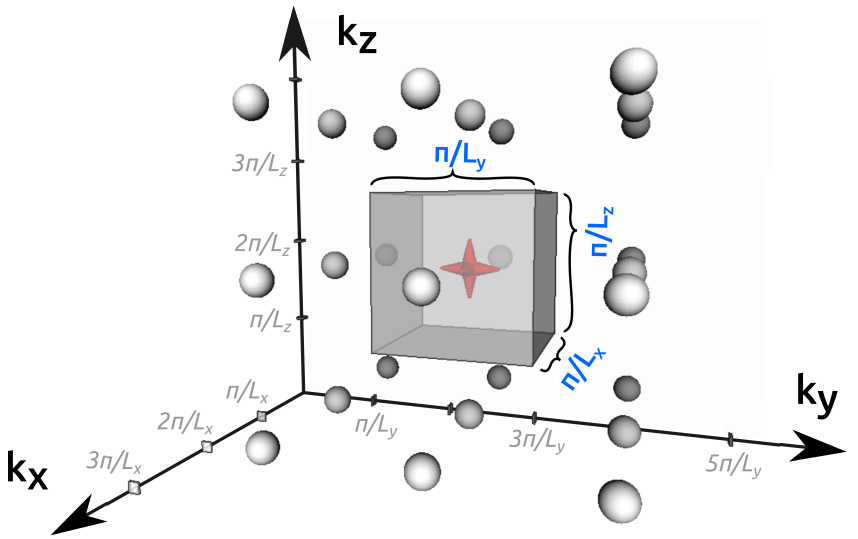

Figure 2.11: If the experiment is enclosed in real space in a cubic box of side L, the separation in the momentum space between allowed states is π/L. Therefore, the volume occupied by each single momentum vector state is $v_k = (\pi/L)^3 = \pi^3/V$.

The dispersion relation in Equation 2.26 also allows to determine that the relationship between the differentials $\mathrm{d}k$ and $\mathrm{d}E$ is

$$\mathrm{d}E = \frac{\hbar^2 k}{m}\mathrm{d}k \tag{2.27}$$

And, finally, substituting the number of momentum states in Equation 2.25 and the relation in Equation 2.27 above into the density of states definition, and taking into account the factor (1/8) due to degenerate energy states, the density of states for neutrons scattered in the direction (θ, ϕ) with energy E_f can finally be put together:

$$d_f \equiv \frac{\mathrm{d}N_E}{\mathrm{d}E} = \left(\frac{\mathrm{d}N_E}{\mathrm{d}k}\right)\left(\frac{\mathrm{d}k}{\mathrm{d}E}\right) \tag{2.28}$$

$$= \left[\frac{1}{8}\left(\frac{V}{\pi^3}\right)k_f^2\mathrm{d}\Omega\right]\left(\frac{m_n}{\hbar^2 k_f}\right) = \frac{V m_n}{8\pi^3\hbar^2}\,k_f\,\mathrm{d}\Omega \tag{2.29}$$

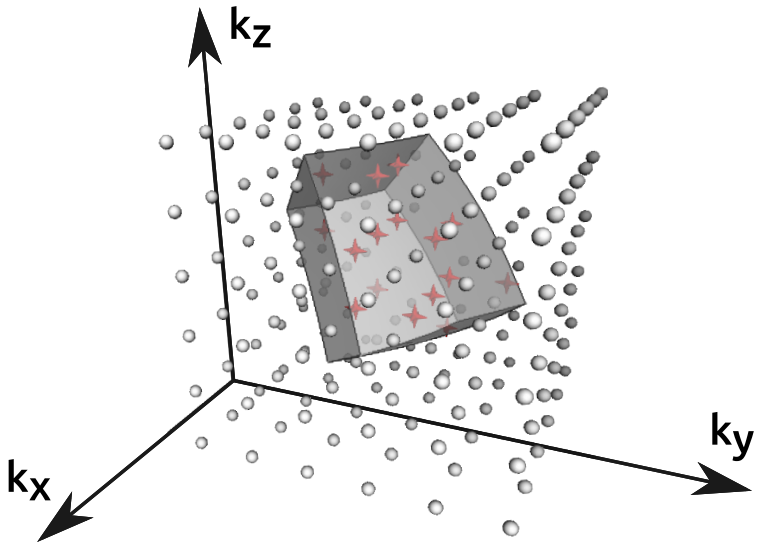

Figure 2.12: To find the number of available momentum states within our interval of interest, we can divide the total volume of the interval of interest by the volume occupied by a single state.

2.3.2.5 Scattering intensity

The two significant magnitudes that appear in Fermi's Golden Rule, i. e. the matrix element for a single fixed nucleus at the origin and the density of states, have now been obtained:

$$\langle f|U|i\rangle = \frac{1}{V}\left(\frac{2\pi\hbar^2}{m_n}\right) b \tag{2.30}$$

$$d_f = \frac{V m_n}{8\pi^3\hbar^2}\, k_f \,\mathrm{d}\Omega \tag{2.31}$$

Whith these, the scattering intensity in a particular direction (θ, ϕ) can now be computed, although the result will not depend on the

direction due to the spherical symmetry of the problem:

$$\mathrm{d}I_s = \frac{2\pi}{\hbar}|\langle f|U|i\rangle|^2 d_f \tag{2.32}$$

$$= \frac{2\pi}{\hbar}\left|\frac{1}{V}\left(\frac{2\pi\hbar^2}{m_n}\right)b\right|^2\left(\frac{Vm_n}{8\pi^3\hbar^2}\,k_f\,\mathrm{d}\Omega\right) \tag{2.33}$$

$$= \frac{\hbar k_f}{Vm_n}\,|b|^2\,\mathrm{d}\Omega = \frac{v_f}{V}\,|b|^2\,\mathrm{d}\Omega \tag{2.34}$$

where $v_f = (\hbar k_f)/m_n$ is the velocity of the scattered neutron.

2.3.3 Differential cross section for a single nucleus

The differential scattering cross section $\mathrm{d}\sigma/\mathrm{d}\Omega$ is proportional to the probability that a neutron leaves the sample in the direction defined by the solid angle element $\mathrm{d}\Omega$. The expression given at the beginning of the section was:

$$\frac{\mathrm{d}\sigma_s}{\mathrm{d}\Omega} = \frac{1}{\Phi_0}\left(\frac{\mathrm{d}I_s}{\mathrm{d}\Omega}\right) \tag{2.35}$$

where $\mathrm{d}I_s$ are the neutrons scattered per unit time counted by an infinitesimal small detector located in the direction (θ,φ), and $\mathrm{d}\Omega$ is the solid angle occupied by this detector.

Now that we have the incident flux Φ_0 (Equation 2.7) and the scattering intensity $\mathrm{d}I_s$ for a particular solid angle differential (Equation 2.34), we can use the differential cross section definition in Equation 2.2 to calculate the scattering due to a fixed single nucleus. Remember that, since the scattering has been assumed to be mainly elastic, the energy of the neutron before and after the interaction is essentially the same, hence, in a general case $v_f \approx v_i$. Applied to this particular case:

$$\frac{\mathrm{d}\sigma_s}{\mathrm{d}\Omega} = \frac{1}{\Phi_0}\left[\frac{\mathrm{d}I_s}{\mathrm{d}\Omega}\right] = \left(\frac{V}{v_0}\right)\left(\frac{v_f}{V}\,|b|^2\right) \overset{\substack{v_f \approx v_0 \\ \downarrow}}{=} |b|^2 \tag{2.36}$$

where the scattering length b is a complex quantity that characterises the neutron-nucleus interaction.

If the neutrons scattered in all directions are taken into account, then the total cross section of the nucleus is recovered:

$$\sigma_s = \int \frac{\mathrm{d}\sigma_s}{\mathrm{d}\Omega}\,\mathrm{d}\Omega = \int |b|^2\,\mathrm{d}\Omega = 4\pi\,|b|^2 \tag{2.37}$$

which exposes the simple relationship that exists between the cross section and the scattering length in this simple case.

Therefore, the macroscopic quantities of the incident neutron flux and the scattered intensity have been successfully described in terms of the microscopic interactions between the particles, which was the goal of this section.

2.4 A few remarks on the scattering length

The neutron scattering length b is introduced by Fermi's pseudopotential (see Section 2.3.2.2), and it is an effective magnitude related to the probability that the neutron and the nucleus interact. Scattering lengths are normally empirical values that are measured and tabulated, as opposed to calculated from first principles [40].

The scattering length is a complex magnitude. By definition its real part is positive if the interaction between the neutron and the nucleus is repulsive, and negative if the interaction is attractive [23]. Most of the naturally occurring elements display a repulsive interaction with neutrons, only about 5% of the isotopes have an attractive interaction. Some of these rare examples are natural hydrogen, lithium, titanium, vanadium, and manganese, which display a negative scattering length. The imaginary part of the scattering length is related to the neutron absorption by the nucleus, and is generally very small [36].

2.4.1 Neutron energy

The probability of interaction between neutrons and nuclei, and thus their scattering length as well, depends on the energy of the incoming

neutrons [1, 41]. However, in reactor sources, diffractometers use monochromatic beams with a well defined incident energy, so the scattering length is usually treated as a constant quantity. Tabulated values normally correspond to thermal neutrons (such as the cross section values used in Figure 2.2) and the scattering length for the energy of interest must be calculated if cold or hot neutrons are used.

2.4.2 Isotopes

Each kind of nucleus has a characteristic interaction with impinging neutrons, which means that the scattering length does not only allow to distinguish between elements, but also between different isotopes of the same element [1, 3].

In practice, most elements are a mix of isotopes with different scattering lengths but, if a random distribution of these isotopes between the atomic sites can be assumed, an average scattering length can be used and this variation only contributes as a flat background without structural information [1, 36].

2.4.3 Nuclear spin

The relative orientation of the neutron spin with respect to that of the nucleus also has an influence on the scattering length. This means that, even in samples with a single isotopic species, the different spin orientations of nuclei give rise to a scattering length distribution.

An exception to this are nuclei from isotopic species without nuclear spin ($I = 0$). In this case, there is no spin contribution to the scattering and all nuclei display the same probability of interaction with incoming neutrons, so they do not have a distribution of scattering lengths. ^{4}He, ^{12}C, ^{16}O, ^{18}O, ^{20}Ne, ^{22}Ne, ^{24}Mg, and ^{56}Fe are some examples of these isotopic species where all nuclei display the same scattering length.

As with the distribution of scattering lengths due to isotopic varieties, a random distribution of nuclear spin orientations among the different atomic sites of the same isotope is normally assumed [36].

Table 2.1: Comparison of the coherent and incoherent scattering lengths for thermal neutrons of the elements used in this work. Incoherent scattering lengths of elements which are a mix of isotopes (H_{nat}, C, Cl, and Br) have been computed from their incoherent cross sections using $b_{incoh} = \sqrt{\sigma_{incoh}/4\pi}$, and their sign is arbitrary. All values have been taken from Ref. [33].

Element	b_{coh} (fm)	b_{incoh} (fm)
H_{nat}	−3.7390	±25.272
D	6.671	4.04
C	6.6460	±0.09
F	5.654	−0.082
Cl	9.5770	±6.5
V	-0.3824	±6.36
Br	6.9	±0.9

2.4.4 Coherent and incoherent scattering lengths

To account for both isotopic and nuclear spin orientation distributions, even present in samples with only one kind of atom, the scattering length is split into two contributions: coherent and incoherent [1].

The coherent scattering length is defined as the average scattering length in the sample: $b_{coh} \equiv \left|\overline{b}\right|$, and the incoherent scattering length is the standard deviation of the distribution with respect to that average:

$$b_{incoh} \equiv \sqrt{\overline{|b|^2} - \left|\overline{b}\right|^2} \tag{2.38}$$

Since isotopic species with nuclear spin $I = 0$ lack a distribution of scattering lengths, they have an incoherent scattering length $b_{incoh} = 0$. Table 2.1 shows the coherent and incoherent values of the scattering length for the particular isotopes and isotopic mixes used in this work.

As already stated above, if the different scattering length values

can be assumed to be randomly distributed between its atomic sites, then the incoherent scattering length of the sample does not contribute to the structural information of the measurement, and is only a homogeneous background.

2.4.5 Free and bound nuclei

It has been assumed up to here that the nucleus is completely fixed and does not experience recoil due to the incident neutron. And, as long as the neutron does not have enough energy to excite the nucleus, this prevents the neutron from losing any energy in the collision and guarantees that the scattering is elastic [42]. The scattering length values that can be found tabulated in the literature normally correspond to this bound scenario.

Although this approximation is assumed to be valid while carrying out diffraction experiments, in practice this is never observed in nature, because the nucleus is never really completely bound.

The other extreme is to consider that the nucleus can move entirely freely, uninfluenced by its surroundings, as it would happen in an ideal gas. There, since the nucleus would undergo recoil, it would lose some energy in the collision and the scattering would be inelastic.

The cross section of a single nucleus bound and totally fixed is $\sigma_s = 4\pi \left|b\right|^2$, but if the nucleus is free and can experience recoil, then its total cross section is modulated by the ratio between the mass of the neutron and that of the nucleus m_n/M:

$$\sigma_s = 4\pi \left| \frac{b}{(1 + m_n/M)} \right|^2 \equiv 4\pi \left|a\right|^2 \tag{2.39}$$

where a is called the free scattering length.

As it can be observed, the probability that a neutron interacts with the nucleus becomes smaller if the latter is free and recoils out of the way, than if it is bound. In the extreme case of hydrogen nuclei (^{1}H isotope), the free scattering length is only half the bound one $a_H = \frac{1}{2} b_H$. It is clear that the larger the nucleus and its inertia, the smaller the m_n/M ratio, and the better the approximation provided by the bound scattering length [42].

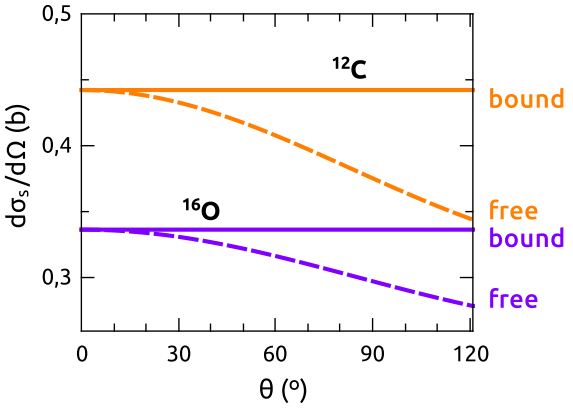

Figure 2.13: Differential cross section for a ^{12}C and ^{16}O isotope. Solid lines correspond to a completely bound nucleus, i. e., without recoil, and dashed lines to a completely free one.

If the nucleus is allowed to recoil, scattering stops being isotropic and starts having a θ dependence even if the scattering object does not have an internal structure [42]. For instance, the differential cross section of a single free nucleus is:

$$\frac{\mathrm{d}\sigma_s}{\mathrm{d}\Omega} = |a|^2 \left[\frac{1 + (m_n/M)^2 \cos 2\theta}{\sqrt{1 - (m_n/M)^2 \sin^2 \theta}} + 2\,(m_n/M) \cos\theta \right] \tag{2.40}$$

where $a = \frac{b}{(1+m_n/M)}$ is the free scattering length, and θ is the scattering angle depicted in Figure 2.4.

Figure 2.13 shows the differential scattering cross section for ^{12}C and ^{16}O isotopes, each with a ratio $m_n/M = 1/12 \sim 8\%$ and $m_n/M = 1/16 \sim 6\%$, respectively, and compares their scattering for a bound and a free nucleus. When the nucleus is bound its differential cross section is the constant $\mathrm{d}\sigma_s/\mathrm{d}\Omega = |b|^2$, as show in Equation 2.36 but, when the nucleus is free, the differential cross section decreases for larger θ angles due to hindered backscattering, although it keeps similar values for smaller ones, where the bound scattering length is always a good approximation.

It must be noted that, in molecular systems, the ones of interest in this work, intramolecular bonds play a significant role, and nuclei are never entirely free, regardless of the intermolecular interaction. In these systems the effective scattering mass is much larger than strictly that of the nucleus, because nuclear movements are transmitted through interatomic potentials allowing the whole molecule to partially experience the recoil. In materials where the molecules are not allowed to undergo a significant translation but are free to rotate as a whole, such as in plastic crystals, the nuclei will still experience a local recoil after the scattering, due to this molecular rotation. However, intermolecular interactions are not negligible in liquids or plastic crystals, so part of the energy lost by the neutron will also be transmitted to nearby atoms and the recoil experienced by a small volume of the sample.

Although it will be assumed from now on that atoms in the disordered materials studied here are perfectly bound, an inelastic correction will have to be carried out to the measurements to account for the inaccuracy of this assumption.

2.5 Scattering by multiple nuclei

2.5.1 From one nucleus to many

The differential cross section for a single atom fixed at the origin has been derived in Section 2.3:

$$\frac{\mathrm{d}\sigma_s}{\mathrm{d}\Omega} = |b|^2 \tag{2.41}$$

where b is the scattering length of that nucleus.

To undertake the computation of the differential cross section of a macroscopic sample, it is possible to assume that its intricate potential is just a superposition of simpler potentials, each corresponding to an individual atom [1]. In this case, the potential can be constructed using a sum of Fermi pseudopotentials $U_j(\boldsymbol{r})$ centred on the

fixed positions of the sample atoms:

$$U(\boldsymbol{r}) = \sum_{j=1}^{N} U_j(\boldsymbol{r}) = \frac{2\pi\hbar^2}{m_n} \sum_{j=1}^{N} b_j \, \delta(\boldsymbol{r} - \boldsymbol{r}_j) \tag{2.42}$$

where j is the atomic site, N is the total number of atoms, m_n is the neutron mass, b_j is the scattering length of the atom at site j, and $\boldsymbol{r}$ and $\boldsymbol{r}_j$ are the neutron and atom positions, respectively.

To derive the differential scattering cross section for a collection of fixed atoms, the procedure used in Section 2.3 can be repeated with the composite potential $U(\boldsymbol{r})$ in Equation 2.42.

The exact steps of the procedure consist in:

1. Calculate the matrix element $\langle f|U|i\rangle$ for this potential:

$$\langle f|U|i\rangle \simeq \frac{1}{V} \int U(\boldsymbol{r}) \, \mathrm{e}^{\mathrm{i}\boldsymbol{q}\cdot\boldsymbol{r}} \, \mathrm{d}\boldsymbol{r} = \frac{2\pi\hbar^2}{V m_n} \sum_{j=1}^{N} b_j \mathrm{e}^{\mathrm{i}\boldsymbol{q}\cdot\boldsymbol{r}_j} \tag{2.43}$$

   where $\boldsymbol{q} = \boldsymbol{k_i} - \boldsymbol{k_f}$ is the momentum transfer.

2. Introduce the matrix element $\langle f|U|i\rangle$, together with the density of final states $d_f = (V m_n k_f \, \mathrm{d}\Omega)/(8\pi^3\hbar^2)$ (details of its calculation in Section 2.3.2.4) into Fermi's Golden Rule, to obtain the scattering intensity differential:

$$\mathrm{d}I_s = \frac{2\pi}{\hbar} |\langle f|U|i\rangle|^2 d_f = \frac{v_f}{V} \left| \sum_{j=1}^{N} b_j \mathrm{e}^{\mathrm{i}\boldsymbol{q}\cdot\boldsymbol{r}_j} \right|^2 \mathrm{d}\Omega \tag{2.44}$$

   where v_f is the velocity of the scattered neutron, and V is the volume of an imaginary box that encloses the experiment.

   (Remember that the use of Fermi's Golden Rule is only possible because it has been assumed that neutrons do not experience any multiple scattering.)

3. Use the incoming flux ($\Phi_0 = v_0/V$), the just calculated scattering intensity $\mathrm{d}I_s$, and the elastic approximation (no significant

amount of energy is lost in the collision, hence, $v_o \simeq v_f$) to obtain the differential scattering cross section:

$$\frac{\mathrm{d}\sigma_s}{\mathrm{d}\Omega}(\boldsymbol{q}) = \frac{1}{\Phi_0}\left[\frac{\mathrm{d}I_s}{\mathrm{d}\Omega}\right] = \left|\sum_{j=1}^{N} b_j \mathrm{e}^{\mathrm{i}\boldsymbol{q}\cdot\boldsymbol{r}_j}\right|^2 \tag{2.45}$$

The scattering length b_j is in general a complex magnitude with real and imaginary components, so the property that $|z|^2 = zz^*$ allows to develop the equation a little further, yielding:

$$\frac{\mathrm{d}\sigma_s}{\mathrm{d}\Omega}(\boldsymbol{q}) = \sum_{j=1}^{N} b_j \mathrm{e}^{\mathrm{i}\boldsymbol{q}\cdot\boldsymbol{r}_j} \sum_{k=1}^{N} b_k^* \mathrm{e}^{-\mathrm{i}\boldsymbol{q}\cdot\boldsymbol{r}_k} \tag{2.46}$$

$$= \sum_{j,k=1}^{N} b_j b_k^* \, \mathrm{e}^{\mathrm{i}\boldsymbol{q}\cdot(\boldsymbol{r}_j - \boldsymbol{r}_k)} \equiv \sum_{j,k=1}^{N} b_j b_k^* \, \mathrm{e}^{\mathrm{i}\boldsymbol{q}\cdot\boldsymbol{r}_{jk}} \tag{2.47}$$

where $\boldsymbol{r}_{jk} \equiv \boldsymbol{r}_j - \boldsymbol{r}_k$ is the relative position between atoms j and k.

This equation describes the differential scattering cross section for a collection of atoms fixed in their positions, each with its known and well defined scattering length b_j.

Since the cross section is an extensive magnitude and grows with the number of atoms that contribute to the scattering, it is often convenient to normalize this magnitude to the total number of atoms in the neutron beam. Such a normalization yields the average differential scattering cross section per atom (DCS), which allows an easier comparison between samples and experiments.

$$\frac{1}{N}\left(\frac{\mathrm{d}\sigma_s}{\mathrm{d}\Omega}\right)(\boldsymbol{q}) = \frac{1}{N}\sum_{j,k=1}^{N} b_j b_k^* \, \mathrm{e}^{\mathrm{i}\boldsymbol{q}\cdot\boldsymbol{r}_{jk}} \tag{2.48}$$

2.5.2 Distribution of scattering lengths

In practice, most samples are composed of atoms with nuclear spin, which scatter differently depending on the relative orientation between the neutron and nuclear spin, or with more than one isotopic

species. This has the consequence that, instead of a unique and well defined scattering length b_j, each atomic species has a distribution of them.

To account for this variability, the different scattering length values are assumed to be randomly distributed among the available atomic sites, and then an average of the differential cross section for all possible permutations of the system is carried out.

Hence, the differential scattering cross section for a collection of atoms fixed at their positions, with nuclear spin or a mixture of isotopic species, is:

$$\frac{\mathrm{d}\sigma_s}{\mathrm{d}\Omega}(\boldsymbol{q}) = \overline{\sum_{j,k=1}^{N} b_j b_k^* \, \mathrm{e}^{\mathrm{i}\boldsymbol{q}\cdot\boldsymbol{r}_{jk}}} = \sum_{j,k=1}^{N} \overline{b_j b_k^*} \, \mathrm{e}^{\mathrm{i}\boldsymbol{q}\cdot\boldsymbol{r}_{jk}} \tag{2.49}$$

where it has been used that $\overline{X+Y} = \overline{X} + \overline{Y}$, and also that $\overline{XY} = \overline{X}\,\overline{Y}$, thanks to the assumption that the scattering lengths distribute randomly among the available atomic sites, and therefore, that they and the positions are independent variables. In this equation, $\overline{b_j b_k^*}$ denotes the average over possible b_j and b_k permutations.

2.5.3 Thermal agitation and ergodicity

Atoms in real matter do not sit perfectly still at their sites. Even in crystalline systems, where nuclei are rather localized, they will always vibrate about their equilibrium positions. As temperature is increased, thermal agitation quickly becomes the dominant contribution to that vibration but, even at the absolute zero, a minimum vibration always remains due to the uncertainty principle. This means that neutrons scattered at different moments interact with slightly different structures, even if they are scattered from the same region, i. e. coherence volume, of the sample.

Disordered systems also undergo such vibrations, but they have an additional disorder arising from the variability of local arrangements that makes distances between its atoms slightly different at each spot, hence, a disordered macroscopic sample is really a collection of many different local structures, even if just a snapshot is taken into account.

Neutron diffraction experiments only allow to extract information about the distribution of structures within the sample. This means that structures that take place at distinct spatial regions are averaged together with structures that take place at different instants of time, and the dynamical disorder caused by thermal agitation is mixed with the static spatial disorder that the sample may have.

Homogeneous systems in equilibrium such as liquids or plastic crystals are ergodic, which means that structures coexisting in different regions of the sample at a particular moment are equivalent to the structures that a particular region explores with time. Therefore, the differential cross section of homogeneous samples in equilibrium can be written as:

$$\frac{\mathrm{d}\sigma_s}{\mathrm{d}\Omega}(\boldsymbol{q}) = \left\langle \sum_{j,k=1}^{N} \overline{b_j b_k^*} \mathrm{e}^{\mathrm{i}\boldsymbol{q}\cdot\boldsymbol{r}_{jk}} \right\rangle \tag{2.50}$$

where the angle brackets $\langle\ \rangle$ denote the average over structural variations due to thermal agitation.

In systems out of equilibrium such as glasses, ergodic theorems do not apply any more, because the system dynamics is arrested and the structure variation between different regions in the sample is much larger than its structural variations through time (see Section 1.2.3.3) [43].

2.5.4 Distinct and self contributions

The differential scattering cross section in Equation 2.50 can be separated in two contributions, one due to the scattering of pairs of atoms located in different sites (distinct), and the other due to the individual scattering of each atom (self):

$$\frac{\mathrm{d}\sigma_s}{\mathrm{d}\Omega}(\boldsymbol{q}) = \underbrace{\left\langle \sum_{\substack{j,k=1 \\ j\neq k}}^{N} \overline{b_j b_k^*}\ \mathrm{e}^{\mathrm{i}\boldsymbol{q}\cdot\boldsymbol{r}_{jk}} \right\rangle}_{\text{distinct}} + \underbrace{\left\langle \sum_{j=1}^{N} \overline{b_j b_j^*}\ \cancel{\mathrm{e}^{\mathrm{i}\boldsymbol{q}\cdot\boldsymbol{r}_{jj}}} \right\rangle}_{\text{self}} \tag{2.51}$$

where $\boldsymbol{r}_{jk} \equiv \boldsymbol{r}_j - \boldsymbol{r}_k$ is the relative position between sites j and k.

Apart from the equivalence $zz^* = |z|^2$, if the different scattering lengths are randomly distributed between the scattering sites and the average includes all possible permutations, its averaged magnitudes do not depend on the site, so the property $\overline{XY} = \overline{X}\,\overline{Y}$ for independent variables can also be used, and the site index in b_j can be dropped, because the average of scattering lengths or their squares will be the same at each site.

For the distinct contribution on the left, it can be derived that:

$$j \neq k \quad \rightarrow \quad \overline{b_j b_k^*} \overset{\text{(independent variables)}}{\overset{\downarrow}{=}} \overline{b_j}\;\overline{b_k^*} \underset{(\overline{b_k}=\overline{b_j})}{\overset{\uparrow}{=}} \overline{b_j}\;\overline{b_j^*} = \overline{b_j}\;\overline{b_j}^* = \left|\overline{b_j}\right|^2 \equiv \left|\overline{b}\right|^2 \tag{2.52}$$

And for the self contribution on the right,

$$j = k \quad \rightarrow \quad \overline{b_j b_k^*} \underset{(k=j)}{\overset{\uparrow}{=}} \overline{b_j b_j^*} = \overline{|b_j|^2} \equiv \overline{|b|^2} \tag{2.53}$$

Since it has been shown that the scattering length factors do not depend on the site, they can be brought outside of the sums:

$$\frac{\mathrm{d}\sigma_s}{\mathrm{d}\Omega}(\boldsymbol{q}) = \left\langle \sum_{\substack{j,k=1 \\ j\neq k}}^{N} \left|\overline{b}\right|^2 \mathrm{e}^{\mathrm{i}\boldsymbol{q}\cdot\boldsymbol{r}_{jk}} \right\rangle + \sum_{j=1}^{N} \overline{|b|^2} \tag{2.54}$$

$$= \underbrace{\left|\overline{b}\right|^2 \left\langle \sum_{\substack{j,k=1 \\ j\neq k}}^{N} \mathrm{e}^{\mathrm{i}\boldsymbol{q}\cdot\boldsymbol{r}_{jk}} \right\rangle}_{\text{distinct}} + \underbrace{\overline{|b|^2}\, N}_{\text{self}} \tag{2.55}$$

The self term accounts for the diffraction of individual sites. It is independent of the position and provides a uniform intensity level of scattering. The distinct term accounts for the diffraction of nuclei pairs, which depends on their relative position and causes interference, reflecting spatial correlations between the two nuclei. This contribution oscillates around the constant intensity value provided by

the self term and becomes zero when there are no spatial correlations between the pairs.

For convenience, the interference function $H(\boldsymbol{q})$, containing all spatial correlations, can be defined:

$$H(\boldsymbol{q}) \equiv \frac{1}{N} \left\langle \sum_{\substack{j,k=1 \\ j \neq k}}^{N} \mathrm{e}^{\mathrm{i}\boldsymbol{q}\cdot\boldsymbol{r}_{jk}} \right\rangle \tag{2.56}$$

This function reflects local correlation fluctuations, so it will oscillate around zero, its value in absence of spatial correlations, and provides a measure of the underlying order. It is also a dimensionless magnitude normalised to the total number of atoms in the sample N, which allows to easily compare the degree of ordering between samples.

Replacing this definition of $H(\boldsymbol{q})$ in Equation 2.55, the differential scattering cross section per atom becomes:

$$\frac{1}{N}\left[\frac{\mathrm{d}\sigma_s}{\mathrm{d}\Omega}(\boldsymbol{q})\right] = \underbrace{\left|\bar{b}\right|^2 H(\boldsymbol{q})}_{\text{distinct}} + \underbrace{\overline{|b|^2}}_{\text{self}} \tag{2.57}$$

2.5.5 Coherent and incoherent contributions

The distinct contribution on the left of Equation 2.55 does not include any terms where $j = k$. These missing terms can be easily added together yielding

$$\left|\bar{b}\right|^2 \left\langle \sum_{j=1}^{N} \mathrm{e}^{\mathrm{i}\boldsymbol{q}\cdot\boldsymbol{r}_{jj}} \right\rangle = \left|\bar{b}\right|^2 N \tag{2.58}$$

and then added to the left addend and subtracted to the right addend of Equation 2.55, to be able to perform the summation for all combinations of j and k values.

This operation allows to obtain another version of the general equation for the scattering cross section that is separated into coher-

ent and incoherent contributions instead:

$$\frac{\mathrm{d}\sigma_s}{\mathrm{d}\Omega}(\boldsymbol{q}) = \underbrace{\left|\overline{b}\right|^2 \left\langle \sum_{j,k=1}^{N} \mathrm{e}^{\mathrm{i}\boldsymbol{q}\cdot\boldsymbol{r}_{jk}} \right\rangle}_{\text{coherent}} + \underbrace{\left(\overline{|b|^2} - \left|\overline{b}\right|^2\right) N}_{\text{incoherent}} \tag{2.59}$$

The coherent term accounts for the average scattering in terms of the scattering length of all atomic sites, including the scattering of individual sites and the scattering of nuclei pairs with spatial correlations that give rise to interference. And the incoherent term accounts for the individual variations of scattering lengths across the sample and provides a constant value that is independent from any spatial correlations. Please note that, although they are often confused, the incoherent term and the self term are not equivalent magnitudes and have different meanings (see Equations 2.55 and 2.59).

As was already explained in Section 2.4.4, the average scattering length is also called the coherent scattering length ($\left|\overline{b}\right| \equiv b_{\mathrm{coh}}$) and its standard deviation is the incoherent scattering length ($\overline{|b|^2} - \left|\overline{b}\right|^2 \equiv b_{\mathrm{incoh}}^2$).

For convenience, a function called structure factor $S(\boldsymbol{q})$, containing all spatial correlations plus the coherent (i. e. average) self terms, can be defined:

$$S(\boldsymbol{q}) \equiv \frac{1}{N} \left\langle \sum_{j,k=1}^{N} e^{\mathrm{i}\boldsymbol{q}\cdot\boldsymbol{r}_{jk}} \right\rangle \tag{2.60}$$

This function contains all contributions except the incoherent (i. e. variation from the average) self terms, that don't give rise to any interferences. Since this function contains local correlation fluctuations deviating from a uniform average (represented by one), it allows to quantify the order in the sample. Therefore, its value is one when no correlations are present and, otherwise, positive and negative correlations oscillate around this value. It is a dimensionless magnitude normalised to the total number of atoms in the sample N, such as the interference function $H(\boldsymbol{q})$ in Equation 2.56, so it allows to compare the ordering degree in a similar way.

The only difference between both magnitudes is that $H(\boldsymbol{q})$ contains only distinct terms and thus oscillates about zero, while $S(\boldsymbol{q})$ also contains the constant coherent self terms so it oscillates around one. Hence, they are simply related by $H(\boldsymbol{q}) = S(\boldsymbol{q}) - 1$. And for completely uncorrelated samples, such as ideal gases, their values will be $H(\mathrm{q}) = 0$ and $S(\mathrm{q}) = 1$ [1].

Replacing this definition of $S(\boldsymbol{q})$ in Equation 2.59, the differential scattering cross section per atom becomes:

$$\frac{1}{N}\left[\frac{d\sigma_s}{d\Omega}(\boldsymbol{q})\right] = \underbrace{b_{\mathrm{coh}}^2\, S(\boldsymbol{q})}_{\text{coherent}} + \underbrace{b_{\mathrm{incoh}}^2}_{\text{incoherent}} \tag{2.61}$$

2.6 Scattering by disordered samples

2.6.1 Monoatomic systems

By monoatomic liquid or glass is meant a substance formed by individual atoms, not molecules, and where all of them are from the same atomic species, that is, they have the same atomic number.

As has already been mentioned, more often than not, a range of scattering lengths will be present in the sample due to different isotopes of the same element or, if the nucleus has a non zero spin, due to the different spin states. However, the scattering lengths will be considered to be randomly distributed among the nuclear sites and not correlated.

2.6.1.1 DCS of monoatomic liquids and glasses

The differential scattering cross section per atom (DCS) depends in general of the vectors $\boldsymbol{q}$ and $\boldsymbol{r}_{jk}$ and their relative orientation (see Equations 2.50, 2.55, and 2.59). However, in homogeneous samples for which the average structure is isotropic, such as in many liquids and glasses, the orientational variations are averaged out and only their norms $q = |\boldsymbol{q}|$ and $r_{jk} = |\boldsymbol{r}_{jk}|$ can have a role in the the calculation.

This is because in such disordered arrangements of atoms, there are still characteristic distances between atom pairs, but the vector $\boldsymbol{r}_{jk}$ describing their relative position takes random directions, which means that the relative orientation between $\boldsymbol{q}$ and $\boldsymbol{r}_{jk}$ is also random. If the average of the exponential factor is computed for such a distribution of relative orientations, we obtain:

$$\left\langle\left\langle \mathrm{e}^{\mathrm{i}\boldsymbol{q}\cdot\boldsymbol{r}_{ij}} \right\rangle\right\rangle = j_0\left(q\, r_{ij}\right) = \frac{\sin\left(q\, r_{ij}\right)}{\left(q\, r_{ij}\right)} \tag{2.62}$$

where $\langle\langle\ \ \rangle\rangle$ denotes an average over all possible directions, and $j_0\left(z\right)$ is the zeroth order spherical Bessel function [42].

This allows to simplify the exponential in the interference function and to exchange the vector $\boldsymbol{q}$ dependence by the norm q:

$$H\left(q\right) = \frac{1}{N}\left\langle \sum_{\substack{j,k=1 \\ j\neq k}}^{N} \frac{\sin\left(q\, r_{jk}\right)}{q\, r_{jk}} \right\rangle \tag{2.63}$$

On a practical note, it is interesting to determine the value of the self term, on the right of Equation 2.57, because it provides the baseline level for the correlation oscillations and it can help to quickly determine the accuracy of the normalisations performed to the experimental data.

Since the scattering length can be written in terms of the scattering cross section ($\sigma_s = 4\pi\left|b\right|^2$), it is quite clear that the self term is simply:

$$\overline{\left|b\right|^2} = \frac{\overline{\sigma_s}}{4\pi} = \frac{1}{4\pi}\sum_{\alpha=1}^{n} c_\alpha \sigma_s^\alpha \tag{2.64}$$

where α designates each different isotope in the sample, n is the total number of isotopes, and c_α is the concentration of that particular species.

Therefore, the differential cross section per atom in **monoatomic** liquids or glasses will be:

$$\frac{1}{N}\left[\frac{\mathrm{d}\sigma_s}{\mathrm{d}\Omega}(q)\right] = b_{\mathrm{coh}}^2 H(q) + \frac{\overline{\sigma_s}}{4\pi}$$

$$\boxed{\frac{1}{N}\left[\frac{\mathrm{d}\sigma}{\mathrm{d}\Omega}(q)\right] = b_{\mathrm{coh}}^2 \frac{1}{N}\left\langle \sum_{\substack{j,k=1 \\ j\neq k}}^{N} \frac{\sin\left(qr_{jk}\right)}{qr_{jk}} \right\rangle + \frac{\overline{\sigma_s}}{4\pi}} \tag{2.65}$$

Remember that q is directly related the the scattering angle θ through the following relationship (only valid when the scattering is essentially elastic and $k_i \simeq k_f$):

$$q = |\boldsymbol{q}| \simeq \frac{4\pi}{\lambda} \sin\frac{\theta}{2} \,, \tag{2.66}$$

where λ is the neutron wavelength. Hence, the scattering intensity in isotropic materials has an axial symmetry around the direction of the incoming beam, and the measured diffractogram will be a series of concentric rings only dependent on the θ angle.

2.6.1.2 Correlation functions in real space

A microscopic description has been obtained for the DCS measurement, which can be already used to analyse the sample. However, it is not straightforward to grasp the characteristics of the system through a function in reciprocal space, such as the DCS, the interference function or the structure factor, because the contributions of the characteristic distances are spread in the form of complex oscillations.

On the other hand, the pair correlation function, which is in real space, is proportional to the probability of finding an atom at a certain distance from a reference atom, so a description of the experiment in terms of this more intuitive magnitude is quite useful.

In real samples, atoms occupy a certain volume and it is impossible to find another particle in the very same spot, so this probability must be zero at very small distances. And at large distances the probability becomes constant, because the disordered nature of the systems provides a range of different possible structures that average out, yielding a featureless profile. The pair correlation function is constructed so that for large distances this constant is normalised to one.

Luckily, the pair correlation function $g\,(r)$ and the interference function $H\,(q)$ or the structure factor $S\,(q)$ are simply related by a Fourier transform:

$$g(r) = 1 + \frac{1}{2\pi^2 \rho r} \int_0^\infty q\, H(q)\, \sin\,(qr)\, \mathrm{d}q \tag{2.67}$$

$$\begin{aligned} H(q) &= \frac{4\pi\rho}{q} \int_0^\infty r\, \left[\, g(r) - 1\right] \sin\,(qr)\, \mathrm{d}r \\ &= S(q) - 1 \end{aligned} \tag{2.68}$$

where ρ is the average number density of atoms in the sample.

From this expression is clear that, since $g\,(r) \to 1$ for $r \to \infty$, the integral to infinity would diverge if a direct Fourier transform of $g\,(r)$ was carried out. This is why the function $g\,(r) - 1$ has to be transformed instead to shift from the real to the reciprocal space.

In practice it is not easy to obtain the experimental pair correlation function of the sample. Any diffraction experiment has practical limitations that make it impossible to measure $H\,(q)$ for arbitrarily small values or up to infinity, so the integral in Equation 2.67 can only be carried out between a certain q-range, and errors inevitably build up on the resulting $g\,(r)$ [1].

The radial distribution function (RDF) is the average number of elements in a spherical shell of radius r and differential thickness dr, and is defined as [2]:

$$\mathrm{RDF}\,(r) \equiv 4\pi r^2 \rho\, g(r) \tag{2.69}$$

where ρ is the average number density of atoms in the sample, and $g(r)$ accounts for the local density fluctuations. Hence, the RDF is the radial density of the sample at a certain distance of the reference molecule, which means that, for purely geometric reasons, homogeneous systems will not yield a constant value with the distance, but a quadratic growth instead.

It can also be integrated to obtain the coordination number (CN) of a certain shell, which gives the average number of atoms at a

certain range of distances from the reference atom:

$$\mathrm{CN} = \int_{r_1}^{r_2} \mathrm{RDF}\,(r)\,\mathrm{d}r = 4\pi\rho \int_{r_1}^{r_2} g\,(r)\,r^2\mathrm{d}r \tag{2.70}$$

where r_1 and r_2 are the minimum and the maximum distances, respectively.

These distribution functions in real space must all be zero for distances smaller than the hard core of the reference element, which reflects that strong repulsion forces prevent atoms from occupying the same space [1].

2.6.2 Polyatomic systems

Here a polyatomic liquid or glass is understood as a substance formed by a mixture of different atomic elements, but where these still do not form molecular structures.

A different approach is needed for these systems, because there is normally a spatial correlation between the scattering lengths corresponding to different types of atoms, i. e., atoms with positive charge may have a tendency to be surrounded by negatively charged atoms. However, the different scattering lengths that correspond to the same atomic species, i. e., due to isotopic or nuclear spin state variations, are still considered as randomly distributed between those atoms.

2.6.2.1 DCS for polyatomic liquids and glasses

The aim in this section is to elaborate the distinct and self terms to obtain an expression for the DCS that allows to determine the structure of these samples.

The self term does not depend on the position so it remains identical as in Equation 2.65 ($\overline{\sigma_s}/4\pi$). However, the distinct term in Equation 2.55 is represented here for polyatomic liquids and glasses by the total interference function $F(q)$ instead of the $b_{\mathrm{coh}}^2 H(q)$ used in the previous section:

$$\frac{1}{N}\left[\frac{\mathrm{d}\sigma_s}{\mathrm{d}\Omega}(q)\right] = F(q) + \frac{\overline{\sigma_s}}{4\pi} \tag{2.71}$$

The average scattering cross section per atom includes here all isotopes of every atomic species. Since every kind of atom is likely to show a disparate distribution of other atoms around it, there is really a superposition of intrinsically different structures. The definition of the total interference function $F(q)$ allows to compute the distinct term from separate atomic species contributions and weight them with their scattering lengths and concentrations:

$$F(q) \equiv \sum_{\alpha,\beta}^{n} c_\alpha c_\beta \bar{b}_\alpha \bar{b}_\beta^* H_{\alpha\beta}(q) \tag{2.72}$$

where α and β designate the species of the atom pairs of each contribution, n is the number of different atomic species in the sample, c_α and c_β are the fraction of α and β atoms in the sample, and $H_{\alpha\beta}$ is the contribution to the distinct term of the distribution of atoms β surrounding a reference atom α.

The partial interference functions can be calculated using the expression:

$$H_{\alpha\beta}(q) = \frac{1}{c_\alpha c_\beta N} \left\langle \sum_{\substack{j,k=1 \\ j\neq k}}^{N_\alpha, N_\beta} \frac{\sin(qr_{jk})}{(qr_{jk})} \right\rangle \tag{2.73}$$

where N is the total number of atoms in the sample, j and k label the atomic sites, and N_α and N_β are the number of atoms of the α and β species, respectively. Since the system is isotropic and $r_{jk} = r_{kj}$, it is clear that $H_{\alpha\beta} = H_{\beta\alpha}$.

Note that since there is one partial interference function $H_{\alpha\beta}$ for each possible combination of atomic species pair, the number of contributions will rapidly increase with the number of components in the liquid. For instance, a polyatomic liquid with two kind of atoms will have three partial interference functions $H_{\alpha\beta}$: the distribution of α atoms around an α atom, idem for a β atom, and the distribution of β atoms around a reference atom α. But for a liquid with three kinds of atoms, the number of contributions will already increase to six, and for four atoms to ten.

These partial interference functions $H_{\alpha\beta}(q)$ are dimensionless and have the same properties than the monoatomic interference function, namely $H_{\alpha\beta}(q \to \infty) = 0$. However, the total interference function defined here, $F(q)$, is the sum of these dimensionless functions **weighted** by the scattering lengths of the pairs. Which means that, although it still goes to zero for high q values, i. e., $F(q \to \infty) = 0$, it is not dimensionless and has cross section dimensions.

If all these definitions are merged together:

$$\frac{1}{N}\left[\frac{\mathrm{d}\sigma}{\mathrm{d}\Omega}(q)\right] = \underbrace{\sum_{\alpha,\beta}^{n} c_\alpha c_\beta \bar{b}_\alpha \bar{b}_\beta^* \overbrace{\left[\frac{1}{c_\alpha c_\beta N}\left\langle \sum_{\substack{j,k=1 \\ j\neq k}}^{N_\alpha, N_\beta} \frac{\sin(qr_{jk})}{(qr_{jk})} \right\rangle\right]}^{H_{\alpha\beta}(q) = S_{\alpha\beta}(q) - 1}}_{F(q)} + \frac{\overline{\sigma_s}}{4\pi}$$

Therefore, the differential cross section per atom of **polyatomic** liquids or glasses can be calculated with:

$$\boxed{\frac{1}{N}\left[\frac{\mathrm{d}\sigma}{\mathrm{d}\Omega}(q)\right] = \frac{1}{N}\sum_{\alpha,\beta}^{n} \bar{b}_\alpha \bar{b}_\beta^* \left\langle \sum_{\substack{j,k=1 \\ j\neq k}}^{N_\alpha, N_\beta} \frac{\sin(qr_{jk})}{(qr_{jk})} \right\rangle + \frac{\overline{\sigma_s}}{4\pi}} \tag{2.74}$$

2.6.2.2 Correlation functions in real space

A real space function $G(r)$ can be defined in this case as well through the Fourier transform of the total interference function $F(q)$:

$$G(r) \equiv \frac{1}{2\pi^2 r\rho}\int_0^\infty q\, F(q)\sin(qr)\,\mathrm{d}q \tag{2.75}$$

$$= \frac{1}{2\pi^2 r\rho}\sum_{\alpha,\beta}^{n} c_\alpha c_\beta \bar{b}_\alpha \bar{b}_\beta^* \int_0^\infty q\, H_{\alpha\beta}(q)\sin(qr)\,\mathrm{d}q \tag{2.76}$$

However, due to all α and β pair contributions being weighted by their scattering lengths, this total pair correlation function cannot be interpreted any more in terms of probability distribution alone, which renders it a less intuitive magnitude than the $g(r)$ available in the monoatomic case.

In the case of neutron diffraction, it can be considered that the scattering lengths are independent of q, and then the $G(r)$ can be written as a weighted sum of partial $g_{\alpha\beta}(r)$:

$$G(r) \equiv \sum_{\alpha,\beta}^{n} c_\alpha c_\beta \overline{b}_\alpha \overline{b}_\beta^{*} \left[g_{\alpha\beta}(r) - 1 \right] \tag{2.77}$$

where the individual partial pair distribution functions shown here do have a straightforward interpretation in terms of probability: each $g_{\alpha\beta}(r)$ is proportional to the probability of finding an atom β at a certain distance from a reference atom α.

Additionally, every partial pair correlation function $g_{\alpha\beta}(r)$ is related with its corresponding partial interference function $H_{\alpha\beta}(a)$ through a Fourier transform as well, with the exact same form as Equations 2.67 and 2.68.

A partial coordination number $\mathrm{CN}_{\alpha\beta}$, providing the average number of neighbours of species β contained in a certain shell of a reference atom α, can also be calculated from the integration of the partial pair correlation function $g_{\alpha\beta}(r)$ using an expression of the same form as Equation 2.70.

In Equation 2.77 it can be clearly seen that the definition of the total pair correlation function $G(r)$ makes it very different from its monoatomic analogous $g(r)$. Apart from not being dimensionless and displaying cross section dimensions, exactly like its corresponding reciprocal space function $F(q)$, it does not tend to unity for high q values, but to zero: $G(r \to \infty) = 0$.

An alternative real space correlation function with a closer resemblance with the monoatomic $g(r)$ form could be defined by adding a

constant term to the $G(r)$ definition such as:

$$\mathcal{G}(r) \equiv \sum_{\alpha,\beta}^{n} c_\alpha c_\beta \bar{b}_\alpha \bar{b}_\beta^* + \frac{1}{2\pi^2 r\rho} \int_0^\infty q\, F(q) \sin(qr)\, \mathrm{d}q \tag{2.78}$$

This function would tend to the constant value of the first term for high q and could be written as a simple weighted sum of $g_{\alpha\beta}(r)$ contributions such as the $F(q)$ in Equation 2.72. However, its interpretation is certainly not simpler, so it is not clear whether it is really more advantageous as to justify the additional complexity of the expression.

2.6.3 Molecular systems

By molecular liquid or glass is meant here a substance that is formed by a single type of molecule composed of the same or different atomic species. As in the polyatomic case, the different scattering lengths, due to isotopic and nuclear spin variations, that correspond to the same atomic species, will be considered as randomly distributed between those atoms.

Since the interactions at play in neutron diffraction are with atomic nuclei, neutron diffraction is sensitive to the internal structure of the molecules composing the liquid (or glass) as well as their orientations. This is in strong contrast with the mono- and polyatomic cases, where only the position of point-like constituents has to be taken into account.

Therefore, the spherical symmetry of the problem is normally broken by the molecular structure, which cannot be expressed as a one-dimensional radial fluctuation function any more but a full three-dimensional structure instead. Besides, diffraction measurements contain a superposition of these multiple structural levels, enormously increasing the complexity of the analysis. As a consequence, many assumptions are needed to quantitatively analyse the data, and solutions are rarely unambiguous.

2.6.3.1 DCS for molecular liquids and glasses

The goal in this section is to obtain a DCS for these systems that allows to separate the contribution of the molecular structure from the contribution of their arrangement within the compound, to facilitate the analysis.

For the sake of clarity, the differential cross section will only be normalised to the behaviour per atom later on and will be extensively separated in its different contributions, which will be calculated individually. First, it will be divided into its distinct and self parts, and then the distinct term will be further decomposed into its intramolecular and intermolecular contributions (the separation between coherent and incoherent terms in this calculation is irrelevant, but is it indicated for completeness):

$$\left[\frac{\mathrm{d}\sigma}{\mathrm{d}\Omega}\right] = \overbrace{\underbrace{\left[\frac{\mathrm{d}\sigma}{\mathrm{d}\Omega}\right]_{\mathrm{dist}}^{\mathrm{intra}} + \left[\frac{\mathrm{d}\sigma}{\mathrm{d}\Omega}\right]_{\mathrm{dist}}^{\mathrm{inter}}}_{\text{distinct}} + \underbrace{\left[\frac{\mathrm{d}\sigma}{\mathrm{d}\Omega}\right]_{\mathrm{self}}^{\mathrm{coh}}}_{\text{self}}}^{\text{coherent}} + \overbrace{\underbrace{\left[\frac{\mathrm{d}\sigma}{\mathrm{d}\Omega}\right]_{\mathrm{self}}^{\mathrm{incoh}}}_{\text{self}}}^{\text{incoherent}} \tag{2.79}$$

where the explicit q dependence has been dropped for compactness. This separation simply means that the terms corresponding to each atomic pair in Equation 2.50 will be grouped at convenience.

Regarding the molecular structure contribution, only spatial correlations between atoms of the same molecule are included in the summation, and then this average structure is simply multiplied by the total number of molecules N_{mol}:

$$\left[\frac{\mathrm{d}\sigma_s}{\mathrm{d}\Omega}(q)\right]_{\mathrm{dist}}^{\mathrm{intra}} = N_{\mathrm{mol}} \left\langle \sum_{j,k=1}^{m} \overline{b}_j \overline{b}_k^* \frac{\sin(qr_{jk})}{(qr_{jk})} \right\rangle \tag{2.80}$$

where j and k refer to sites on the same molecule, and r_{jk} is their separation. Since this calculation is for the distinct intramolecular contribution, the $j = k$ self terms from the same sites of the same molecule are not taken into account.

Due to the bonds existing between atoms in the molecule, their thermal agitation can be considered to respond to a harmonic potential. If this is the case, the thermal average $\langle\ \rangle$ can be simply taken into account by the Debye-Waller factor, an exponential that smears out each atom pair contribution:

$$\left[\frac{\mathrm{d}\sigma}{\mathrm{d}\Omega}(q)\right]_{\mathrm{dist}}^{\mathrm{intra}} = N_{\mathrm{mol}} \sum_{j,k\neq j}^{m} \overline{b}_j \overline{b}_k^{*} \frac{\sin(qr_{jk})}{(qr_{jk})} \mathrm{e}^{-\left\langle \delta r_{jk}^2 \right\rangle q^2/2} \tag{2.81}$$

where, in the Debye-Waller factor, $\langle \delta r_{jk}^2 \rangle = \left\langle u_j^2 \right\rangle + \langle u_k^2 \rangle$ is the mean square amplitude of thermal vibrations projected on the vector between sites j and k, with $\left\langle u_j^2 \right\rangle$ the component corresponding to the mean squared vibrational amplitude of the atom at site j [4, 44].

Regarding the intermolecular structure contribution, due to correlations between atomic pairs in different molecules, it requires two summations, one accounting for all sites within each molecule and another accounting for all molecules:

$$\left[\frac{\mathrm{d}\sigma}{\mathrm{d}\Omega}(q)\right]_{\mathrm{dist}}^{\mathrm{inter}} = \left\langle \sum_{\substack{A,B \\ A\neq B}}^{N_{\mathrm{mol}}} \sum_{j,k}^{m} \overline{b}_j \overline{b}_k^{*} \frac{\sin(q\, r_{j_A k_B})}{(q\, r_{j_A k_B})} \right\rangle \tag{2.82}$$

where j and k are atomic sites within the molecule, A and B refer to different molecules, and $r_{j_A k_B} = |\boldsymbol{r}_{j_A} - \boldsymbol{r}_{k_B}|$ is the distance between a pair of atoms in different molecules. Since this calculation is for the distinct intermolecular contribution, self terms must be left out, but atom pairs are already required here to belong to different molecules, so this is ensured even if the atoms belong to the same molecular site.

The remaining two self terms of the differential scattering cross section in Equation 2.79 correspond to individual contributions from all atoms in the sample. Since the self terms do not depend on the atomic positions, the result is exactly the same that has been used

in the previous DCS equations:

$$\left[\frac{\mathrm{d}\sigma}{\mathrm{d}\Omega}\right]_{\text{self}} = \left[\frac{\mathrm{d}\sigma}{\mathrm{d}\Omega}\right]_{\text{self}}^{\text{coh}} + \left[\frac{\mathrm{d}\sigma}{\mathrm{d}\Omega}\right]_{\text{self}}^{\text{incoh}} \tag{2.83}$$

$$= \underbrace{\cancel{|\overline{b}|^2 N}}_{\text{coherent}} + \underbrace{\left(\overline{|b|^2} - \cancel{|\overline{b}|^2}\right) N}_{\text{incoherent}} = \overline{|b|^2} N = \frac{\overline{\sigma_s}}{4\pi} N \tag{2.84}$$

where $\overline{\sigma_s}$ is the average scattering cross section per atom, and N is the total number of atoms.

The last step consists in normalising everything to the total number of atoms in the sample N and merging the intra- and intermolecular distinct contributions (Equations 2.81 and 2.82), which corresponds to the interference function $H(q)$ and contains the correlation fluctuations, together with the self contribution (Equation 2.84), which is just a constant background:

$$\frac{1}{N}\left[\frac{\mathrm{d}\sigma}{\mathrm{d}\Omega}(q)\right] = \frac{1}{N}\left[\frac{\mathrm{d}\sigma}{\mathrm{d}\Omega}(q)\right]_{\text{dist}}^{\text{intra}} + \frac{1}{N}\left[\frac{\mathrm{d}\sigma}{\mathrm{d}\Omega}(q)\right]_{\text{dist}}^{\text{inter}} + \frac{1}{N}\left[\frac{\mathrm{d}\sigma}{\mathrm{d}\Omega}(q)\right]_{\text{self}}$$

So, in conclusion, the result for the differential scattering cross section per atom for a molecular system is:

$$\boxed{\begin{aligned}\frac{1}{N}\left[\frac{\mathrm{d}\sigma}{\mathrm{d}\Omega}(q)\right] &= \frac{1}{m}\sum_{j,k\neq j}^{m} \overline{b}_j \overline{b}_k^{*} \frac{\sin\left(q r_{jk}\right)}{\left(q r_{jk}\right)} \mathrm{e}^{-\left\langle \delta r_{jk}^2 \right\rangle q^2/2} \\ &+ \frac{1}{N}\left\langle \sum_{\substack{A,B \\ A\neq B}}^{N_{\text{mol}}} \sum_{j,k}^{m} \overline{b}_j \overline{b}_k^{*} \frac{\sin\left(q\, r_{j_A k_B}\right)}{\left(q\, r_{j_A k_B}\right)} \right\rangle + \frac{\overline{\sigma_s}}{4\pi}\end{aligned}} \tag{2.85}$$

2.6.3.2 Correlation functions in real space

Fourier transforming the oscillations in Equation 2.85 to obtain a real space correlation function is not a straightforward task.

As in the polyatomic case, the contributions arising from each pair of atomic species are weighted by their scattering length. Since

this factor changes the relative heights between correlation peaks, the total function in real space does not have a direct interpretation in terms of probability or density fluctuations. This complication hinders a quantitative analysis of the data if a model is not available for comparison, although the partial contributions from each pair of atomic species can still be interpreted as a probability when properly normalised.

Most general observations regarding a total correlation function in real space for polyatomic systems, apply to molecular systems as well. The main difference in this case is that the spherical symmetry of the problem is broken due to the intramolecular structure.

Luckily, the linearity property of the Fourier transform $\mathscr{F}$

$$\mathscr{F}\left[A\,g(q) + B\,h(q)\right] = A\,\mathscr{F}\left[g(q)\right] + B\,\mathscr{F}\left[h(q)\right] \tag{2.86}$$

allows to transform separately the intra- and intermolecular contributions to obtain their corresponding functions in real space, where structural correlations can also be decomposed into a sum of intramolecular and intermolecular terms.

Regarding the intramolecular contribution, its real space correlation function is calculated taking advantage of the detailed equation that was presented in the previous section:

$$K(q) \equiv \frac{1}{m}\sum_{j,k\neq j}^{m} \overline{b}_j \overline{b}_k^{*} \frac{\sin\left(qr_{jk}\right)}{\left(qr_{jk}\right)} \mathrm{e}^{-\left\langle \delta r_{jk}^2 \right\rangle q^2/2} \tag{2.87}$$

A Fourier transform in spherical coordinates has to be carried out upon $K(q)$, the intramolecular contribution of the differential cross section per atom:

$$\widetilde{K}(r) = \frac{1}{2\pi^2 r\rho}\int_0^{\infty} q\,K(q)\sin\left(qr\right)\mathrm{d}q \tag{2.88}$$

$$= \frac{1}{2\pi^2 r\rho m}\sum_{j,k\neq j}^{m} \frac{\overline{b}_j \overline{b}_k^{*}}{r_{jk}} \int_0^{\infty} \sin\left(qr_{jk}\right)\mathrm{e}^{-\left\langle \delta r_{jk}^2 \right\rangle q^2/2}\sin\left(qr\right)\mathrm{d}q \tag{2.89}$$

Mathematically, the solution to the integral is:

$$\begin{aligned}\int_0^\infty \sin(qr_{jk})\,\mathrm{e}^{-\langle\delta r_{jk}^2\rangle q^2/2}\sin(qr)\,\mathrm{d}q \\ &= \sqrt{\frac{\pi}{2\langle\delta r_{jk}^2\rangle}}\;\mathrm{e}^{-\frac{\left({r_{jk}}^2+r^2\right)}{2\left\langle\delta r_{jk}^2\right\rangle}}\;\sinh\left[\frac{r\,r_{jk}}{\langle\delta r_{jk}^2\rangle}\right] \\ &= \sqrt{\frac{\pi}{8\langle\delta r_{jk}^2\rangle}}\left[\mathrm{e}^{-\frac{\left(r-r_{jk}\right)^2}{2\left\langle\delta r_{jk}^2\right\rangle}} - \mathrm{e}^{-\frac{\left(r+r_{jk}\right)^2}{2\left\langle\delta r_{jk}^2\right\rangle}}\right]\end{aligned} \tag{2.90}$$

which is a sum of a Gaussian function centred at r_{jk} with variance $\langle\delta r_{jk}^2\rangle$, together with an identical negative function centred at $-r_{jk}$.

Since the function $\widetilde{K}(r)$ does not have physical meaning for values $r < 0$, and the contribution of the second term is negligible for positive r values, even for small intramolecular distances, the negative term can be entirely disregarded (see Figure 2.14).

Therefore, the real space total correlation function per atom $\widetilde{K}(r)$, corresponding to the intramolecular contribution of the differential scattering cross section $K(q)$, is:

$$\boxed{\widetilde{K}(r) \simeq \frac{\sqrt{\pi/2}}{4\pi^2 r\rho\, m}\sum_{j,k\neq j}^{m}\frac{\bar{b}_j\bar{b}_k^*}{r_{jk}\langle\delta r_{jk}^2\rangle}\;e^{-\frac{\left(r-r_{jk}\right)^2}{2\langle\delta r_{jk}^2\rangle}}} \tag{2.91}$$

where ρ is the average number density of the sample, m the number of atoms within the molecule, j and k are different atomic sites within the molecule, $\bar{b}_j$ is the coherent scattering length of atoms in site j, r_{jk} is the distance between sites j and k, and $\langle\delta r_{jk}^2\rangle$ is its variance.

Although we have not found the preceding calculation elsewhere in the literature, the correspondence of a Gaussian distribution for each intramolecular distance is often used (albeit sometimes the factor $(1/r_{jk})$ is missing), and Johnson et al. quoted a similar equation with a different normalization [45].

The individual terms corresponding to each intramolecular distance can be normalized separately ensuring that the probability of

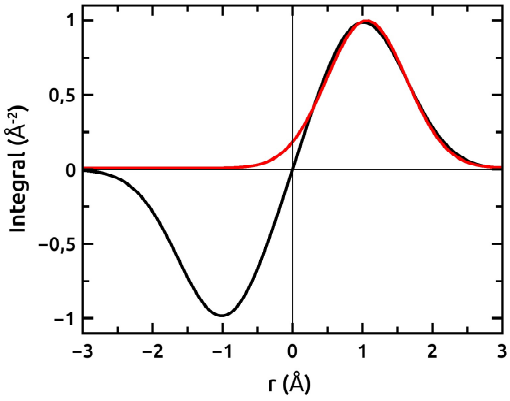

Figure 2.14: Gaussian fit (red line) of the integral in Equation 2.90 (black line) for an intramolecular distance of $r_{jk} = 1$ Å with $\langle \delta r_{jk}^2 \rangle = 0.4$ Å^2. It is clear that even in this extreme case of small interatomic distance and large displacements from the equilibrium position, the contribution of the negative term to the positive peak shape is negligible.

finding the atom k at about a distance r_{jk} of atom j is one, which is analogous to assume that the molecular geometry will remain akin:

$$\widetilde{K}_{jk}(r) = \frac{1}{\sqrt{2\pi \langle \delta r_{jk}^2 \rangle}} \; e^{-\frac{\left(r - r_{jk}\right)^2}{2 \langle \delta r_{jk}^2 \rangle}} \tag{2.92}$$

Obviously, this may not be true for all distances in molecules with various conformations, but in these cases Equation 2.87 for $K(q)$ is not valid anyway, because the atom pair does not fulfil the requirement of following a harmonic potential, which was assumed to obtain Equation 2.81.

If the molecule under study has a central atom, such as the simpler tetrahedral molecules, the partial pair correlation function of that atom may conform to a good approximation with the one describing the overall molecular positions [42]. However, the coincidence between the central atom of a particular molecule and the centre of

mass will never be exact, because thermal agitation distorts molecules from their equilibrium geometries, and thus effectively displaces their centre of mass.

2.6.4 Isotopic substitution

The partial functions, i. e. the series of probabilities of finding an atom of species β at a certain distance of an atom of species α, provide valuable quantitative information about the structure under study.

In a single experiment, all partial contributions are jammed together in one diffractogram. However, it is possible to obtain them experimentally using isotopic substitution, a technique unique to neutron scattering [3].

Ideally, the methodology to obtain these magnitudes consists in measuring materials which have exactly the same structure but where the weights of the partial contributions of each kind of atom is altered in a controlled manner.

It is indeed possible to exchange a fraction of the isotopes in a substance without a significant transformation of its chemical properties, because different isotopes of the same element normally interact in a very similar fashion with other atoms. However, if the sample is enriched with a particular isotope, this changes the weight of the partial contribution in neutron scattering, because neutron scattering lengths depend mainly on the nuclei character, not the electronic shell.

However, this does not mean that they are easily measured. Isotopic substitution within a sample is often difficult and expensive, and is not possible in all cases. Besides, alteration of the sample behaviour is frequently underestimated, specially for hydrogen, which is one of the most commonly targeted elements. Deuterium is twice as heavy than hydrogen, so its mobility is quite different, which has consequences in any property affected by the dynamics of the system: transition temperatures (which decrease a few degrees with deuteration), hydrogen bonding, pH variations, etc. For this reason, great care must be taken before trying to change the contrast through iso-

topic substitution, to make sure that the properties that need to be measured are not altered. For example, performing measurements of related properties with other techniques.

Chapter 3

Neutron scattering experiments

What is measured in neutron scattering is the number of neutrons in a range of energies that has been scattered by the sample in a certain direction. There are a myriad of neutron scattering techniques and, moreover, even each single instrument usually has several working configurations with different characteristics. Therefore,

a comprehensive listing of all of them is out of the scope of this thesis and only a few details of the instruments and configurations that have been used for the experiments will be mentioned here. Figure 3.1 shows an overview of the different neutron scattering techniques, together with the length and time scales that can be measured with each of them.

Although most theoretical derivations use the same nomenclature that has been used in this work, it is customary in experimental neutron scattering to define the scattering angle θ as 2θ. Thus, there is no consistent notation across literature and it is important when consulting other works to ascertain how the author has defined the scattering angle. To avoid any confusion and facilitate equation comparison, the scattering angle will be called on the following experimental chapters $2\theta_E$ instead.

3.1 Neutron sources

There are two different kinds of neutron sources used in neutron scattering: research nuclear reactors, and spallation sources. The basic difference is that reactors provide a continuous flux of neutrons to the instruments, while most spallation sources provide neutron pulses. Although essentially the same kind of instruments can be built in either of them, depending on the technique the instruments will differ in their performance and efficiency.

In reactor sources, neutrons produced by spontaneous fission of heavy atoms are slowed down by the large body of water in which they are immersed and these moderated neutrons induce in turn more fission events in other atoms, hence sustaining a chain reaction. This yields a neutron flux ϕ with more or less a Maxwell-Boltzmann distribution of neutron energies:

$$\phi(E) \propto E \, \exp\left(-\frac{E}{k_{\mathrm{B}} T_m}\right) \tag{3.1}$$

where E is the energy of the neutron, k_{B} is the Boltzmann constant, and T_m is the moderator temperature (see Figure 3.2(a)) [23, 47].

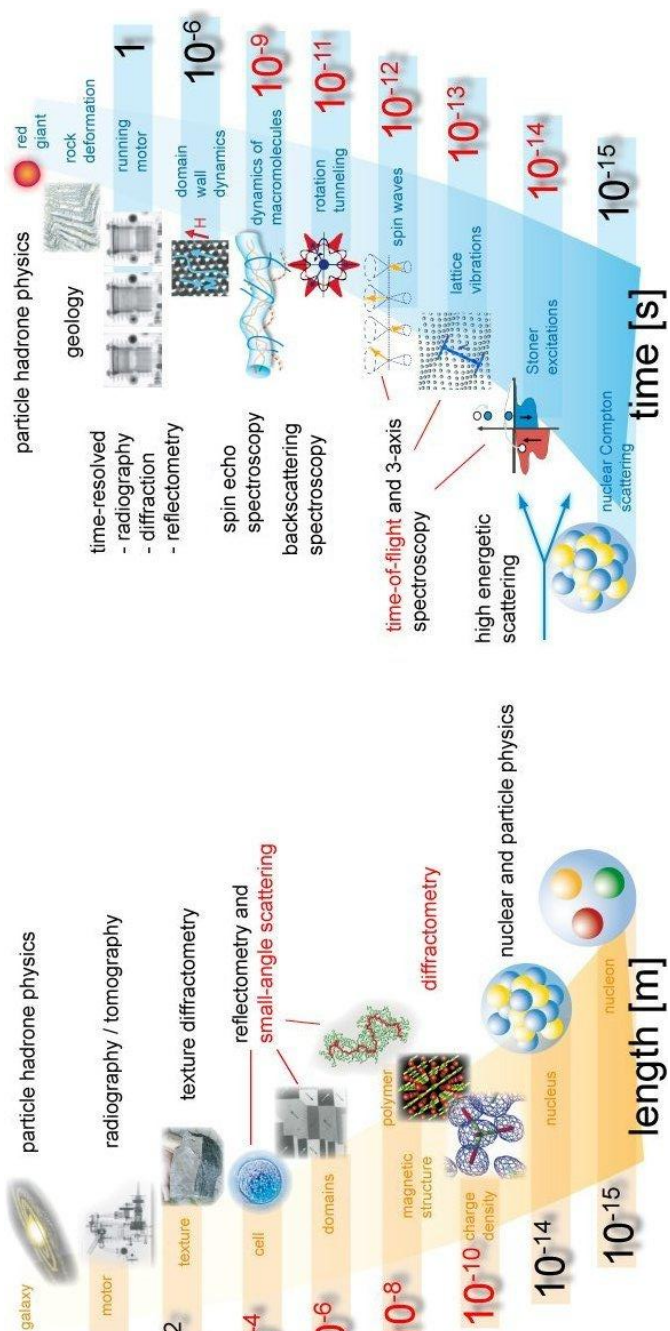

Figure 3.1: Length and time scales accessible with each neutron scattering technique. Those which have been used are shown in red. *Modified from Ref. [46].*

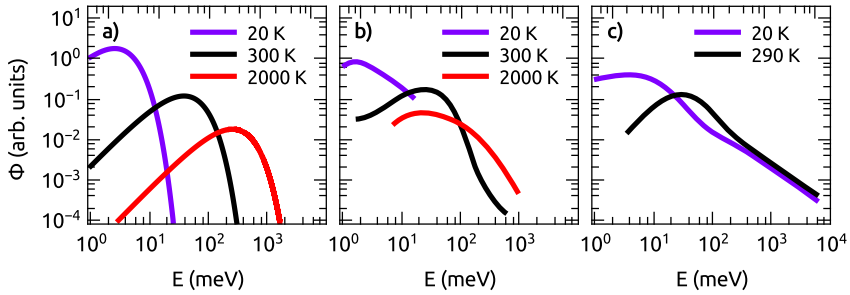

Figure 3.2: Energy distributions of the neutron flux. (a) Theoretical Maxwell-Boltzmann distributions at different T_m temperatures. (b) Distributions obtained from different moderators in a reactor source, and (c) a spallation source. *Experimental data in (b) and (c) taken from Ref. [48].*

The peak of this distribution is at $E = k_{\mathrm{B}}T_m$, hence the convention to say that a neutron with energy E is at a temperature T_m.

Thermal neutrons are considered to be the ones with velocity $v_t \equiv 2.2$ km/s ($E = 25.3$ meV, and $T_m = 293.5$ K). At this thermal velocity the de Broglie wavelength of a neutron is $\lambda = h/(mv_t) \simeq 1.8$ Å, where h is the Planck constant and m the neutron mass [23]. However, since the absorption cross section is higher for neutrons with lower energy (see Figure 3.3) [47], a larger fraction of them will be absorbed and the neutrons yielded by the reactor will show a peak at higher energies than those predicted by the Maxwell-Boltzmann distribution. This distribution of neutron wavelengths is appropriate to study interatomic distances and many of the excitations in condensed matter, but to explore the whole range of characteristic distances and excitations more efficiently it is convenient to use in some experiments a neutron distribution with the maximum at a higher or lower energy.

To do that, a moderator at a much higher or lower temperature than the surrounding water is placed close to the reactor core [49]. Neutrons going through the moderator thermalise at its temperature after multiple scattering events, and yield an energy distribution with a substantial enhancement of neutrons at the energy range of interest (see different curves in Figure 3.2(b)) [48], hence a moderator can be

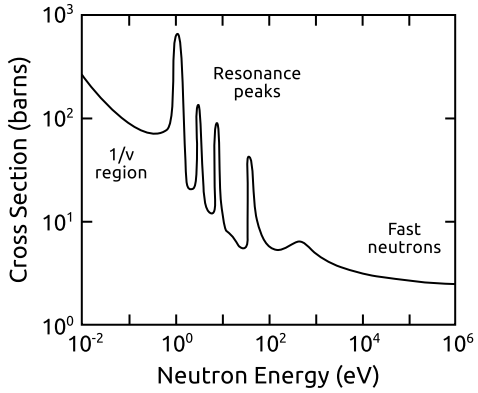

Figure 3.3: Typical neutron absorption cross section of an atomic nucleus as a function of the neutron energy. *Restored from Ref. [47].*

used as a hot or cold source.

In spallation sources, protons are accelerated and concentrated in small clusters that hit a target made of heavy atoms. That process ejects neutrons which are then also slowed down with moderators at the appropriate temperatures required by the instruments. However, since the time spent in the moderator broadens the neutron pulse, moderators in these sources have to be small to keep a good time-of-flight resolution, which results in neutrons being undermoderated and not yielding a Maxwell-Boltzmann distribution for energies approximately above 100 meV, where the energy distribution of the neutron flux is proportional to $1/E$ instead (see Figure 3.2(c)) [50, 51].

3.2 Instruments to determine the structure

Reactor diffractometers are instruments with detectors that count all neutrons scattered in certain directions from a more or less monochromatic incoming beam, but disregarding altogether their energy distribution. They mainly allow to obtain information about the structure of the sample but not its dynamics.

Depending on whether our interest is on the structure of the molecule itself, the relative arrangement of close molecules, or the formation of superstructures, the length scales of interest will be different, so an instrument that can measure within the appropriate range must be chosen (see Figure 3.1).

As seen in Chapter 2, interatomic distances in the system, r, and the modulus of the scattering vector, q, are related through the Fourier transforms of the structure factor $S(q)$ and the pair correlation function $g(r)$ (see Equations 2.67 and 2.68 in Section 2.6 for the monoatomic case). And, if the scattering is elastic, that is, neutrons do not transfer any energy to the sample, the relation between q and θ_E is [42]:

$$q = 2k_0 \sin\theta_E = \frac{4\pi}{\lambda_0} \sin\theta_E \tag{3.2}$$

where k_0 and λ_0 are the wave number and the wavelength of the incident neutrons, respectively. Thus, the wavelength of the incoming neutrons and the angular range that the detectors cover will determine the characteristic distances that can be measured with each instrument.

Apart from that, some systems of interest display a mixture of ordered and disordered structural features that must be studied with differently optimized instruments. For example, disordered features are more conveniently studied with low resolution instruments while ordered features need higher resolutions. This is the case for plastic crystals and orientational glasses, which have positional but not orientational long range order. The study of structural variations in non-equilibrium states (for instance, across phase transitions) will require an instrument capable of fast measurements, a practical issue that has to be taken into account too.

3.2.1 D4 liquid and amorphous materials diffractometer

D4 is a two-axis diffractometer specially designed to study the local atomic order of amorphous materials like liquids and glasses. It is located at the Institut Laue-Langevin (ILL) in Grenoble, France [49]

(see Figure 3.4). The short wavelength of the incoming neutrons and the angular range measurable by its detectors ($2\theta_E = 1.5°$ to $138°$), allows to obtain good quality data up to rather high values of q, which is a significant factor when data has to be Fourier transformed to real space, because it gives a better resolution.

To determine the short range order of liquid and glassy samples, diffractograms were measured with a wavelength of $\lambda = 0.5$ Å (327 meV), which yielded a momentum transfer range up to $q_{\max} = 23.5$ Å^{-1}.

The high flux reactor at the ILL generates the largest neutron flux in the world. Thermal neutrons coming from its water moderator at 300 K have a peak at 1.2 Å, but neutrons at D4 come from its hot source at 2600 K instead (peak flux at 200 meV), which increases the flux of neutrons at smaller wavelengths (< 0.8 Å). This moderator is a graphite sphere heated by the radiation generated inside the reactor core [53, 54]. In Figure 3.2(b) an example of how a hot moderator modifies the energy distribution of the reactor is shown.

The neutron beam goes through a monochromator that selects neutrons within a small range of wavelengths. Since the neutron energy distribution of the source is normally fixed, the more precise the wavelength, the less neutrons are available for the experiment, so an equilibrium must be found. The monochromator at D4 to obtain neutrons at $\lambda = 0.5$ Å is a very large copper single crystal cut parallel to the (220) crystallographic plane.

A low-efficiency detector, called monitor, is placed in the path of the beam before the sample. The monitor allows to have a measure of the incident neutron flux, needed for normalization, but lets most neutrons travel through so that they can be used in the experiment, interacting with only 0.1 to 1 % of them [55].

An orange cryostat ($T = 1.5$ K to 300 K) or a furnace ($T = 300$ K to 1100 K) were used as sample environments in the different experiments. In Figure 3.5 an orange cryostat and the stick that holds the sample holder inside the cryostat are shown. Since hydrogen is a highly neutron scattering element (see Figure 2.2), the sample stick must be carefully warmed and dried from condensed water vapour at every sample change to avoid any spurious water contribution to the

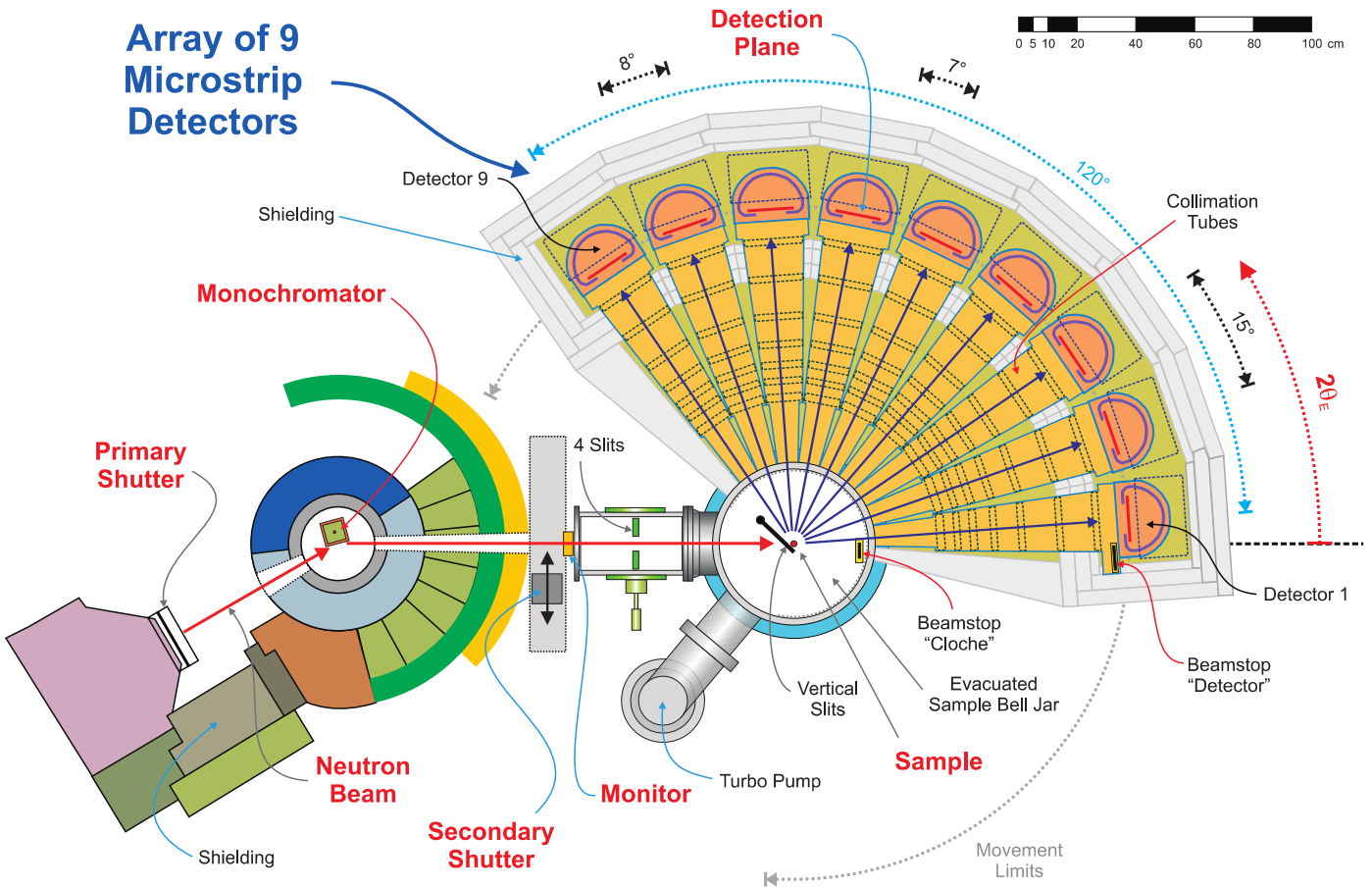

Figure 3.4: Scheme of D4, a liquid and amorphous materials diffractometer at the ILL. *From Ref. [52] by G. Cuello.*

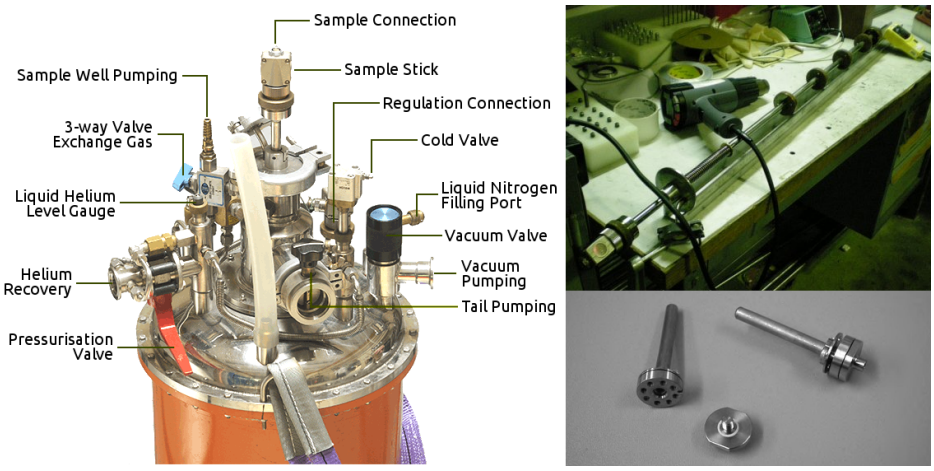

Figure 3.5: Orange cryostat with the sample stick in place (left). Warming and drying of the stick during a sample change (upper right). Vanadium-aluminium sample holders used in D4, D1B and D20 (lower right). *Respectively from Ref. [56], own picture, and Ref. [57].*

measurements.

Sample holders are typically made of a vanadium body with an aluminium cap and have cylindrical geometry (see Figure 3.5).

To remove from the measurement the unwanted high intensity direct beam of neutrons that do not interact with the sample, two beamstops of an absorbent material ($^{10}B_4C$) are located at the lowest scattering angles between the sample and the detector to block their path (see Figure 3.4).

The collimation tube in front of each detector ensures that scattered neutrons which could arrive to the detector but are not even coming from the direction of the sample, such as most of the neutrons scattered by the cryostat walls, will be absorbed and will not reach the detector. The drawback of this system is that the measured signal has alternating illuminated and blind spots cast by the shadow of the collimator and also by the angular separation between the detectors. Thus, to obtain a continuous measurement of the whole scattering range, multiple measurements must be performed with the

detector block at slightly different angles. A technique that, although it greatly improves the quality of the signal, inevitably increases the overall measuring time.

For example, five scans can be used to measure from $2\theta_E = 1.5°$ to 140°, which corresponds to setting the first detector at different offsets of the angular position: $2\theta_E = 0°$, 4.5°, 7°, 9°, and 11°. These angles are carefully selected to avoid intense aluminium Bragg peaks arising outside the sample position but that, albeit the collimator, would find certain small windows to reach the detector. Aluminium is an element frequently used in the building of sample environment devices due to its high transparency to neutrons [33].

The detector bank is composed of nine microstrip gas chamber detectors with pressurized ^{3}He (15.4 bar) and a small quantity of CF_4 (0.6 bar). Neutrons are captured by ^{3}He nuclei, which have a large neutron absorption cross section (see Table 4.1), and then decay to charged tritium and protons through the following nuclear reaction:

$$^3\mathrm{He} + \mathrm{n} \rightarrow {}^3\mathrm{H} + {}^1\mathrm{H} + \Delta E \tag{3.3}$$

where $\Delta E = 0.764$ MeV is released as kinetic energy. The free electrons that result from this ionization are attracted by the strong electric field of the metallic strips which in turn causes an avalanche of secondary ionization. This kind of detectors have a good efficiency even at small neutron wavelengths (82% at 0.5 Å) [58, 59]. However, since ^{3}He is mostly obtained from dismantling nuclear weapons and this need has been gradually decreasing, there is now an acute worldwide shortage of this isotope that is hampering the development and fabrication of these detectors [60].

Since D4 is designed to measure the smooth features of disordered systems, it has a low resolution in q and is not suitable to measure the sharp diffraction peaks resulting from highly ordered structures.

To reduce the background and increase the quality of the measurement, most of the path of the neutrons through the instrument is within vacuum. For instance, the cryostat tail is held inside a vacuum chamber, the collimating tube of each detector is also evacuated, etc. However, due to the intrinsic disorder of the samples

measured at D4, the intensity of their coherent scattering is not very high and the time needed to measure a complete diffractogram that allows for quantitative analysis is usually of the order of hours [52]. For the samples studied in this work, a single good quality measurement (with the aforementioned five scans at different offset angles) takes around three hours, although it can take up to eight hours if the isotopic substitution technique is used, due to the fact that, for a successful subtraction of the different contributions, data quality has to be extremely good.

Besides measuring the sample in the different external conditions of interest, for each experiment a series of additional measurements will have to be carried out to perform the subsequent corrections and normalization of the sample measurements.

For instance, to subtract the background radiation as well as the sample environment and sample holder contributions to the scattering, the empty cryostat or furnace, and the empty sample holder inside the sample environment have to be measured for at least as long as the sample. This is because a large error in these measurements would propagate to the corrected sample measurement during the addition or subtraction operations, and a large final error would be then obtained regardless of how long the sample itself had been measured (see Section 4.1.5). Besides, since the sample attenuates part of the neutrons, these separate measurements without the sample yield higher intensity readings than the actual values. Thus, to avoid subtracting too many neutrons, an attenuation correction must be performed. This correction requires an additional measurement that consists in replacing the sample by a highly absorbent material, normally $^{10}B_4C$ or cadmium.

Finally, to be able to normalise the sample measurement to obtain absolute scattering units, a known sample of reference must be measured as well. Usually a vanadium rod is used for this purpose, because this material has very weak Bragg peaks and gives a more or less uniform intensity. But, since only the overall height is sought, a precise measurement of the vanadium rod is not needed and a much shorter scan than those of the sample is required.

3.2.2 D1B two-axis diffractometer

D1B is a two-axis neutron diffractometer located at the ILL (see Figure 3.6). The efficiency of its large detector and its high neutron flux make this instrument suited for real time experiments with very small samples. Diffraction patterns with enough statistics can be measured in just a few minutes. Thus, a complete scan of diffraction patterns with temperature can be obtained in just a few hours.

In disordered systems like plastic crystals and orientational glasses the centres of mass of the molecules have a high positional symmetry, often extremely high, such as body or face centred cubic lattices, thus, they have a few distinct Bragg peaks that can be easily distinguished through neutron diffraction without the need of high resolution measurements. Several experiments were performed at D1B to explore the variations of the ordered features in these systems as a function of the temperature. Thanks to the fast acquisition rate of this instrument, long range order structural changes could be followed through phase transitions, and real-time measurements of the thermal history dependence of the sample could be performed.

This instrument is located at a thermal guide, which means that neutrons have been thermalised in the water moderator at 300 K and have a peak at a wavelength of $\lambda = 1.2$ Å. Three monochromators made of pyrolytic graphite cut parallel to the (002) crystallographic plane focus on the sample and select neutrons with a wavelength of $\lambda = 2.52$ Å.

Just as in D4, an orange cryostat (1.7 to 300 K) and vanadium sample holders with cylindrical geometry were used to measure the samples (see Figure 3.5).

During the measurements of this work, D1B had a multiwire position sensitive ^{3}He/Xe gas detector that covered 80° of the scattering range, although it could be moved to allow it to collect a complete diffractogram from $2\theta_E = 2°$ to 130°, and had a 60% efficiency at $\lambda = 2.52$ Å [62]. Recently, its detector has been upgraded to a microstrip ^{3}He/CF_4 position sensitive detector that covers 128° of the scattering range (from $2\theta_E = 0.8°$ to 128.8°), and has an increased efficiency at the same wavelength of detecting 86% of the neutrons.

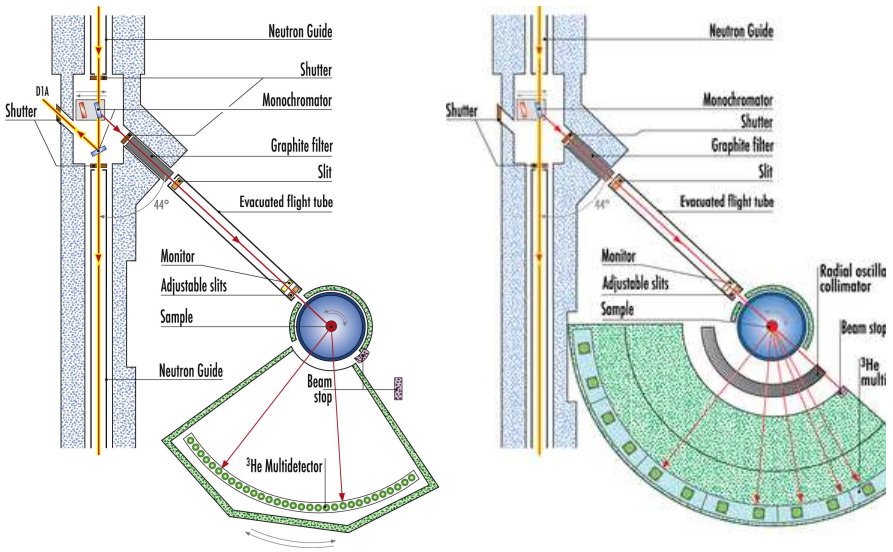

Figure 3.6: Scheme of D1B, a two-axis diffractometer at the ILL, before (left) and after (right) the detector upgrade. *From Refs. [49] and [61].*

3.2.3 D20 high-intensity two-axis diffractometer with variable resolution

D20 is a versatile extremely high flux diffractometer with variable resolution located at the ILL (see Figure 3.7). The combination of a very large position sensitive detector and its high neutron flux results in the reactor diffractometer with the highest counting rate of the world [63]. This allows to make very fast measurements of the structure of a sample as the temperature is continuously changed, even for disordered materials that normally require long measurements.

In our case, about three minutes were needed to obtain a complete diffraction pattern for liquid trans-1,2-dichloroethene. Hence, real-time measurements at D20 of the structure factor of this compound as a function of the temperature could be performed allowing to detect any phase transition.

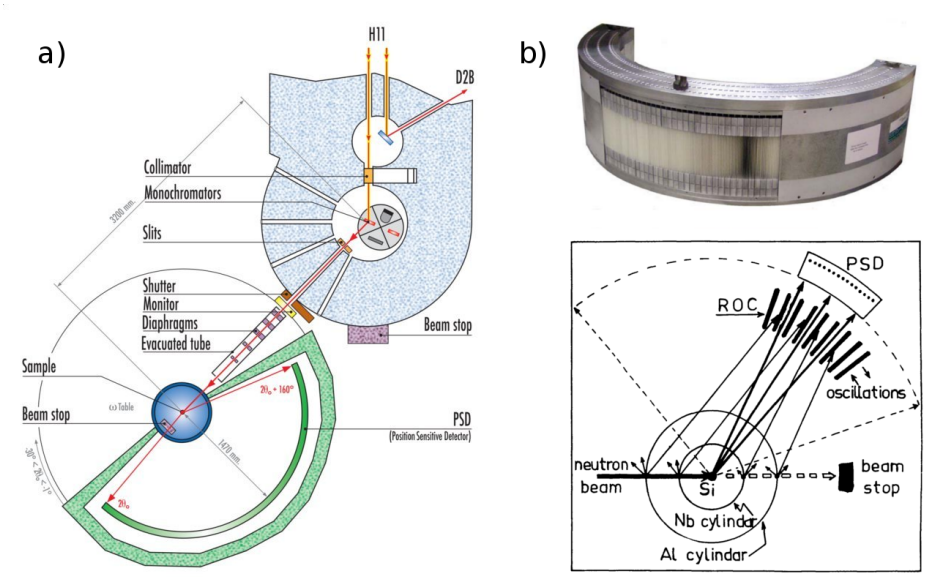

Figure 3.7: (a) Sceme of D20, a high-intensity two-axis diffractometer at the ILL (b) Radial oscillating collimator. *From Refs. [49, 64, 65].*

Neutrons at D20 are provided by a high flux thermal guide. A range of wavelengths can be used, but a copper monochromator cut in the (200) crystallographic plane that selects neutrons with a wavelength of $\lambda = 1.3$ Å is the configuration that yields the highest flux.

A radial oscillating collimator was used to remove spurious signal generated by neutrons impinging on the components of the sample environment (see Fig. 3.7(b)). If no collimator at all had been used in front of the detector, plenty of neutrons scattered on various parts of the cryofurnace would also have been measured together with the sample. The radial collimator focuses on the sample and absorbs any neutron coming from a point farther than 11 mm to the left or right of the sample. There are still a few neutrons measured by each detector that have been scattered from the cryofurnace components located in the same direction as the sample, but their overall contribution is greatly diminished (see Figure 3.7(b)).

Due to the shadow cast by the collimator walls, to obtain a contin-

uous diffractogram, more than one measurement has to be performed setting the collimator at different positions. These are carried out through an oscillation of the collimator, which is synchronised with the capture times of the detector to avoid measuring during the displacement of the collimator. This lateral oscillation of the collimator is equivalent to the D4 procedure of measuring at different angles. In our case, the time between the two farthest collimator positions was set to 11.3 seconds.

The sample environment was controlled with a cryofurnace (1.5 to 550 K) and vanadium sample holders with cylindrical geometry were used for the samples (see sample holders at Figure 3.5).

The large microstrip detector of D20 covers the full scattering range: $2\theta_E = 0.1$ to 154°, which at $\lambda = 1.3$ Å becomes a q range from $q = 0.08$ to 9.30 Å in the diffractograms.

3.2.4 KWS 2 Small Angle Neutron Scattering

KWS 2 is a small angle neutron scattering diffractometer of the Jülich Centre for Neutron Science located at the Forschungs-Neutronenquelle Heinz Maier-Leibnitz (FRM II) in Garching, Germany (see Figure 3.8).

Small angle scattering measures the deviation of neutrons from their path after they interact with structures which are much larger than the wavelength of the neutrons. This technique allows to measure size, shape and orientation of structures between $\simeq$ 10 and 1000 Å, also in partially or fully disordered systems.

Although the neutron flux generated by FRM II is lower than at the high flux reactor of the ILL, a fuel element design enhancing emission of neutrons, and the particular attention paid to reduce background around the instruments and their detectors, make its signal to noise ratio very good, which partially compensates for a more modest reactor and results in very good quality measurements.

The neutron beam for this instrument comes from the cold source at FRM II. The liquid deuterium moderator is at 25 K and the maximum of the distribution of neutron wavelengths is at $\lambda = 1.4$ Å ($E = 40$ meV), which means that a wide range of momentum trans-

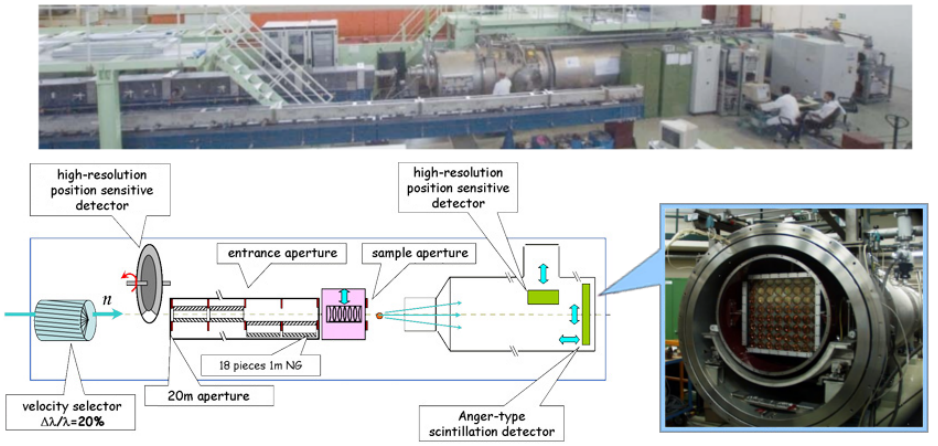

Figure 3.8: Scheme of KWS 2, a small angle neutron scattering instrument at the FRM II. *Modified from Ref. [66].*

fers q can be explored (between 10^{-4} and 0.5 Å^{-1}).

For instance, for the experiments designed to detect any possible nematic ordering taking place in trans-1,2-dichloroethylene, the sample was located at two meters of the detector and a wavelength of 4.5 Å was selected. This yielded a measurement in the q range between 0.003 and 0.3 Å^{-1}, which corresponds to measure structures in the range between 20 to 2000 Å.

3.3 Instruments to determine the dynamics

Contrary to diffractometers, spectrometers are usually designed so that the energy distribution of neutrons scattered in each direction can be determined. This allows to infer the energy exchange between each neutron and the sample as a function of q, so that information about the sample dynamics can be obtained. Figure 3.1 shows the time scale accessible with each neutron spectroscopy technique. In these techniques it is crucial to avoid multiple scattering of the neu-

trons that go through the sample for the measurement to be reliable. Thus, a calculation of the optimal width of the sample must be performed. The desired transmission of the beam through the sample is conventionally taken as being about 90%, this way only about 10% of the incoming neutrons interact with the sample, most of them accounting for the single scattering contribution to the measurement, so that only a small part of the incoming neutrons are scattered twice, an even smaller part is scattered thrice, etc.

3.3.1 TOFTOF High Resolution Direct Geometry Time-of-Flight Spectrometer

TOFTOF is a flexible time-of-flight spectrometer of the Technische Universität München with a high flux and high resolution located at the Forschungsneutronenquelle Heinz Maier-Leibnitz (FRM II) in Garching, Germany (see Figure 3.9). Among many other things, it can be used to study the diffusion of atoms or molecules in liquids.

A small bunch of neutrons with the same wavelength are sent simultaneously towards the sample, a few of them will interact with it and will loose or gain kinetic energy before they continue their path, which will in turn affect their velocity. Thus, the energy exchange experienced by scattered neutrons is directly reflected by the measurement of the time-of-flight it takes for these neutrons to reach the detectors.

Neutrons at the TOFTOF spectrometer are provided by the cold source at 25 K. The maximum of the distribution of neutron wavelengths is at $\lambda = 1.4$ Å ($E = 40$ meV). This allows a variety of wavelengths of interest. For instance, in trans-1,2-dichloroethylene experiments, a wavelength of 6 Å and a resolution of 60 μeV were used.

The neutron beam that must be used in a time-of-flight instrument has to be composed by monochromatic pulses. In a continuous neutron source, such as a reactor, this is usually achieved with a number of choppers. These are large disks made of a neutron absorbing material, with small windows that let neutrons pass through (see Figure 3.9), so that the beam can be interrupted periodically. The first

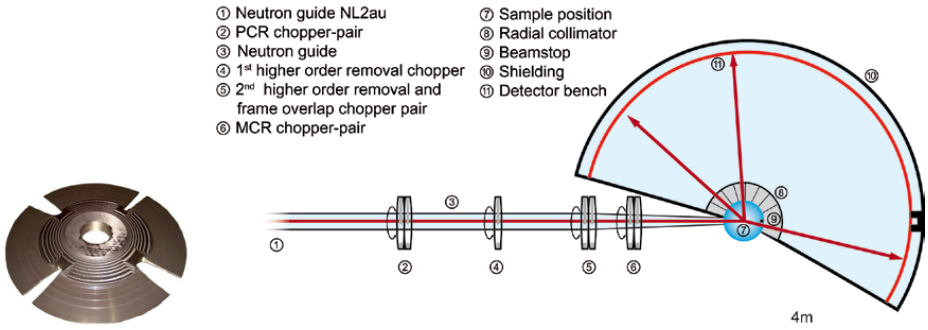

Figure 3.9: Scheme of TOFTOF, a time-of-flight high-resolution spectrometer, together with a picture of one of its chopper disks. *From Refs. [67, 68].*

rotating disk stops most of the neutrons and converts the continuous beam generated by the reactor into bunches. Some subsequent disks remove fast neutrons travelling at higher harmonics of the desired wavelength, which can make it through the first disk, and avoid overlap between different pulses. The last disk is synchronised with the first so that neutrons faster or slower than the desired speed will reach this second chopper too soon or too late and will also be absorbed. The faster the disks rotate the shorter the pulse and, therefore, the higher the time resolution [69].

Typically, TOFTOF sample holders have a hollow cylinder geometry, which allows tiny sample thicknesses, and are made of aluminium, which is quite transparent to neutrons.

Neutrons from these monochromatic bunches will exchange a variety of momenta and energies with the sample which in turn will change the velocities of the scattered neutrons. Therefore, after being scattered by the sample, the bunch will not be monochromatic any more and neutrons will need different times-of-flight to arrive at the detector. Measured detection times in each direction are converted into neutron momentum and energy and, since the character of the neutrons before being scattered is known, this allows to infer the momentum and energy transferred between the sample and the neutron [70, 71].

To avoid background scattering from air molecules as the neutrons scattered by the sample reach the detector bench, the four meters that scattered neutrons must cross to reach the detector are inside a chamber filled with argon gas. The detector bench covers a scattering angle from $-15°$ to $140°$, where ^{3}He counting tubes are placed on Debye-Scherrer rings (see Section 2.2.2 or Figure 4.2).

Chapter 4

D4 data treatment

The detectors at D4 count the number of neutrons that are scattered in each direction, but this quantity depends on many parameters that are not directly related with the characteristic distances present in the measured samples. Therefore, we seek to remove spurious contributions and normalize the measurements to obtain magnitudes such as the differential scattering cross-section per atom (DCS), the scattering function, the pair-correlation function, or the radial distribution function (see Chapter 2).

4.1 Data treatment performed with REGD4C

A fair amount of instrument-dependent data treatment is usually carried out already at the instrument computer with programs REGD4C or D4CREG [72], two variations of the same program.

These manipulations account for the detector dead time correction, normalisation to monitor counts, the different efficiencies of each detector cell, grouping of numors that correspond to the same measurement, and calculation of experimental errors. A magnitude proportional to the experimental differential cross-section per atom of the sample and its surroundings, as well as its errors, is obtained.

4.1.1 Detector dead time

The detector dead time τ is the minimum amount of time that must separate two neutrons arriving to the detector so that they will be recorded as distinct events. Neutrons arriving too soon after a previous neutron has been detected, and the detector is still not ready, will not be counted. This means that the detector will underestimate

the number of neutrons that should be measured, specially as the intensity increases.

In some detectors every particle that arrives to the detector triggers again the dead time, even when this particle arrives during a previous dead time and will not be counted. Such detectors are called paralysable because they become overwhelmed in high event rate situations, overlapping several dead times and thus becoming unable to detect any event at all.

Other detectors are unaffected by events that take place during dead time. These detectors are said to have a nonparalysable response and are able to measure again as soon as the dead time of the previous event is over. Their counting rate upper limit is one event per τ, and the overall fraction of the total time that the detector is dead, f_τ, is directly proportional to the dead time and the measured counting rate ν_m [73]:

$$f_\tau = \nu_m \, \tau \tag{4.1}$$

Assuming a nonparalysable response of the detector, a simple expression can be found to correct the dead time effect from the measurements at D4 so that they can be compared to experiments carried out in other instruments.

On the one hand, the rate ν_τ at which true events are lost, is the product of the dead time fraction f_τ by the true event rate ν:

$$\nu_\tau = f_\tau \, \nu = (\nu_m \, \tau) \, \nu \tag{4.2}$$

And on the other hand, the rate at which true events are lost can also be simply computed by subtracting the measured counting rate from the true event rate: $\nu_\tau = \nu - \nu_m$.

Merging these two expressions allows to estimate the true event rate using the measured counting rate and the dead time of the detector:

$$\nu = \frac{\nu_m}{(1 - \nu_m \tau)} \tag{4.3}$$

Since the monitor is a detector as well, albeit a low-efficiency one, the monitor counts are also underestimated. If the monitor response is nonparalysable this correction can also be performed to obtain the true monitor count value.

4.1.2 Monitor count normalization

The neutron flux at the reactor is very stable, however, it has small fluctuations and may differ at different moments of the fuel cycle or between different cycles.

Additionally, it is obvious that the detector will count more neutrons for long measurements of a sample than for short measurements of the same sample. To account for this, all measurements are normalized to the number of neutrons detected by the monitor (or a multiple of that, such as millions of monitor counts), because this is proportional to the number of neutrons that impinged in the sample. This way, measurements of different lengths or experiments performed at different times of the fuel cycle can be compared.

4.1.3 Detector efficiency

All detectors register a different number of neutrons when the same flux is impinging on them. Even each one of the 574 cells (64 per detector) that constitute the detector bank in D4 has a different efficiency.

This is normally calibrated before the experiment so that the efficiency of each cell is a known parameter of the instrument. In D4 these values are kept in a file and are afterwards used to weight the data measured at the different cells.

This file can also be conveniently used to disregard data coming from malfunctioning cells, or too heavily affected by collimator shadowing effects to be successfully merged with the rest.

4.1.4 Numor grouping

As was explained in Section 3.2.1, due to the radial collimator shadow and the angular separation between detectors at D4, several measurements have to be performed with the detector bank at different offset angles to be able to measure the whole scattering range. Each one of these single measurements is called numor (number of run) and yields an incomplete spectrum (see Figure 4.1). The grouping and averag-

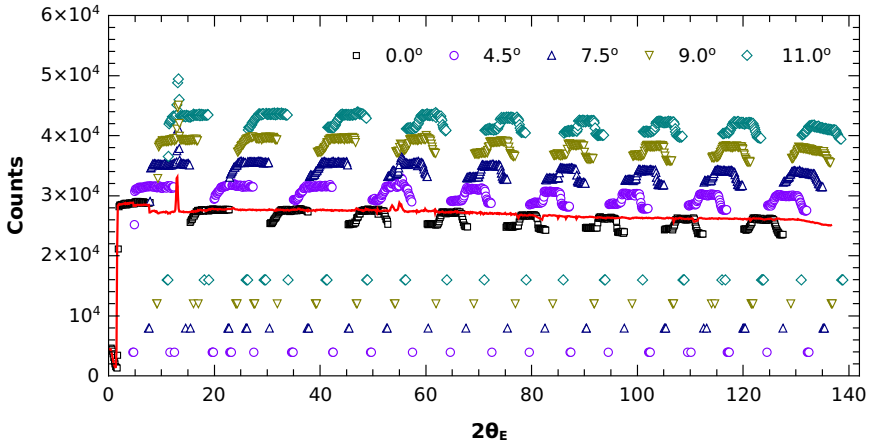

Figure 4.1: Numors measured at D4 for a vanadium rod at offset angles $2\theta_E = 0°$, 4.5°, 7.5°, 9°, and 11° (empty symbols) compared to the merged measurement without corrections (red line). The central channels of the nine detectors measure the proper intensity of the sample but in the edges the shadow effect of the collimator becomes apparent and there is an intensity drop. For the sake of clarity, 0.4x10^4 counts have been added to each subsequent numor.

ing of the different numors into a single measurement is also usually performed at the instrument computer by the program RegD4c.

Since each cell will be in general at a different scattering angle position for each numor, a $2\theta_E$ value has to be assigned to every one of them before the counts of the different numors can be merged (as shown in Figure 4.1). This calculation takes into account the offset angle of the detector bank during the measurement of each particular numor and the detector geometry.

Apart from the different offset angles needed to scan the whole scattering range, usually two or more short runs are preferred at the same angle than a single long run. This way, even if a problem occurs during the measurement of a numor which forces to discard it, a measurement in the whole scattering range, albeit noisier, can still be reconstructed taking the remaining runs that have been performed

at the same angle.

REGD4C divides each count by the efficiency of that detector cell and carries out for the selected numors an average of the values of all the channels that correspond to the same angle. When grouping the numors, this program will ignore any detector with a negative value in the efficiency, thus, any detector cell can be easily removed if necessary to minimize problems associated to shadow or to detector malfunctioning.

Scattering occurring outside of the sample position is normally absorbed by the collimators, but unfortunately a few intense Bragg peaks coming from the sample environment do manage to get through a small window and reach the detector at certain angles below 4.5°. The Bragg peaks are simply avoided by not measuring at the troublesome angles, and to compensate for the lower statistics in that range, measurements at the 0° position, where the Bragg peaks are successfully absorbed by the collimation, may be performed twice or run for longer times.

4.1.5 Errors and resolution

The experimental error of a measurement quantifies how much this measurement differs from the true value of the magnitude. When the true values of the magnitudes are not observable, such as in this work, data errors are often estimated instead using the concept of residual, which quantifies how much this particular measurement differs from the average of all measurements ($\varepsilon_i = x_i - \overline{x}$).

Errors are estimated here using the fact that the standard deviation in a counting experiment is predicted to tend to $\sigma = \sqrt{N}$ as the number of counts N tends to infinity [73]. This approximation is of course only valid as long as the number of counts remains very large.

The counts of each detector cell d_k are divided by the monitor counts M in order to normalise them:

$$n_k = \frac{d_k}{M} \tag{4.4}$$

where n_k is the count of the k-th detector cell normalised to the monitor counts. Since both magnitudes have certain error ε, the

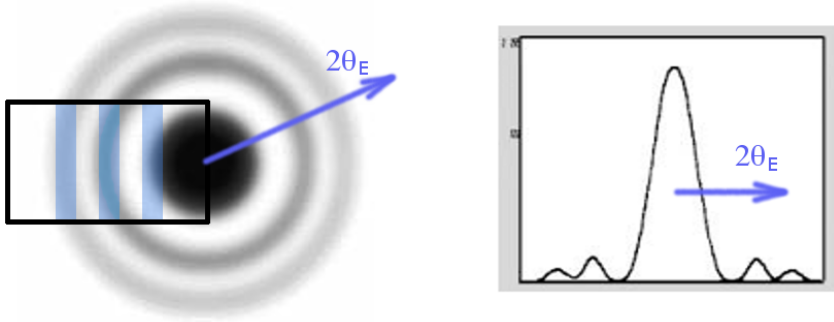

Figure 4.2: Left: Curvy diffraction pattern corresponding to Debye-Scherrer rings (shades of gray) measured by straight detectors (blue rectangles) are the cause of the umbrella effect, which worsens the instrumental resolution at angles near $2\theta_E = 0°, 180°$ but has no effect at $2\theta_E = 90°$. The incoming neutron beam is perpendicular to the text, and darker shade means more neutrons are scattered in that direction. Right: Slice of the diffraction pattern on the left (passing through the origin). *Modified from Ref. [74].*

method of error propagation is used to calculate the error of the resulting diffractogram:

$$\varepsilon_{n_k} = \sqrt{\left(\frac{\partial n_k}{\partial d_k}\right)^2 {\varepsilon_{d_k}}^2 + \left(\frac{\partial n_k}{\partial M}\right)^2 {\varepsilon_M}^2} \tag{4.5}$$

$$= \sqrt{\left(\frac{1}{M}\right)^2 d_k + \left(\frac{d_k}{M^2}\right)^2 M} \tag{4.6}$$

$$\varepsilon_{n_k} = \frac{d_k}{M}\sqrt{\frac{1}{d_k} + \frac{1}{M}} \tag{4.7}$$

where $\varepsilon \simeq \sqrt{N}$ has been used in the first step.

The samples studied in this work are liquids and other amorphous materials, so they are isotropic and the experiment has cylindrical geometry along the axis of the neutron beam. That means that the diffraction pattern only depends on $2\theta_E$ and it consists of a series of concentric rings.

However, the detectors at D4 are straight and do not follow the cylindrical symmetry. This gives rise to the umbrella effect, which affects the resolution of the measurement as a function of the scattering angle (see Figure 4.2), and has to be taken into account in addition to the intrinsic detector resolution. At low angles the radii of the diffraction rings are smaller, and their curvature is more apparent, so the effect on the resolution is larger. As the scattering angle increases, this effect becomes less significant, until it reaches $2\theta_E = 90°$ where the pattern becomes a straight line, and as $2\theta_E$ is further increased beyond this angle the effect starts becoming significant again.

4.2 Data treatment performed with Correct

After the corrections and normalizations usually applied at the instrument with the program RegD4c, a diffraction pattern of the neutrons scattered by the sample and its surroundings normalized to monitor counts (or a fixed multiple of them) is obtained. Further data treatment is required to single out the sample contribution. The goal is to obtain a scattering function in absolute units that can be compared to experiments of the same material performed in similar conditions in other instruments, or even with other techniques.

The computer code Correct [75] has been used to perform the background, multiple scattering and container attenuation corrections to the neutron diffraction data, as well as the normalization to a known sample, modified by a parameter accounting for the fullness of the sample holder.

The program has also an adjustable parameter to multiply, if necessary, the vanadium rod or the sample holder spectra by a factor (for instance to account for a partially filled sample holder), and an option that allows to perform the Placzek correction, but these features have not been used.

If all corrections and normalizations are successful, the differential scattering cross-section per atom of the sample and its errors will be obtained.

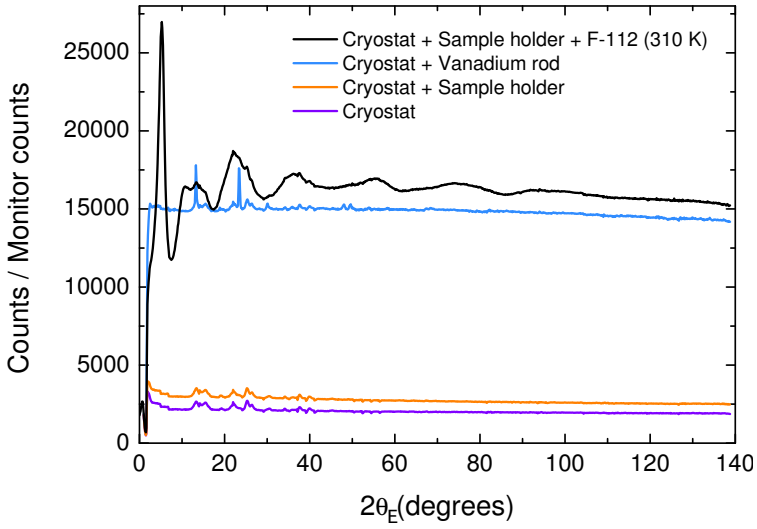

Figure 4.3: Standard set of measurements for a liquid sample at D4 after RegD4c. They include: 1) sample environment + sample holder + sample (black), 2) sample environment + known sample (blue), 3) sample environment + sample holder (orange), 4) sample environment (violet), and 5) sample environment + sample holder + absorbing sample (not shown).

4.2.1 Non-sample contributions

The contribution to the detector counts arising from the background radiation and electronic noise, and from neutrons scattered in the sample environment and sample holder must be removed from the measurement to be able to extract the sample contribution.

In our case, a measurement of the empty sample environment (cryostat, furnace, or cryofurnace) will be considered to be the background. But a separate measurement of an absorbing sample ($^{10}B_4C$) and of the empty sample holder within the sample environment will also be carried out to remove the sample holder contribution and to perform the attenuation corrections (see Figure 4.3).

An even finer correction can be performed if the sample environment is considered to be a second container (besides the sample

holder) and a measurement of the empty instrument without the sample environment is considered to be the background. However, such fine correction was not necessary in our case.

4.2.2 Attenuation and multiple scattering

If the sample is considered point-like or very small, the mean free path of the neutrons before they interact with the sample will be much larger than the sample dimensions, thus virtually all of them will travel through the sample undisturbed, and the tiny fraction of neutrons that are indeed disturbed will certainly have not interacted with the sample more than once. In this case a simple background (sample environment and holder) subtraction would be enough to obtain the scattering of the sample.

However, samples are usually not that small and they may absorb or scatter several times a significant amount of the neutrons that go through it. Therefore, we need to take into account attenuation and multiple scattering when subtracting the different contributions to go beyond this point-like limit case and account for a finite sample volume [76]. These corrections are specially important when the sample of interest has nuclei with substantial absorption and scattering cross sections.

This means that, normally, unwanted background contributions can not be simply removed by subtracting the measurements that have been carried out without the sample, because their scattering is not additive. For instance, due to the fact that the sample absorbs and scatters a fraction of the neutrons, less neutrons can be scattered by the sample holder in the presence of the sample.

Using a highly absorbing sample, in our case $^{10}B_4C$ powder, with the same dimensions and within the same container and sample environment than the sample of interest, allows to measure the background contribution of neutrons that do not go through the sample position, and thus will be unaffected by its presence.

This measurement can be subtracted from the total background to obtain the background contribution of neutrons that do indeed go through the sample position, and apply a sample attenuation correc-

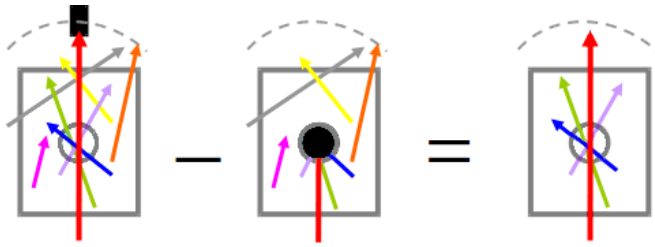

Figure 4.4: Scheme of the parenthesis in the second term of Equation 4.8. The background contribution of neutrons that go through the sample position can not be measured directly, but can be obtained subtracting the absorbent (I_{abs}) from the background (I_{empty}) measurements. *Modified from Ref. [77].*

tion to them (see Figure 4.4):

$$I_{\text{bkgd}} \equiv \underbrace{I_{\text{abs}}}_{\substack{\text{Background not}\\ \text{passing through}\\ \text{sample position}}} + \underbrace{T_{\text{sam}} \underbrace{[I_{\text{empty}} - I_{\text{abs}}]}_{\substack{\text{Background arriving}\\ \text{at sample position}}}}_{\substack{\text{Background transmitted}\\ \text{by the sample}}} \tag{4.8}$$

where I_{bkgd} is the total background contribution to the intensity when measuring the sample, I_{abs} is the measured intensity of the absorbing sample, i. e., the contribution of neutrons that did not go through the sample, I_{empty} is the measurement of the empty sample holder within the sample environment, i. e., the background without the sample, and T_{sam} is the transmission of the sample.

Paalman and Pings [78] calculated the attenuation corrections arising from absorption and scattering of an uniformly illuminated sample and its container in a setup with cylindrical symmetry. The coefficients, which depend on the scattering angle, allow to subtract the empty sample holder measurement taking into account the sample and container attenuation.

To be able to calculate those attenuation coefficients by the sample holder and the sample, their geometry, as well as their cross sections, must be known parameters. Thus, the external and internal

radii of the sample holder must be carefully measured. The latter being also the radius of the sample.

The approach described above assumes that neutrons measured by the detector have been scattered only once, not taking into account multiple scattering effects.

Multiple scattering corrections are quite complex and highly dependent on sample and sample holder composition and geometry. Numerical solutions which usually assume isotropic and elastic scattering can be carried out to correct multiple scattering [79–81]. Monte Carlo multiple scattering simulations can be quite precise and can also be used for complex geometries, but require more computing time [82–84].

4.2.3 Normalization

The normalization of the diffraction intensity of a particular sample to an absolute cross section can be performed by comparing it to another sample of known cross-section and volume in the beam. In our case, a vanadium rod was measured in the experiments for this purpose, as well as the empty sample environment, which corresponds to the background of this measurement.

The advantage of using vanadium for normalization is that it has an isotropic and almost fully incoherent cross section with just a few Bragg peaks of low intensity (see Figure 4.1 or 4.3). This means that it yields a diffraction pattern which is essentially a horizontal line, quite appropriate to use for normalization purposes.

The scattering from the empty sample environment will have to be subtracted from the vanadium to remove its background. If the vanadium measurement is available, this is the calculation that the program CORRECT carries out:

$$\mathbb{C} = \frac{\mathbb{S}}{\mathbb{V}} \left(\frac{\rho_{\mathrm{v}}\, r_{\mathrm{v}}^2}{\rho_{\mathrm{s}}\, r_{\mathrm{s}}^2} \right) \frac{\sigma_{\mathrm{v}}^{\mathrm{scat}}}{4\pi} \tag{4.9}$$

where $\mathbb{C}$ is the output magnitude of the program, $\mathbb{S}$ is the measurement corresponding to the sample (with the corrections mentioned in Sections 4.1, 4.2.1 and 4.2.2 already performed), $\mathbb{V}$ is a polynomial

fit to the vanadium rod measurement which effectively removes its undesired Bragg peaks, ρ_{v} i ρ_{s} are the densities of scattering centres, i. e., number of atomic nuclei, from the vanadium and the sample, r_{v} and r_{s} are the radii of the vanadium rod and the sample, and $\sigma_{\mathrm{v}}^{\mathrm{scat}}$ is the scattering cross section of vanadium.

Since the geometry of the sample of interest and the sample of reference must be known parameters, both radius must be carefully measured. From a practical point of view, due to vanadium being a quite malleable material, it may be not so straightforward to obtain precise measurements of these two magnitudes, specially in the case of the sample holder, which determines the sample radius. This is because sample holder walls are very thin and, hence, quite fragile. Therefore, they are susceptible of larger deformations that may yield a different radius depending on the measurement.

Input data is usually the number of neutrons registered by the detector normalized to the monitor counts of the instrument, but after the additional normalization shown in Equation 4.9 we obtain an absolute magnitude in cross section units.

If we take into account the cylindrical geometry of the experiment and consider that the sample and the vanadium both have the same height h within the neutron beam, the volumes of the vanadium and the sample illuminated by the beam are $V_v = \pi r_v^2 h$ and $V_s = \pi r_s^2 h$, respectively. Thus, it is clear that this operation is no more than a normalization by the number of nuclei contributing to the scattering:

$$\mathbb{C} = \frac{\mathbb{S}}{\mathbb{V}} \left[\frac{\rho_{\mathrm{v}} \overbrace{(\pi r_{\mathrm{v}}^2 h)}^{V_{\mathrm{v}}}}{\rho_{\mathrm{s}} \underbrace{(\pi r_{\mathrm{s}}^2 h)}_{V_{\mathrm{s}}}} \right] \frac{\sigma_{\mathrm{v}}^{\mathrm{scat}}}{4\pi} = \left[\frac{\frac{1}{\overbrace{N_{\mathrm{s}}}^{N_{\mathrm{v}}}} \mathbb{S}}{\frac{1}{\underbrace{N_{\mathrm{v}}}_{N_{\mathrm{s}}}} \mathbb{V}} \right] \frac{\sigma_{\mathrm{v}}^{\mathrm{scat}}}{4\pi} \tag{4.10}$$

where N_{v} and N_{s} are the number of scattering centres of the vanadium and the sample within the neutron beam, respectively.

To get further insight on the magnitude that we are obtaining, we can use the fact that the vanadium rod is a monoatomic sample

and write its differential scattering cross section per atom ($\frac{\mathrm{d}\sigma_\mathrm{v}}{\mathrm{d}\Omega}$) as a function of its coherent ($b_{\mathrm{coh,v}}$) and incoherent ($b_{\mathrm{incoh,v}}$) scattering lengths [4]:

$$\frac{1}{N_\mathrm{v}}\left[\frac{\mathrm{d}\sigma_\mathrm{v}}{\mathrm{d}\Omega}(q)\right] = \cancel{b^2_{\mathrm{coh,v}} S_\mathrm{v}(q)} + b^2_{\mathrm{incoh,v}} \cong \frac{\sigma_\mathrm{v}^{\mathrm{scat}}}{4\pi} \tag{4.11}$$

where $S_\mathrm{v}(q)$ is the vanadium structure factor. Here, the coherent q-dependent contribution can be disregarded because the scattering of vanadium is mainly incoherent (total scattering cross section is $\sigma_\mathrm{v}^{\mathrm{scat}} = 5.1$ b, with the coherent contribution being only $\sigma_\mathrm{v}^{\mathrm{scat,\,coh}} = 0.018$ b), thus it yields a differential cross section per atom which is essentially constant and does not show a q-dependence. With this approximation it can be inferred that the magnitude that the program CORRECT computes is the differential cross section per atom of the sample:

$$\mathbb{C} \cong \frac{1}{N_\mathrm{s}}\left[\frac{d\sigma_\mathrm{s}}{d\Omega}(q)\right] \qquad \lim_{q\to\infty}\mathbb{C} = \frac{\overline{\sigma}_{\mathrm{scat}}}{4\pi} \tag{4.12}$$

where $\overline{\sigma}_{\mathrm{scat}}$ is the mean scattering cross section per atom of the sample. Which means that, if the scattering is purely elastic, $\mathbb{C}$ should oscillate around the $\overline{\sigma}_{\mathrm{scat}}/4\pi$ value.

Just to cite two examples, according to this, the measured diffractograms of deuterated trans-1,2-dichloroethene ($C_2Cl_2D_2$) should oscillate for large q around 0.80 b, and those of 1,1,2,2-tetrachloro-1,2-difluoroethane and 1,1,1,2-tetrachloro-2,2-difluoroethane (F-112 and 112a, $C_2Cl_4F_2$) should oscillate around 0.86 b:

$$\lim_{q\to\infty}\mathbb{C}_{\mathrm{TDCE}} = \frac{1}{4\pi}\left[\frac{1}{3}\left(\sigma_\mathrm{C} + \sigma_\mathrm{Cl} + \sigma_\mathrm{D}\right)\right] = 0.7955 \text{ b} \tag{4.13}$$

$$\lim_{q\to\infty}\mathbb{C}_{\text{F-112}} = \frac{1}{4\pi}\left[\frac{1}{4}\left(\sigma_\mathrm{C} + 2\sigma_\mathrm{Cl} + \sigma_\mathrm{D}\right)\right] = 0.8588 \text{ b} \tag{4.14}$$

However, some compounds may be highly affected by inelastic scattering so, even if the normalization procedure is carried out with great care, their differential cross section per atom would not oscillate around this value until inelastic corrections were also carried out.

4.2.3.1 Normalization using the vanadium sample holder

By default, if there is no normalization measurement, CORRECT assumes that the sample holder is made of vanadium and normalizes the sample with it:

$$\mathbb{C} = \frac{\mathbb{S}}{\mathbb{H}} \left[\frac{\rho_{\mathrm{v}} \left(r_{\mathrm{h,ext}}^2 - r_{\mathrm{h,int}}^2 \right)}{\rho_{\mathrm{s}}\, r_{\mathrm{s}}^2} \right] \frac{\sigma_{\mathrm{v}}^{\mathrm{scat}}}{4\pi} \tag{4.15}$$

where $\mathbb{H}$ is the measurement of the empty sample holder without the background, and $r_{\mathrm{h,ext}}$ and $r_{\mathrm{h,int}}$ are the external and internal radii of the container.

This is equivalent to Equation 4.10 but taking into account that instead of a vanadium rod to normalize we are using a hollow cylinder. This kind of normalization yields a worse result because the sample holder measurement is much noisier than the vanadium rod measurement.

4.2.3.2 Scattering lengths

Accurate quantitative interpretation of normalized data must be undertaken with great caution. Usually, due to the limitations of the approximations that are used to correct and analyse the data, a strict coincidence of the experiment and the theoretical expressions can not be expected. In particular, that holds for the limiting values at high q, around which the scattering function oscillates.

To begin with, the tabulated values of the neutron scattering lengths which are available for consultation usually refer to bound scattering lengths b, and bound scattering lengths are the ones associated with nuclei that are fixed and have no recoil, either due to their large masses compared to that of the neutron, or because they are rigidly attached to such a large mass. This is an approximation and in reality it never happens:

- Nuclei at finite temperature are never completely still.

- Nuclei in molecules are not rigidly fixed because the bonds to other atoms have certain flexibility. For instance, they can be modelled as harmonic oscillator potentials.

- In molecular liquids, and even supposing completely rigid molecular structures, the molecule as a whole recoils when a neutron is scattered.

- In molecular liquids, and even supposing completely rigid molecular structures and a high mass that prevents translational recoil, the molecule can always reorient itself, allowing sort of a local "recoil" of the scattering atom due to rotation.

The nucleus' recoil energy lost by the neutron gives rise to inelastic effects. All those effects depend on the scattering angle and are hard to correct accurately, because they yield complex expressions as a function of this angle [42].

On the other hand, in the case of free and stationary nuclei, the differential cross section is modulated by the free scattering length a (see Section 2.4.5). But in molecular liquids the nuclei are never completely free either.

In the case of a free rigid molecule where the energy of the neutron is smaller than the typical energy between rotation states, each nucleus has an effective mass of M_{mol} and the differential cross section per atom can be computed using Equation 2.40.

As can be seen in Figure 3.3, cross sections, and hence scattering lengths, are in general a function of the incoming neutron energy. This means that we also need to take into account the neutron wavelength to determine the scattering length of the sample.

Tabulated scattering lengths usually refer to thermal neutrons but, in the case of D4, neutrons are coming from the hot source, therefore, they are more energetic than thermal neutrons, something that has to be taken into account through the whole treatment of data. The program CORRECT already does take it into account through the neutron wavelength parameter.

Additionally, absorption cross sections are generally small at standard neutron diffraction energies. A notable exception to this small

Table 4.1: Comparison of the absorption cross sections for thermal neutrons of the elements used in this work together with Cd and ^{10}B, which are two of the elements most commonly used for shielding, as well as ^{3}He, which is used to build neutron detectors. Scattering cross sections are also quoted. All values are expressed in barns and have been taken from Ref. [33].

Element	σ_{abs} (b)	σ_{scat} (b)
D	0.000519	7.64
C	0.0035	5.551
F	0.0096	4.018
H_{nat}	0.3326	82.02
Br	6.9	5.9
Cl	**33.5**	**16.8**
Cd	2520.	6.5
^{10}B	3835.	3.1
^{3}He	5333.	6.

absorption cross section is chlorine, which is a constituent atom of all the materials studied in this work. Chlorine has an absorption cross section which is not as large as the elements used for shielding (like cadmium or 10-boron) but that is very large when compared to other materials studied by neutron diffraction (see Table 4.1). Additionally, its scattering cross section is also quite large compared to the rest of the nuclides, with the only exception of hydrogen.

The possible presence of neutron absorption resonances, where the absorption as well as the scattering cross sections, undergo strong variations as a function of neutron energies, has also to be taken into account (see Figure 3.3). Luckily, they are rare at standard diffraction wavelengths.

Some of the materials with absorption resonances at standard diffraction wavelengths are ^{103}Rh, ^{113}Cd, ^{149}Sm, ^{151}Eu, ^{155}Gd, ^{157}Gd, ^{164}Dy, ^{167}Er, ^{176}Lu, ^{180}Ta, and ^{191}Ir. None of the studied samples contained any of these isotopes.

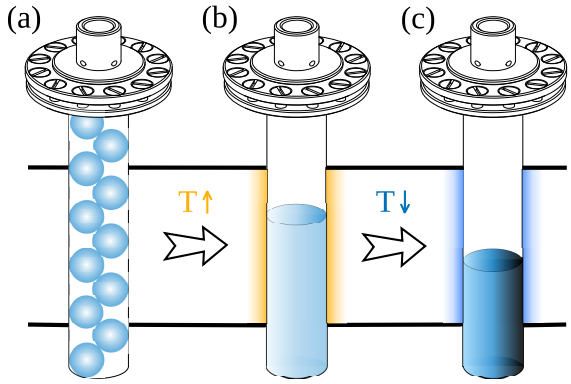

Figure 4.5: Example of complications that a partially full container can pose. (a) Sample holder is filled with a mix of solid pellets and air at room temperature. (b) Increasing the temperature melts the sample, that is drained to the bottom. Part of the neutron beam illuminates the empty container and, although sample concentration is higher, the drainage to the bottom results in less scattering centres within the beam. (c) Cooling to the previous temperature again increases the density of the sample, but due to contraction, it results in a further decrease of the scattering centres within the beam. *Modified from sample holder by T. Unruh.*

4.2.3.3 Partially filled sample holder

To perform the normalization with cylindrical geometry, the heights of the sample and the vanadium within the neutron beam are assumed to be the same and to fill the whole height of the beam. Otherwise, it has to be taken into account through the fullness of the sample holder parameter.

The most desirable situation is that the sample holder is full so we do not run into normalization problems, but in some situations this is hard to avoid. Special attention must be put to this matter in experiments where the temperature range causes the sample to experience phase changes (see Figure 4.5).

When the sample holder is properly filled, and the beam is narrow enough to illuminate the central portion of the sample holder leav-

ing some margin above and below, temperature variations within the same phase change the sample density but not its volume inside the beam. That is because there is enough material above the beam to allow for some contraction of the sample without affecting the measurement. Thus, the intensity of the scattering is normally expected to increase together with the density of the sample, because so does the number of scattering centres in the beam.

If the sample is solid at room temperature and pellets of it are used to fill the sample holder, some air will always remain between the sample bits. The proper way to fill the sample holder would be by melting the sample to make sure that no air bubbles were left inside. Otherwise, this could pose a normalization problem when the sample was afterwards melted during the experiment, because the liquid would fall to the bottom of the sample holder filling the empty spaces and the container would be only partially full. A partially filled sample holder results in a sample volume inside the beam that changes with temperature due to contraction and dilatation, an effect more significant when phase transformations are taking place and the sample experiences larger volume changes. In this worst case scenario, density would seem to increase with temperature in materials that have the opposite behaviour, and a manual adjustment of the container fullness would be necessary for each temperature to obtain normalized measurements.

Highly volatile samples can also pose a problem because a large fraction of them might evaporate before it is possible to close the sample holder. Cooling the sample previously and filling the sample holder in a cold environment might help alleviate this problem.

Great care must be taken to ensure that the sample holder is air tight when dealing with liquid samples, otherwise the high vacuum inside the sample environment could also drain the sample from the container.

If the sample holder is set to partially full, CORRECT does not normalise using the whole measurements, but just taking the proportional part.

4.2.4 Sample density

It is indispensable to know the density of scattering centres of the sample to be able to normalize the diffractogram. Usually density changes are not large, except if the sample experiences phase transformations, thus a reasonably approximate value for the density will be normally enough. Small pressure differences will build inside the air tight sample holder as the temperature is changed, but its effect on the sample volume is negligible.

4.2.5 Error calculation

Calculation of errors in the code CORRECT is performed through error propagation and is calculated every time the experimental data is manipulated.

For instance, when measurements are added or subtracted, like in the case of the background correction, the error ε_k^z of each point k of the corrected scattering function is calculated using the following expression:

$$\varepsilon_{z,k} = \sqrt{{\varepsilon_{x,k}}^2 + {\varepsilon_{y,k}}^2} \tag{4.16}$$

where k is the data bin, $\varepsilon_{x,k}$ and $\varepsilon_{y,k}$ are the errors in each measured spectra, and $\varepsilon_{x,k}$ are the errors of the corrected data. On the other hand, when data is multiplied by a factor C, like in the case of the fullness of the sample holder correction, the errors of the resulting data are simply scaled with this factor: $\varepsilon_{z,k} = C\varepsilon_{x,k}$.

4.3 Inelasticity correction

To derive the neutron diffraction expressions that have been used in this work, the static approximation has been adopted. This approximation holds when the energy exchange between the scattered neutron and the nucleus is much smaller than the initial energy of the neutron or, equivalently, when the structure of the sample is sufficiently static compared to the speed of the neutron. The fact that the neutrons used for this purpose are relatively slow and that their

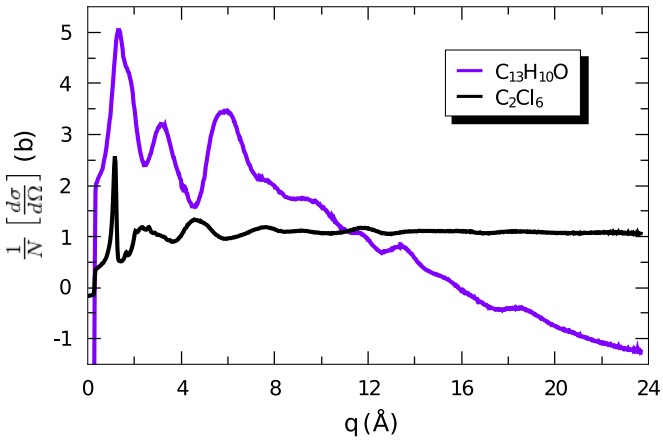

Figure 4.6: Diffractograms of benzophenone ($C_{13}H_{10}O$) and hexachloroethane (C_2Cl_6) at 400 K, fully corrected except for the inelasticity effects. The greater effect on high q and molecules with lighter atoms, which can have a larger recoil after the scattering, can be observed. In fact, atoms from the heavier and stiffer hexachloroethane molecule appear on average essentially unaffected by inelasticiy. After correcting this effect, benzophenone's diffractogram should oscillate around 2.97 b and hexachloroethane's around 1.11 b.

mass is comparable to that of the nuclei explains why inelasticity corrections are rather large in neutron diffraction when compared to x-ray diffraction.

Breakdown of the static approximation takes place for higher scattering angles, where the energy and momentum exchange is greater, and for samples that contain light atoms, more subject to large recoil after the scattering event (see Figure 4.6). Additionally, when this happens, the scattering angle begins depending on the energy exchange as well, and q values do not correspond so well to $2\theta_E$.

A more intuitive explanation to this is that, although in non-elastic scattering events, the atom is "free" and a fraction of the incident neutron's momentum is always lost due to the atom's recoil, in practice very little momentum is lost at low momentum transfers,

so the event is almost elastic and the atom appears to be "bound". However, for large momentum transfers, a larger absolute amount of momentum is lost to the atom recoil, and the scattered neutron is measured at significantly lower momentum transfers, which explains why there is a drop in the neutron count for large q.

Among the differential cross section contributions, the self part, which corresponds to the recoil of each individual atom, is more affected by inelastic effects than the distinct part. This happens because the momentum transfer of the distinct contribution is distributed between all the atoms in the coherence volume, and since the atoms tend to move together, their relative distances are less distorted, and so is the distinct term. To be fully precise, an inelasticity correction to the distinct term of the scattering function should be performed, specially for samples with lighter atoms, because otherwise inaccurate interatomic distances may be obtained in the analyses [4]. However, its evaluation is not straightforward and is out of the scope of this work.

4.3.1 Placzek correction

The most common way to perform inelastic corrections in diffractograms of liquids and glasses measured at reactor sources is following the approximation devised by Placzek [85]. This method consists in assuming that the static approximation is the best fit and deriving corrections to that, which is reasonable for nuclei with little recoil. This is not the only possible approach, since other authors have assumed on the contrary that the free nucleus is the best approximation, and then derived the corresponding corrections to that [86]. See Refs. [42] and [87] for discussions on other alternative procedures.

The relationship between the measured self part of the scattering function and its inelasticity corrected version can be expressed as

$$\frac{1}{N}\left[\frac{\mathrm{d}\sigma}{\mathrm{d}\Omega}\right]^{\mathrm{self}}_{\mathrm{meas}}(q) = \frac{1}{N}\left[\frac{\mathrm{d}\sigma}{\mathrm{d}\Omega}\right]^{\mathrm{self}}_{\mathrm{corr}}[1 + P(q)] \tag{4.17}$$

where $P(q)$ is a polynomial expansion in powers of q^2 and the ratio m_n/M_α of the neutron's mass to that of atoms in the sample. The

self part of the scattering function should yield the constant value $\overline{\sigma}_{\text{scat}}/4\pi$ after inelasticity corrections have been performed [4] (see Equation 2.64).

This equation concerns solely the inelastic correction of the self term, it must not be generalized to the whole scattering function. If the measured diffractogram, i. e., with both self and distinct part contributions, were divided by $[1 + P(q)]$, this would also improperly modify the relative height of each oscillation in the distinct part as a function of q, yielding a diffractogram corresponding to a different structure.

Formulae are available to calculate the coefficients of the polynomial expansion $P(q)$ but, since they strongly depend on the detector efficiency, they must be calculated particularly for each instrument [88]. Additionally, when dealing with molecular liquids or glasses, the M_α needed to calculate the $P(q)$ coefficients does not necessarily strictly mean the mass of the atom, but rather an effective mass that takes into account that the atom is neither bound nor free but in a potential, so that the vibration of the molecular bonds, and the molecular mobility within the liquid (both translational and rotational) are considered. In a molecular glass the movement of the atoms will be more restricted but it will still not correspond to a completely bound atom.

In practice, the self and distinct contributions are mixed, but a simple approach can be taken just by fitting the polynomial expansion in q^2 to the higher range of q of the measured scattering function, so that the coefficients of the polynomial can be estimated empirically:

$$\mathbb{C} \sim \frac{\overline{\sigma}_{\text{scat}}}{4\pi}[1 + p_2 q^2 + p_4 q^4 + \ldots] \tag{4.18}$$

where $\mathbb{C}$ is the measured scattering function obtained after the corrections and normalization performed by CORRECT (but without the Placzek correction), and p_i is the coefficient of the q^i term of the Placzek polynomial. After subtracting this polynomial from the data, we obtain a scattering function corrected from inelasticity effects on the self part:

$$\mathbb{P} = \mathbb{C} - \frac{\overline{\sigma}_{\text{scat}}}{4\pi}[p_2 q^2 + p_4 q^4 + \ldots] \tag{4.19}$$

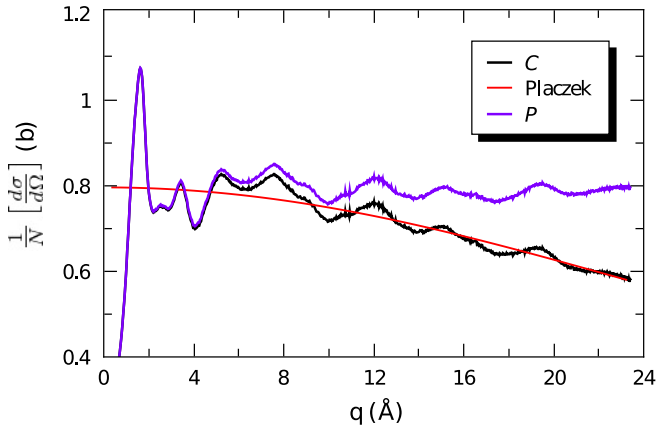

Figure 4.7: Diffractogram of deuterated trans-1,2-dichloroethene ($C_2Cl_2D_2$) at 275 K. Normalized measurement with all corrections except Placzek (black line), corresponding polynomial fit to this curve (red line), and fully corrected diffractogram including Placzek correction which subtracted the polynomial (violet line). Resulting diffractogram should oscillate around 0.80 b.

where $\mathbb{P}$ is the scattering function after all corrections and normalization (including also the Placzek correction), and which will oscillate around the $\overline{\sigma}_{\text{scat}}/4\pi$ value.

Due to the fact that normalization is never perfect and the approximations performed during the derivation of the equations, the $\overline{\sigma}_{\text{scat}}$ value must be left as a parameter of the fit when performing the Placzek correction.

Experience has shown that adding the q^6 term is usually counterproductive and worsens the correction due to overfitting. When too many parameters are used for the fit, the polynomial that aims to describe the falloff of the self contribution to the scattering function starts adapting at high q to the shape of the oscillation, which comes from the distinct contribution, thus distorting the resulting diffraction profile when subtracted. Furthermore, when the Placzek falloff due to inelastic effects is small, fitting the polynomial just up to the

q^2 term will already be enough.

Since this procedure assumes that the static approximation is the best starting point and then derives corrections from that, it can be used for most atoms except the lightest ones. The high q range of the measured scattering function can not be satisfactorily fitted to a Placzek polynomial for hydrogen and other light atoms, but other trial and error methods can be used to fit a curve that will be subtracted afterwards. A pseudo-Voigt function has for instance been found to be well suited for hydrogen concentrations higher than 20% [4].

CORRECT has an option to perform the Placzek correction to measurements from reactor sources using the Yarnell et al. formulae to calculate the coefficients [88], but better results were obtained through the direct polynomial fit of the data discussed above, so it has not been used in this work.

4.4 Alternative normalization

Many factors involved in the normalization of the measurement cause the $\overline{\sigma}_{\text{scat}}$ value obtained through the fit of the Placzek polynomial to differ from the theoretical one, a perfect coincidence should not be expected.

Small differences between the real and the estimated density of the sample cause a slight displacement of the oscillation centre of $\mathbb{P}$ from the theoretical $\overline{\sigma}_{\text{scat}}/4\pi$ value, as well as discrepancies in the peak heights. That means that if the sample is a bit warmer of cooler than estimated, a different value will be found.

If the density of the sample is well known and there is a large discrepancy between the fitted and theoretical values, there are chances that the sample holder was not completely full or that the amount of sample inside the container was not constant throughout the experiment.

When in lack of a normalization standard, or when density, fullness of the sample holder or another key parameter for normalization is unknown or ill defined, the parameter value that has to be used to

obtain a properly normalized diffractogram in absolute units can be obtained from the theoretical value to which the scattering function will tend as q goes to infinity, $\overline{\sigma}_{\text{scat}}/4\pi$.

However, the comparison of the measured value, around which the diffraction pattern oscillates, with the theoretical one can only be performed after the whole set of corrections have been performed. Which means that every time a normalization parameter is slightly adjusted, all the corrections must be carried out again before comparing. So a laborious process of trial and error must be undertaken if any of these normalization parameters is not well known.

The procedure would be as follows: first we perform the corrections with tentative values of the unknown parameter (density, radius, fullness of the sample holder...), then we perform the corrections (including the inelasticity one), and then we compare the value of the measurement as q tends to infinity to the theoretical $\sigma_{\text{v}}^{\text{scat}}/4\pi$ value. If the Placzek correction has been carried out, the theoretical value can be simply compared to the constant parameter in the polynomial. Then, if the corrected measurement yields a smaller value than the theoretical one, it means that we are in one of these situations:

- We have overestimated the number of scattering centres in the sample that contribute to the measurement. Hence, we need to reduce the density, the radius, or the fullness of the sample holder accordingly.

- We have underestimated the number of scattering centres of the vanadium rod that contribute to the normalization measurement. Hence, we need to increase the radius of the vanadium rod accordingly.

On the contrary, if the measurement yields a larger value than the theoretical one, whether we have underestimated the number of scattering centres of the sample or overestimated those of the vanadium rod, we will have to change the unknown parameter accordingly before performing the corrections and comparing again. This procedure will have to be repeated iteratively until an acceptable normalization is reached.

Note that the built-in default value of the vanadium scattering cross section in some versions of CORRECT (i. e. 4.95 b) is different than the one accepted by the scientific community and tabulated in standard tables (i. e. 5.1 b), thus the corrected and normalized measurements could yield appreciable discrepancies with respect to the theoretical value. Therefore, it is safer to manually specify the scattering cross section of vanadium when using the program to perform the corrections and normalization.

4.5 Fourier transform

When all corrections and normalizations have been performed, the experimental differential cross section per atom $\frac{1}{N}\left[\frac{\mathrm{d}\sigma}{\mathrm{d}\Omega}\right]$ is obtained as a function of the scattering vector magnitude q, i. e. in reciprocal space.

Although structural information can be extracted from this function, it is also convenient to have a function in real space to carry out the analyses. For that it is necessary to perform a Fourier transform of the distinct part of the corrected experimental data:

$$\mathbb{T} = \mathscr{F}\left[\mathbb{P} - \frac{\overline{\sigma}_{\mathrm{scat}}}{4\pi}\right] \tag{4.20}$$

where $\mathscr{F}$ is the Fourier transform operator, $\mathbb{P}$ is the fully corrected and normalized data, and $\overline{\sigma}_{\mathrm{scat}}/4\pi$ is the empirical value around which $\mathbb{P}$ is oscillating. By Fourier transforming the distinct part of the measurement, the characteristic distances of the system are obtained from the interference phenomena.

From the point of view of the numerical computation of the discretised Fourier transform of the experimental data, this is the operation that has been carried out:

$$\mathbb{T}(r) = \frac{2}{\pi}\sum_{k=1}^{n} q_k \left[\mathbb{P}(q_k) - \frac{\overline{\sigma}_{\mathrm{scat}}}{4\pi}\right] \sin(rq_k)\Delta q \tag{4.21}$$

where $k = 1, \ldots, n$ are the experimental points, and Δq is the sampling interval.

Other real space functions that can be used for the structural analysis are the experimental radial distribution, pair-correlation functions, or other related functions in the case of polyatomic of molecular liquids and glasses (see Section 2.6), which can be obtained from the following calculation:

$$\mathbb{RDF}(r) = 4\pi\rho r^2 + r\,\mathbb{T}(r) \tag{4.22}$$

$$\mathbb{G}(r) = 1 + \frac{1}{4\pi\rho r}\,\mathbb{T}(r) \tag{4.23}$$

where ρ is the density of scattering centres in the sample, that is, atomic nuclei.

4.5.1 Experimental limitations

To properly perform the Fourier transform $\mathscr{F}$, the reciprocal space function must be integrated up to infinity, which means that in theory we should perform measurements of the scattering function up to $q \to \infty$ to be able to integrate in the whole range. However, the values of q are related to the incoming neutron wavelength λ and the scattering angle $2\theta_E$, and will always have a finite value:

$$q = \frac{4\pi}{\lambda}\sin\theta_E \qquad q_{\max} = \frac{4\pi}{\lambda} \tag{4.24}$$

Additionally, neutron wavelengths used in the experiment can not be arbitrarily small because this is at the cost of having to attain larger and larger neutron energies.

The experimental truncation of the scattering function has two effects in the Fourier transform: it leads to peak broadening in real space thus reducing the resolution, and it gives rise to spurious unphysical oscillations in the real space function. Due to their small frequency, these oscillations pose a greater problem when determining intramolecular distances, because they interfere more significatively with peaks corresponding to the range of smaller distances.

To avoid these ripples and the loss of resolution, the scattering function must be measured up to a q value as large as possible.

Very noisy data also suffer from high frequency spurious oscillations after the Fourier transform, thus, it is not enough to measure up to a high q range, a good quality of data must be ensured as well.

4.5.2 Smoothing

To minimize the unphysical ripples resulting from the Fourier transform of a finite function, we must make sure that the scattering function reaches zero as smoothly as possible when $q \to q_{\text{max}}$.

One way to do that is to Fourier transform the scattering function only up to the oscillation's last zero q_{coff} through multiplying it by a window step function:

$$\left[\mathbb{P}(q) - \frac{\overline{\sigma}_{\text{scat}}}{4\pi}\right] \Theta(q_{\text{coff}} - q) = \begin{cases} \mathbb{P}(q) - \frac{\overline{\sigma}_{\text{scat}}}{4\pi} & \text{for } q < q_{\text{coff}} \\ 0 & \text{for } q > q_{\text{coff}} \end{cases} \tag{4.25}$$

where q_{coff} is the chosen cutoff value of q that will become the new q_{max}, so that any larger value will be discarded.

Another way to do it is applying a damping function to the data before carrying out the Fourier transform, which will forcefully bring the scattering function smoothly to zero at q_{coff}. A normalized sinc function can be used for that purpose, with the advantage that the area of the peaks in real space after performing the Fourier transform will be preserved:

$$\text{sinc}(x) \equiv \frac{\sin \pi x}{\pi x} \qquad \text{where} \quad x = \frac{q}{q_{\text{coff}}} \tag{4.26}$$

The drawback of this method is that the smoothing function does not only reduce the magnitude of the spurious oscillations, it also damps the whole scattering function, including the oscillations that describe the sample, with the consequent loss of meaningful information. The result is that the peaks appear smaller and broadened in real space, effectively reducing the real space resolution and smearing out intra and intermolecular features (Figure 4.8).

Additionally, the smaller the q cutoff value, the more smeared out also the features appear in real space, thus, the chosen q_{coff} value

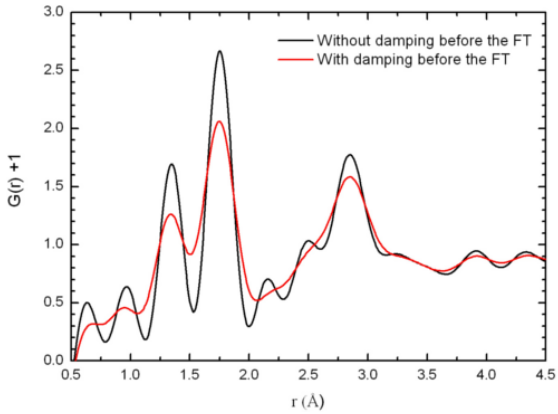

Figure 4.8: Comparison of the obtained Fourier transform of the scattering function of Freon 112a at 320 K when a window step function (black line) or a modulating damping sinc function (red line) are applied.

must correspond to the measured scattering function zero with the highest q possible.

4.5.3 Convolution

The reason that the Fourier transform of experimental data broadens the diffraction peaks in real space as well as generate a series of spurious oscillations is that, due to the finite q-range available in the measurements, in practice it is not the Fourier transform of the scattering function that is carried out:

$$\mathbb{T}(r) = \mathscr{F}\left\{\mathbb{P}(q) - \frac{\overline{\sigma}_{\text{scat}}}{4\pi}\right\} \neq \mathscr{F}\left\{\frac{1}{N}\left[\frac{\mathrm{d}\sigma}{\mathrm{d}\Omega}(q)\right]\right\} = \mathbb{R}(r) \qquad (4.27)$$

where $\mathbb{T}$ is the Fourier transform of the distinct part of the corrected experimental data, and $\mathbb{R}$ is the hypothetical experimental data in real space without broadening of peaks and spurious oscillations, and containing only the structural information of the sample.

What is carried out instead, is the Fourier transform of the product of the scattering function with a Heaviside step function that

represents the finite measuring range [4]:

$$\mathbb{T}(r) = \mathscr{F}\left\{\frac{1}{N}\left[\frac{\mathrm{d}\sigma}{\mathrm{d}\Omega}(q)\right]\Theta(q_{\max}-q)\right\} \tag{4.28}$$

$$= \underbrace{\mathscr{F}\left\{\frac{1}{N}\left[\frac{\mathrm{d}\sigma}{\mathrm{d}\Omega}(q)\right]\right\}}_{\mathbb{R}(r)} \otimes \mathscr{F}\left\{\Theta(q_{\max}-q)\right\} \tag{4.29}$$

and thus $\mathbb{R}$ is not directly accessible through just Fourier transforming the corrected experimental data $\mathbb{P}$.

The bottom line is that if we simply compare the Fourier transformed data with the calculated theoretical models of functions in the real space, they will never be an accurate match. However, the effect of the experimental window can be taken into account together with the theoretical model of $\mathbb{R}$ before this is compared or fitted to the data by performing a convolution in real space of the model with the Fourier transform of the window step function [89, 90]:

$$\mathbb{T}(r) = \mathbb{R}(r) \otimes \left[\frac{\sin\left(q_{\max}r\right)}{r}\right] \tag{4.30}$$

which will yield a function that will fully account for the peak broadening and the unphysical ripples, and can be directly compared to $\mathbb{T}$, the Fourier transform of the data.

This method has the drawback of being more complicated and much more time consuming but it provides a much more accurate and reliable analysis. The procedure has been implemented in the program FABADA and has been used in the data treatment of all samples throughout the whole work.

4.5.4 Error calculation of Fourier transformed data

Data errors are indispensable to quantify the accuracy of analyses but, in the case of a Bayesian fit, they also have a key significance during the fit itself. This is because they determine how much $\chi^2\{P_i\}$

can be increased to explore sets of parameter values farther from the minimum (this will be explained in more detail in Chapter 5).

Since the Fourier transform of the experimental scattering function will also be used to perform the fits, a careful calculation of its errors after such procedure is in order. Since this calculation is not obvious it will be explained in the following sections.

Two approaches have been used to perform this calculation: by error propagation of the discretised Fourier transform, and through a Monte Carlo method.

4.5.4.1 Error propagation

In this approach, error propagation theory is applied to the discretised Fourier transform that has been used to calculate the real space experimental functions [91].

In a general case, the value of function $y = f(u, v, \ldots)$ has been determined from the measurements of its random variables u, v, ... and its error has to be determined as well. Function y must fulfil the condition that its most likely value $\overline{y}$ can be calculated through $\overline{y} = f(\overline{u}, \overline{v}, \ldots)$ and we assume that errors are small enough for a Taylor series expansion up to first order being a good approximation:

$$y_i - \overline{y} \simeq (u_i - \overline{u}) \left(\frac{\partial y}{\partial u} \right) + (v_i - \overline{v}) \left(\frac{\partial y}{\partial v} \right) + \cdots \tag{4.31}$$

where u_i is the value of magnitude u corresponding to the particular measurement i, and $\overline{u}$ is the most probable value of u.

Additionally, the variance and covariance are also defined through data residuals:

$$\sigma_y^2 \equiv \frac{1}{m} \sum_{i=1}^{m} (y_i - \overline{y})^2 \tag{4.32}$$

$$\sigma_{uv}^2 \equiv \frac{1}{m} \sum_{i=1}^{m} (u_i - \overline{u})(v_i - \overline{v}) = \overline{uv} - \overline{u}\,\overline{v} \tag{4.33}$$

where σ_y^2 is the variance of magnitude y, σ_{uv}^2 is the covariance of magnitudes u and v, and m is the number of measurements at each single point of function y.

Squaring linear Equation 4.31 and using the variance and covariance definitions above yields a general equation for the calculation of the variance of y from which the familiar error propagation formula can be obtained:

$$\sigma_y^2 \simeq \sigma_u^2 \left(\frac{\partial y}{\partial u}\right)^2 + \sigma_v^2 \left(\frac{\partial y}{\partial v}\right)^2 + \underbrace{2\sigma_{uv}^2 \left(\frac{\partial y}{\partial u}\right)\left(\frac{\partial y}{\partial v}\right)}_{\substack{\sigma_{uv}^2=0 \\ (u \text{ independent} \\ \text{from } v)}} \to 0 + \cdots \tag{4.34}$$

$$\sigma_y \simeq \sqrt{\sigma_u^2 \left(\frac{\partial y}{\partial u}\right)^2 + \sigma_v^2 \left(\frac{\partial y}{\partial v}\right)^2 + \cdots} \tag{4.35}$$

where the variances σ_u^2, σ_v^2, ...of the measured magnitudes have known values, and σ_{uv}^2 is the covariance between u and v, which will be zero if they are independent variables.

In our case we have n different measurements to describe every experimental scattering function, corresponding to the points in the reciprocal space. The deviations of the values are characterised by standard errors, so that each measured data point yields a normal distribution of values around the "real" one. Considering that these errors are independent random variables with normal distributions, this scheme can be adopted to determine formulae that give the propagated error of the data when using Equations 4.21, 4.22, or 4.23, because these are all equations that transform data to real space through the discretised Fourier transform, i. e, using a sum of terms.

Using the functional dependence of $\mathbb{T}$, $\mathbb{RDF}$, and $\mathbb{G}$, these partial derivatives have been obtained:

$$\frac{\partial \mathbb{T}}{\partial \mathbb{P}} = \frac{2}{\pi} \sum_{k=1}^{n} q_k \sin(r q_k) \Delta q \tag{4.36}$$

$$\frac{\partial \mathbb{RDF}}{\partial \mathbb{P}} = \frac{2r}{\pi} \sum_{k=1}^{n} q_k \sin(r q_k) \Delta q \tag{4.37}$$

$$\frac{\partial \mathbb{G}}{\partial \mathbb{P}} = \frac{1}{2\pi^2 \rho r} \sum_{k=1}^{n} q_k \sin(r q_k) \Delta q \tag{4.38}$$

which can then be substituted in Equation 4.35.

The following relationships between the normally distributed errors of the structure factor and its Fourier transform have been obtained through error propagation theory:

$$\varepsilon_{\mathbb{T}} = \varepsilon_{\mathbb{P}} \left[\frac{2}{\pi} \sum_{k=1}^{n} q_k \sin\left(q_k r\right) \Delta q \right] \tag{4.39}$$

$$\varepsilon_{\mathbb{RDF}} = \varepsilon_{\mathbb{P}} \left[\frac{2r}{\pi} \sum_{k=1}^{n} q_k \sin(r q_k) \Delta q \right] \tag{4.40}$$

$$\varepsilon_{\mathbb{G}} = \varepsilon_{\mathbb{P}} \left[\frac{1}{2\pi^2 \rho r} \sum_{k=1}^{n} q_k \sin(r q_k) \Delta q \right] \tag{4.41}$$

The function 4.40 describing the error of the $\mathbb{RDF}$ has been plotted in Figure 4.9(b) where it can be seen that it displays an overall linear dependence with r but with a tiny sinusoidal modulation on top of that.

4.5.4.2 Monte Carlo method

The Monte Carlo method consists in generating a large number of scattering functions where each data point has a random value of a normal distribution, and then Fourier transforming them to find the probability distribution of the data points in real space [93].

Figure 4.9(a) shows an example of one of these scattering functions generated using random values of a normal distribution with mean value $\mu = 0$ and variance $\sigma^2 = 1$ for the data points. This normal distribution accounts for the experimental error in q.

The Fourier transform of each of these random scattering functions will yield an oscillation in real space of completely different shape. Some examples of Fourier transformed random scattering functions can be seen in Figure 4.9(b).

Using a large number of Fourier transformed random data sets, and calculating the frequency of each value that the Fourier transformed random scattering functions yielded for a particular r, the error distribution at this r can be obtained. The fact that full proba-

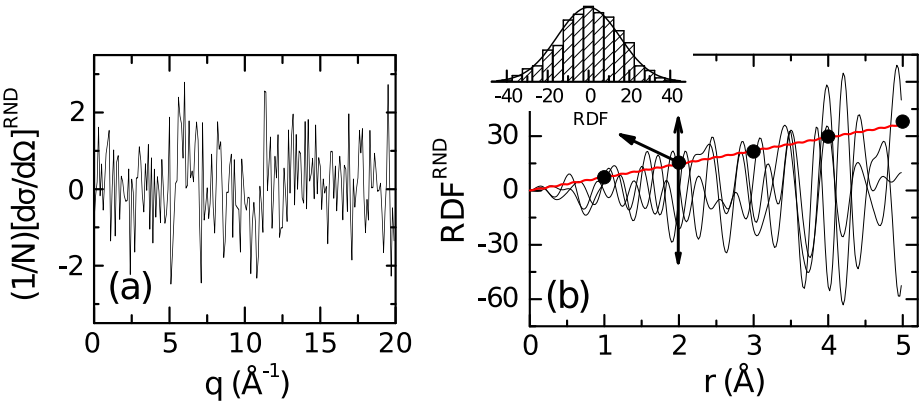

Figure 4.9: (a) Example of a scattering function generated as random data points of a normal distribution. (b) Examples of Fourier transformed random scattering functions (thin black lines). Errors calculated through the Monte Carlo method (circles) and through error propagation (thick red line). A sample of the error distributions in real space can be seen on the inset, showing that the error is also normally distributed. The distribution at $r = 2$ Å was calculated using 1000 random scattering functions. *Modified from Ref. [92].*

bility distribution functions of the error are obtained is a clear advantage of this method, because no assumptions have to be made in this regard, contrary to the error propagation method described before.

Normal probability distributions of errors in reciprocal space yielded normal distributions of errors in real space as well. Although they had different standard deviations for each r value. An example of the probability distributions obtained can be seen in the inset of Figure 4.9(b) where the distribution for $r = 2$ Å calculated through the Fourier transform of 1000 random scattering functions is shown.

The probability distribution functions have been calculated in this manner for five points. And the errors, obtained from the standard deviation of each point's normal distributions, are plotted in Figure 4.9(b).

Results from the these two independent methods lie on top of each other, validating them and showing that they are both consis-

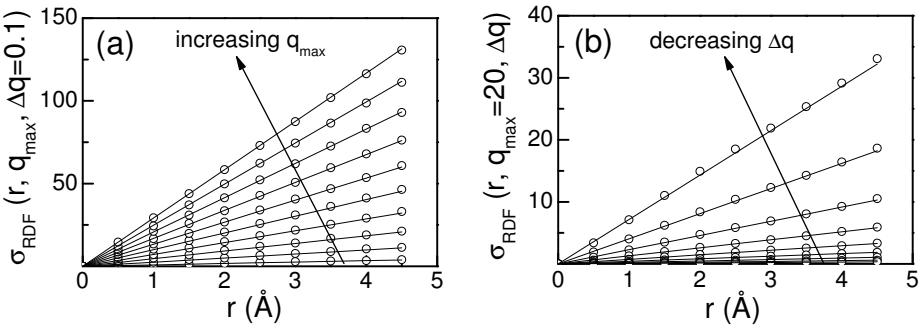

Figure 4.10: Calculation of errors, after Fourier transformation of the scattering function, using error propagation of random data with a normal distribution (circles). Estimation of the same errors using the empirical Equation 4.42 mentioned in this section is also shown (lines). (a) Subset of errors calculated with the same Δq, and (b) with the same $q_{\max}$. *From Ref. [92].*

tent ways to calculate the error after the Fourier transform is carried out. However, the Monte Carlo method takes a much larger computational effort, thus, the error propagation method will be used in the following sections.

4.5.4.3 Empirical equation

A series of systematic calculations of the error as a function of r, the sampling interval Δq, and $q_{\max}$ have been carried out using error propagation so that an empirical equation that describes the dependence of the error with respect to these parameters could be found. The aim was to have a simple and fast method to calculate the errors of the Fourier transformed measurements, so they can be more easily calculated for each data set.

Figures 4.10(a) and (b) show respectively the calculation of more than a hundred errors at the same sampling interval $\Delta q = 0.1$ Å^{-1} but different r and $q_{\max}$, and at the same $q_{\max} = 20$ Å^{-1} but different r and Δq.

From the systematic calculations of the Fourier transformed data

errors, a linear dependency with the variable r could be observed, with the slope m being a function of the other two parameters, Δq and $q_{\max}$:

$$\varepsilon_{\mathbb{RDF}}(r) = m(q_{\max}, \Delta q)\ r\ \varepsilon_{\mathbb{P}}(q) \tag{4.42}$$

Since the $q_{\max}$ and Δq values are usually constant throughout a diffraction experiment, the value of the slope has to be calculated only once for each particular experiment and then the trivial linear Equation 4.42 can be used to estimate the errors of all points in the radial distribution function.

The following empirical relationship between the slope m, $q_{\max}$ and the sampling interval Δq, was observed to yield a good approximation to the calculated errors:

$$m = 0.226 \cdot (q_{\max})^{1.5341} \cdot (\Delta q)^{0.495} \tag{4.43}$$

In Figure 4.10 error estimations calculated through this empirical function can be compared to the points calculated using the method of error propagation. Excellent agreement ascertains the accuracy of the estimation. The validation of this formula provides a convenient and straightforward method (through Equations 4.42 and 4.43) to estimate the errors of the real space functions obtained from the Fourier transform of the experimental scattering functions.

Chapter 5

Analysis methods

To determine whether an hypothesis describing the physical world is more valid than another is necessary to compare them with experimental results and find out which hypothesis describes them better [94].

However, the Occam's razor principle also plays an important role in the decision process to choose between competing hypotheses. The more elements an hypothesis includes, the easier it will be that it describes experimental data accurately, but the more complicated the explanation.

To avoid superfluous complications it is necessary to find an equilibrium between these two aspects and obtain an hypothesis that best describes the data but that is as simple as possible, only adding further elements when this is in exchange of increasing the ability of the hypothesis to explain physical phenomena.

This basic principle that an hypothesis must describe the experiments as accurately as possible and be kept as simple as possible at the same time, can be used to refine models expressed in mathematical form where the parameter values are not determined by theoretical assumptions. In these models, the parameter values can be varied until the combination that makes the model more closely resemble the experiment is found.

Another method widely used to find hypotheses that can describe the collective properties of complex systems with a large series of elements, is to start from simple models that describe only the individual behaviour of these elements and their interactions with only the nearest ones. If the resulting global behaviour is close enough to the experiment, it is considered that the individual models yield a good description of the problem, and the information generated from this calculation can be used to analyse the arrangement and

behaviour of the elements when they are within the group, so that hypotheses that describe the collective phenomena can be obtained.

5.1 Frequentist approach to fit experimental data

5.1.1 Introduction

The frequentist definition of probability assumes that the magnitude being measured does not have a distribution but a true fixed value instead. Whereas it assumes that the measured values do indeed have a distribution, because their confidence interval depends on the particular set of measurements which are random (i. e., that the measurements have errors). In particular, probability is interpreted as the relative frequency to which an event would be observed if the experiment was repeated a large number of trials:

$$P(a) = \lim_{N\to\infty} \frac{n_a}{N} \tag{5.1}$$

where $P(a)$ is the probability of event a, N the total number of trials, and n_a the number of times that the event a is observed.

From the measured distribution of values, a mean and a confidence interval are defined for the sought parameter. The confidence interval gives an estimate of the reliability of the estimated value for the parameter, that is, if the experiment was repeated a large number of trials, which fraction of the estimations calculated from each experiment would yield a value within that reliability interval.

Usually it is assumed that the parameter measurements follow a normal distribution:

$$P(x) = \frac{1}{\sqrt{2\pi\sigma^2}} \exp\left[-\frac{1}{2}\left(\frac{x-\mu}{\sigma}\right)^2\right] \tag{5.2}$$

where x are the possible observed values of the parameter, σ is the standard deviation, and μ the mean of the measured distribution.

Errors are defined using the standard deviation of the measurement so that the confidence interval is 68.3%. That is, if the experiment was repeated many times, 68.3% of such experiments would yield a value of the mean within that range.

5.1.2 Definition of χ^2

The most common way to quantify how well an experiment is described by a model is through the function called χ^2. The smaller its value, the smaller the difference between the experimental data and the model prediction.

Given a set of experimental points $\{D_k\}$, each with an estimated error σ_k, and the set of points predicted by the hypothesis $\{H_k\}$, which will depend on the values used for the parameters of the model $\{p_i\}$, the χ^2 function of the model with a particular choice of parameters is defined as:

$$\chi^2 = \sum_{k=1}^{n} \frac{(H_k\{p_i\} - D_k)^2}{\sigma_k^2} \tag{5.3}$$

where k is a label to designate each point, n is the total number of points, and i is a label to distinguish each parameter of the model.

The procedure to fit the parameters of the mathematical model, so that they describe experimental data as accurately as possible, is normally to find the set of values that minimizes χ^2. This is geometrically equivalent to finding the global minimum of the χ^2 hypersurface as a function of the parameter set $\{p_i\}$.

The result of this procedure will be the estimated set of parameters and their errors $(p_i \pm \sigma_i)$, together with the χ^2 value, which accounts for the goodness of the model to describe the data with that set of parameters.

5.1.3 Levenberg-Marquardt algorithm

This χ^2 minimization procedure as a function of the model parameters is normally carried out using the iterative Levenberg-Marquardt

algorithm, which is a general numerical method to minimize functions [95].

In that iterative process, χ^2 is evaluated from an initial set of parameter values, as well as the direction into which χ^2 decreases, then an optimal magnitude for the parameter jump in that direction is estimated, and finally the χ^2 is evaluated again with the modified new set of parameters. If χ^2 has increased, it means the parameter jump was too large and the slope calculation was not a good approximation up to that distance, so the algorithm goes back that step, and the calculation is repeated with a smaller parameter jump. If χ^2 has decreased, the approximation is assumed to be good and the parameter jump is increased so that the minimum is reached faster.

During the iteration, to find out whether the parameters must be increased or decreased, the algorithm computes the χ^2 gradient and determines the directions with negative slope. However, that does not give information on the length of the jump.

The size of the jump is computed from the performance of the linear approximation of the function. The algorithm compares the estimated value of the approximated function with the actual value of the function at that point. If the linear approximation is good for a large area around that point, the step size can be large, but if it is only a good approximation very close to the point, only a very small step can be taken. This allows each jump to be scaled as a function of the curvature so that the convergence of the iteration process is fast even in the direction of small gradients.

The Levenberg-Marquardt algorithm uses a damping parameter that forces the parameter jump size to larger values when the iteration is far from the χ^2 minimum, and to smaller values as the χ^2 minimum is approached. This optimization of the parameter jump depending on the stage of the fit allows a faster convergence of the algorithm.

Since the Levenberg-Marquardt algorithm is an iterative process that requires the χ^2 value to decrease monotonously as the minimum is approached, it can only systematically reach local minima. Therefore, the solution to the minimization problem can only be reached when the initial parameters given to the algorithm are set close enough to the global minimum, thus, proper parameter initial-

ization is crucial to avoid the algorithm getting stuck at local minima.

As mentioned previously, the result of this minimization procedure yields the set of parameter values $\{p_i\}$, their errors σ_i, and the quantization of that difference through the χ^2 value, where the parameter values $\{p_i\}$ are those that minimize the differences between the model and the experimental data.

5.1.4 Error calculation and parameter correlation

The errors of the parameters resulting from the fit are obtained from the diagonal elements of the covariance matrix, calculated at the minimum χ^2. That is, the error on the i-th parameter is $\sigma_i^2 = (\alpha^{-1})_{ii}$, where α is the curvature matrix:

$$\alpha_{k,l} = \frac{1}{2}\frac{\partial^2 \chi^2(\mathbf{a})}{\partial a_k \partial a_l} \tag{5.4}$$

Estimation of the error in the parameters is very sensitive to how close the solution is from the true minimum.

The correlation between different parameters can be taken into account when errors are calculated within the frequentist scheme through the diagonalisation of the covariant matrix. However, the parameters will be assumed to have a parabolic dependence with χ^2.

This calculation is rarely carried out, which subsequently results in the errors being underestimated.

5.1.5 Frequentist approach advantages and disadvantages

The frequentist method described above is extremely popular in all fields of science and is implemented in most of the statistical packages due to its low computing requirements, but it has many limitations, specially when dealing with complex problems. Some advantages of the frequentist approach are:

- It is a quite robust and reliable method for simple models.

- Due to the damping factor that optimizes the size of the parameter jump at the different stages of the fit, the Levenberg-Marquardt algorithm has a very fast convergence to the minimum.
- It requires a relatively low amount of computing time.

Nevertheless, it also has many drawbacks limiting the complexity of the problems that can be tackled, and also regarding the fit procedure:

- It assumes that the experimental data errors have a normal distribution and are well known.
- The iterative process of the Levenberg-Marquardt algorithm only accepts new sets of parameters when they reduce χ^2, which geometrically means that the algorithm can only travel downhill through the χ^2 hypersurface. A very important consequence is derived from this limitation: this procedure will only be able to find the local minimum where the starting set of values are located.

  For this reason, it will only yield the right solution with simple models, if the χ^2 hypersurface has only one minimum, or if the initial parameters are already within the scope of the global minimum. Otherwise, it will get stuck in local minima, unable to overcome even small barriers and failing to explore other regions which may contain the global minimum, or it will get lost in flat areas of the χ^2 landscape [96].
- To avoid that the Levenberg-Marquardt algorithm gets stuck in local minima and ensure that is able to find the solution of the minimization problem, a careful initialization of the parameters must be performed to make sure they are located already near the global minimum. This initialization can get very tricky, specially in complex problems, and may include physical constrains as well as other non trivial assumptions, which often can not be applied systematically and have to be tackled in a case by case basis or through trial and error.

- By construction, this procedure assumes that the problem has one unique solution, and is unable to cope with problems that have several solutions, multimodal distributions, or where multiple parameter combinations yield equally valid results all compatible with data errors.

- The parameters are assumed to have a quadratic functional dependence on χ^2, and only symmetric errors are considered.

- Although parameter correlations can be evaluated in the frequentist scheme through the covariance matrix, this is too often overlooked when the errors of the fit are computed, which results in the errors being underestimated.

5.1.6 Example: Long range order in orientational glasses

Orientational glasses have the centre of mass of their molecules in a regular lattice but their orientation lacks long range order. These glasses and their plastic crystals show highly ordered translational symmetries such as body- or face-centred cubic lattices (Fig. 5.1).

Since short and long range interactions are usually coupled, a detailed study of their long range translational order has to reflect significant changes in their orientational as well as intramolecular structures (see Fig. 5.2).

A simple way to analyse this long range order is through the determination of the position of their first (or any other) diffraction peak as a function of the temperature. A standard Levenberg-Marquardt frequentist approach has been used to fit a pseudo-Voigt function to the first diffraction peak of each measurement. This function is a sum of a Lorentzian ($\mathscr{L}$) and a Gaussian ($\mathcal{G}$) peaks with η being the Lorentz fraction:

$$I(x) = \eta\,\mathscr{L}(x) + (1-\eta)\,\mathcal{G}(x) \tag{5.5}$$

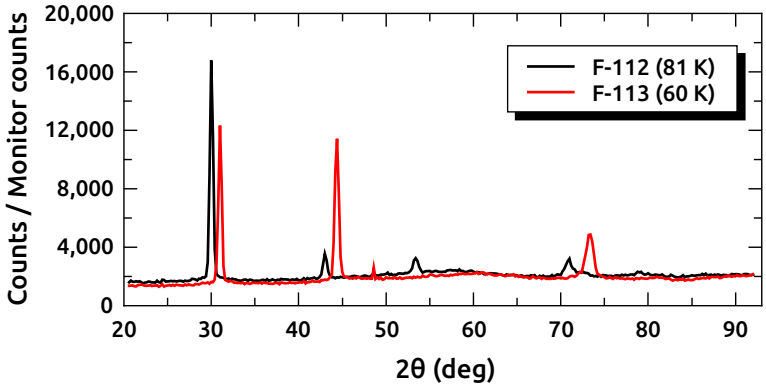

Figure 5.1: Diffractograms of 1,1,2,2-tetrachloro-1,2-difluoroethane (F-112) and 1,1,2-trichloro-1,2,2-trifluoroethane (F-113) orientational glasses. Long range translational order can be observed in the Bragg peaks and short range orientational order in the background undulations.

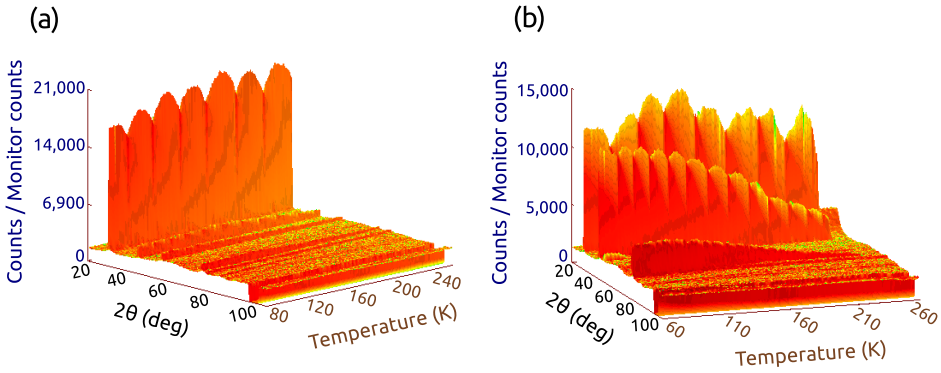

Figure 5.2: (a) Diffractograms of 1,1,2,2-tetrachloro-1,2-difluoroethane (F-112), and (b) 1,1,2-trichloro-1,2,2-trifluoroethane (F-113), warming up after quenching at 80 K and 60 K, respectively. Exotic oscillations in the intensity of the first and second diffraction peaks, due to coupling of the different interactions at play, stress the profound complexity of these compounds.

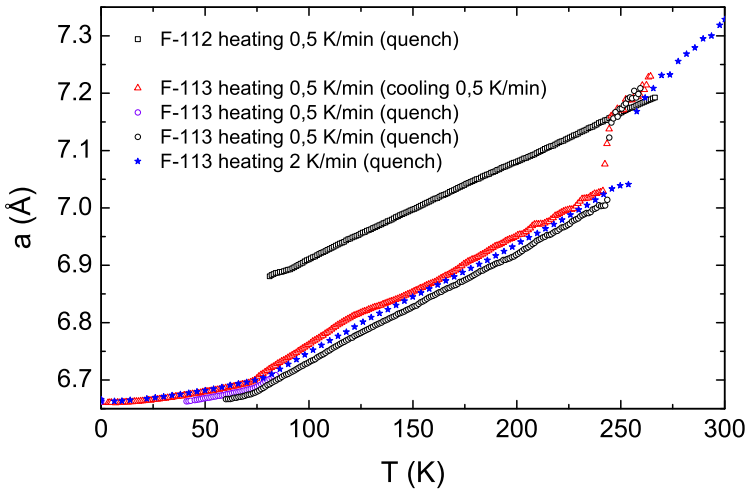

Figure 5.3: Lattice parameter a of 1,1,2,2-tetrachloro-1,2-difluoroethane (F-112) and 1,1,2-trichloro-1,2,2-trifluoroethane (F-113) obtained from the fits to the first diffraction peak at each temperature. Measured on heating, but different curves were obtained for F-113 depending on the thermal history of the sample.

However, the fitted function has a single set of parameters:

$$I(x) = I_0 + A \left\{ \eta \frac{2}{\pi} \frac{w}{4(x - x_0)^2 + w^2} \right. \tag{5.6}$$

$$\left. + (1 - \eta) \frac{\sqrt{4 \ln 2}}{\sqrt{\pi} w} \exp \left[- \frac{4 \ln 2}{w^2} (x - x_0)^2 \right] \right\} \tag{5.7}$$

where x_0 is the peak position, w is the full width at half maximum, A is the amplitude, and I_0 is the background intensity.

The frequentist approach is quite appropriate for this problem because the model is rather simple, with only four parameters, and the peak position is very well defined in the plastic crystal and the orientational glass, thus being a fast and reliable method.

If the structure of the lattice is known, a simple transformation using Bragg's law and taking into account the crystallographic planes

allows to obtain the lattice parameter a from the peak position x_0. In the case of the body centred cubic:

$$a = \sqrt{2}\, d = \sqrt{2} \left(\frac{\lambda}{2 \sin \theta} \right) = \frac{\lambda}{\sqrt{2} \sin \theta} \tag{5.8}$$

where d is the distance between the crystallographic planes of the closest centres of mass, λ is the neutron wavelength, and θ is the Bragg peak position obtained from the fit.

The dependence of the lattice parameter a on the temperature of 1,1,2,2-tetrachloro-1,2-difluoroethane (F-112) and 1,1,2-trichloro-1,2,2-trifluoroethane (F-113) was calculated this way and presented in Figure 5.3. The results show that different results were obtained for samples with different thermal histories, thus proving that for some compounds it is very important to determine their thermal history in order to analyse the results meaningfully. However, this representation does not allow to clearly distinguish the changes in the slope.

To emphasize the different temperature regimes in the thermal expansion of F-112 and F-113 samples, two curves in Figure 5.3 have been normalised to a straight line (see Figures 5.4 and 5.5). This representation reveals slope variations which were not apparent before the normalisation.

For instance, in Figure 5.4, F-112 orientational and conformational glass transitions can be observed around 90 K and 120 K, respectively, and in Figure 5.4, those of F-113 can be observed around 70 K and 120 K. Several other effects of unknown nature, which were also observed in some neutron backscattering measurements, can be observed as well at higher temperatures, reflecting the particularly complex nature of these systems.

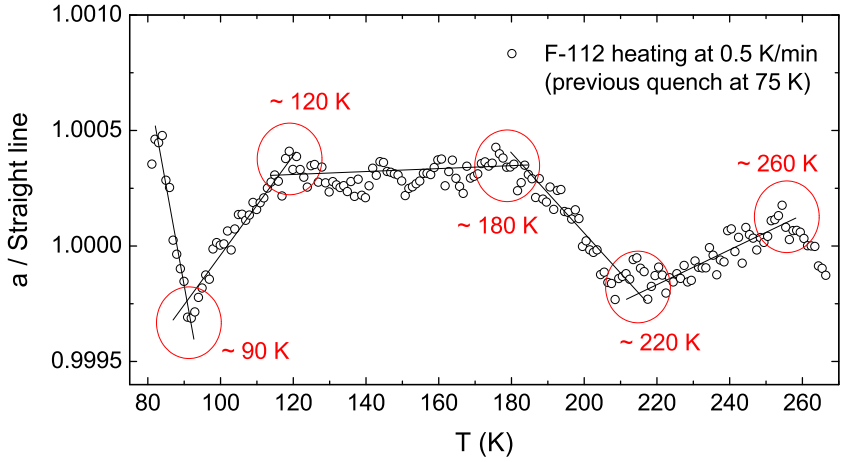

Figure 5.4: Lattice parameter a of 1,1,2,2-tetrachloro-1,2-difluoroethane (F-112) obtained from the fits to the first diffraction peak at each temperature and then normalised to a straight line to emphasize the different regimes.

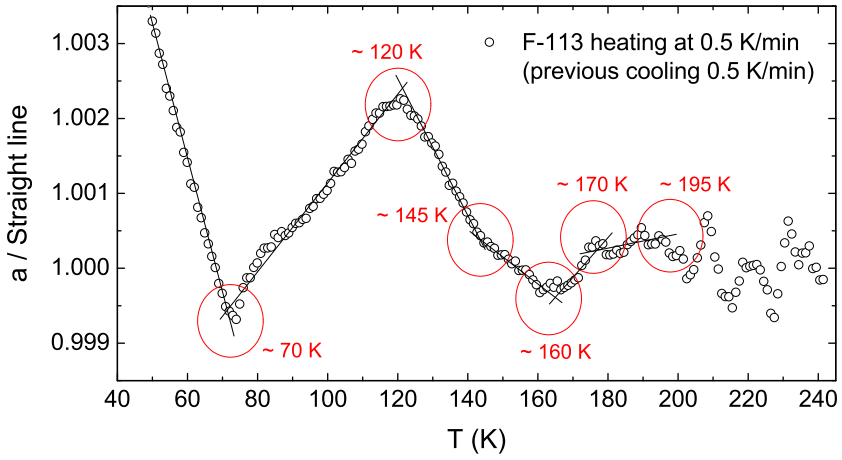

Figure 5.5: Lattice parameter a of 1,1,2-trichloro-1,2,2-trifluoroethane (F-113) obtained from the fits to the first diffraction peak at each temperature and then normalised to a straight line to emphasize the different regimes.

5.2 Bayesian approach to fit experimental data

5.2.1 Introduction

The Bayesian definition of probability represents a state of knowledge, and it can be assigned theoretically or be the degree to which a statement is supported by the evidence. So it is possible to assign a probability to any statement, even if there is no random process taking place whatsoever.

All physical constrains and assumptions that are used in a frequentist approach in a somewhat concealed and unclear manner are made explicit in the Bayesian scheme, where a probability distribution is assigned to them (prior) and they are merged with the information obtained from the experimental data, thus contributing to the final result (posterior).

In the frequentist approach, a given fraction of the experiments would yield a calculated confidence interval that would include the true value of the measured magnitude. This true value, although it is unknown, it is not considered to be random, so the probability that it lies within the interval it can only be 1 or 0 (either it is there or it is not).

In the Bayesian approach the magnitude being measured is assumed to have itself a probability distribution (prior) which can be known and very well defined, pure speculation, or just very uninformative (maximum ignorance prior). This starting information contained in the prior is then modified by the available data to yield the posterior, a new probability distribution for the magnitude. Of course, the prior used in the fit can be complete nonsense, but this information is explicitly stated up-front so that all assumptions are readily available for examination and criticism.

Although the results obtained from a Bayesian fit are the probability distribution functions of the parameters, they can be summarized using a credible interval, which just indicates the probability that the parameter takes a value within that range.

5.2.2 Bayes theorem

Bayesian methods [97] try to find the probability $P(H \mid D)$ that a hypothesis H is true given certain experimental evidence D. This probability is also called posterior and can be computed using the Bayes theorem [98]:

$$P(H \mid D) = \frac{P(D \mid H)\ P(H)}{P(D)} \tag{5.9}$$

where $P(H)$ is the prior that contains the previous knowledge about the hypothesis, $P(D)$ is a normalization factor so that the posterior probability adds up to unity, and $P(D \mid H)$ represents the likelihood or probability of obtaining this particular set of data points given the hypothesis was true.

Regarding the previous knowledge about the hypothesis, it can always be assumed that there is no available information at all and that all values are equally probable, therefore using a uniform distribution for the probability $P(H)$. This is called the maximum ignorance prior [97] and in this case it can be seen from the Bayes theorem expression that $P(H \mid D) \propto P(D \mid H)$. So that the set of parameters that yields the largest likelihood will also be the one to yield the most probable hypothesis.

This maximum ignorance prior assumption will be adopted hereafter. Hence, the issue has now been reduced to finding for each kind of problem the expression to compute the likelihood, which depends on the distribution of the experimental data.

In the case of independent observations, the likelihood $\mathcal{L}$ can be calculated from the joint density function of all observations:

$$\mathcal{L} = P(D \mid H) = \prod_{k=1}^{n} P(D_k \mid H) \tag{5.10}$$

where k is a label for each point, n is the total number of points, and $P(D_k \mid H)$ is the probability that the data point D_k is observed given a certain model H. This means that, if the measurement at each point is independent from the measurement at other points,

the probability of obtaining that particular combination of values is simply the product of the individual probabilities of obtaining a particular value at each point.

5.2.3 Likelihood in a counting experiment

In the case of neutron diffraction, we are dealing with a counting experiment so the probability to observe a particular number of neutrons at a certain point, given our hypothesis is true, will follow a Poisson distribution:

$$P\left(D_k, H\right) = \frac{{H_k}^{D_k}\ e^{-H_k}}{D_k!} \tag{5.11}$$

where H_k is the expected value for that point predicted by the model, and D_k is the observed value. And thus its likelihood will be:

$$\mathcal{L} = \prod_{k=1}^{n} \frac{{H_k}^{D_k}\ e^{-H_k}}{D_k!} \tag{5.12}$$

where k is a label for each point, and n is the total number of points.

When then number of counts in a counting experiment becomes very large, the Poissson distribution can be well approximated with a normal distribution [97]. Therefore, the probability of measuring a number of counts D_k given that our hypothesis H is true, can also be expressed as:

$$P(D_k \mid H) = \frac{1}{\sqrt{2\pi\sigma_k^2}}\ \exp\left[-\frac{1}{2}\left(\frac{D_k - H_k}{\sigma_k}\right)^2\right] \tag{5.13}$$

where H_k is the expected value for that point predicted by the model, D_k is the observed value, and σ_k is the standard deviation predicted by the model, assuming a particular distribution of experimental points around H_k.

The likelihood in this case (when the number of counts is very large and the normal distribution is a good approximation) can be

written as:

$$\mathcal{L} = \prod_{k=1}^{n} \left\{ \frac{1}{\sqrt{2\pi\sigma_k}} \exp\left[-\frac{1}{2} \left(\frac{D_k - H_k}{\sigma_k} \right)^2 \right] \right\} \tag{5.14}$$

$$= \left[\prod_{k=1}^{n} \left(\frac{1}{\sqrt{2\pi\sigma_k}} \right) \right] \underbrace{\exp\left[-\frac{1}{2} \sum_{k=1}^{n} \left(\frac{D_k - H_k}{\sigma_k} \right)^2 \right]}_{\exp\left(-\frac{1}{2}\chi^2 \right)} \tag{5.15}$$

As can be seen, the χ^2 function that was defined (but not justified) in section 5.1.2, and is normally used in the frequentist scheme, is closely related to this likelihood, which is derived only from probabilistic grounds and used in the Bayesian approach.

Finding the parameters of the model that maximize the likelihood is equivalent to finding the parameters that minimize χ^2. Thus, the χ^2 function gives a measure of the probability that the data is described by our model when experimental points are normally distributed. If the data follows a Poisson distribution, other alternate definitions can be constructed for χ^2 [99].

Although this method is quite general, only the particular case of the normal distribution of measured data at each point will be considered hereafter.

5.2.4 Metropolis algorithm variation

A general Bayesian approach has been implemented in the program FABADA to perform fits of models to experimental data, so they describe the data as accurately as possible while taking their errors into account [100].

This modification of the Metropolis algorithm generates at every iteration a new parameter set from the previous one and compares their χ^2. If the new set reduces the χ^2 value, is always accepted, if it does not, it is accepted only with a certain probability closely related to the data distribution around the values predicted by the model (usually interpreted as the experimental errors) [101].

To provide with an effective exploration of the parameter space, clever modification of the parameter jump sizes is carried out for each parameter, and also through an adjustable factor that artificially increases the effective errors of the data, thus allowing the algorithm to explore farther regions in the first stages of the fit and guarantee that the global minimum is found.

The parameter space is explored to account for all the parameter combinations that yield models predicting H_k values within the experimental error of D_k. Finally, the list of accepted parameter combinations is used to construct a histogram for each parameter and also χ^2, these histograms are proportional to the probability density function of these quantities and contain all the complexity of the problem.

Although the resulting probability distribution functions can take an arbitrary shape, errors can be summarized for comparison with frequentist results using the credible interval, which includes 68% of the parameter probability around the most probable value.

5.2.4.1 Markov chain Monte Carlo

Markov chains are a succession of different states in a system, where every new state only depends on the last state, but not on the history of states. In this problem, each set of parameters $\{p_i\}$ will be a state of the chain, generated through a Metropolis algorithm [101].

The algorithm has two phases: at first it explores large regions of the parameter space to locate the section where the parameters yield predictions that fall within data errors and, once such section has been found, it explores that vicinity in detail to sample and construct the probability distribution functions of the parameters and χ^2.

Regardless of the starting values, the parameter Markov chain will eventually reach the equilibrium distribution. That is, in this case, the distribution of the parameter sets that yield model predictions compatible with the data errors. However, the number of steps that the chain will require to reach the stationary distribution is difficult to determine.

Markov chain Monte Carlo methods are algorithms that are used

to obtain random events with a certain probability distribution. Here, the unknown probability distribution of the acceptable sets of parameters will be sampled a large number of times so that we can estimate its distribution from the frequency that each set gets accepted.

5.2.4.2 Parameter sampling

Gibbs sampling in a multivariate distribution entails changing the variables one at a time. This way each parameter is changed separately from the others, and the rest of the parameters which are not being sampled take the values of the last accepted parameter set, instead of simultaneously changing all of them.

The parameter that will be changed is chosen randomly and its new value is also generated randomly using this formula:

$$p_i^{\text{new}} = p_i^{\text{old}} + R \cdot \Delta p_i^{\max} \tag{5.16}$$

where R is a random number between -1 and 1, and $\Delta p_i^{\max}$ is the maximum change allowed for the parameter i, hereafter simply called parameter jump.

New parameter sets will be always accepted if they reduce the computed χ^2 value, but they will also be accepted with a certain probability if they increase it. The main consequence of this feature is that the algorithm is able to travel uphill across the χ^2 hypersurface to overcome small barriers.

The probability that a new set of parameters is accepted given a particular old set or parameters is the ratio of their likelihoods:

$$P_a = \frac{\mathcal{L}^{\text{new}}}{\mathcal{L}^{\text{old}}} = \frac{P(H\{p_i^{\text{new}}\} \mid D_k)}{P(H\{p_i^{\text{old}}\} \mid D_k)} = \frac{\exp\left(-\frac{1}{2}\chi^2_{\text{new}}\right)}{\exp\left(-\frac{1}{2}\chi^2_{\text{old}}\right)} \tag{5.17}$$

$$= \exp\left[-\frac{1}{2}\left(\chi^2_{\text{new}} - \chi^2_{\text{old}}\right)\right]. \tag{5.18}$$

where this expression is only used when $\chi^2_{\text{new}} > \chi^2_{\text{old}}$, as has already been mentioned.

Clearly, if the new set of parameters increases χ^2 by a small amount it is more likely to be accepted than if it is by a large quantity. Likewise, if data errors are large, χ^2 are smaller, and any new

sets of parameters that increase χ^2 are more likely to be accepted anyway.

Experimental errors play a very important role during the fit process in this approach, therefore, their proper determination is one of the keys for the success of the procedure.

5.2.4.3 Boundary prior effects

The algorithm described here uses the maximum ignorance prior in the sense that all sets of parameter values have *a priori* the same probability of being considered and their probability of being accepted and taken into account will depend solely on the resulting χ^2 value of the parameter set given by the experimental errors.

However, for practical reasons, a lower and upper boundary are defined for each parameter. This reflects our previous knowledge about the parameter values and is in fact equivalent to considering a prior where any parameter value within the range is equally probable, but the probability of being outside this range is zero. We are trying to answer the question "If we assume that the parameter values are within that range, what would be the probability distribution of the parameters within these limits according to the experimental data?".

If the boundaries are far from the probable parameter values, the χ^2 of any set of parameters located close to them will be very large and these regions will never be explored. It means that, in these cases, just through the use of the experimental data all those values would already have been dismissed, so the use of a prior is superfluous and is equivalent to not using a prior at all in the first place.

Thus, boundaries are usually defined in a non restrictive way so that they will be very far from the likely values of the distribution, and they could be used simply to ensure that the obtained results for the parameters will have physical meaning. For instance, the lower boundary of a parameter representing a distance could be set to zero to guarantee the parameter would take only positive values, even when the mathematical expression of the model does not allow to determine the sign of this parameter.

However, sometimes we may erroneously define boundary limits

that are more restrictive than what experimental data really allows. Either because we made erroneous assumptions about the possible parameter values, which are not true in our case, or because our assumptions are right but data quality is not very good and the experimental error does not allow to get such precise information about that parameter.

To avoid this and make sure the boundaries are in a region of the probability distribution where the probability of the parameter having that value is zero, parameter boundaries can be chosen farther away when it is detected that the resulting probability distribution has still high values at the boundaries that were initially set.

Occasionally, a certain parameter of the model may be ill defined or represent an information which can not be determined from the data. This can be due to wrongly choosing parameters that do not affect the experiment outcome (and thus can not be measured through that kind of experiment) or simply because data quality is too bad to extract the details of all magnitudes that affect the measurements.

In these situations, further increasing the boundaries does not help because the parameter distribution may not decrease to zero at the edges. For instance, if the parameter cannot be determined at all, it will yield equal probability for any value regardless of the boundaries (maximum ignorance posterior), or if only a maximum or minimum value of the parameter can be determined, the distribution will decrease to zero on just one of its sides.

This can be a very powerful tool because some other methods would not allow to extract any kind of information about a parameter that is ill defined or perhaps they would yield a misleading result. Here all the complexity of the problem is reflected through the probability distribution of the parameter.

Setting a boundary prior improves the efficiency of the algorithm avoiding it to lose computing time exploring parameter values which are believed to be impossible, and prevents ill defined model parameters (maybe just due to the bad quality of the data) to impede obtaining a global solution that defines the probability distributions of the rest of parameters.

When the boundaries lie within regions of the parameter values

that have a non negligible probability, those regions will be more often visited and it will happen more frequently that random parameter jumps end up being outbounds. Depending on how these proposed random parameter sets that lie outbounds are handled, it may lead to poor sampling of the regions near the boundaries.

For instance, if outbound parameter sets are treated as non accepted values, and the algorithm returns to the previous accepted value to try to generate another parameter set that lies within the boundaries, it will be more difficult for the algorithm to get to the edges, and regions near the boundary will not be properly explored (they will be less likely to be explored the closer they are to the boundary). Thus, this way of handling outbound parameter sets, generates an artefact that interferes with the natural space exploration process of the algorithm and artificially decreases the probability distribution of parameters near the edges, which is no longer guided based only on experimental data distribution and its errors (see Figure 5.6(a)).

To avoid this artefact, when an outbound parameter is proposed, the algorithm does not simply return to the previous accepted value, but it transforms the proposed outbound parameter value using a mirror effect and bounces it back inside the interval:

$$p_{\text{in}}^{\text{new}} = 2B - p_{\text{out}}^{\text{new}} = B - \Delta p_{\text{out}}^{\text{new}} \tag{5.19}$$

where B is the boundary value, $p_{\text{out}}^{\text{new}}$ is the parameter value obtained randomly that falls outside one of the boundaries, $\Delta p_{\text{out}}^{\text{new}}$ is the excess value of the random parameter that falls outside of the boundary, and $p_{\text{in}}^{\text{new}}$ is the corresponding value inside the allowed parameter range.

The advantage of the mirror effect obtained through Equation 5.19 is that if the proposed jump is outbound but very close to the boundary, the corresponding value inside the interval will be also very close to the boundary. And likewise, if the proposed outbound values are far, their corresponding values inside will be far from the boundary as well. This way the the random sampling of near/far values is not artificially forced to favour values far from the boundary as it would if outbound parameter sets were simply not accepted.

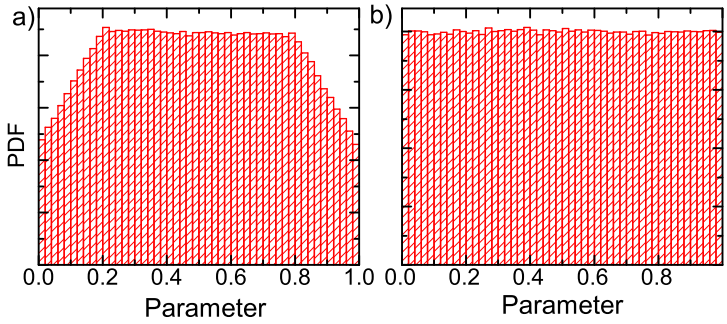

Figure 5.6: Resulting probability distribution function of a parameter that can take any value, that is, the proposed parameter values are always accepted as long as they lie within the boundaries. The two cases correspond to (a) outbound proposed parameter values are simply not accepted, and (b) outbound proposed parameter values are reinserted into the interval using Equation 5.19.

To illustrate the difference between both behaviours, an example is shown in Figure 5.6(a) where all proposed parameter values inside the interval are accepted and values outside the interval are not. Since the distribution should be flat, it is clearly concluded that this method would yield wrong results near the boundaries. Another example in shown in Figure 5.6(b) where all values inside the interval are accepted and values outside are bounced back in through Equation 5.19 and then accepted. As can be seen in the figure, this procedure succeeds in getting rid of the artefact at the boundaries.

The algorithm does not allow parameter jumps larger than the parameter interval to prevent successive proposed parameter values to jump outbounds from one side to the other.

This procedure is inspired by the periodic boundary conditions used in molecular dynamics, where molecules that travel outside of the box on one side are reinserted on the other side of the box (contrary to our case where parameters are reinserted again from the same

boundary).

5.2.4.4 Parameter jumps

5.2.4.4.1 Algorithm efficiency We saw in section 5.1.3 that, in the Levenberg-Marquardt algorithm, parameter initialization is crucial to guarantee a successful convergence to the global χ^2 minimum. In the case of the Metropolis algorithm, the critical issue is choosing the most appropriate size for the parameter jumps (that is, for the maximum size of the random parameter jumps $\Delta p_i^{\max}$).

If parameter jumps are small, the algorithm will sample with great detail a small region of the probability distribution and, if they are large, it will sample very distant regions but without any details. Ideally, the goal would be that the algorithm samples the whole parameter space, and not just a region, to make sure that the local minimum is reached, and at the same time explores the global minimum in detail, that is, where the stationary distribution of the Markov chain is found.

Regarding efficiency considerations, it has to be taken into account that this algorithm is able to travel uphill across the χ^2 hypersurface but, as the χ^2 difference between the two parameter sets increases, the probability of doing so decreases exponentially. It is easy for the algorithm to go uphill between close regions that will have similar χ^2, but it is not so easy to do so between distant regions of the parameter space that may have very different χ^2.

Therefore, exploring the whole parameter space with too large jumps may be very inefficient because most of the jumps would be rejected, but exploring it with too small jumps would be inefficient too because it would cause the algorithm to get stuck in local minima for a large number of steps before it travelled to other regions.

Additionally, the model is not equally sensitive to the modification of all parameters and the χ^2 landscape does not have the same topography in all directions. A certain change may cause a large χ^2 variation in some parameters and go unnoticed in others, so that what is considered an adequate jump size to explore each region may be completely different for each parameter (i. e., direction in the χ^2

hyperspace).

To overcome the aforementioned obstacles and achieve maximum efficiency in the exploration of the parameter space, the maximum parameter jump for each parameter is changed to adapt it to the shape of the χ^2 hypersurface in that direction and it can also be changed to adapt it to the phase of the fit process.

5.2.4.4.2 Adaptative parameter jumps To tailor the maximum parameter jump size to the χ^2 shape, the method of an Adaptive Markov Chain Monte Carlo Through Regeneration has been implemented in the algorithm. This changes the way the parameter sets are generated taking into account the history of the already accepted parameter sets [102].

A good gauge to measure whether the maximum size of the parameter jumps is appropriate or not is using the acceptance ratio, which is the fraction of proposed parameter jumps that have been accepted. If the acceptance ratio is large this is an indication that the algorithm is behaving conservatively and that the parameter jumps are too small, if the acceptance ratio is small it means that the algorithm is behaving too venturesome and the parameter jumps are too large.

Therefore, a desired acceptance ratio of the proposed parameter sets is predetermined initially, and the algorithm tries to adjust through the iterative process the maximum jumps to fulfil this ratio. Since we want to explore the parameter space with the same efficiency in all directions and only one parameter is changed at a time in every iteration, the desired total acceptance ratio R^{des} will be equally distributed among the different parameters, and the desired acceptance ratio for each parameter R_i^{des} will be used instead:

$$R_i^{\text{des}} = \frac{R^{\text{des}}}{m} \tag{5.20}$$

where m is the number of parameters.

Before the algorithm starts the iteration process, a first guess has to be made for the maximum parameter jumps $\Delta p_i^{\max}$. However, the

particular value chosen for this purpose is not relevant because the algorithm converges very fast to the appropriate values.

After a certain number of iterations N has been carried out with this set of maximum parameter jumps, the real acceptance ratio of each parameter R_i^{real} is evaluated and compared to its desired ratio R_i^{des}, and the maximum parameter jump of each parameter is changed accordingly:

$$\Delta P_i^{\text{max,new}} = \Delta P_i^{\text{max,old}} \left(\frac{R_i^{\text{real}}}{R_i^{\text{des}}} \right) = \Delta P_i^{\text{max,old}} \left(\frac{K_i/N}{R_i^{\text{des}}} \right) \tag{5.21}$$

where K_i is the number of accepted jumps of the parameter i.

Note that if the changes in a parameter are already being accepted with the desired ratio, that is, if $R_i^{\text{real}}/R_i^{\text{des}} = 1$, the maximum parameter jump will not be modified.

This equation increases the maximum jump of the parameters accepted too often and decreases the maximum jump of parameters which are rarely accepted, setting different jump sizes for every parameter and adapting to arbitrarily complicated shapes of the χ^2 landscape, which results in an efficient exploration of the parameter space in all directions.

5.2.4.4.3 Simulated annealing As has been mentioned in section 5.2.4.1, the fit process has several phases: in the beginning large portions of the parameter space must be explored to locate the global minimum, but then only the region corresponding to that minimum (the stable configuration of the Markov chain) must be explored in detail.

Therefore, to optimise the efficiency of the algorithm, the maximum parameter jumps must be initially set to large values and then progressively diminished to smaller values towards the end. This effectively smears out details of the χ^2 landscape in the beginning so that local minima are disregarded and, when the global minimum is found, the algorithm focuses in that region to get a detailed χ^2 probability distribution that is compatible with experimental errors of the parameter values at the relevant points.

To carry out such optimization of the parameter jumps, a parameter T is introduced in the calculation of an artificially constructed χ^2 value:

$$\chi^2_T = \sum_{k=1}^{n} \frac{(H_k - D_k)^2}{T\sigma^2}. \tag{5.22}$$

where χ^2_T is the altered χ^2 value modified artificially by the factor T.

Setting this parameter to higher values ($T > 1$) is equivalent to artificially increasing the nominal error of the experimental data, so that the overall acceptance of parameter sets will increase as well:

$$P_a = \exp\left[-\frac{1}{2T}\left(\chi^2_{\text{new}} - \chi^2_{\text{old}}\right)\right]. \tag{5.23}$$

This favours uphill displacements of the algorithm beyond the probability already allowed by the error, avoiding the need to realise a large number of iterations in local minima and even overcoming large barriers, so that the global minimum can be easily found. Reducing its value again to $T = 1$ will return the ability of the algorithm to go uphill with the probability given solely by the real error, so that, in the last phase of the process, the actual probability distribution of the parameters in the global minimum can be sampled.

This technique is called simulated annealing and it is analogous to what is used in statistical physics when molecular configurations at a certain temperature are determined through Monte Carlo methods [103]. Since in that context this parameter T represents the temperature, it will be called likewise here, although it has a completely different meaning in this case.

5.2.5 Bayesian approach advantages and disadvantages

The Bayesian approach is routinely used in many fields of science and, although it is not as common in condensed matter physics, it has been used successfully to analyze experimental data from several kind of measurements, specially those requiring more complex models and a more sophisticated approach for the data analysis [92, 104–107].

It is a general method, but is specially useful when the χ^2 landscape is particularly rough and the fit gets stuck in local minima every now and then, the parameters are strongly correlated, or when multiple solutions are possible. These are its main advantages in the form that has been described here:

- Since parameter changes that increase χ^2, i. e., uphill movements, are allowed with a probability related to the experimental data error, it does not get stuck in local minima of the χ^2 landscape during the fit process when barriers are smaller than the associated experimental error, i. e., when the actual parameter set is not globally the best fit but any parameter change increases χ^2.

- The results of the fit are not single parameter values and their errors, but the probability distribution functions of the parameter values which are compatible with the experimental errors. Therefore, all the complexity of the problem is reflected in the solution.

- Even in cases where parameters of the model are ill defined, any meaningful information contained in the data can still be extracted, for instance, when only a maximum or minimum value can be determined for that parameter.

- Due to the fact that the whole region of the parameter space around the minimum will be sampled, no assumptions regarding the parameter correlations have to be made. They are directly taken into account through the process and are reflected in the resulting probability distribution functions of the parameters.

- No assumptions have to be made regarding the geometry of the χ^2 landscape, because this will be explicitly explored using the data and its errors. Thus, its dependence with the parameters in the minimum does not need to be well described by a quadratic approximation like in the frequentist approach.

- Since the result of the fit are the parameter probability distribution functions and a normal distribution is not assumed, errors do not have to be symmetric and can be arbitrarily complex.

- Since there is no need to assume that the χ^2 landscape has only one minimum able to describe the data and its error, sensible results can be found as well in the case of multimodal problems, where there may be several disparate parameter sets with a high probability. This will be simply reflected in the probability distribution function of the parameters that will display more than one peak.

- In cases where the normal distribution is not a good approximation of the measured points (for instance, for experiments with very little counts that follow a Poisson distribution), the whole procedure can be carried out as well simply redefining the χ^2 used for minimization by a function suited to the problem.

- Jump sizes are tailored for each parameter so that the parameter space is explored with the same degree of efficiency in all directions. The Levenberg-Marquardt algorithm uses a different jump for each parameter as well.

- Using the temperature parameter, uphill movements can be artificially enhanced in the first phase of the fit, beyond what the experimental errors allow, to increase the efficiency of the algorithm.

- Initialization of parameters and maximum parameter jumps are not relevant to obtain a good result efficiently, even if very small acceptance ratios are used.

- The result of the fit also includes the probability distribution function of the likelihood, directly related to the χ^2, this means that a more advanced quantitative model selection can be carried out taking into account all parameter combinations compatible with the experiment.

- Assumptions about acceptable parameter values can be included upfront in the analysis through the prior boundaries.

It also has some **disadvantages** such as:

- It requires longer computing times than the frequentist approach.
- Although errors must be well known quantities in both methods because they determine the shape of the χ^2 hypersurface, in the Bayesian approach they also greatly influence the way the whole fit is carried out.

5.2.6 Example: Determination of molecular structure

Fits with a Bayesian approach have been extensively used in this work to determine the intramolecular structure of the compounds.

Realistic geometrical models of the molecules, with a large number of parameters, which are not all completely independent from one another, required an advanced method which was robust and that could cope with complex χ^2 topographies.

Probability distribution functions of the geometrical parameters were obtained from the neutron diffraction measurements, and this information was often used to shape the individual molecules before carrying out the molecular dynamics simulations or the reverse Monte Carlo molecular modelling.

Multiple examples of these fits can be found in Chapter 6, where the results of this work are explained in more detail.

The Bayesian approach to fits has been implemented in the program FABADA [100].

5.3 Model selection

Many interpretations of the outcome of the experiments are always possible for any problem. Thus, to be able to choose between different

models, we need to use a way to quantify how appropriate a model is. This quantification can be easily carried out on both frequentist and Bayesian approaches, but surprisingly this analysis is seldom performed.

As has already been discussed, χ^2 allows to compute how well the hypothesis describes the data. However, this is just half of the issue, because more complicated models can always be constructed so that their predictions are closer to the data than the existing ones, but without adding any explanatory insight. This means that, usually, it is easier for models with more parameters to closely resemble the experiment. This forces us to quantify Occam's razor too so that an equilibrium is found and the chosen models are those that yield a good prediction of the experiment but also remain as simple as possible.

Both considerations can be taken into account concurrently through the use of the reduced χ^2, which can be expressed as follows:

$$\chi^2_\nu = \frac{\chi^2}{n-m} \tag{5.24}$$

where χ^2_ν is the reduced χ^2, n is the number of experimental points, and m is the number of parameters, so $n-m$ is the number of degrees of freedom.

This means that models that yield the same χ^2 will be penalised for each extra parameter they introduce to the explanation. Therefore, this function allows to compare on equal footing mathematical models with different numbers of parameters, so that models with a high number of parameters, which normally yield smaller χ^2, are only favoured when they really introduce a significant improvement on the description of data.

The reduced χ^2 can be used in both, the frequentist and the Bayesian approach, with the difference that in the first case it will be expressed as a single number (only its smallest value) and in the second case as a probability distribution function (all values within the global minimum compatible with data error).

The frequentist approach to model selection has the same drawbacks as the frequentist fit, including that a number of assumptions

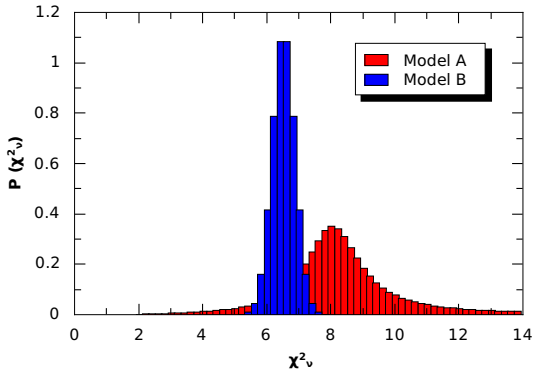

Figure 5.7: χ^2_ν probability distribution functions of two models A and B, where model A achieves the smallest χ^2_ν value, but where the probable values of model B are mostly smaller than probable values of model A, as well as being better defined. The frequentist approach would wrongly lead to choose model A as the preferred model.

are made regarding the topography of the χ^2_ν hypersurface: that it has a single minimum, that its shape is parabolic in all directions (i. e., it has a square dependence with all parameters), and that parameters are not correlated.

Besides, all the information contained in the χ^2_ν probability distribution function that was obtained in the Bayesian approach and would be useful for decision making is lost when only the smallest value of the distribution is considered, such as whether a model is better defined than another.

For instance, it is possible that a model A is chosen over a model B using frequentist approach based on the criterion that the first yields the smallest χ^2_ν value. But that, when full information is obtained in the Bayesian approach through the probability distribution, the model B is chosen instead due to the fact that its most probable values (the peak of the distribution) are smaller than those of model A (see an example in Figure 5.7).

Bayes model selection is useful in cases of models which are complex, ill defined and have more than one solution, or when some

parameters can only be determined to be smaller or larger than a certain value. An interesting example can be seen in Ref. [106].

5.4 Molecular modelling

Very often it is not straightforward to devise a model that describes the arrangement of the molecules in a material, and thus having a method to quantify the goodness of models is not enough.

However, several models describing the fundamental interactions that take place between atoms are available and they can be used to predict which will be the behaviour of an atom in the presence of another atom (or multiple other atoms, depending on its sophistication). And since most molecular systems are composed of a large number of atoms, iterative numerical methods can be used to find out their collective behaviour.

Alternatively, an approach can also be carried out where no assumption is made regarding the molecular interactions, and the atomic positions of an initial configuration are modified until they fit the experimental data.

In either method, other details, such as the intramolecular structure of the material or its density at a certain temperature, can also be used to constrain the system and help to find a better solution.

From these procedures, a possible configuration of all atomic positions of the molecules can be obtained.

Normally this is performed several times with different initial configurations so that a representative statistical sample is obtained and the particularities of each resulting configuration can be averaged out.

Once the positions of the atoms are available, a very deep analysis of the properties and arrangement of the molecules within the material can be performed. In the case of molecular dynamics, not only their short range order can be modelled from the configurations, but plenty of dynamic information can be extracted as well, because the velocities of the atoms are also taken into account.

5.4.1 Molecular modelling techniques

5.4.1.1 Molecular dynamics

Molecular dynamics is a simulation of the movements of the atoms or molecules in a material. An initial state is defined and then it is calculated how this is modified by the interaction models used in our case, so that the variation which the atomic or molecular velocities would experience under the influence of such interactions can be determined.

The interaction models or potentials may display any degree of precision. Less precise models will require less computing time, so that simulations with a lot of molecules and for longer times will be possible. More precise models require more computing time, so that only simulations with fewer molecules and simulating a shorter period of time will be possible. Depending on the kind of phenomenon that must be mimicked and explained, a less or a more accurate interaction model will be required.

Ideally, after a certain number of iterations, the molecular system will reach an equilibrium state, which frequently is the one of interest. However, the convergence of the system to the equilibrium state depends strongly on the initialization. If the initial state that has been defined for the atoms or molecules is very far from the equilibrium one, a long simulated time may be needed for its components to achieve it, and hence it may never be reached within the available computing time.

A simpler interaction model will be sometimes not capable of reproducing certain behaviours, but a more complex one may not be able to run with a number of atoms or molecules large enough so that the behaviour can be reproduced either. Physical phenomena which take place through long periods of time, such as glass transitions, are also very difficult to reproduce due to computational time limitations.

5.4.1.1.1 Standard potentials Most common interaction potentials or models are empirical and have many adjustable parameters, they include interactions between bonded atoms (stretch, bends and torsions), and non bonded atoms (van der Waals and electro-

static forces). But they assume classical behaviour of the mechanics of the molecules, and quantum-mechanical effects are only somewhat represented through the empirical functions. Thus, most structural and conformational changes can be reproduced, but rarely chemical reactions.

In this scheme two approximations are usually made:

- Electrons are so fast that they move together with the nucleus (Born-Oppenheimer approximation), and thus they can be treated separately as a single potential energy surface representing the ground state.
- The nuclei are treated as classical heavy point particles.

In this work, several molecular dynamics simulations were analysed to explain in detail molecular short range order particularities, conformational populations, and some dynamical properties of liquids.

5.4.1.1.2 Ab initio potentials Ab initio molecular dynamics is a specific case of molecular dynamics simulations where electronic behaviour is calculated from first principles using quantum mechanics (for instance, through the Density Functional Theory). No empirical fit is used to describe these interactions, although some theoretical considerations may allow to carry out a certain degree of approximation.

It can be used in situations where quantum interactions play an important role or the electronic cloud needs to be represented with a detail beyond what empirical methods allow.

However, these simulations require much larger computational efforts than classical molecular dynamics, so only a small number of atoms during brief periods of time can be simulated.

In this work, ab initio molecular dynamics simulations have been used to provide an estimation of molecular geometries. Due to computational time limitations, no interaction between molecules has been taken into account at all in these simulations, so they only reproduce the molecular shape of single molecules in the void or at the

limit of a highly diluted gas. In condensed matter, depending on the rigidity of the molecule, molecular geometry can be highly affected by the surrounding neighbours. Thus, extrapolation of such results to liquid or solid states must be always taken with a grain of salt.

5.4.1.2 Reverse Monte Carlo

Reverse Monte Carlo is a method based on experimental data for modelling the structure of disordered materials such as liquids, glasses, amorphous materials, or disordered crystals.

Starting from an initial configuration which should be a reasonably good guess, the experimental measurement that would correspond to this structure is calculated and compared with the actual experiment.

If the calculation does not match the experiment, the positions of the atoms in the configuration are randomly varied, within manually predefined ranges, and the measurement that the new configuration would yield is calculated again. If the new configuration resembles the actual measurement more closely, it then becomes the starting point of the next iteration. And if it is worse, the new configuration is only accepted with a probability proportional to $e^{-\left(\frac{1}{2}\right)\chi^2}$ to avoid that the algorithm gets stuck in local minima. If the configuration is disregarded, other variations in the atom positions of the old configuration are explored, iterating until the modelled structure is compatible with the data.

The process is repeated with several initial configurations so that the particular deviations of each configuration can be averaged out with the rest.

This is essentially a minimization procedure such as the one described in Section 5.2. Thus, the same strategies can be used to avoid getting stuck in local minima, and certain additional physical constraints regarding the molecular geometry or macroscopic magnitudes of the system can be implemented as well.

The main advantage of this method is that it allows to obtain a microscopic model of the structure of the system without any supposition on the interactions between the atoms or the molecules, so no

previous knowledge about their functional form is needed.

However, due to the huge number of degrees of freedom of this method, the χ^2 hypersurface is very rough and the choice of the initial structure is crucial to avoid the algorithm getting stuck in a local minimum, a decision which is not trivial. Atoms in the same molecular site from two identical molecules are allowed to behave differently, even when they have the same environment, which is not physically meaningful. It also tends to yield the most disordered configurations compatible with the experimental results, and usually multiple disparate solutions are equally complying with the data (for instance, a configuration that has three neighbours in some molecules and five in others may be indistinguishable from a configuration where all molecules have four neighbours).

This method allows a refinement of the atom positions to obtain a fit compatible with the experimental data without the need to know the interactions, but it is not reliable when the system structure is totally unknown.

5.4.1.3 Empirical Potential Structure Refinement

The Empirical Potential Structure Refinement is a hybrid method that combines a direct Monte Carlo simulation with an energy minimisation procedure to overcome the limitations of the previous methods. Mainly, that if the available empirical or theoretical potentials are not good enough, a solution that resembles the experimental data might never be found with molecular dynamics simulations, and that is necessary to start already with an extremely good structural model to refine in reverse Monte Carlo, due to the large number of degrees of freedom involved.

In the Empirical Potential Structure Refinement method, a first guess on the atomic empirical potentials is used to calculate the energy of an initial configuration of the system. The positions of the atoms are then randomly changed and the configurations that allow to minimize the energy of the configuration are accepted until an energetic equilibrium with the first potential is reached. Once the energetic equilibrium of the configuration is found, its pair correla-

tion function or structure factor is compared to that obtained from a neutron or x-ray diffraction experiment or from a molecular dynamics simulation, and the potential is slightly changed repeating the whole process until the modelled configuration matches the experimental o simulated structure, within the estimated errors.

The main advantage of this method is that, although we don't need to abide to a predefined rigid set of interactions between the atoms, all atoms that are located in the same molecular site of different molecules will yield the same behaviour when in a similar situation, which is much more realistic from a physical point of view.

Besides, the number of degrees of freedom is much smaller than in the case of the Reverse Monte Carlo fit, therefore a precise initialization of the empirical potentials is not as important to reach the global minimum.

Its main disadvantage is that the empirical potentials to be adjusted concern only intermolecular interactions, which means that the intramolecular structure must be very well known in order to find a good fit to the experimental data.

5.4.2 Neighbours in the coordination shells

Once the configurations of the system have been obtained using any of the molecular modelling methods, their geometry must be analysed in order to understand the resulting microscopic structure contained in our solution. All structural calculations are averaged for all molecules within the same configuration and for all other available equivalent configurations as well.

The simplest analysis concerning the intermolecular structure that can be carried out is to determine the average number of neighbour molecules. This is done by taking the centre of mass of a reference molecule and counting how many centres of mass of other molecules can be found at a certain distance from it. Such histogram will yield the molecular coordination number as a function of the distance (see Figure 5.8).

This magnitude can theoretically be obtained as well from the experimental data, but only when they are perfectly normalised, which

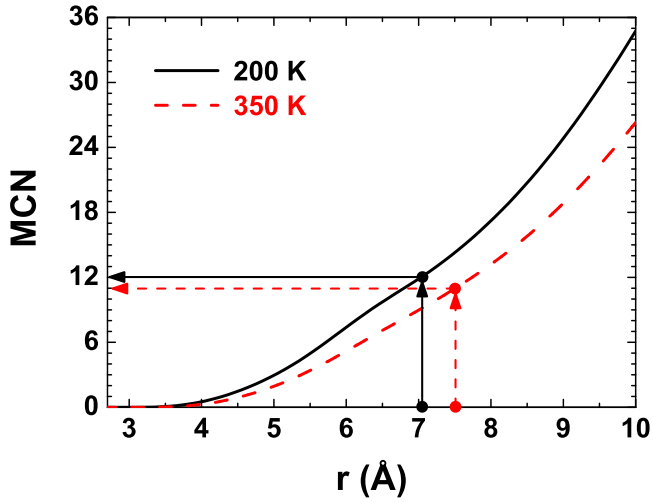

Figure 5.8: Molecular coordination number of liquid trans-1,2-dichloroethene at two different temperatures (200 and 350 K). Arrows correspond to the first coordination shell distances (about 7 and 7.5 Å, respectively) which, as can be seen, accommodate in average a different number of molecules at each temperature (12 and 11 molecules, respectively).

in practice is quite tricky.

So, instead of using this magnitude to compare it with the experiment, we can use its derivative:

$$g_{\mathrm{CM}}(r) = \frac{1}{4\pi\rho_0 r^2}\left[\frac{\mathrm{d}\,\mathrm{MCN}}{\mathrm{d}r}\right] \tag{5.25}$$

To extract this information from the configurations, the number of molecules that can be found at every small distance interval from the reference molecule is counted, and then this number is normalised to the surface of the spherical shell at that distance. This normalization is done to remove the effect of the ever increasing volumes as farther distances from the reference molecule are analysed, which happens when a constant solid angle and distance interval are taken. The result is also normalised to the number density ρ_0 so that the re-

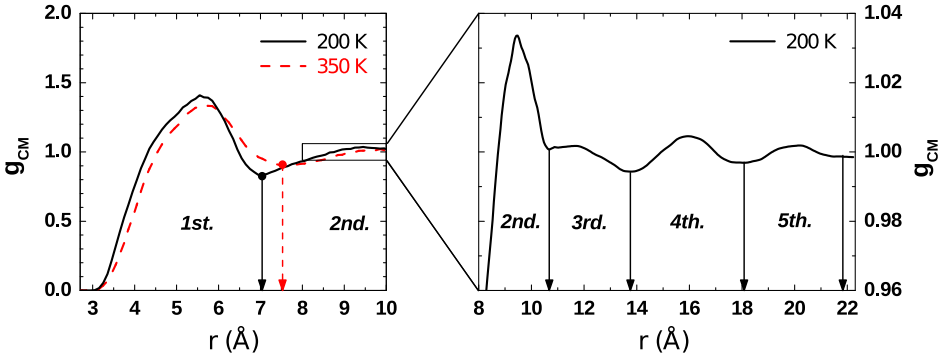

Figure 5.9: Pair-correlation function of the molecular centres of mass of liquid trans-1,2-dichloroethene at two different temperatures (200 and 350 K), and a close up of the function at 200 K in a range of larger distances. Arrows indicate the distances from the reference molecule to the minima, which are used to define the extent of the coordination shells (around 7 and 7.5 Å for the first coordination shell at 200 K and 300 K, respectively).

sulting magnitude $g_{\mathrm{CM}}(r)$ is proportional to the probability of finding a neighbour molecule at a certain distance of the reference one (see Figure 5.9). This magnitude can be obtained from the experimental data in some special cases such as monoatomic systems, or when isotopic substitution is carried out in systems with certain molecular geometries.

The distinct features that this quantity shows allow us to define the concept of neighbour (or coordination) shells in disordered systems: each peak corresponds to one of the shells, whose extent will be defined using the positions of the surrounding local minima. Once the extent of the coordination shell is determined, its average number of neighbours can be read from the molecular coordination number.

For example, the first coordination shell of the system depicted in Figure 5.9 at 200 K will include all molecules up to a distance of about 7 Å. Looking at the molecular coordination number of the same system, shown in Figure 5.8, it can be observed that the number of neighbours contained up to 7 Å, which corresponds to the first

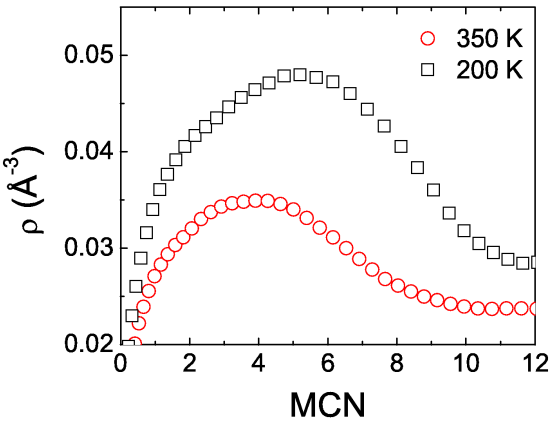

Figure 5.10: Molecular density within the first neighbour shell for liquid trans-1,2-dichloroethene at two different temperatures as a function of the molecular coordination number. The density at 350 K increases up to the fourth neighbour and then decreases, while the density at 200 K starts decreasing at the fifth neighbour. This is reflecting a difference in the arrangement of the molecules in the first coordination shell, which are better packed at the lower temperature.

coordination shell, is about 12 molecules. The number of neighbours in farther coordination shells can be found simply by subtracting the molecular coordination number values at the minima positions surrounding the peak.

Another representation which can provide further insight on the distribution of neighbours in the first neighbour shell is the local density. This can be depicted as a function of the molecular coordination number (see Figure 5.10). This magnitude can provide information on the packing behaviour of the compound, providing much more information than just the number of neighbours in the shell.

The general advantage of using the molecular coordination number as a variable instead of the distance is that the expansion or contraction effects of the temperature on the materials are naturally removed, and thus allows to compare the differences between purely structural behaviours at various temperatures without the interfer-

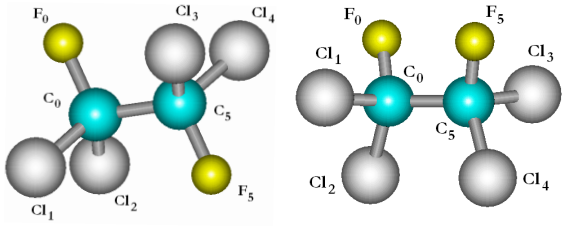

Figure 5.11: Liquid 1,1,2,2-tetrachloro-1,2-difluoroethane has a carbon-carbon bond that allows rotations, and thus displays two conformations. These two conformations coexist and their population changes with temperature.

ence of the expansion coefficient. For this reason, this variable will be often used henceforth in many of the analyses.

5.4.3 Intramolecular structure

Although intramolecular structure displayed by the configurations obtained through molecular modelling is often a feature already built in with the constraints, this is not always the case. Some simulations allow detailed internal interaction potentials which can couple to the other contributions and yield realistic variations of the intramolecular structure driven by the surrounding molecules. An example of that are simulations that have been carried out for the 1,1,2,2-tetrachloro-1,2-difluoroethane liquid (see Chapter 6 for a detailed description), which displays two conformations that coexist and whose population changes with temperature, and that are affected by intermolecular interactions (see Figure 5.11).

These simulations were carried out with an intramolecular potential that allowed the two sides of the molecule to rotate with respect to each other, to account for the behaviour of the conformer population. To find out the population distribution of each conformer in the liquid phase yielded by the simulation, a histogram was calculated counting the number of molecules that displayed an intramolecular dihedral angle within each small angular interval (see Figure 5.12).

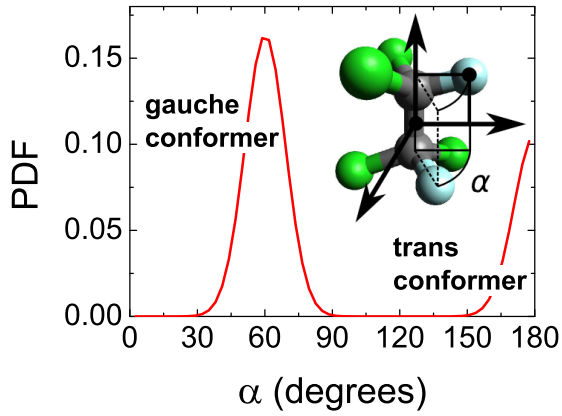

Figure 5.12: Probability distribution function (PDF) of the dihedral angle F–C–C–F of the 1,1,2,2-tetrachloro-1,2-difluoroethane molecule in the liquid phase as simulated by molecular dynamics. A scheme of the molecule and its dihedral angle (α) is also depicted.

The histograms obtained from counting the number of molecules in a certain geometric range are proportional to the probability distribution functions of each arrangement. Dividing by the total number of molecules that are being counted normalises its integral to one, so that it yields exactly the probability distribution function. These functions contain a lot of information and are the basis of the analyses that have been normally carried out in this work to account for a detailed description of the intra- and intermolecular structure.

5.4.4 Intermolecular structure

In highly disordered materials such as the ones we are studying here, the molecular short range order is not a precise position and orientation of a certain neighbour with respect to the reference molecule, but rather a tendency of the molecules of being in a certain relative arrangement. For that reason, the use of probability distribution functions where all information is contained is much more adequate than just its most probable value.

A particular molecule of the configuration will be chosen as the

reference molecule and the relative orientation and position of all other molecules with respect to this one will be accounted. Then another molecule in the configuration will be chosen as the reference molecule, and the process will be repeated until every molecule in the configuration and all its neighbours have contributed to the histogram. As explained before, this histogram can be normalised, using the total number of molecules and molecular pairs which have been counted, to obtain the probability distribution function of every particular magnitude.

If more than one equivalent configuration is available, the average will be performed over all molecules included in all configurations.

5.4.4.1 Definition of reference system

The reference system will be built upon the reference molecule. Depending on the molecular geometry, it may be convenient to use one of the atoms as the origin of the reference system. For instance, this may be the case if the molecule has an atom at its centre.

In Figure 5.13 two examples can be seen where the origin of the coordinate system has been chosen to coincide with one of the atoms (in both cases a central carbon atom).

In the case of trichlorobromomethane, shown in Figure 5.13(a), the direction of the bromine atom in each molecule has been used to define the z axis, and one of the chlorines to define the yz plane. While in the case of dibromodichloromethane, shown in Figure 5.13(b), the direction of the molecule dipole (between the bromine atoms) has been used to define the z axis, and the plane formed by the carbon and the chlorines to define the xz plane.

Note that choosing one of the atoms as the origin of the reference system implies in nearly all cases that the analyses will not be performed strictly with respect to the centres of mass. This is because in most simulations the atoms within the molecule do not stand still and are allowed to realistically vibrate within certain boundaries about their equilibrium positions driven by thermal agitation. Which means that every molecule in the configuration will be slightly distorted, and at best this central atom will only be a good approximation of

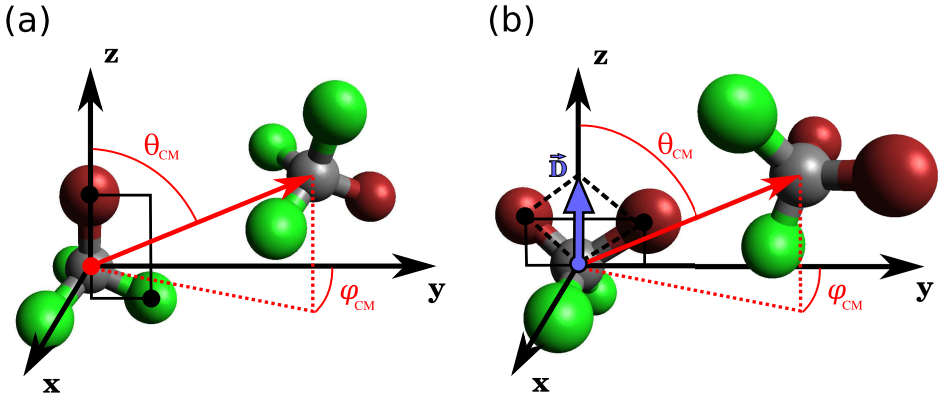

Figure 5.13: Examples of reference system definitions with the origin on one of the atoms of the molecule: (a) trichlorobromomethane ($CBrCl_3$), and (b) dibromodichloromethane (CBr_2Cl_2).

its centre of mass.

However, even in cases where the molecular geometry would be reasonably convenient as to define the origin of the reference system on one of the atoms, the real centre of mass of each molecule can always be calculated and used as the origin of the reference system.

Figure 5.14 depicts two cases where, instead of a particular atom, the centre of mass of each molecule in the configuration has been calculated in order to define the origin of the coordinate system with it.

In Figure 5.14(a) the case of trans-1,2-dichloroethene is shown, which is a planar and rather rigid molecule due to its carbon-carbon double bond. Here, the axis running through the chlorine atoms has been used to define the z axis, the molecular plane has been used to define the yz plane of the reference system and, finally, to uniquely distinguish between two possible mirror images of the molecule, the positive direction of y has been defined using the hydrogen atom also bonded to the chlorine atom that defines the positive direction of z.

The example for 1,1,2,2-tetrachloro-1,2-difluoroethane, shown in Figure 5.14(b), is a bit more complicated because the molecular structure can be completely disparate from one molecule to the next, due to the carbon-carbon flexible single bond that allows the molecule to

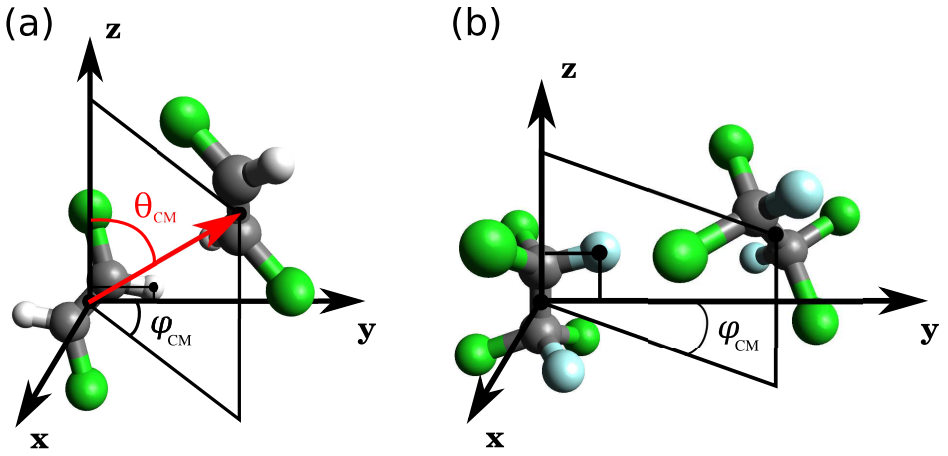

Figure 5.14: Examples of reference system definitions with the origin on the centre of mass of the molecule: (a) trans-1,2-dichloroethene ($C_2Cl_2H_2$), and (b) 1,1,2,2-tetrachloro-1,2-difluoroethane ($C_2Cl_4F_2$).

rotate and adopt different conformations. For this reason, the system of reference has been defined using only one half of the molecule, unaffected by the rotation of the other half. The axis that runs through the carbon-carbon atoms has been used to define the z axis, and the fluorine atom in the positive z direction has been used to define the yz plane and, in particular, the positive y direction. This definition is unique regardless of the conformational disorder of the molecules and allows to easily measure the intramolecular dihedral angle with the same reference system as the intermolecular short range order, which is quite convenient to better understand the interplay between both interactions.

5.4.4.2 Distance range selection

When an analysis of the arrangement of neighbour molecules is carried out, a meaningful selection of the volume that will be averaged out in the analysis will have a huge impact on the insight that the results will provide.

In this work the simulation box has been divided in concentric

spherical shells around the reference molecule, but the inner and outer radius of each shell (r_i and r_{i+1}, respectively) can be arbitrarily chosen. This allows to analyse separately the behaviour of the molecules located at each range of distances from the reference molecule. For every particular magnitude, a probability distribution function of the neighbours has been calculated for each shell. Typically, the first volume will include the origin ($r_i = 0$ Å) so strictly speaking it will not be a spherical shell but a sphere.

A fine grained counting of the molecules in each arrangement for each distance interval will provide with a more noisy probability distribution function, but also with a more precise localization of different behaviours. If no restrictions are made, an average of all neighbours within the simulation box will be carried out, which in general may not be very informative for disordered systems, due to the fact that usually only the closest molecules will retain certain level of preferred order and the farther ones tend to be uncorrelated.

Four of the possible approaches to divide the volumes that will be explored are: equal distance intervals, equal volumes, by coordination shells, and by molecular coordination number.

5.4.4.2.1 Distance This approach consists in using distance as a variable disregarding any possible structural information. The simplest way to cover the whole space would be to define consecutive spherical shells using regular intervals of r_i and r_{i+1} distances (see Table 5.1). Although it has the problem that the volume to analyse becomes always larger as the distance increases:

$$V = (4\pi/3)\left(r_{i+1}^3 - r_i^3\right) \tag{5.26}$$

Thus involving an ever increasing number of molecules and behaviours, which makes it more difficult to compare the results of different shells.

Another alternative is to define spherical shells with smaller thicknesses Δr as distance increases, to ensure they will all have the same volume V (see Table 5.2). Of course, there will be density fluctuations in the system from one shell to the other that will modify the number of molecules accounted, but the differences will be kept smaller

Table 5.1: Example of dividing the volume to analyse in spherical shells with the **same thickness** Δr (liquid trans-1,2-dichloroethene molecular dynamics simulation at 200 K).

Shell	Δr (Å)	r_i (Å)	r_{i+1} (Å)	V (Å^3)
1st	1	0	1	4.2
2nd	1	1	2	29.3
3rd	1	2	3	79.6
4th	1	3	4	155.0
5th	1	4	5	255.5

Table 5.2: Example of dividing the volume to analyse in spherical shells with a **constant volume** V (liquid trans-1,2-dichloroethene molecular dynamics simulation at 200 K).

Shell	V (Å^3)	r_i (Å)	r_{i+1} (Å)	Δr (Å)
1st	100	0.0	2.88	2.88
2nd	100	2.88	3.63	0.75
3rd	100	3.63	4.15	0.52
4th	100	4.15	4.57	0.42
5th	100	4.57	4.92	0.35

than in the previous case. The upper boundaries of the volumes are calculated recursively using:

$$r_{i+1} = \sqrt[3]{\frac{3V}{4\pi} + r_i^3} \tag{5.27}$$

5.4.4.2.2 Coordination shells Considering that neighbours organise themselves in coordination shells, analysing the behaviour of molecules separately in these naturally occurring subdivisions can be quite insightful (see example of liquid trans-1,2-dichloroethene at 200 K in Table 5.3). The boundaries for the coordination shells have

Table 5.3: Example of using the **coordination shells** to divide the volume to analyse (liquid trans-1,2-dichloroethene molecular dynamics simulation at 200 K).

Shell	r_i (Å)	r_{i+1} (Å)	Δr (Å)	V (Å^3)
1st	0.0	7.06	7.06	1474
2nd	7.06	10.68	3.62	3629
3rd	10.68	13.76	3.08	5810
4th	13.76	18.08	4.32	13843
5th	18.08	21.83	3.75	18820

been taken from the local minima positions of the pair correlation function g_{CM} shown in Figure 5.9.

5.4.4.2.3 Molecular coordination number However, using the coordination shells is a quite rough separation because it includes a bunch of molecules that might be displaying a variety of behaviours. A range of potentially distinct molecular arrangements which are effectively averaged out before they can even be examined.

In this work, to achieve an equilibrium between meaningful and informative divisions and that at the same time do not average out distinct arrangements too much, the approach of the average location of each neighbour has been used. That is, using the molecular coordination number as a function of the distance, it is determined at which range of distances is each neighbour located on average, and then these are the divisions used to analyse the behaviour of the molecules.

Of course, since this is only an average, frequently a part of the analysed molecules will be occupying the shell of the previous or the next neighbour, but although it cannot be stated that certain neighbour will take this or that configuration is still very useful to see their tendencies.

This method has several advantages:

- It allows a qualitative analysis of the problem, and not only

Table 5.4: Example of using the **number of neighbour** to divide the volume to analyse (liquid trans-1,2-dichloroethene molecular dynamics simulation at 200 K).

Neighbour	r_i (Å)	r_{i+1} (Å)	Δr (Å)	V (Å^3)
1st	0.0	4.37	4.37	349.6
2nd	4.37	4.79	0.42	110.8
3rd	4.79	5.10	0.31	95.3
4th	5.10	5.37	0.27	93.0
5th	5.37	5.60	0.23	87.0
6th	5.60	5.81	0.21	85.9
7th	5.81	6.01	0.20	87.8
8th	6.01	6.21	0.20	93.8
9th	6.21	6.42	0.21	105.2
10th	6.42	6.65	0.23	123.4
11th	6.65	6.89	0.24	138.2
12th	6.89	7.12	0.23	141.8

quantitative. It is more intuitive to determine the preferred orientation of the molecules located at the average distance of the third neighbour than the behaviour of molecules between certain arbitrary range of distances.

- Emphasizes similarities and differences between different neighbours that we might have not realised previously.

- The replacement of distance in favour of the neighbour number in the analyses naturally removes the density effects such as the expansion coefficient as temperature is changed or the simple fact of dissimilar densities between different substances, which allows to better compare strictly the short range order structure of the different systems on absolute terms.

As said previously, shell boundaries can be defined using any set of arbitrary values, hence, if neighbours in different ranges are as-

Table 5.5: Example of using a neighbour grouping by their short range order similarity to divide the volume to analyse (liquid trans-1,2-dichloroethene molecular dynamics simulation at 200 K).

Shell	Neighbours	r_i (Å)	r_{i+1} (Å)	Δr (Å)	V (Å^3)
1st	1st	0.0	4.37	4.37	349.6
2nd	2nd+3rd	4.37	5.10	0.73	206.1
3rd	4th+5th	5.10	5.60	0.50	180.0
4th	6th+7th	5.60	6.01	0.41	173.7
5th	8th+9th+10th +11th+12th	6.01	7.12	1.11	602.4

certained to yield similar results, the volumes can always be subsequently merged to optimise the analysis.

An example of dividing the analysis volume using the number of neighbours, corresponding to liquid trans-1,2-dichloroethene at 200 K, is shown in Table 5.4. The values have been taken from its corresponding molecular coordination number, depicted in Figure 5.8. A version dividing analysed volume into neighbours with a similar behaviour is shown in Table 5.5.

5.4.4.3 Neighbour position

Once the coordinate frame is well defined on the reference molecule, and the simulation has been divided in volumes to analyse separately, the direction in which the central atom or the centre of mass of each neighbour molecule is located can be determined.

With the range of distances to the reference molecule determined by the shell division, two angles will be enough to describe the position of the neighbour molecule. Figures 5.13 and 5.14 show several examples where the two positional angles have been defined similarly with respect to the reference frame: the standard polar angle measured from the z axis, θ_{CM}, and a variation of the azimuth angle measured from the y axis towards the x axis instead of the usual reversed definition, φ_{CM}. Please note that at this point the orientation

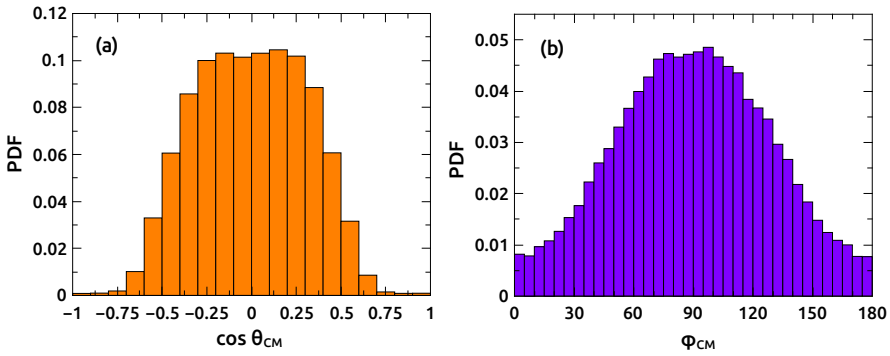

Figure 5.15: Probability distribution functions of the position of the neighbour molecules located at less than 4.37 Å from the reference molecule for liquid trans-1,2-dichloroethene at 200 K, which in average corresponds to the first neighbour. θ_{CM} and φ_{CM} are the angles described in Figure 5.14.

of the neighbour molecule is completely disregarded and the analysis is focused only on the position of its central atom or centre of mass.

The relative position of the neighbour molecules has been analysed for liquid trans-1,2-dichloroethene at 200 K and is shown in Figure 5.15 as an example. The probability distribution function has been calculated from the molecules up to a distance of 4.37 Å, which on average corresponds to the location of the first neighbour. As can be seen, the centres of mass of these molecules locate preferably at angles around $\theta_{\mathrm{CM}} = 90°$ and $\varphi_{\mathrm{CM}} = 90°$ (average of all possible orientations), but the liquid is quite disordered in this regard so the distribution is not sharp but rather spread. This effect increases with temperature due to thermal agitation, therefore, less contrasted probability distribution functions will be always obtained for higher temperatures even if the molecular short range order remains essentially the same.

The information in Figures 5.15(a) and (b) can also be combined in a 2D graph and be presented as a bivariate analysis (see Figure 5.16). The advantage of this graph is that no information is lost as in the projections shown in Figure 5.15 so that, once some interpretation

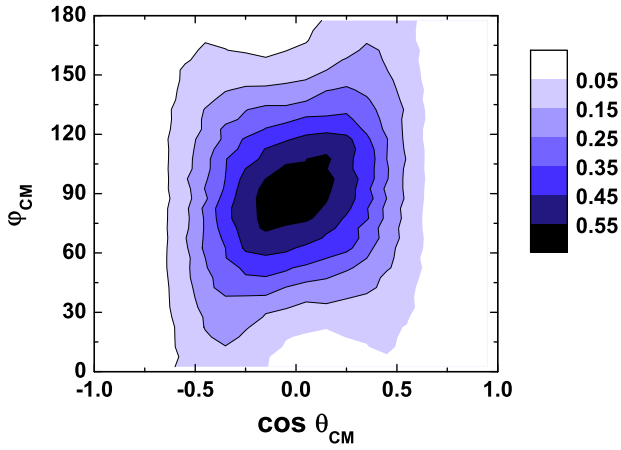

Figure 5.16: Probability distribution function of the angular position of the first neighbour with respect to the reference molecule in liquid trans-1,2-dichloroethene at 200 K. Darker shade means higher probability.

skill is acquired, the location of the neighbours can be grasped in full detail in just a glimpse.

For instance, although this graph still shows the position $\theta_{\mathrm{CM}} = 90°$ and $\varphi_{\mathrm{CM}} = 90°$ as the most probable, it can be observed that the centre of mass of the neighbour molecule is more likely to be at the upper right and lower left sections of the graph than at the upper left and lower right sections. This reflects the molecular geometry, and it means that if the centre of mass of the first neighbour is located in the molecular plane of the reference molecule ($\varphi_{\mathrm{CM}} = 0$ or $180°$), it will rather be in the direction between the chlorine and the hydrogen not bonded to the same carbon, albeit being in this plane is globally not its most likely position in the first place anyway.

Note that in the case of the θ_{CM} angle, the probability distribution function of its cosine is shown instead of the angle itself. The reason behind this is simply to guarantee that space is divided in equal bins when molecules are counted. In spherical coordinates, for equal

angular intervals the covered solid angle is larger for θ_{CM} near the equatorial plane than near the pole, which means that larger bins would be considered if the angle was taken. Therefore, the probability distribution function of θ_{CM} would yield a higher probability of molecules being in angles near the equatorial plane in situations where they are in fact evenly distributed in space, because it would be counting more molecules simply by construction. On the contrary, its cosine guarantees a regular binning and will indeed display a flat distribution when molecules are evenly distributed in space. Thus, to simplify the analysis and avoid any underlying shape of the uniform distribution to mislead to wrong conclusions, the cosine has been always used instead of the angle in cases like this.

A fast and reliable way to identify similarly behaved molecules is to first define the analysis volumes with the range of positions corresponding to each neighbour (see Table 5.4), and then depicting side by side their short range order patterns for comparison. Similar patterns can then be easily identified and its volumes grouped to treat them jointly thereafter (see Table 5.5).

Depicting side by side the short range order patterns of the molecules located in the volumes corresponding in average to every neighbour, can be a fast and reliable way to identify similarly behaved molecules, which can be treated jointly thereafter.

For instance, Figure 5.17 shows the probability distribution functions regarding the relative position of the fourth to seventh neighbours in liquid trans-1,2-dichloroethene at 200 K. In this case, two kinds of distinct patterns can be identified: one that describes the arrangement of neighbours fourth and fifth, and another that describes the arrangement of the sixth and seventh. This realisation allows to treat together the fourth and fifth neighbours on one hand and the sixth and seventh on the other by defining a larger volume that includes the average location of both neighbours involved. This increases the statistics, reducing noise and enhancing the contrast of the patterns, which allows for a better short range order analysis, and it has the advantage that no assumptions are made regarding the neighbours' short range order, as was done in the case of the coordination shells. Here, conclusions about similar arrangement of

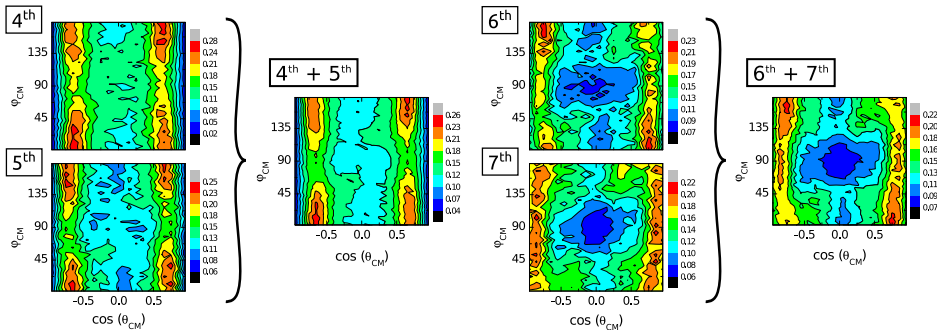

Figure 5.17: Probability distribution functions of the angular position of the fourth to seventh neighbours with respect to the reference molecule in liquid trans-1,2-dichloroethene at 200 K. Similar patterns are averaged together to obtain better statistics.

molecules are drawn only after the actual short range order has been examined.

However, this process must be carried out with great caution because molecules that display the same relative position may still have very different orientations and vice versa, or they could even display differences in just one of the orientation angles, while keeping the rest very much alike. Therefore, if no details are to be missed, molecules should only be grouped after similar behaviour has been ascertained for all magnitudes under analysis.

A complete set of probability distribution functions describing the position of the neighbours in the first neighbour shell of liquid trans-1,2-dichloroethene at 200 K is shown in Figure 5.18 as an example. The following neighbour groups with a similar short range order were determined:

- Group A: 1st neighbour
- Group B: 2nd and 3rd neighbours
- Group C: 4th and 5th neighbours
- Group D: 6th and 7th neighbours

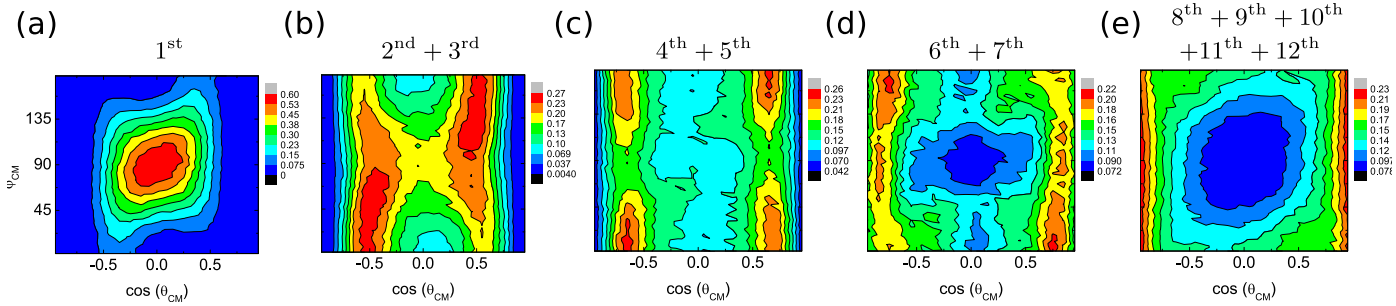

Figure 5.18: Probability distribution functions of the position of the centres of mass of the neighbours in the first coordination shell in liquid trans-1,2-dichloroethene at 200 K. Higher probability is shown in red.

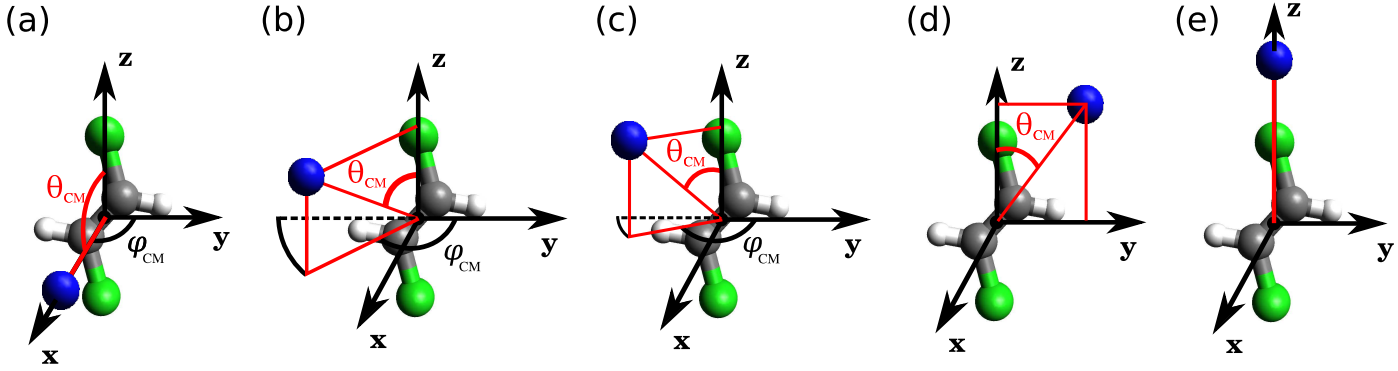

Figure 5.19: Scheme of the most probable positions of the centres of mass of the neighbours in the first coordination shell in liquid trans-1,2-dichloroethene at 200 K. Each scheme belongs to the corresponding probability distribution function depicted above.

- Group E: 8^{th}, 9^{th}, 10^{th}, 11^{th} and 12^{th} neighbours.

This grouping of the analysis volumes is the one shown in Table 5.5.

Although only positional angles are shown here, neighbours have been grouped using criteria regarding their relative orientations similarity as well.

For illustration purposes, a scheme of the most probable relative position of the centres of mass of the molecules for each group of neighbours is shown in Figure 5.19: $\theta_{\text{CM}} = \varphi_{\text{CM}} = 90°$ for the first neighbour, $\theta_{\text{CM}} = 60°$ and the wide range of $\varphi_{\text{CM}} = 110 - 180°$ for neighbours second and third, $\theta_{\text{CM}} = 51°$ and $\varphi_{\text{CM}} = 160 - 180°$ for neighbours fourth and fifth, $\theta_{\text{CM}} = 41°$ and $\varphi_{\text{CM}} = 0°$ for neighbours fourth and fifth, and the poles for neighbours eighth to twelfth. However, this is just a fraction of all the information contained in the probability distribution functions, which allows to represent the whole complexity of the short range order.

5.4.4.4 Neighbour orientation

Relative orientation of neighbours with respect to the reference molecule can be determined using a number of angle combinations, depending on the molecular geometry.

The trans-1,2-dichloroethene example has been used again to illustrate one of the possibilities for orientational angles definitions. The particular choice of angles can be seen in Figures 5.20, (b), (c), and (d). α is the angle between the axes than run through the hydrogen atoms of each molecule, β is the angle between the axes than run through the chlorine atoms of each molecule, and γ is the angle between the axis than runs through the chlorine atoms of the reference molecule and the hydrogen atoms of the neighbour.

The probability distribution function of one of the orientational angles is shown in Figure 5.21 for liquid trans-1,2-dichloroethene molecules in the volume that corresponds to the average location of the first neighbour. A drastic difference can be seen between the lower and higher temperature distributions of angle α: at low temperature this angle has a higher tendency to be 0°or 180 °, which corresponds to the hydrogen axes being parallel, and at high temperature it tends to

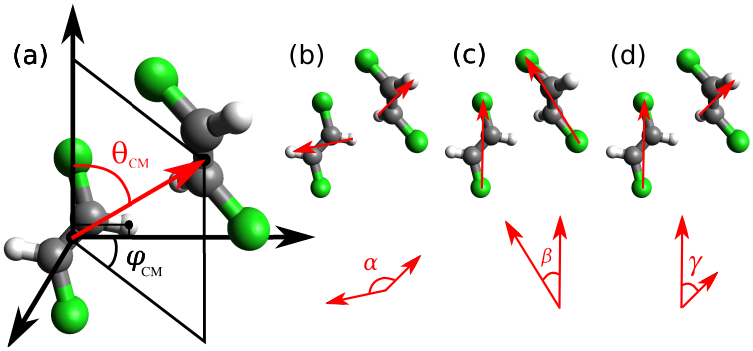

Figure 5.20: Scheme of the positional and orientational angles definition system for the trans-1,2-dichloroethene molecule: (a) positional angles θ_{CM} and φ_{CM}, (b) orientational angle α between the hydrogen axes of both molecules, (c) orientational angle β between the chlorine axes of both molecules, and (d) orientational angle γ between the chlorine axis in one molecule and the hydrogen axis on the other.

have any other orientation, corresponding to perpendicular or slanted relative orientations of the hydrogen axes.

Bivariant analysis can also be used with orientational angles which can be represented as a function of some positional angle, to find out the orientation of molecules located in a certain direction of the reference molecule. Some examples for the first coordination shell of liquid trans-1,2-dichloroethene at 200 K can be seen in Figures 5.22 and 5.23. As it can be seen in Figure 5.22, the chlorine axes are very likely to be parallel ($\beta = 0°$ or $180°$) between the closest neighbours and the reference molecule, but from the sixth or seven neighbour of the first coordination shell it becomes more likely that they are perpendicular. However, for the very first neighbour the distribution is not sharp and a whole range of intermediate angles are probable as well.

Figure 5.23 shows that the most probable situation for the first neighbour is that its hydrogen axis is parallel to the chlorine axis of the reference molecule, for the second and third neighbours the most likely value of the same angle is about $\gamma \approx 70°$, from the fourth to

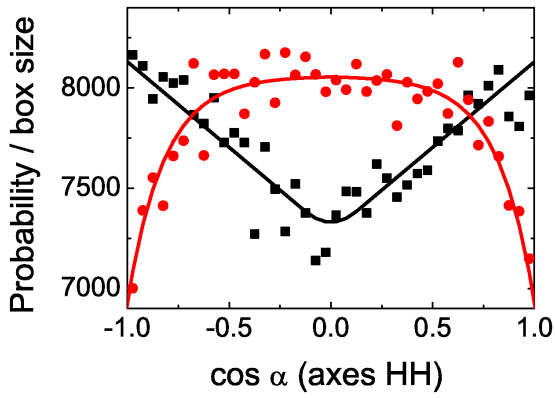

Figure 5.21: Probability distribution function of the orientational α angle for the first neighbour in liquid trans-1,2-dichloroethene at 200 K (black squares) and 350 K (red circles).

seventh neighbours the most probable orientation for their hydrogen axis is perpendicular to the chlorine axis of the reference molecule, and from the eighth to the twelfth neighbour they become parallel again.

Apart from representing the probability distributions of the neighbours' orientation as a function of the positional angle, another representation which can be very powerful is to calculate the probability distribution function only in terms of orientational angles. Keeping the neighbour distance boundaries for the analysis allows us to use two orientational angles instead of one, so that the preferred orientation of every neighbour can be explored without the previous ambiguity.

In Figure 5.24 the probability distribution function of two orientational angles, β and γ, are shown for the very first neighbour of liquid trans-1,2-dichloroethene at 200 K. These two angles determine uniquely the relative orientation between the neighbours and the reference molecule.

This representation is a bit different from those shown before because here the molecule cannot just take any combination of angle values. In this case, molecular geometry highly restricts the possible

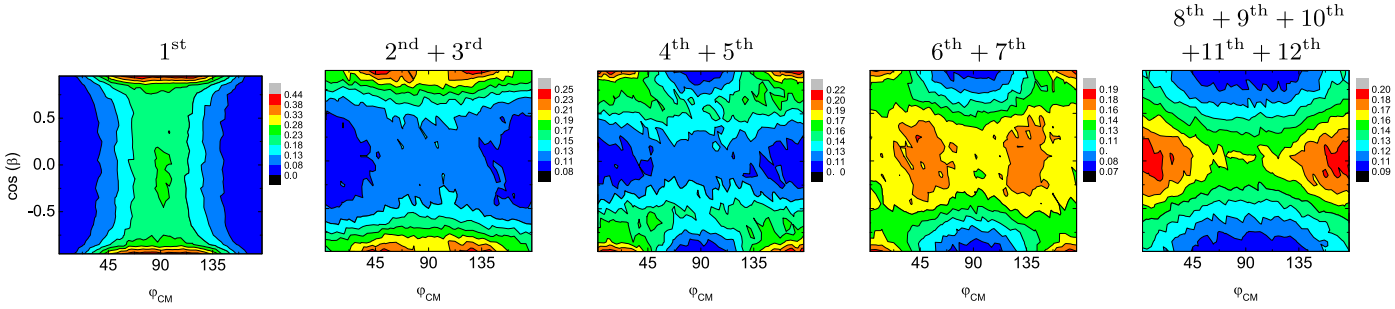

Figure 5.22: Probability distribution functions of the orientational angle β as a function of the positional angle φ_{CM} for neighbours of the first coordination shell in liquid trans-1,2-dichloroethene at 200 K. Higher probability is shown in red.

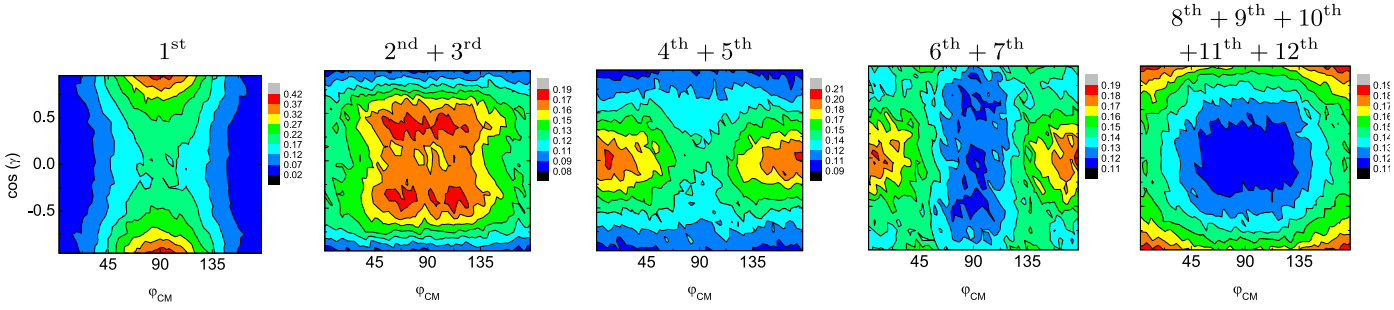

Figure 5.23: Probability distribution functions of the orientational angle γ as a function of the positional angle φ_{CM} for neighbours of the first coordination shell in liquid trans-1,2-dichloroethene at 200 K. Higher probability is shown in red.

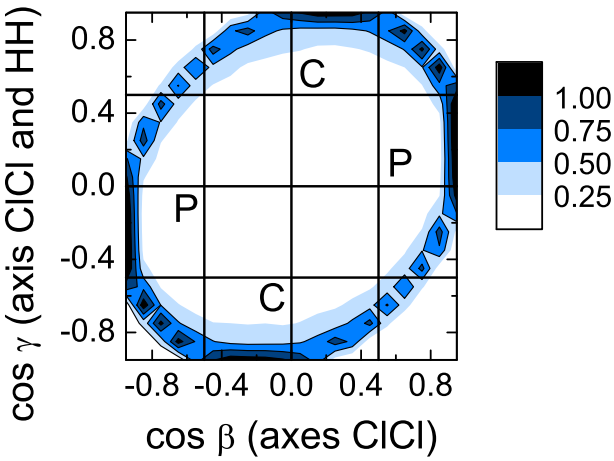

Figure 5.24: Bivariant probability distribution function of the β and γ angles in liquid trans-1,2-dichloroethene molecule at 200 K.

combinations of the two angles, which means that a significant departure from the circle apparent in Figure 5.24 would only be possible if the intramolecular structure was highly distorted.

Even with the restriction that all angle combinations must lay near the circle, there's a continuous range of possible orientations. The four black spots in the graph show that there are a some configurations that are preferred over the rest. The configurational space has been divided in 16 regions, each corresponding to a continuous range of angle combinations. The four regions that contain the most probable orientations have been labelled as P and C.

Configuration P corresponds to the chlorine axes of both molecules being parallel ($\beta = 0°$), and the hydrogen axis of the neighbour molecule crossed with respect to the chlorine axis of the reference molecule (in the range $\gamma = 60° - 90°$). And in configuration C the hydrogen axis of the neighbour molecule is parallel to the chlorine axis of the reference molecule ($\gamma = 0°$), and the chlorine axes are crossed (in the range $\beta = 60° - 90°$). In fact, due to the molecular symmetry of the trans-1,2-dichloroethene molecule, the configurations in

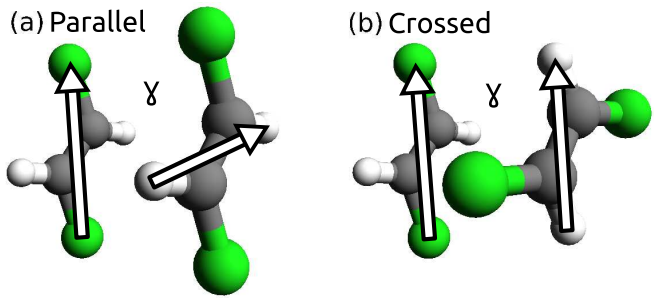

Figure 5.25: Two sample configurations of the first neighbour in trans-1,2-dichloroethene. The position of the centre of mass of the neighbour molecule is $\theta_{\mathrm{CM}} = \varphi_{\mathrm{CM}} = 90°$ in both cases. The arrows indicate the two axes that determine angle γ. Relative orientations shown correspond to configurations (a) Parallel or P with $\alpha = \beta = 0°$, and (b) Crossed or C with $\gamma = 0°$. The configuration names correspond to the relative orientation of angles α and β.

the regions labelled as P are equivalent, and the configurations in the regions labelled as C are equivalent as well.

An example of the Parallel (or P) orientational configuration can be seen in Figure 5.25(a) and an example of the Crossed (or C) configuration can be seen in Figure 5.25(b).

Since we are handling probability distribution functions, it is always possible to go beyond the qualitative description of the data, and quantify what proportion of molecules contributes to each positional or orientational configuration simply through integrating this function in our region of interest. In this case, it could be used to calculate the fraction of molecules in each of the configurations.

Analysing all these orientations to try and get a picture of the short range order can be very complicated. Mainly due to the fact that the high disorder in these systems yields a continuous range of different configurations which coexist without a clear separation, regarding both their position as well as their orientation. And also because every representation is just a projection of the complex positional and orientational higher-dimensional space, allowing the vi-

sualization of only part of the information every time. This means that considering only the most probable value of each magnitude can be quite misleading, because they may not correspond to each other, i. e., the molecules at the most likely position may not necessarily yield the most likely orientation, wich may be simply the preferred orientation for all other molecules.

A strategy that can be useful is to try to limit the analysis even more and analyse the arrangement of neighbours in a compartmented way. This is already what is being done through the division in spherical volumes but further restrictions can be imposed through any of the studied magnitudes so that only the molecules within a certain range of values will be accounted in the description.

In the case of trans-1,2-dichloroethene, a whole additional short range order analysis was carried out separately for molecules in a Parallel configuration and for molecules in a Crossed configuration, so the relative positions of neighbours in each configuration could be compared.

Chapter 6

Results

The results of this work have been already presented in the form of published articles and book chapters. These publications have been included in this section for completeness reasons.

Although all articles rely on common experimental and analysis techniques, they have been grouped by their main topic: either the compound being studied (TDCE, F-112, CCl_4, and CBr_xCl_y) or the method described (Bayesian analysis of data).

6.1 Structural and dynamic anomalies in liquid trans-1,2-dichloroethene (TDCE)

TDCE has a series of structural and dynamical anomalies within its liquid phase, which some authors have attributed to a liquid-liquid phase transition. The purpose of this research was to understand the microscopic explanation behind these anomalies.

Molecular short-range order and dynamics changes were shown to go hand in hand: both are more cooperative at the high-density than

the low-density liquid. The microscopic mechanism driving these cooperative motions was found to be a strongly correlated molecular ordering.

Structural differences between both liquids were analysed in rich detail and it was found that the number of molecules in the first neighbour shell is 12 for the high-density liquid and 11 for the low-density one. The angular position of the centre of mass of the first neighbour is roughly the same but its molecular orientation is not: In both liquids the first neighbour and its reference molecule arrange mainly in two configurations, each being the most probable in one of the liquids.

First neighbours in the configuration that predominates in the high-density liquid tend to locate themselves closer to the reference molecule, an evidence that they are more strongly bonded. This arrangement facilitates a better packing of the rest of molecules in the first neighbour shell so that on average an additional molecule can be included, and explains both, the structural and the dynamical anomalies.

Results were presented in several conferences, even obtaining a best poster award at the 9th Conference on Quasielastic Neutron Scattering (Villigen, Switzerland, 2009), and they have been published mainly in the articles: M. Rovira-Esteva, N. A. Murugan, L. C. Pardo, S. Busch, et al., Phy. Rev. B **81**, 099902 (2010); and M. Rovira-Esteva, N. A. Murugan, L. C. Pardo, S. Busch, et al., J. Chem. Phys. **136**, 124514 (2012).

TOPIC 1: Microscopic structure and dynamics of high and low density trans-1,2-dichloroethylene liquids

M. Rovira-Esteva,[1] A. Murugan,[1] L. C. Pardo,[1] S. Busch,[2] M. D. Ruiz-Martín[1] M.-S. Appavou,[3] J. Ll. Tamarit,[1] C. Smuda,[4] T. Unruh,[2] F. J. Bermejo,[5] G. J. Cuello,[6] and S. J. Rzoska[7]

[1]Grup de Caracterització de Materials, Departament de Física i Enginyeria Nuclear, ETSEIB, Universitat Politècnica de Catalunya, Diagonal 647, E-08028 Barcelona, Catalonia, Spain

[2]Physik Department E13 and Forschungs-Neutronenquelle Heinz Maier-Leibnitz (FRM II), Technische Universität München, Lichtenbergstr. 1, D-85748 Garching, Germany

[3]Forschungszentrum Jülich GmbH, Institut für Festkörperforschung (IFF), Jülich Centre for Neutron Science (JCNS), FRM II outstation, Lichtenbergstr. 1, 85748 Garching, Germany

[4]ETH Zürich, Center for Radiopharmaceutical Science, Wolfgang-Pauli-Str. 10, CH-8093 Zürich, Switzerland

[5]Facultad de Ciencia y Tecnología, Universidad del País Vasco / EHU, P. Box 644, E-48080 Bilbao, Spain

[6]Institut Laue Langevin, 6 Rue Jules Horowitz, BP. 156, F-38042 Grenoble Cedex 9, France

[7]Institute of Physics, Silesian University, Uniwersytecka 4, 40-007 Katowice, Poland

Published: **Physical Review B 81, 092202 (March 2010).**
DOI: http://dx.doi.org/10.1103/PhysRevB.81.092202

Abstract

We present a study of the dynamics and structural changes for trans-1,2-dichloroethylene between high and low density liquids using neutron scattering techniques (diffraction, small angle neutron scattering and time of flight spectroscopy) and molecular dynamics simulations. We show that changes in the short range ordering of molecules goes along with a change of the molecular dynamics: both structure and dynamics of the high density liquid are more cooperative than those of the low density liquid. The microscopic mechanism underlying the cooperative motions in the high density liquid has been found to be related to the backscattering of molecules due to a strong correlation of molecular ordering.

Article

Classical thermodynamics establishes the existence of one unique liquid state and one unique vapour state for any material. Nevertheless, recent experimental results and molecular dynamics (MD) simulations suggest that, even for one-component systems, several liquid phases can appear with an associated liquid-liquid phase transition (LLPT). A noticeable number of cases has been found for atomic liquids, the best-known example concerning liquid phosphorus [1, 2], where the LLPT appears as a transition between thermodynamically stable phases with strong structural changes [3]. As far as molecular liquids are concerned, the number of experimental evidences for LLPT is still rather scarce and comprises only a limited number of compounds such as triphenyl phosphite [4] and n-butanol [5]. According to the so called two order parameter theories that propose an explanation for the LLPT, liquids must be described not only by their density but also by an additional order parameter accounting for changes in the molecular arrangement [6–9]. The LLPT can end in a liquid-liquid critical point between a high-density liquid (HDL) and a low-density liquid (LDL). However, changes in the dynamics with an associated change in structural features can also be explained by a singularity-free scenario [10]. In the latter case, changes in both dynamics and structure from a HDL to a LDL also take place at the

point where the isobaric heat capacity C_P has a maximum, but no critical point or LLPT are observed at non-zero temperature.

An early work on trans-1,2-dichloroethylene ($T_{\mathrm{melt}} = 223$ K) suggested the existence of a LLPT at $T_t = 247\ K > T_{\mathrm{melt}}$ based on a small jump in density (less than 0.06%) as well as in the compressibility, and a clear discontinuity on the spin-lattice relaxation time T_1 [11, 12]. The observed changes in T_1 were tentatively related to a lack of freedom of the molecular rotation in the HDL, not present in the LDL. The change on the dynamics of this substance between both liquids, was thereafter also supported by discontinuities in the viscosity measurements and the slope of the rotational relaxation time [13], and by the absorbance, frequency and linewidth of several infrared vibrational spectroscopy bands [14]. Concerning structural related magnitudes, subsequent measurements of the density as a function of the temperature did not find a jump at the expected LLPT but only a change in its slope [13]. More recently, some of the authors of the present work have also undertaken calorimetric and nonlinear dielectric experiments [15]. In that work a strong pre-transitional anomaly of nonlinear dielectric effect was obtained, similar to the one observed in the isotropic phase of nematic liquid crystals, together with a maximum of C_P. Therefore, experimental results unambiguously show a clear change in the dynamics, together with a slight change in the structure, between HDL and LDL, that takes place when C_p is in a maximum. However, those facts are not enough to unambiguously determine if they are related to a singularity-free or a liquid-liquid critical point scenario [10], i. e., the liquid undergoes a first-order phase transition. The present study is aimed to investigate the microscopic structural and dynamical differences between the HDL and LDL, from the experimental point of view and from MD simulations, irrespective of which scenario would describe the present case.

Because the differences between the HDL and LDL in trans-1,2-dichloroethylene were related to a change from a nematic-like to an isotropic molecular ordering as temperature is raised [11, 12], we have performed a series of small angle neutron scattering (SANS) measurements from 220 K to room temperature to ascertain whether there is formation of intermediate range nematic-like structures or clustering

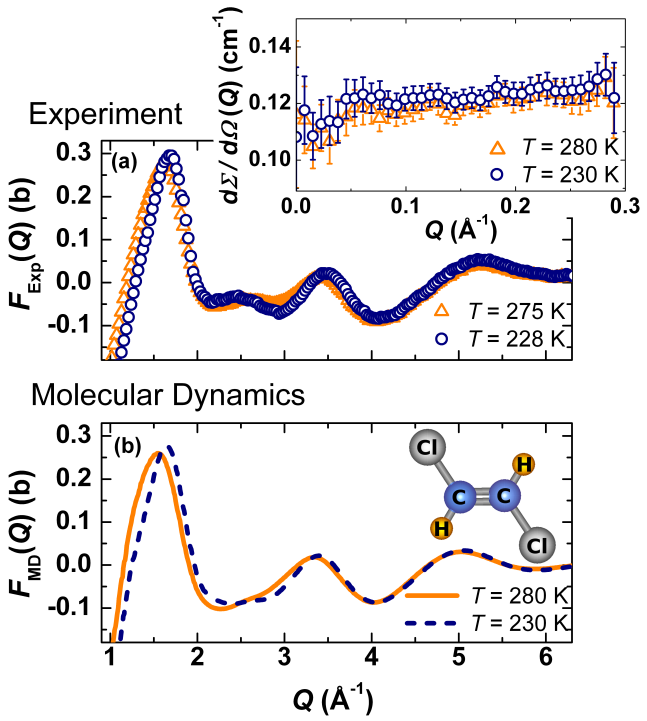

Figure 6.1: Total interference function of trans-1,2-dichloroethylene for the LDL and the HDL, obtained by neutron scattering experiments (a) and by molecular dynamics simulations (b), where an ab initio calculation of the molecular structure is also shown. Inset shows the macroscopic cross section for low Q values obtained by SANS experiments also for temperatures above and below T_t.

in the HDL. Experiments were performed on the KWS-2 diffractometer of the Jülich Centre for Neutron Science at the Forschungsneutronenquelle Heinz Maier-Leibnitz (FRM II, Munich, Germany) [16] using a wavelength of 4.5 Å and a sample-detector distance of 2.0 m that allowed to perform measurements in the Q range between 0.003 and 0.3 $Å^{-1}$. The program QTIKWS [17] was used to perform data correction and normalization. Results are shown in the inset of Fig. 6.1 for the HDL and LDL. No pronounced signal has been obtained within the experimental error in the measured Q-range, which disfavors the existence of a long range nematic-like ordering for the HDL [18]. The data exclude that the differences between both liquids are related to the emergence of molecular clustering on length scales of about 20–2000 Å.

Going down in the spatial range, the microscopic short range order (SRO) concerning a length scale of the order of a few molecular lengths ($l_{\mathrm{mol}} \approx 4$ Å) has been analysed by means of neutron scattering experiments on the D4c diffractometer at the Institute Laue-Langevin (ILL, Grenoble, France) [19] using a wavelength of 0.5 Å and a deuterated sample. Data were corrected and normalized using the program CORRECT [20] and inelastic corrections were also carried out (for details on data reduction see Ref. [21]). The obtained total interference function $F(Q)$ [22] is shown in Fig. 6.1 for two representative temperatures. A change in the shape of the profile emerges between the first and second peak which reflects a change in the SRO. This change was also observed in a series of temperature dependent experiments on the D20 diffractometer (ILL) using a wavelength of 1.3 Å, giving better access to the low-Q region. It should be pointed out that similar changes have been found in the case of experiments performed on HDL water at high pressures [23] and MD simulations on HDL silicon [24–27].

The microscopic mechanisms giving rise to the changes in the interference function $F(Q)$ have been investigated through a series of MD simulations (Fig. 6.1). Those were performed using the program AMBER8 [28, 29] with a simulation box containing 3629 molecules and a time step of 1 fs. The inter- and intra-molecular interactions for the trans-1,2-dichloroethylene molecule were described using the

GAFF force field [28, 29]. The simulations were carried out for the temperature range 200–350 K in the NPT ensemble, therefore allowing the box size to change, and the total time scale of each simulation run was 40–50 ns [30, 31]. As can be seen in Fig. 6.1, the agreement between simulations and experiment is excellent. Note that not only the shapes of the simulated $F(Q)$ closely resemble the experimental ones, but also positions and intensities are equal within the experimental error.

To emphasize quantitatively which are the SRO changes between the HDL and LDL, we show in Fig. 6.2 the probability of finding two molecules with a determined relative orientation for increasing distances. To present the distance dependent SRO, the molecular coordination number (MCN) has been chosen rather than distance in order to avoid trivial effects due to density changes. Figure 6.2 shows that the relative orientation of nearest neighbours is virtually the same and strongly defined for both liquids, in such a way that their C–C vectors are parallel, i.e., with $\cos\alpha = \pm 1$. However, upon increasing distance between the molecules (third to tenth neighbour), a clear difference between the LDL and HDL can be seen in the SRO. For instance, for MCN between eight and ten, more molecules are arranged in an orthogonal way for HDL and are randomly oriented for the LDL. Further analysis (not shown) tell us that besides the relative orientation of the C–C axes of two molecules, the reported changes are also reflected in the relative position of two molecules and in the relative orientation of the planes defined by the Cl–C–H bonds of two molecules. As proposed in the frame of two order parameter theories [6–10], this liquid can therefore not be simply characterized by its density, but also a parameter reflecting the SRO should account for the changes occurring between the two liquids.

To ascertain the influence of the aforementioned structural changes in the dynamics of the system, we have performed a series of quasielastic neutron scattering (QENS) experiments for temperatures ranging from 220 to 300 K, conducted with the TOFTOF spectrometer at FRM II on a hydrogenated sample. Spectra were measured using an energy resolution of 60 μeV and a wavelength of 6 Å, and data reduction was performed using the program FRIDA [32]. Two

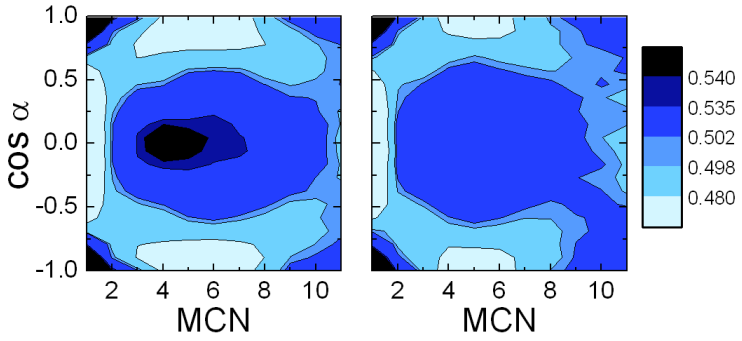

Figure 6.2: (color online). Short range order for the HDL (left) and the LDL (right), at 230 and 280 K respectively. The y-axis is the cosine of the angle α formed between the vectors defined by the C–C double bonds of two neighbour molecules and the x-axis is the number of molecules surrounding a central one. The z-axis represents the probability of finding two molecules at a distance determined by the MCN with a relative orientation defined by the α angle.

representative spectra at $Q = 0.3$ Å^{-1} at the LDL and HDL are shown in Fig. 6.3(a).

To have a first insight of possible changes in the dynamics, a stretched exponential $\exp(-t/\tau)^{\beta}$ was fitted to the intermediate scattering function, obtaining a decrease of the exponent β in the HDL, which is related to a broadening of the relaxation time distribution, i.e., an increase of the cooperativity of the molecular motion. A deeper analysis was performed through a careful fit of data to several models using a Bayesian approach with the program FABADA [33–35]. In order to keep the number of physical parameters describing the data to a minimum, we performed the fits to the whole scattering law $S(Q,\omega)$. Model selection was performed calculating the maximum of the likelihood $\mathcal{L}^{\max}$ for each model.

The first model used to describe the data is composed by a diffusion motion plus an isotropic rotation of the molecule [36]. In this way, the only physical parameters to describe the whole experimental scattering function were the translational and rotational diffusion

coefficients as well as the radius of rotation R. This simple model is able to describe LDL data giving rise to a good quality fit and a radius of rotation almost independent of temperature ($R \approx 1.72$ Å, see inset in Fig. 6.3(a)), in agreement with the aforementioned NMR measurements [11, 12]. For the HDL an inability of this model to describe experimental data (on quantitative grounds, a decrease on the $\mathcal{L}^{\max}$ of the fit), makes the isotropic model for rotation not valid to describe molecular rotation. This is also reflected on the sudden drop of R below T_t (inset in Fig. 6.3(a)). Even when assuming a free diffusion model for rotations [37] and assuming an anisotropic rotation of molecules [38, 39], models could not account for spectra obtained in the HDL. Only adding a confined motion to the previous model, data could be successfully described. For the latter model, $S(Q,\omega)$ can be expressed as:

$$\begin{aligned} S(Q,\omega) &= [A(Q)\delta(\omega) + (1 - A(Q)) \cdot L(\omega)] \\ &\otimes S_{\text{rot}}(Q,\omega) \otimes S_{\text{diff}}(Q,\omega) \otimes R(Q,\omega) \end{aligned}$$

where $A(Q)$ is the elastic incoherent structure factor of the confined motion, $L(\omega)$ is a Lorentzian function accounting for a confined motion, $S_{\text{rot}}(Q,\omega)$ is the component accounting for the molecular rotation, $S_{\text{diff}}(Q,\omega)$ the component for molecular diffusion [36], and $R(Q,w)$ is the instrumental resolution. Agreement with HDL spectra is shown in Fig. 6.3(a). To estimate the length scale at which the confined motion is taking place, $A(Q)$ values have been fitted with a model of diffusion inside a sphere, yielding $R = 1.91 \pm 0.07$ Å and, more realistically, a three-dimensional Brownian oscillator [40], yielding a mean squared displacement $\sqrt{\delta^2} = 2.12 \pm 0.07$ Å. Moreover, the obtained $A(Q)$ are almost independent of temperature for the HDL, which means that the length scale of the confined motion is roughly temperature independent for this liquid.

As previously performed for the microscopic structure investigation, the dynamics obtained from MD simulations have been analysed as well. The liquid-like behaviour of the mean square displacement guarantees that the simulation is within the liquid phase in all temperature range (see inset in Fig. 6.3(b)). Agreement between translational diffusion activation energy determined using the neutron ex-

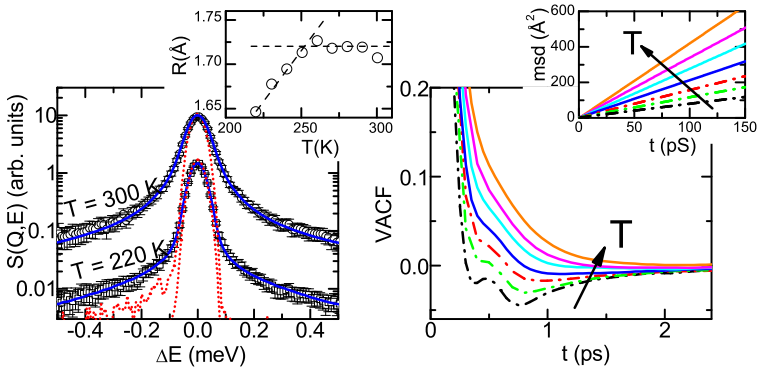

Figure 6.3: (color online). (a) Fits of QENS spectra for $Q = 0.3$ Å^{-1} at 300 K (shifted upwards) to a model considering diffusion and rotation motions, and to a model with an additional confined motion for 220 K (solid lines). Dotted lines show the experimental resolution. Inset shows radius of rotation in function of temperature for the model with only diffusion and rotation (dashed lines are a guide to the eye). (b) VACF obtained by MD simulations as a function of time, for temperatures from 200 to 320 K in steps of 20 K (solid lines for the LDL and dashed lines for the HDL). The inset shows the obtained mean square displacement from simulations (solid lines for the LDL and dashed lines for the HDL).

periments ($E_A = 76 \pm 1$ meV) and MD simulations ($E_A = 75 \pm 2$ meV) confirms that the simulation is indeed describing the dynamics of our system. The normalized velocity autocorrelation function (VACF) is shown in Fig. 6.3(b). The fastest decay for the HDL is higher than that of LDL indicating that interaction with neighbouring molecules appears before in that phase. As can be seen, there is a clear change in the dynamics of the two liquids, the VACF reaching negative values for HDL. Although interactions between neighbour molecules at the LDL seem not to impede molecular diffusion, for the HDL a well defined backscattering effect emerges, displaying a VACF with two

minima characteristic to that of hydrogen bonded systems [41]. Such a change in the dynamics is not expected to be due to temperature effects [42]. Additionally, a change of density of the system would not be able to explain this change in the dynamics since a change as large as about 15% in density is needed to produce an effect on the liquid dynamics in other systems [42]. Therefore, only a change in the SRO is able to account for the change in the dynamics seen by experiments and simulations.

The need for an additional confined motion at low temperatures to describe the QENS data goes along with a backscattering effect observed in the simulations. We can therefore assert that a cooperative molecular motion is present for the HDL but not for the LDL, which agrees with other experimental results [14]. The complex dynamics of the HDL agrees with a stronger molecular ordering present in this liquid, where on average there are many orthogonally oriented molecular pairs. This strong correlation is partially lost in the LDL, where molecular movements are due to non-coupled movements of diffusion and rotation.

We have shown that the microscopic ordering of molecules and molecular dynamics are different between the HDL and the LDL. The changes in the dynamics are not due to temperature or density effects, but due to changes in the SRO: for the HDL there are molecules perpendicularly oriented while for the LDL they are randomly oriented. This accounts for the change of molecular dynamics from simple non-cooperative motions in the LDL to cooperative motions for the HDL. However, if these effects are to be explained in the frame of a singularity-free scenario or a liquid-liquid critical point scenario associated to a first-order phase transition remains an open question.

Acknowledgments

The authors would like to thank C. A. Angell, G. Franzese, G. Sesé and T. Strässle for helpful discussions and X. Ariza for deuterating the sample. This work has been supported by the Spanish Ministry of Science and Technology (FIS2008-00837, BES-2007-17418), by the Government of Catalonia (2009SGR-1251) and by the Euro-

pean Commission (NMI3/FP7).

References

All online references accessed on July 22, 2014.

[1] Y. Akahama, W. Utsumi, S. Endo, T. Kikegawa, et al. *Phys. Lett.* **122**(2), 129 (1987).

[2] T. Kikegawa, H. Iwasaki, T. Fujimura, S. Endo, et al. *J. Appl. Crystallogr.* **20**(Part 5), 406 (1987).

[3] Y. Katayama, T. Mizutani, W. Utsumi, O. Shimomura, et al. *Nature* **403**(6766), 170 (2000).

[4] H. Tanaka, R. Kurita, and H. Mataki. *Phys. Rev. Lett.* **92**(2), 025701 (2004).

[5] R. Kurita and H. Tanaka. *J. Phys.: Condens. Matter* **17**(27), L293 (2005).

[6] H. Tanaka. *J. Chem. Phys.* **111**(7), 3163 (1999).

[7] H. Tanaka. *Phys. Rev. E* **62**(5, Part B), 6968 (2000).

[8] G. Franzese and H. E. Stanley. *J. Phys.: Condens. Matter* **19**(20) (2007).

[9] G. Deutscher, M. Rappaport, and Z. Ovadyahu. *Solid State Commun.* **28**(8), 593 (1978).

[10] P. Kumar, G. Franzese, and H. E. Stanley. *Phys. Rev. Lett.* **100**(10), 105701 (2008).

[11] S. Kawanishi, T. Sasuga, and M. Takehisa. *J. Phys. Soc. Jpn.* **50**(9), 3080 (1981).

[12] S. Kawanishi, T. Sasuga, and M. Takehisa. *J. Phys. Soc. Jpn.* **51**(5), 1579 (1982).

[13] B. Zegrodnik, A. Hacura, W. Carius, and O. Schröter. *Acta Phys. Pol.* **75**(4), 469 (1989).

[14] K. Merkel, A. Kocot, R. Wrzalik, and J. Ziolo. *J. Chem. Phys.* **129**(7), 074503 (2008).

[15] S. Rzoska, J. Ziolo, A. Drozd-Rzoska, J. L. Tamarit, et al. *J. Phys.: Condens. Matter* **20**(24), 244124 (2008).

[16] A. Radulescu and A. Loffe. *Nucl. Instrum. Methods A* **586**(1), 55 (2008).

[17] V. Pipich. *QtiKWS* (2009). URL http://iffwww.iff.kfa-juelich.de/~pipich/.

[18] R. M. Richardson. In D. Demus, J. W. Goodby, G. W. Gray, H. W. Spiess, et al., editors, *Handbook of liquid crystals*, chapter 4. Wiley-VCH (1998).

[19] H. E. Fischer, G. J. Cuello, P. Palleau, D. Feltin, et al. *Appl. Phys. A: Mater. Sci. Process.* **74**(Part 1 Suppl. S), S160 (2002).

[20] M. Howe, R. McGreevy, and P. Zetterström. *Computer code CORRECT, correction program for neutron diffraction data* (1996). NFL Studsvik internal report.

[21] L. C. Pardo, J. L. Tamarit, N. Veglio, F. J. Bermejo, et al. *Phys. Rev. B* **76**(13) (2007).

[22] H. E. Fischer, A. C. Barnes, and P. S. Salmon. *Rep. Prog. Phys.* **69**(1), 233 (2006).

[23] T. Strässle, A. Saitta, Y. Le Godec, G. Hamel, et al. *Phys. Rev. Lett.* **96**(6), 067801 (2006).

[24] S. Sastry and C. A. Angell. *Nature Mater.* **2**(11), 739 (2003).

[25] N. Jakse and A. Pasturel. *J. Chem. Phys.* **129**(10), 104503 (2008).

[26] S. N. Yannopoulos. *J. Chem. Phys.* **130**(24), 247102 (2009).

[27] N. Jakse, A. Pasturel, S. Sastry, and C. A. Angell. *J. Chem. Phys.* **130**(24), 247103 (2009).

[28] J. Wang, R. Wolf, J. Caldwell, P. Kollman, et al. *J. Comput. Chem.* **25**(9), 1157 (2004).

[29] D. A. Case, T. E. Cheatham, III, C. L. Simmerling, J. Wang, et al. *AMBER 8*. University of California, San Francisco (2004).

[30] N. A. Murugan and H. W. Hugosson. *J. Phys. Chem. B* **113**(4), 1012 (2009).

[31] N. A. Murugan and H. W. Hugosson. *Phys. Chem. Chem. Phys.* **10**(40), 6135 (2008).

[32] J. Wuttke. *FRIDA: Fast Reliable Interactive Data Analysis* (1990). URL http://sourceforge.net/projects/frida/.

[33] D. Sivia and J. Skilling. *Data Analysis: A Bayesian Tutorial*. Oxford University Press (2006).

[34] L. C. Pardo, M. Rovira-Esteva, S. Busch, M. D. Ruiz-Martín, et al. (2009). arXiv:0907.3711v3[physics.data-an].

[35] L. C. Pardo. *FABADA (Fitting Algortihm for Bayesian Analysis of DAta)* (2009). URL http://fisicaetseib.upc.es/gcm/members/lcpardo/software.

[36] M. Bée. *Quasielastic Neutron Scattering*. Adam Hilger, Bristol (1988).

[37] P. A. Egelstaff. *J. Chem. Phys.* **53**(7), 2590 (1970).

[38] G. Hinze, G. Diezemann, and T. Basche. *Phys. Rev. Lett.* **93**(20), 203001 (2004).

[39] F. J. Bermejo, F. Batallán, E. Enciso, R. White, et al. *J. Phys.: Condens. Matter* **2**(5), 1301 (1990).

[40] W. Doster. In J. Fitter, T. Gutberlet, and J. Katsaras, editors, *Neutron Scattering in Biology, Methods and Applications*, pages 461–483. Springer Verlag (2006).

[41] E. Guàrdia, G. Sesé, and J. A. Padró. *J. Mol. Liq.* **62**, 1 (1994).

[42] Y. Hirata. *J. Phys. Chem. A* **106**(10), 2187 (2002).

TOPIC 2: Differences in first neighbor orientation behind the anomalies in the low and high density trans-1,2-dichloroethene liquid

M. Rovira-Esteva,[1] A. Murugan,[2] L. C. Pardo,[1] S. Busch,[3] J. Ll. Tamarit,[1] G. J. Cuello,[4,5] and F. J. Bermejo,[4,6]

[1]Grup de Caracterització de Materials, Departament de Física i Enginyeria Nuclear, ETSEIB, Universitat Politècnica de Catalunya, Diagonal 647, E-08028 Barcelona, Catalonia, Spain

[2]Division of Theoretical Chemistry and Biology, School of Biotechnology, Royal Institute of Technology, S-106 91 Stockholm, Sweden

[3]Physik Department E13 and Forschungs-Neutronenquelle Heinz Maier-Leibnitz (FRM II), Technische Universität München, Lichtenbergstr. 1, D-85748 Garching, Germany

[4]Facultad de Ciencia y Tecnología, Universidad del País Vasco / EHU, P. Box 644, E-48080 Bilbao, Spain

[5]Institut Laue Langevin, 6 Rue Jules Horowitz, BP. 156, F-38042 Grenoble Cedex 9, France

[6]Instituto de Estructura de la Materia, CSIC, Serrano 123, E-28006 Madrid, Community of Madrid, Spain

Published: **The Journal of Chemical Physics 136, 124514 (March 2012).**

DOI: http://dx.doi.org/10.1063/1.3697849

Abstract

Trans-1,2-dichloroethene (HClC=CClH) has several structural and dynamic anomalies between its low and high-density liquid, previously found through neutron scattering experiments. To explain the

microscopic origin of the differences found in those experiments, a series of molecular dynamics simulations were performed. The analysis of molecular short-range order shows that the number of molecules in the first neighbour shell is 12 for the high density liquid and 11 for the low density one. It also shows that the angular position of the centre of mass of the first neighbour is roughly the same although the molecular orientation is not. In both liquids the first neighbour and its reference molecule arrange mainly in two configurations, each being the most probable in one of the liquids. First neighbours in the configuration that predominates in the high density liquid tend to locate themselves closer to the reference molecule, an evidence that they are more strongly bonded. This arrangement facilitates a better packing of the rest of molecules in the first neighbour shell so that on average an additional molecule can be included, and is proposed to be the key in the explanation of all the observed anomalies in the characteristics of both liquids.

Introduction

Description of short-range order in molecular liquids poses a highly challenging conundrum. The need to determine not only the correlation between the molecular centres of mass but also the relative molecular orientations to provide a complete picture of the structure of the liquid makes that, even when considering reasonably simple molecules, the number of degrees of freedom quickly increases with respect to mono- or polyatomic liquids. These orientational correlations are usually strongly dependent on the distance for the closest neighbours but have no correlation for the farther ones.

The molecular arrangement has in turn a vast impingement on the dynamics of a system [1, 2]. Thus, a detailed and careful analysis of molecular short-range order is essential to the proper understanding of any system. Several different approaches are used to study molecular short-range order, such as Reverse Monte Carlo [3, 4], Empirical Potential Structure Refinement [5, 6], and Molecular Dynamic simulations [7, 8].

Trans-1,2-dichloroethene (HClC=CClH, in the following TDCE)

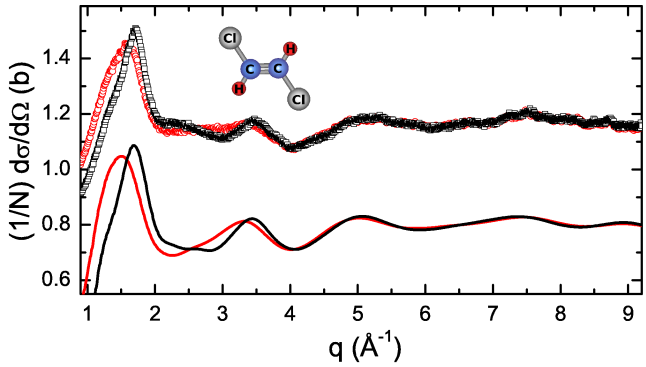

Figure 6.4: Differential cross section per atom obtained at the D20 diffractometer (points, with a translation of +0.4 b) and from molecular dynamics (lines) for the low (red) and high (black) density liquid. The inset shows an ab initio calculation of the molecular structure of TDCE in the gas phase. Close reproduction of the features in the experimental differential cross section per atom validates the results obtained from analysis of the simulation.

is a molecular liquid which manifests several anomalies in the behaviour of its high density liquid when compared with its low density liquid. The molecular geometry of TDCE obtained from an ab initio calculation in the gas phase can be seen in the inset of Fig. 6.4, where calculated intramolecular angles and distances are shown. First claims of an anomalous behaviour in liquid TDCE between 243 and 257 K were made based on a small density singularity, and a local minimum of the spin-lattice relaxation time (T_1) measured by NMR, as well as a T_1 discontinuity, which was assigned to the appearance of a nematic-like molecular ordering where the molecules have no rotational freedom [9, 10]. A later measurement found a change in the slope of the density but no discontinuity, although the study did find a discontinuity in some dynamic magnitudes as viscosity or as the slope of the rotational relaxation time measured by Raman spectroscopy.

It was therefore concluded that dynamic planar structures were likely to form [11]. An infrared vibrational spectroscopy study also

accounted for a clear discontinuity in several bands, attributed to the existence of a weak Cl-H hydrogen bond which induces the formation of dimers with a dipolar moment giving rise to local ordering [12]. These locally favoured structures increase the molecular cooperativity, and thus their reduced mass, slowing down the molecular motion. Kawanishi et al. had even suggested the existence of a liquid-liquid transition [9, 10], but a recent optical Kerr-effect experiment reported that, although it is not a simple liquid, there is no sign of a first order transition in TDCE .[13].

Some of the authors of the present work reported calorimetric and nonlinear dielectric results (a maximum on c_{p} and a strong pretransitional anomaly, respectively), and suggested that multimolecular heterogeneities (fluctuations with dielectric permittivity slightly different from the "isotropic" surrounding) appear in the high density TDCE liquid [14].

Structure and dynamics of TDCE molecules in the high and low density liquids have been approached through neutron scattering measurements and molecular dynamics simulations in a previous work [15]. There, diffraction experiments yielded structural changes in the molecular short-range order domain, although no molecular clustering was observed. Experiments on the dynamics showed that the low density liquid could be well described through a diffusion motion plus an isotropic rotation, whereas in the high density liquid a confined motion due to cooperative molecular behaviour had to be added. Analysis of molecular dynamics simulations showed that molecules are much more ordered in the high density liquid, and revealed the appearance of two minima in its velocity autocorrelation function, which is characteristic of a backscattering effect. Since the density increase is too small to account for such backscattering effect, this result supports that the confined motion found in the high density liquid can only be accounted for through a change in the short-range order.

Although it was rather clear that the dynamic anomalies found between the high and low TDCE density liquids come down to a change in the molecular arrangement, the precise nature of this structural difference was not analysed. The aim of the present study is to

focus on the microscopic structure and elucidate the details behind these anomalies in the high and low density TDCE liquids. Neutron diffraction experiments of liquid TDCE performed in both density domains, together with molecular dynamics simulations closely reproducing the experiments, has allowed a thorough statistical analysis of the simulation configurations, unraveling the structural differences in the molecular short-range order of the liquid at both densities.

Experiment and simulation details

Neutron diffraction experiments on the short-range order of the low and high density TDCE liquid were carried out with consistent results at the diffractometer dedicated to glasses and liquids D4c [16] and at the high-intensity two-axis diffractometer D20 [17], both at the Institute Laue-Langevin (ILL, Grenoble, France). A 99.70% purity sample was purchased from Acros Organics (Geel, Belgium) and deuterated to 99% for both experiments.

Details of the measurement performed at the D4c diffractometer and the obtained results have been published elsewhere (see Ref. [15]). At D20, an incident neutron wavelength of $\lambda = 1.30$ Å was used together with a radially oscillating collimator. In order to correct and normalize the data, an empty sample holder and a vanadium rod were also measured. Absorption and multiple scattering corrections and the normalization of the data were performed using the program CORRECT [18].

A series of molecular dynamics simulations of the low and high density TDCE liquid were performed using the program AMBER8 [19, 20] with a simulation box containing 3629 molecules and a time step of 1 fs for the integration of the equations of motion. The inter- and intramolecular interactions for the TDCE molecule were described using the GAFF force field [19, 20]. The simulations were carried out for the temperature range 200–350 K in the NPT ensemble, therefore allowing the box size to change, and the total time of each simulation run was 40–50 ns [21, 22]. This simulation is the same that was used in Ref. [15] for the preliminary analysis of the short-range order in liquid TDCE.

The differential cross sections per atom obtained from the simulations for the low and high density liquids are shown in Fig. 6.4 together with the experimental ones, so they can be compared. The structural differences between the low and high density liquids in the short-range order domain, already established in a previous work [15], can be observed. As can also be seen in this figure, agreement of the simulation with the experimental data is extremely good and absolute intensities are the same within the error. This close agreement provides a solid ground for a detailed analysis of the simulation in search of a microscopic explanation.

Angle definitions

To study the short-range order of molecules in the low and high density TDCE liquids, two kinds of degrees of freedom have been analysed separately: those regarding the relative positions of the molecules and those regarding their relative orientations.

All the angles used in the analysis of the relative positions and orientations of the molecules obtained from the simulation have been depicted in Fig. 6.5.

The angles describing the relative position of the centre of mass of a molecule with respect to the reference molecule, θ_{CM} and φ_{CM}, can be seen in Fig. 6.5(a). θ_{CM} is the angle between the axis defined by the chlorine atoms of the reference molecule and the vector that goes through the centres of mass of both molecules. φ_{CM} is the angle between the plane that contains the whole reference molecule and the plane that contains the chlorine-chlorine axis of the reference molecule and the centre of mass of the other molecule. θ_{CM} and φ_{CM} will be referred to as angular position of the centres of mass to stress the fact that the relative distance between the molecular centres of mass is already fixed when the neighbours are analysed individually.

The angles α, β, and γ describing the relative orientation between both molecules have been depicted in Figs. 6.5(b), (c), and (d), respectively. α is the angle between the axes defined by the hydrogen atoms of each molecule, β is the angle between the axes defined by the chlorine atoms of each molecule, and γ is the angle between the

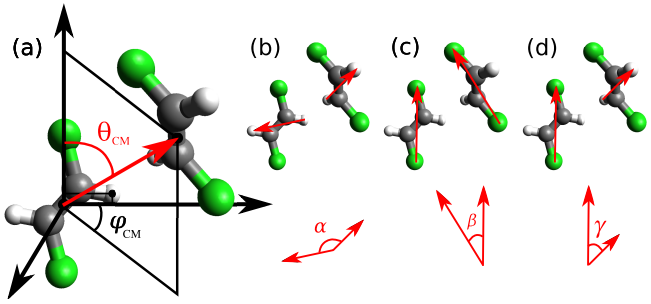

Figure 6.5: (a) Angles θ_{CM} and φ_{CM} describing the position of the centre of mass of one molecule with respect to the centre of mass of the reference molecule. (b) Angle α between the axes formed by the hydrogen atoms of both molecules. (c) Angle β between the axes formed by the chlorine atoms of both molecules. (d) Angle γ between the axes formed by the hydrogen atoms of a molecule and the chlorine atoms of the reference molecule.

axis defined by the chlorine atoms of the reference molecule and the axis defined by the hydrogen atoms of the other molecule.

Note that, strictly due to geometrical considerations, an isotropic distribution of molecules around the reference molecule will yield a higher probability of angle θ_{CM} being perpendicular rather than parallel. The same happens with angles α, β, and γ, although it does not happen with φ_{CM}. To prevent misleading figures arising from this fact, probability distributions have been plotted as a function of the angle or the cosine of the angle to ensure they will appear as flat functions for isotropic distributions.

Results and Discussion

A first step for the analysis of the relative positions of the molecules in a liquid is to find out how many molecules can be found within the first neighbour shell. Figure 6.6 shows the pair-correlation function of the centres of mass of the TDCE molecules calculated from the simulations for the low and high density liquid, which is proportional to the probability of finding a molecule at a certain distance of a

reference molecule. The first neighbour shell is defined as the molecules comprised within the first peak of the pair-correlation function. Figure 6.6 also shows the molecular coordination number for the two liquids, calculated from the integration of the pair-correlation function. Usually, since density decreases as temperature increases within the same phase, the g_{CM} minimum that defines the first neighbour shell moves to higher values of r because the mean distance between the molecules is also increased. However, since the growth of the molecular coordination number with respect to the distance is also slower due to a lower density, the corresponding number of molecules in the first neighbour shell ends up being the same. In the present case, contrary to what would be commonly expected, a different number of molecules was found within the first neighbour shell for each liquid, 12 molecules in the case of the high density liquid compared with only 11 in the case of the low density one, an indication that the liquid is undergoing a change in the molecular short-range order and not only a density variation.

Another representation that can provide further insight into the difference between the first neighbour shells of the two liquids, because it takes into account the volume change of the spherical shell as the distance increases, is the density within the first neighbour shell as a function of the molecular coordination number (see Fig. 6.7). Using the molecular coordination number instead of r as abscissa removes the expansion effects of increasing the temperature. In the high density TDCE liquid the density increases up to the fifth neighbour and then starts to decrease, while in the case of the low density TDCE liquid the same behaviour is observed at the fourth neighbour. This is a good indication that the structural differences between both liquids are originating at the very first molecules.

A detailed analysis of the angular position of the centres of mass and relative orientation with respect to the reference molecule was performed for all molecules in the first neighbour shell. A strong agreement was found with the observation that there is a gap of one molecule in the structure patterns followed by both liquids, i.e., except for the first neighbour, the position and orientation of neighbour molecules in both liquids is qualitatively the same if every molecule

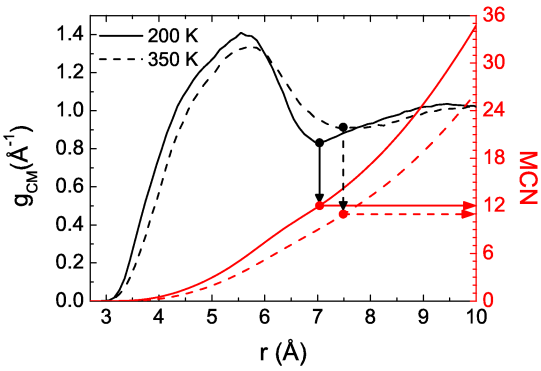

Figure 6.6: Pair-correlation function of the centres of mass of the molecules (g_{CM}, black lines, scale on the left) and molecular coordination number (MCN, red lines, scale on the right) for the low and high density liquids (dashed and continuous lines, respectively) calculated from the simulation. The first neighbours shell contains 11 molecules in the case of the low density liquid and 12 in the case of the high density liquid.

in the low density liquid is compared to the next molecule in the high density liquid instead of comparing the same molecule in both liquids. The interested reader can turn to the supplementary material available online for more details on this result [23].

Because the changes happen on the very first neighbours and the orientational correlations in molecular liquids are lost as distance increases, in this work we have focused on the analysis of just the single first neighbour, to which the following molecules will have to accommodate [24]. Figure 6.8 shows the angular position (θ_{CM} and φ_{CM}) of the centre of mass of the first neighbour with respect to the reference molecule (for more details and examples on bivariate analysis see Refs. [25–28]), where no qualitative difference has been observed between both liquids, since their first neighbour is equally located around $\theta_{\mathrm{CM}} \approx 90°$ and $\varphi_{\mathrm{CM}} \approx 90°$. Figure 6.9 shows two examples of molecular pairs in such angular position. Although the high density liquid is much more structured, it was a feature already expected due

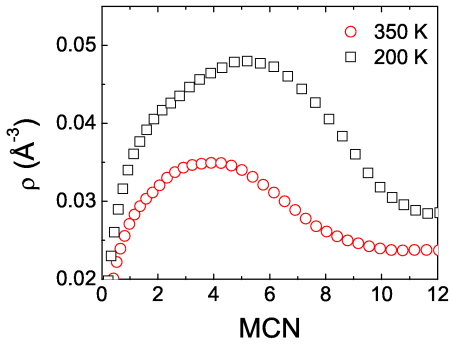

Figure 6.7: Density within the first neighbour shell for the high and low density TDCE liquids (black squares and red circles, respectively) as a function of the molecular coordination number. A maximum is observed at the fifth and fourth neighbour for the high and low density TDCE liquids, respectively, which shows that there is a gap of one molecule in the structure patterns between both liquids and that the difference originates in the closest neighbours.

to the smaller effects of thermal agitation, and cannot be viewed as a meaningful difference in the structure.

Concerning the analysis of the relative orientation of the first neighbour with respect to the reference molecule, the probability distribution of the angle α (angle between the hydrogen axes of both molecules) of the first neighbour is shown in Fig. 6.10 for both liquids, where a discrepancy in the shape of the high and low density liquid distributions evidences an orientational contribution of the first neighbour to the differences in the molecular short-range order. No qualitative differences were observed when the same analyses were performed for the orientational angles β and γ.

Although the observed angular position of the centre of mass of the first neighbour with respect to the reference molecule between both densities is almost the same, the relative orientation between the molecules is conspicuously divergent, pointing out that this is where the key for the explanation must be sought.

Figure 6.10 shows that there is a discrepancy in the molecular

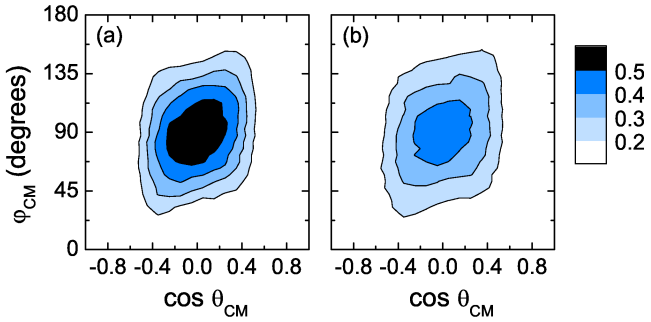

Figure 6.8: Probability of the angular position (θ_{CM} and φ_{CM}) of the centre of mass of the first neighbour for the (a) high and (b) low density liquid (darker shade means higher probability). As expected, the high density liquid is more structured, but there are no qualitative differences in the angular position of the first neighbour between both liquids (around $\theta_{\mathrm{CM}} \approx 90°$ and $\varphi_{\mathrm{CM}} \approx 90°$).

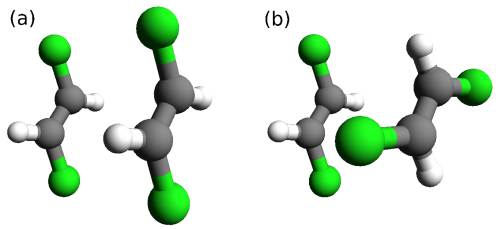

Figure 6.9: Scheme of the two most likely configurations of the first neighbour and the reference molecule: (a) parallel or P, and (b) crossed or C. To illustrate the P configuration a molecular arrangement with $\alpha = 0°$, $\beta = 0°$, and $\gamma = 76.9°$ has been chosen, while in the case of the C configuration it has been chosen with $\alpha = 76.9°$, $\beta = 76.9°$, and $\gamma = 0°$. Both examples have the same relative angular position ($\theta_{\mathrm{CM}} = 90°$ and $\varphi_{\mathrm{CM}} = 90°$).

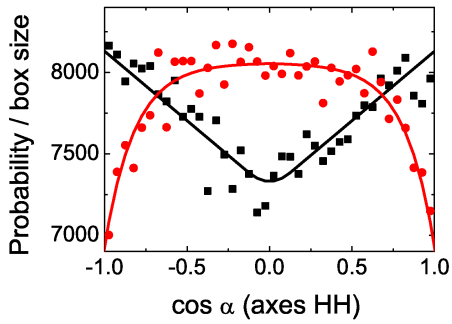

Figure 6.10: Probability of the cosine of angle α of the first neighbour for the low and high density liquid (red dots and black squares, respectively). Lines are a guide to the eye. There is a difference in the relative orientation of the first neighbour with respect to the reference molecule between both liquids.

orientation of the two liquids but it does not explain the origin of the density anomaly [10, 11]. Thus, a detailed analysis of the molecular orientations must be undertaken to understand the reasons behind the different molecular arrangements.

To learn which are the preferred relative orientations of the first neighbour and the reference molecule, a mapping of the configuration space is depicted in Fig. 6.11. This figure shows the probability distribution of the orientation between the first neighbour and the reference molecule (angles β and γ) for the high and low density TDCE liquids. As expected in a highly disordered system, there is a continuum of possible configurations, although not all of them are equally probable. The configuration space has been divided into 16 regions of possible configurations, corresponding to the grid drawn in this figure. In both liquids, the same four regions (labelled P and C in Fig. 6.11) have a higher probability than the rest but, for molecular symmetry reasons, they account only for two possible configurations of the reference molecule and its first neighbour. The definition of each configuration includes all the molecular arrangements between the first neighbour and the reference molecule that contribute to the two equivalent regions in Fig. 6.11. The combinations of ranges of

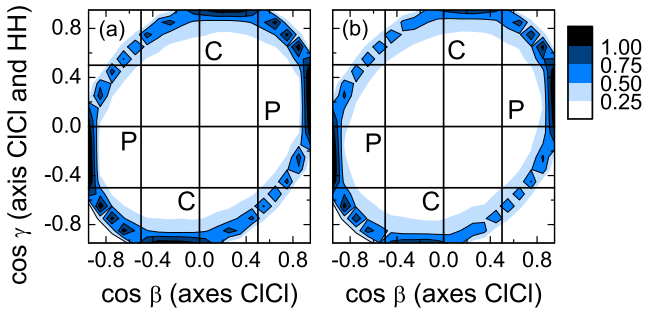

Figure 6.11: Probability of combinations of β and γ cosines of the first neighbour for the high (a) and low (b) density liquids (darker shade means higher probability). The continuum of configurations between the first neighbour and the reference molecule have been grouped into 16 regions of possible configurations (grid), from which those labelled P and C are the most likely at both temperatures.

Table 6.1: Range of values used to define which molecular pairs are in P or C configuration.

Configuration	$\cos\beta$	$\cos\gamma$
P	0.5 to 1.0	0.0 to 0.5
P	-1.0 to -0.5	-0.5 to 0.0
C	0.0 to 0.5	0.5 to 1.0
C	-0.5 to 0.0	-1.0 to -0.5

$\cos\beta$ and $\cos\gamma$ values that define the regions of P and C configurations are shown in Table 6.1.

In Fig. 6.9 representative arrangements of molecular pairs in the P and C configurations have been depicted to provide a scheme of the relative orientation between the first neighbour and the reference molecule. As can be seen in this figure, molecular pairs with parallel chlorine axes and parallel hydrogen axes are denoted as P configuration (Fig. 6.9(a)), while molecules with their chlorine axis parallel to the hydrogen axis of the reference molecule and vice versa (crossed

Table 6.2: Ratios of first neighbour molecules in P and C configurations with respect to the total number of first neighbour molecules. Δ represents the increment of the fraction of molecules in that configuration with respect to the total number of molecules, as the temperature is decreased from 350 to 200 K.

Configuration	350 K	200 K	Δ
P	0.19002	0.17494	-1.5%
C	0.17648	0.19880	$+2.2\%$

molecules), are denoted as C configuration (Fig. 6.9(b)).

Although qualitatively Figs. 6.11(a) and (b) appear to be very similar, a quantitative analysis shows that for the low density liquid, configuration P represents a higher fraction of first neighbours than configuration C. This situation is reversed in the high density liquid (see Table 6.2). Hence, as the temperature is changed, there is an inversion of the dominant population in the liquid.

Could this difference of population in the configurations of the first neighbour between the low and high density liquid be the underlying cause of the observed anomalies between both densities? To ascertain whether having the first neighbour in different configurations can explain the observed short-range order discrepancies of liquid TDCE (and its dynamic properties), a separate analysis has been performed to each configuration to compare their particularities.

As it has been previously explained, Fig. 6.8 shows the most probable relative position of the molecular centres of mass when the first neighbours in any of the configurations are taken into account. To obtain more detailed information from this magnitude, in Fig. 6.12 the probability density functions of the same angles (θ_{CM} and φ_{CM}) have been evaluated but only for first neighbours in configurations P and C, making a distinction between both configurations. From Fig. 6.12 it is inferred that first neighbours in P and C configuration tend to locate themselves roughly around $\theta_{\mathrm{CM}} \approx 90^\circ$ and $\varphi_{\mathrm{CM}} \approx 90^\circ$ regardless of their configuration (the same position seen in the analysis of

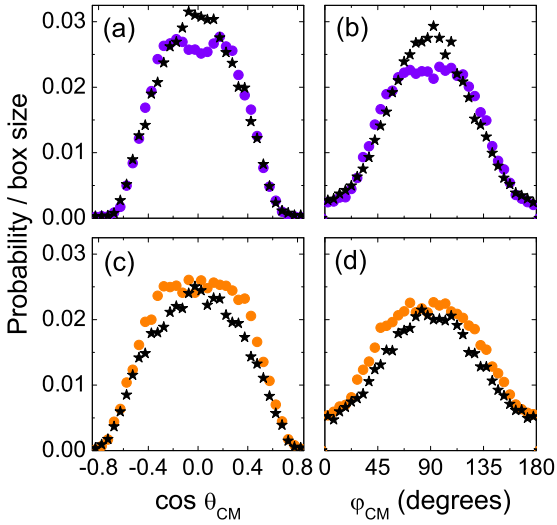

Figure 6.12: Contribution of configurations P (circles) and C (stars) to the probability of the centre of mass position of the first neighbour molecule with respect to the reference molecule. (a) and (b) show the cosine of θ_{CM} and φ_{CM}, respectively, for the high density liquid. And (c) and (d) show the cosine of θ_{CM} and φ_{CM}, respectively, for the low density liquid. The centre of mass of the molecules in the C configuration tends to be exactly in front of the reference molecule (θ_{CM} and $\varphi_{\mathrm{CM}} = 90°$) while the centre of mass of the molecules in the P configuration tends to be slightly on a side or is evenly distributed on a higher range of angles around this value. For the high density liquid, the total contribution of the C configuration (area in this graph) is greater than the contribution from the P configuration. This situation is reversed in the low density liquid.

all first neighbours in Fig. 6.8). Further analyses of the remaining configurations showed that this is the preferred arrangement of all first neighbours and not only of those in configurations P and C.

Nevertheless, the angular position distributions of the first neighbours are not completely equivalent for both configurations. In the high density liquid (Figs. 6.12(a) and (b)), where the difference be-

tween configurations is more easily observed, θ_{CM} and φ_{CM} distributions for the C configuration peak clearly at 90° while the P configuration displays a double peak for the θ_{CM} and a flat top for the φ_{CM} distribution that spans to a wider range of values. This means that molecular pairs in C configuration sit comfortably in front of each other while molecules in configuration P prefer to be slightly displaced from that central position.

Probability distribution functions in Fig. 6.12 have been normalized to the total number of molecules so that their area is directly proportional to the number of molecules in that configuration, to make the contribution to the total probability of each configuration clear. Consequently, in this figure it is easier than in Fig. 6.11 to appreciate, from the area of the distributions, that in the high density liquid the contribution of C configuration is higher than the P configuration, and that in the low density liquid it is lower.

In addition to the difference in angular position between molecules in configurations C and P, the distance between first neighbours in one or the other configuration also varies significantly. Figure 6.13 shows the contribution to the probability that a first neighbour is at a certain distance from a reference molecule for each of the configurations for the high and low density liquids. As can be seen in this figure, the centres of mass of molecules in the C configuration are on average closer than in the P configuration, showing that molecules in C configuration are more tightly bonded than those in P configuration.

Abundance of a configuration with a stronger bond between molecules means that on average they are closer to each other, and a more ordered arrangement of the molecules makes it even easier to pack them tighter and to fit in the first neighbour shell the additional molecule that we have observed in the high density liquid.

The fact that there is a favoured local structure is in agreement with the previous works [9–12, 15].

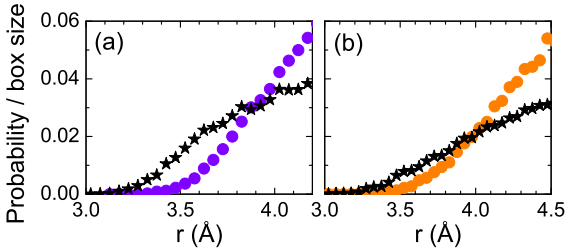

Figure 6.13: Contribution of configurations P (circles) and C (stars) to the probability of the centre of mass distance of the first neighbour molecule with respect to the reference molecule for the (a) high and (b) low density liquid. Irrespective of temperature, the centres of mass of molecules in the C configuration are on average closer to the reference molecule than in the P configuration.

Conclusions

We have unravelled the structural causes behind the density and spin-relaxation time singularities, and the viscosity and slope of the rotational relaxation time discontinuities in the TDCE liquid by means of a detailed analysis of the molecular short-range order.

Except for the first neighbour, the position and orientation of neighbour molecules in both liquids has been found to be qualitatively the same if an offset of one molecule is taken into account. The first neighbour shell in the low density TDCE liquid contains 11 molecules. An additional molecule is contained in the first neighbour shell of the high density liquid, adding up to 12 molecules. According to the density distribution analysis, the difference in the molecular arrangement must originate in the closest four to five molecules of the first neighbour shell.

The angular position of the centre of mass of the first neighbour is almost identical for both liquids, molecules gather around $\theta_{\mathrm{CM}} \approx 90°$ and $\varphi_{\mathrm{CM}} \approx 90°$. But a strong difference is observed in the distribution of α, the angle between the hydrogen axes, regarding the relative orientation of the molecular pairs.

Further analysis of the relative molecular orientation of the first

neighbour and the reference molecule reveals that two of the configurations that have been defined are more probable than the rest (parallel, P, and crossed, C). While the P configuration prevails in the low density liquid, the C configuration prevails in the high density one. There is an inversion of the configuration populations when the low density TDCE liquid turns into the high density one and vice versa.

The first neighbours in C configuration have a tendency to locate themselves closer to the reference molecule and exactly at the angular position $\theta_{\mathrm{CM}} = 90^\circ$ and $\varphi_{\mathrm{CM}} = 90^\circ$ displaying strong bonding. In contrast, the first neighbours in P configuration tend to be further apart and with their centres of mass slightly displaced from that angular position.

Hydrogen bonding between the chlorine atoms of one molecule and the hydrogen atoms of the other explains why molecular pairs in C configuration can bond more tightly than those in P configuration.

A larger proportion of first neighbours in C configuration, that can sit exactly in front of the reference molecule in an orderly manner and much closer, facilitates a better packing, so that an additional molecule fits in the first coordination shell of the high density TDCE liquid, as it has been observed. This can also explain the density anomaly between the high and low density TDCE liquids.

More structured molecular pairs given by a stronger bonding of the first neighbours in C configuration is likely to be also the key to the explanation of the dynamical anomalies reported in previous studies [9–12, 15].

Acknowledgements

The authors would like to thank X. Ariza for the deuteration of the sample. This work was supported by the Spanish Ministry of Science and Innovation (FIS2008-00837) and by the Government of Catalonia (2009SGR-1251).

References

All online references accessed on July 22, 2014.

[1] C. Talón, M. A. Ramos, S. Vieira, G. J. Cuello, et al. *Phys. Rev. B* **58**(2), 745 (1998).

[2] P. S. Salmon, R. A. Martin, P. E. Mason, and G. J. Cuello. *Nature* **435**(7038), 75 (2005).

[3] O. Gereben, P. Jovari, L. Temleitner, and L. Pusztai. *J. Optoelectron. Adv. Mater.* **9**(10), 3021 (2007). 3rd International conference on Amorphous and Nanostructured Chalcogenides, Brasov, Romania, Jul 02-06, 2007.

[4] S. Pothoczki, L. Temleitner, and L. Pusztai. *J. Chem. Phys.* **134**(4), 044521 (2011).

[5] A. K. Soper. *Chem. Phys.* **202**(2-3), 295 (1996).

[6] A. K. Soper. *Chem. Phys.* **258**(2-3), 121 (2000).

[7] M. P. Allen and D. J. Tildesley. *Computer simulation of liquids*. Clarendon Press, New York, NY, USA (1989).

[8] M. Haughney, M. Ferrario, and I. R. McDonald. *J. Phys. Chem.* **91**(19), 4934 (1987).

[9] S. Kawanishi, T. Sasuga, and M. Takehisa. *J. Phys. Soc. Jpn.* **50**(9), 3080 (1981).

[10] S. Kawanishi, T. Sasuga, and M. Takehisa. *J. Phys. Soc. Jpn.* **51**(5), 1579 (1982).

[11] B. Zegrodnik, A. Hacura, W. Carius, and O. Schröter. *Acta Phys. Pol.* **75**(4), 469 (1989).

[12] K. Merkel, A. Kocot, R. Wrzalik, and J. Ziolo. *J. Chem. Phys.* **129**(7), 074503 (2008).

[13] D. A. Turton, D. F. Martin, and K. Wynne. *Phys. Chem. Chem. Phys.* **12**(16), 4191 (2010).

[14] S. Rzoska, J. Ziolo, A. Drozd-Rzoska, J. Ll. Tamarit, et al. *J. Phys.: Condens. Matter* **20**(24), 244124 (2008). European-

Science-Foundation Exploratory Workshop on Glassy Liquids Under Pressure, Ustron, Poland, Oct 10-12, 2007.

[15] M. Rovira-Esteva, A. Murugan, L. C. Pardo, S. Busch, et al. *Phys. Rev. B* **81**(9), 092202 (2010).

[16] H. E. Fischer, G. J. Cuello, P. Palleau, D. Feltin, et al. *Appl. Phys. A: Mater. Sci. Process.* **74**(Part 1 Suppl. S), S160 (2002). International Conference on Neutron Scattering, Munich, Germany, Sep 09-13, 2001.

[17] T. C. Hansen, P. F. Henry, H. E. Fischer, J. Torregrossa, et al. *Meas. Sci. Technol.* **19**(3), 034001 (2008).

[18] M. Howe, R. McGreevy, and P. Zetterström. *Computer code CORRECT, correction program for neutron diffraction data* (1996). NFL Studsvik internal report.

[19] J. Wang, R. Wolf, J. Caldwell, P. Kollman, et al. *J. Comput. Chem.* **25**(9), 1157 (2004).

[20] D. A. Case, T. E. Cheatham, III, C. L. Simmerling, J. Wang, et al. *AMBER 8*. University of California, San Francisco (2004).

[21] N. A. Murugan and H. W. Hugosson. *J. Phys. Chem. B* **113**(4), 1012 (2009).

[22] N. A. Murugan and H. W. Hugosson. *Phys. Chem. Chem. Phys.* **10**(40), 6135 (2008).

[23] See supplementary material at [URL will be inserted by AIP] for full details on the observation that there is a gap of one molecule in the structure patterns followed by both liquids.

[24] L. C. Pardo, J. Ll. Tamarit, N. Veglio, F. J. Bermejo, et al. *Phys. Rev. B* **76**(13), 134203 (2007).

[25] M. Rovira-Esteva, L. C. Pardo, J. Ll. Tamarit, and F. J. Bermejo. In S. J. Rzoska, A. Drozd-Rzoska, and V. Mazur, editors, *Metastable Systems under Pressure*, NATO Science for Peace and Security Series: A. Chemistry and Biology, pages 63–77. Springer Netherlands (2009).

[26] L. C. Pardo, M. Rovira-Esteva, J. Ll. Tamarit, N. Veglio, et al.

In S. J. Rzoska, A. Drozd-Rzoska, and V. Mazur, editors, *Metastable Systems under Pressure*, NATO Science for Peace and Security Series: A. Chemistry and Biology, pages 79–91. Springer Netherlands (2009).

[27] M. Rovira-Esteva, N. A. Murugan, L. C. Pardo, S. Busch, et al. *Phys. Rev. B* **84**(6), 064202 (2011).

[28] Sz. Pothoczki, A. Ottochian, M. Rovira-Esteva, L. C. Pardo, et al. *Phys. Rev. B* **85**(1), 014202 (2012).

Supplementary material to "Differences in first neighbour orientation behind the anomalies in the low and high density trans-1,2-dichloroethene liquid"

M. Rovira-Esteva,[1] A. Murugan,[2] L. C. Pardo,[1] S. Busch,[3] J. Ll. Tamarit,[1] G. J. Cuello,[4,5] and F. J. Bermejo,[4,6]

[1]Grup de Caracterització de Materials, Departament de Física i Enginyeria Nuclear, ETSEIB, Universitat Politècnica de Catalunya, Diagonal 647, E-08028 Barcelona, Catalonia, Spain

[2]Division of Theoretical Chemistry and Biology, School of Biotechnology, Royal Institute of Technology, S-106 91 Stockholm, Sweden

[3]Physik Department E13 and Forschungs-Neutronenquelle Heinz Maier-Leibnitz (FRM II), Technische Universität München, Lichtenbergstr. 1, D-85748 Garching, Germany

[4]Facultad de Ciencia y Tecnología, Universidad del País Vasco / EHU, P. Box 644, E-48080 Bilbao, Spain

[5]Institut Laue Langevin, 6 Rue Jules Horowitz, BP. 156, F-38042 Grenoble Cedex 9, France

[6]Instituto de Estructura de la Materia, CSIC, Serrano 123, E-28006 Madrid, Community of Madrid, Spain

Published: **The Journal of Chemical Physics 136, 124514 (March 2012).**

DOI: **ftp://ftp.aip.org/epaps/journ_chem_phys/E-JCPSA6-136-045213/**

Abstract

Trans-1,2-dichloroethene (HClC=CClH) has several structural and dynamic anomalies between its low and high-density liquid, previ-

ously found through neutron scattering experiments. To explain the microscopic origin of the differences found in those experiments, a series of molecular dynamics simulations were performed. The analysis of molecular short-range order shows that the number of molecules in the first neighbour shell is 12 for the high density liquid and 11 for the low density one. It also shows that the angular position of the centre of mass of the first neighbour is roughly the same although the molecular orientation is not. In both liquids the first neighbour and its reference molecule arrange mainly in two configurations, each being the most probable in one of the liquids. First neighbours in the configuration that predominates in the high density liquid tend to locate themselves closer to the reference molecule, an evidence that they are more strongly bonded. This arrangement facilitates a better packing of the rest of molecules in the first neighbour shell so that on average an additional molecule can be included, and is proposed to be the key in the explanation of all the observed anomalies in the characteristics of both liquids.

Angle definitions

To study the short-range order of molecules in the low and high density TDCE liquids, two kinds of degrees of freedom have been analysed separately: those regarding the relative positions of the molecules and those regarding their relative orientations.

All the angles used in the analysis of the relative positions and orientations of the molecules obtained from the simulation have been depicted in Fig. 6.14.

The angles describing the relative position of the centre of mass of a molecule with respect to the reference molecule, θ_{CM} and φ_{CM}, can be seen in Fig. 6.14(a). θ_{CM} is the angle between the axis defined by the chlorine atoms of the reference molecule and the vector that goes through the centres of mass of both molecules. φ_{CM} is the angle between the plane that contains the whole reference molecule and the plane that contains the chlorine-chlorine axis of the reference molecule and the centre of mass of the other molecule. θ_{CM} and φ_{CM} will be referred to as angular position of the centres of mass to stress

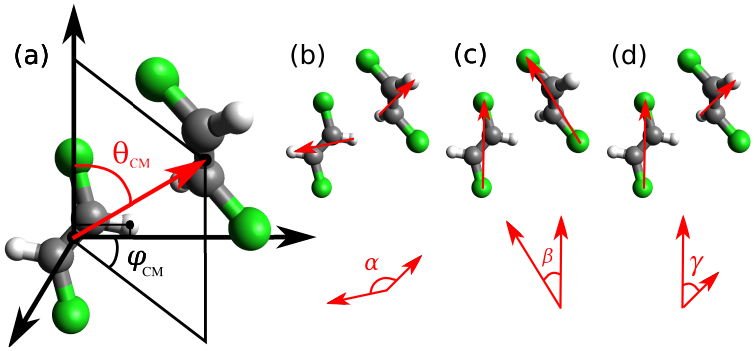

Figure 6.14: (a) Angles θ_{CM} and φ_{CM} describing the position of the centre of mass of one molecule with respect to the centre of mass of the reference molecule. (b) Angle α between the axes formed by the hydrogen atoms of both molecules. (c) Angle β between the axes formed by the chlorine atoms of both molecules. (d) Angle γ between the axes formed by the hydrogen atoms of a molecule and the chlorine atoms of the reference molecule.

the fact that the relative distance between the molecular centres of mass is already fixed when the neighbours are analysed individually.

The angles α, β, and γ describing the relative orientation between both molecules have been depicted in Figs. 6.14(b), (c), and (d), respectively. α is the angle between the axes defined by the hydrogen atoms of each molecule, β is the angle between the axes defined by the chlorine atoms of each molecule, and γ is the angle between the axis defined by the chlorine atoms of the reference molecule and the axis defined by the hydrogen atoms of the other molecule.

Note that, strictly due to geometrical considerations, an isotropic distribution of molecules around the reference molecule will yield a higher probability of angle θ_{CM} being perpendicular rather than parallel. The same happens with angles α, β, and γ, although it does not happen with φ_{CM}. To prevent misleading figures arising from this fact, probability distributions have been plotted as a function of the angle or the cosine of the angle as appropiate to ensure they will appear as flat functions in the case of isotropic distributions.

Structure patterns

A thorough analysis of the position and orientation of the trans-1,2-dichloroethene (HClC=CClH, in the following TDCE) molecules in the first neighbour shell of the low and high density liquids obtained from the molecular simulation has been performed. Although a lot of information is presented from that analysis, the detailed short range order results will not be discussed, the only objective here is to show that there is an offset of one molecule between the patterns at 200 K and 350 K, so special attention must be drawn to the fact that the structure patterns of the low and high density liquids are matched only when molecules within the first coordination shell are grouped differently for the low and high density liquids before comparison.

The probabilities of the 1^{st} to the $11^{th}/12^{th}$ neighbours of being at a certain position and orientation with respect to a reference molecule has been averaged for all the molecules in 100 independent simulations of 3629 molecules each. More details of the molecular simulations performed can be found in the main text of the article.

The neighbours within the first neighbour shell have been grouped by positional or orientational pattern similarity.

In all cases, simple visual inspection yielded the following neighbour groups at 200 K:

- Group A: 1^{st} neighbour
- Group B: 2^{nd} and 3^{rd} neighbours
- Group C: 4^{th} and 5^{th} neighbours
- Group D: 6^{th} and 7^{th} neighbours
- Group E: 8^{th}, 9^{th}, 10^{th}, 11^{th} and 12^{th} neighbours.

And the following neighbour groups at 350 K:

- Group A: 1^{st} neighbour
- Group B: 2^{nd} neighbour
- Group C: 3^{rd} and 4^{th} neighbours

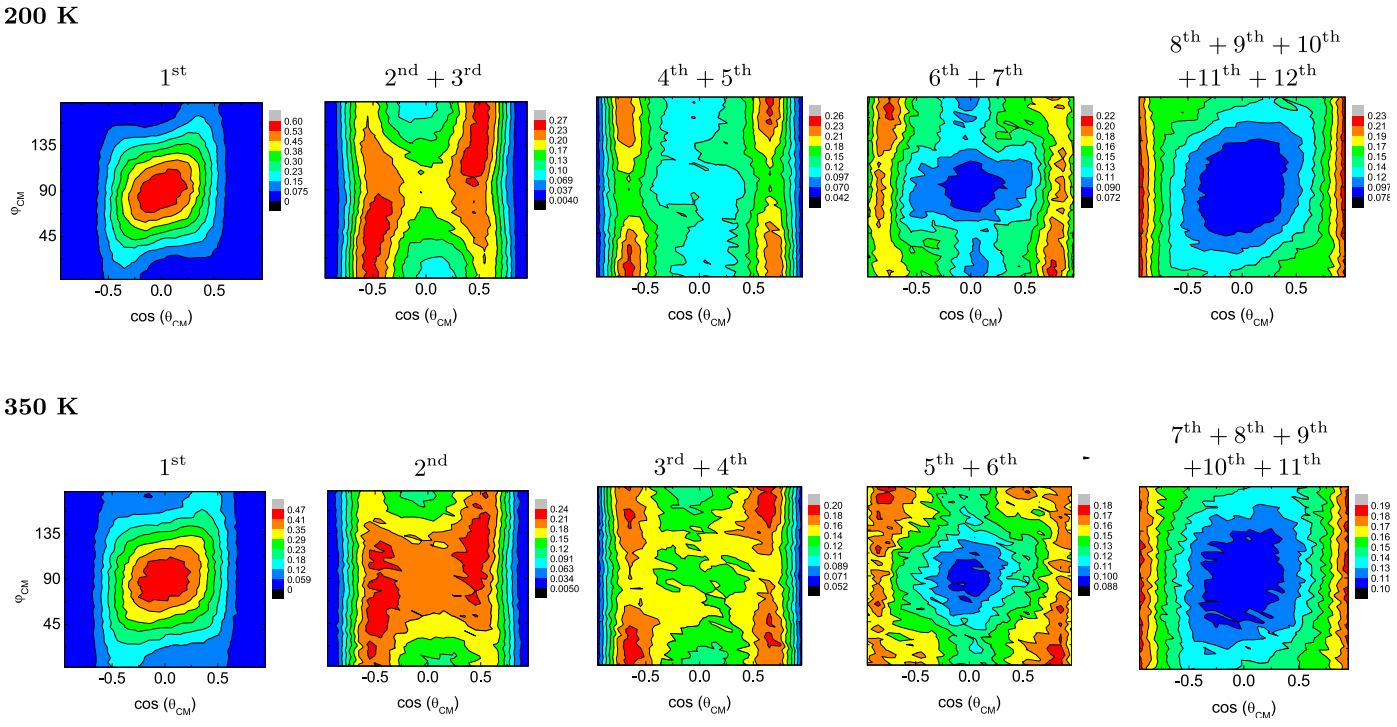

Figure 6.15: Angular position of the centre of mass of the molecules with respect to a reference molecule within the first neighbour shell at 200 and 350 K.

- Group D: 5^{th} and 6^{th} neighbours
- Group E: 7^{th}, 8^{th}, 9^{th}, 10^{th} and 11^{th} neighbours.

Figure 6.15 shows the probability of each angular position (angles θ_{CM} and φ_{CM}) of the neighbour centre of mass with respecto to the reference molecule.

Figures 6.16–6.21 allow the analysis of the neighbour orientation as a funtion of the neighbour position with respect to a reference molecule. In particular, the probability of the orientational angle α as a function of the positional angles θ_{CM} and ϕ_{CM} is shown in Figs. 6.16 and 6.17, β is shown in Figs. 6.16 and 6.19, and γ is shown in Figs. 6.18 and 6.21.

Except for the first neighbour, it can be seen that the patterns at both temperatures for each group are virtually the same. The only difference is that, due to thermal agitation, patterns of the low density liquid at 350 K appear less contrasted than patterns of the high density liquid at 200 K. To ease the qualitative comparison of the patterns, the probability colour scales have not been unified.

Here it has been shown that the structure patterns of the molecules in the first neighbour shell have a gap of one neighbour between the low and high density TDCE liquids, therefore supporting the conclusion that the high density TDCE liquid first coordination shell has one more molecule than the low density one.

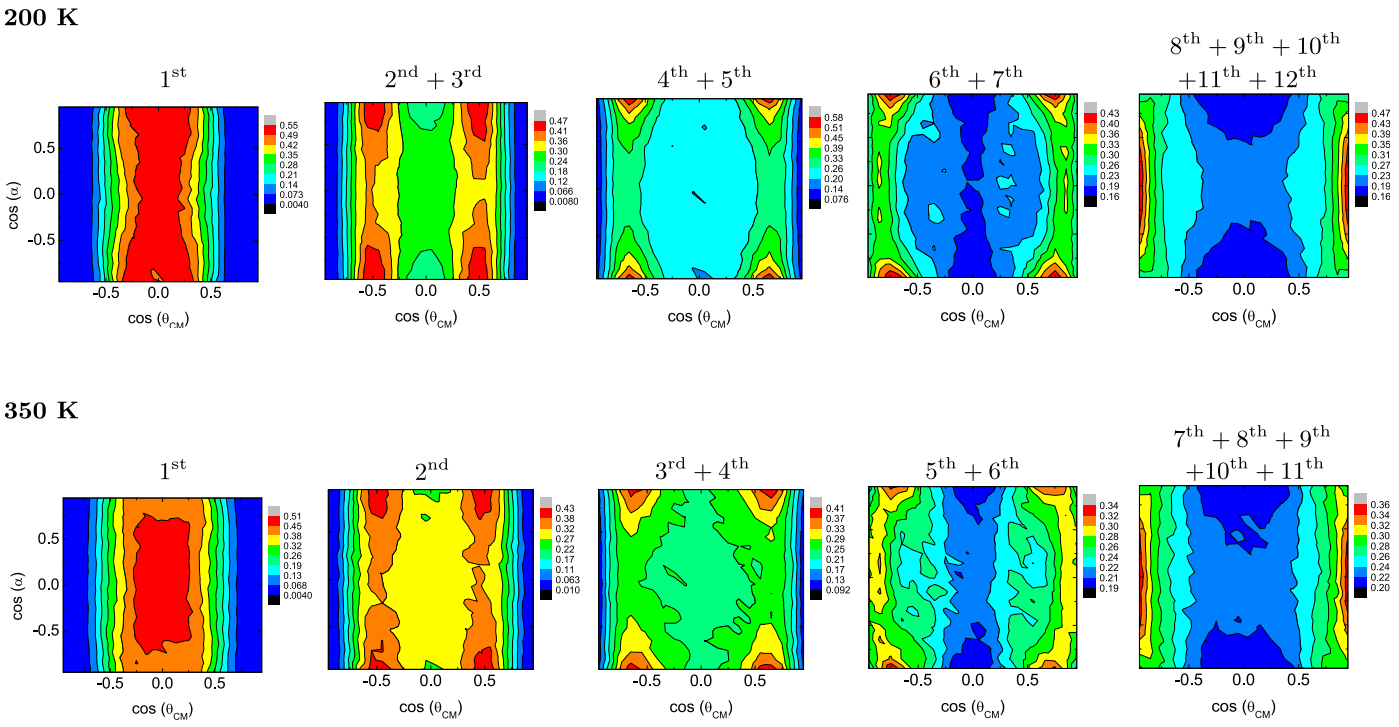

Figure 6.16: Probability of the neighbour molecules having and orientational angle α with respect to the reference molecule as a function of the positional angle θ_{CM} for the high (top) and low (bottom) density liquids.

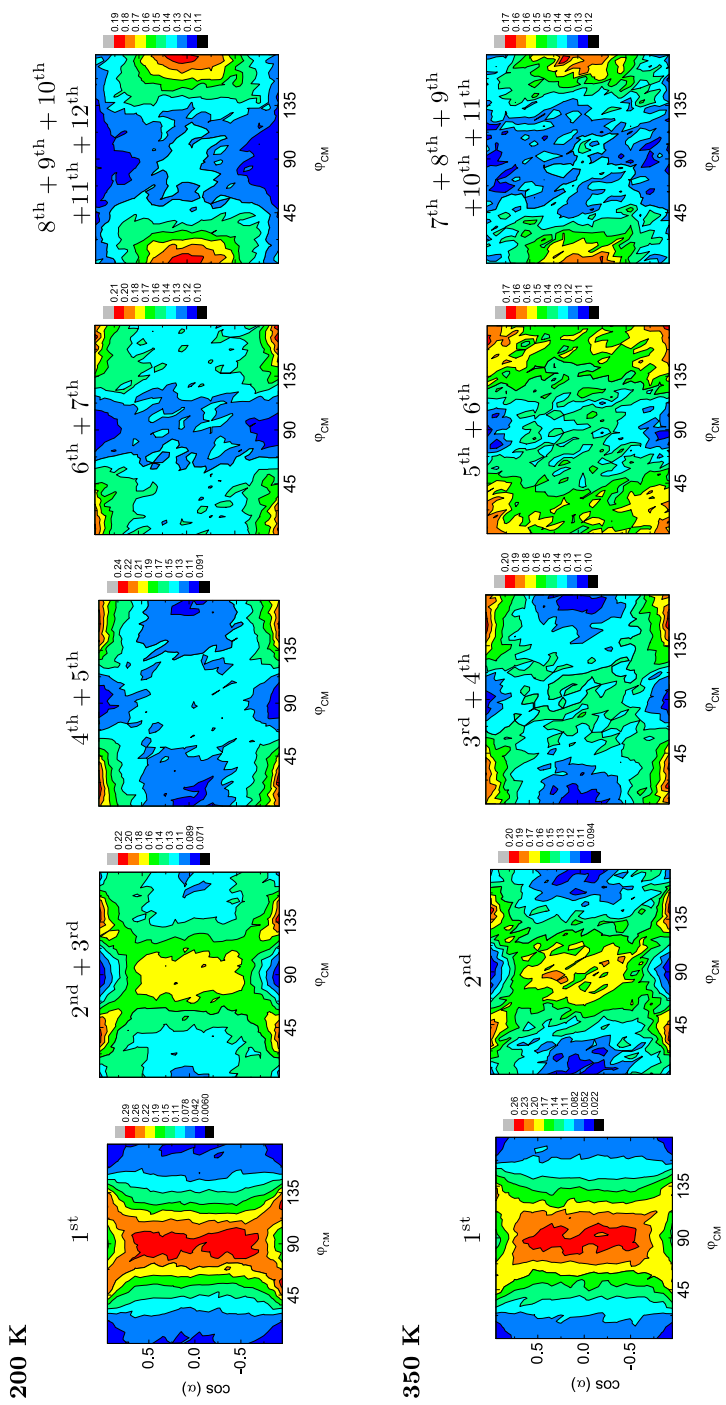

Figure 6.17: Probability of the neighbour molecules having and orientational angle α with respect to the reference molecule as a function of the positional angle φ_{CM} for the high (top) and low (bottom) density liquids.

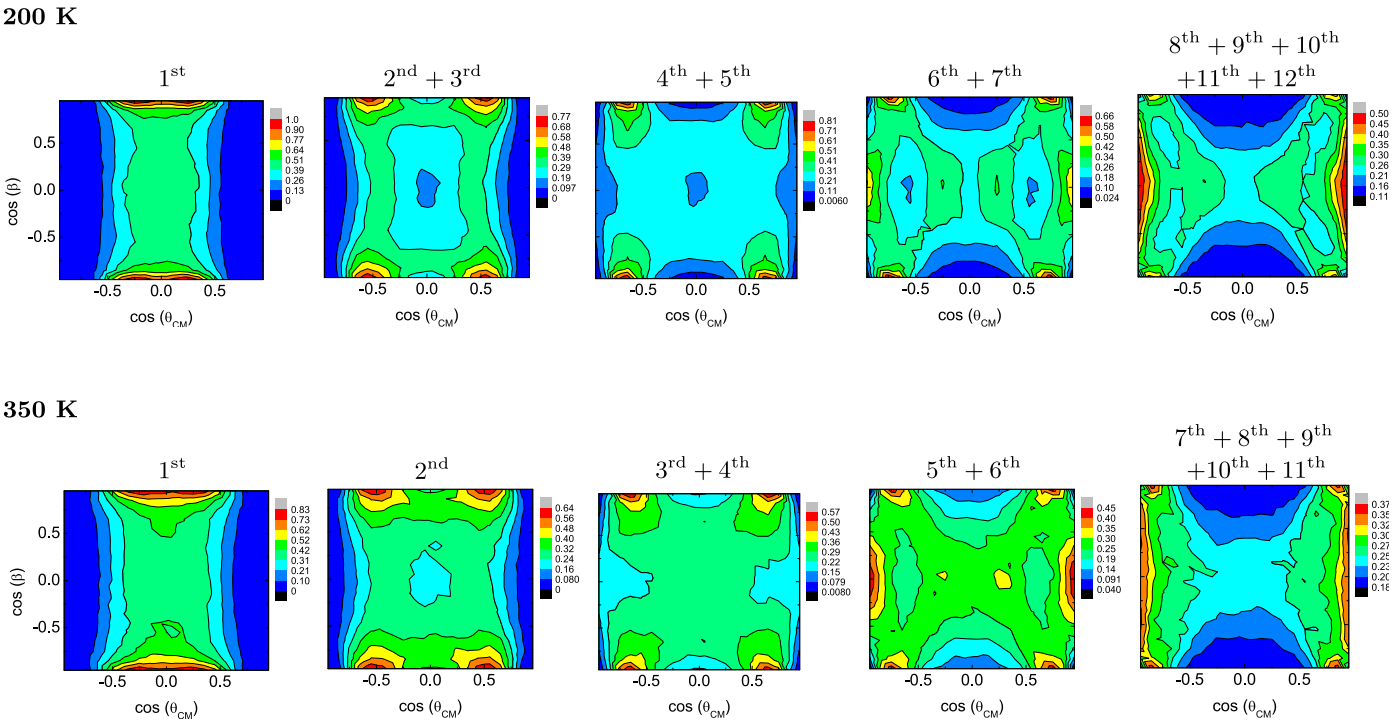

Figure 6.18: Probability of the neighbour molecules having and orientational angle β with respect to the reference molecule as a function of the positional angle θ_{CM} for the high (top) and low (bottom) density liquids.

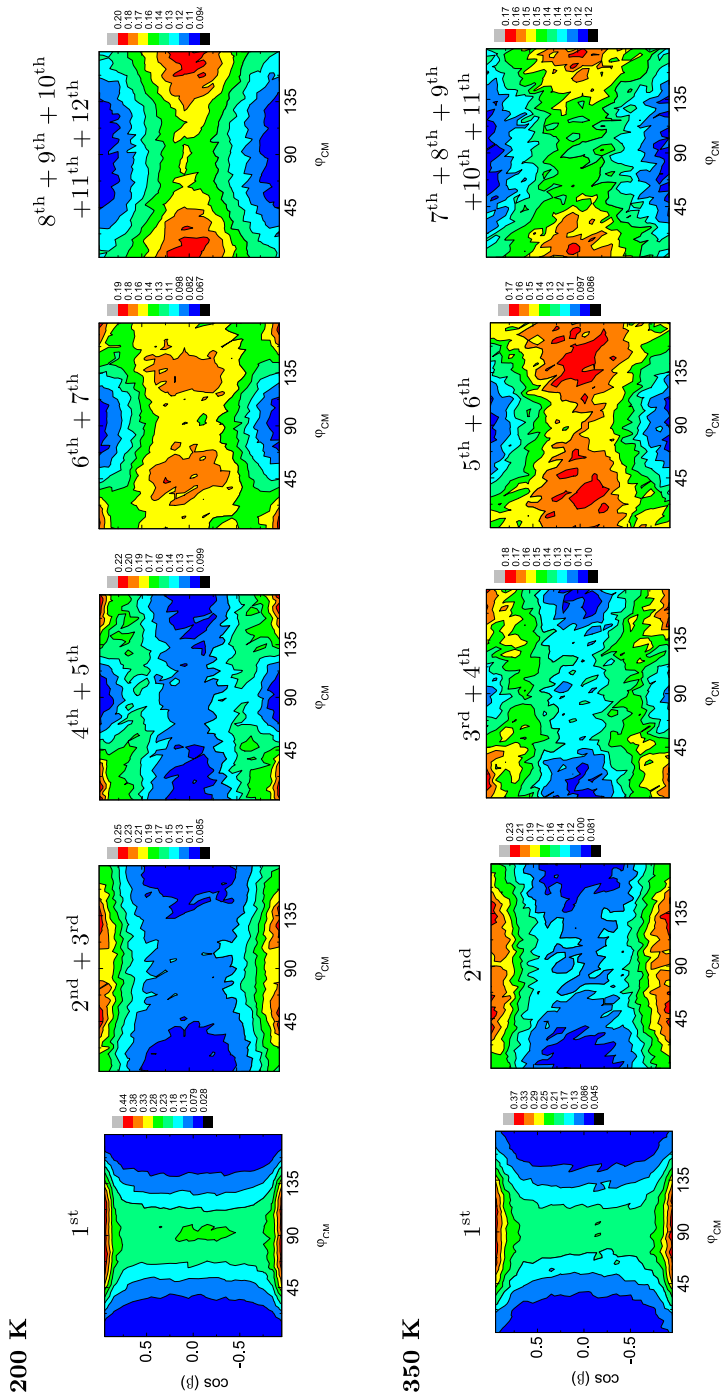

Figure 6.19: Probability of the neighbour molecules having and orientational angle β with respect to the reference molecule as a function of the positional angle φ_{CM} for the high (top) and low (bottom) density liquids.

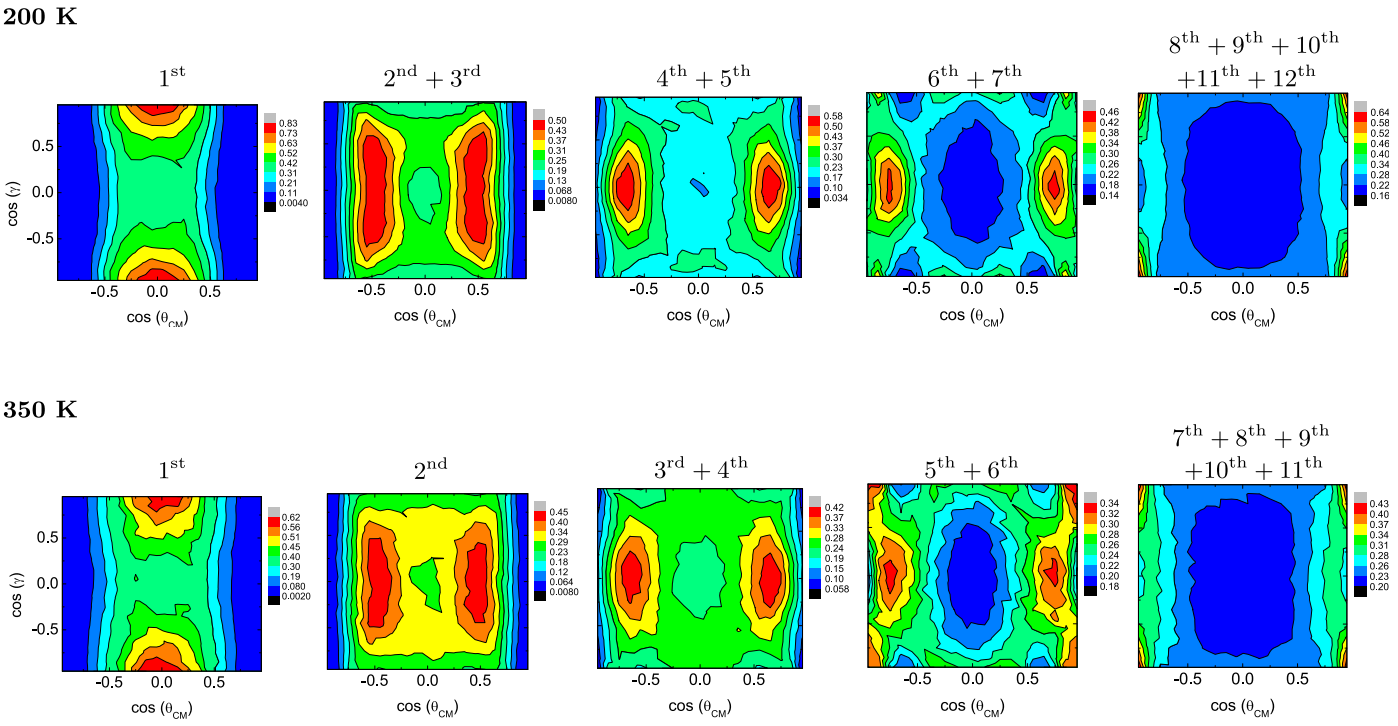

Figure 6.20: Probability of the neighbour molecules having and orientational angle γ with respect to the reference molecule as a function of the positional angle θ_{CM} for the high (top) and low (bottom) density liquids.

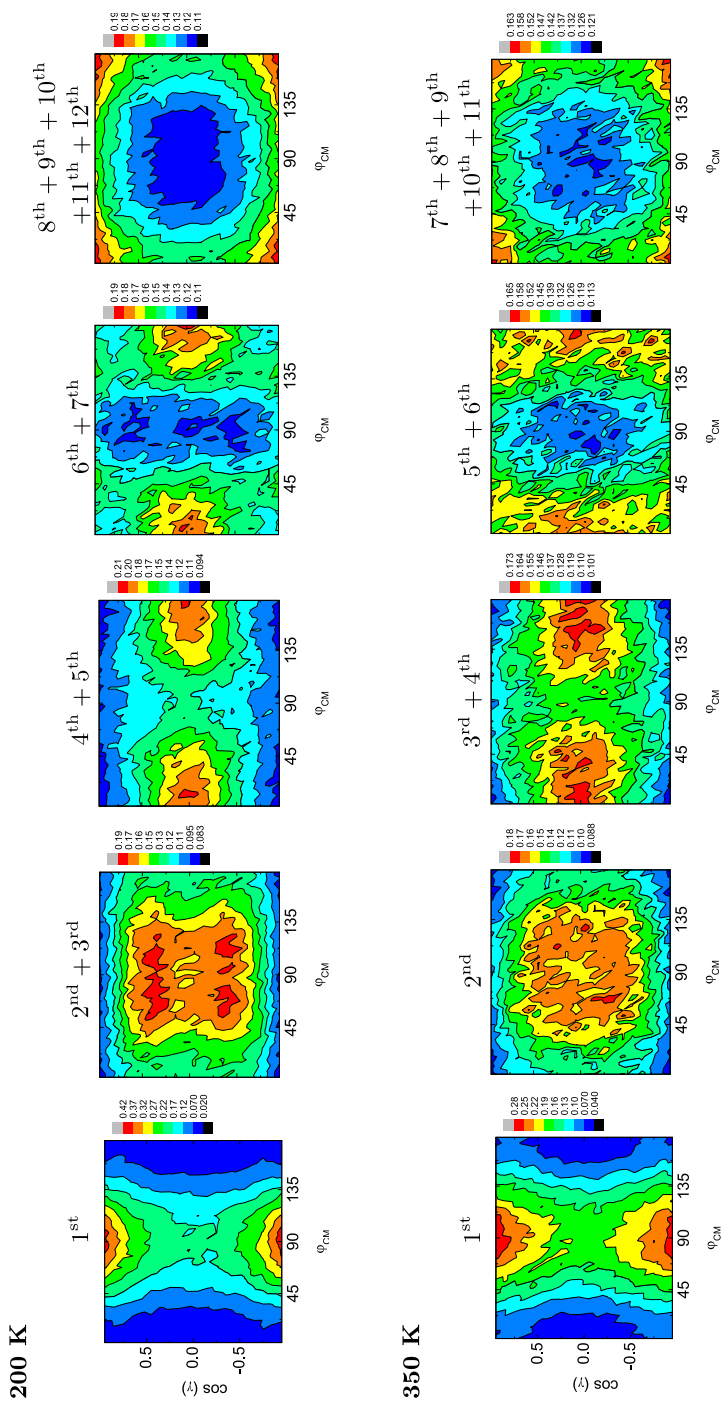

Figure 6.21: Probability of the neighbour molecules having and orientational angle γ with respect to the reference molecule as a function of the positional angle φ_{CM} for the high (top) and low (bottom) density liquids.

6.2 Role of the conformational disorder in the notable fragility of 1,1,2,2-tetrachloro-1,2-difluoroethane (F-112)

In a glass transition one of the degrees of freedom of a system slows down to a point that it effectively becomes arrested. In plastic crystals the centres of mass of the molecules are located in a regular lattice but they can rotate more or less freely. If this orientational disorder freezes, an orientational glass (OG) is obtained. These kind of glasses are usually strong, but F-112 is a remarkable exception, being the most fragile OG known so far. The purpose of this research was to understand the microscopic reasons behind its outstanding fragility.

F-112 has an additional disorder due to the fact that the molecule has two possible conformations, which coexist with a different proportion depending on the temperature. A secondary glass transition takes place when this conformational disorder gets frozen as well. Large short-range order variations were observed throughout the whole temperature range, but a sharp tendency change was observed precisely at this secondary glass transition temperature. Analyses of the liquid showed that, contrary to most compounds, the gauche conformer is more stable than the trans.

For comparison reasons, a similar molecule but without conformations, 1,1,1,2-tetrachloro-2,2-difluoroethane (F-112a), was studied as well. This compound displayed a strong behaviour, as other OG, evidencing the idea that conformations played a key role.

Fragility has been associated with the energy landscape complexity. The lack of translational disorder of molecules in OGs can explain why they are usually strong glasses, but in the case of F-112, the conformational degree of freedom originates competing intra- and intermolecular interactions yielding a very complex energy landscape and thus explaining its outstanding fragility.

Results were presented in several conferences, and published

mainly in the articles: M. Rovira-Esteva, L. C. Pardo, J. Ll. Tamarit, and F. J. Bermejo, *Metastable Systems under Pressure*, pp. 63-77 (book chapter) (2009); and M. Rovira-Esteva, N. A. Murugan, L. C. Pardo, S. Busch, et al., Phys. Rev. B **84**, 064202 (2011).

TOPIC 3: Neutron diffraction as a tool to explore the free energy landscape in orientationally disordered phases

M. Rovira-Esteva,[1] L. C. Pardo,[1] and J. Ll. Tamarit,[1] and F. J. Bermejo[2]

[1]Grup de Caracterització de Materials, Departament de Física i Enginyeria Nuclear, ETSEIB, Universitat Politècnica de Catalunya, Diagonal 647, E-08028 Barcelona, Catalonia, Spain

[2]CSIC, Instituto de Estructura de la Materia and Departamento de Electricidad y Electrónica, Facultad de Ciencia y Tecnología, Universidad del País Vasco, P.O. Box 48080 Bilbao, Spain

Book: **Metastable Systems under Pressure, p. 63, Springer Verlag (November 2009).**
Collection: **NATO Science for Peace and Security Series A - Chemistry and Biology**
Editors: **S. Rzoska, A. Drozd-Rzoska, and V. Mazur**
ISBN: **978-90-481-3406-9**
DOI: http://dx.doi.org/10.1007/978-90-481-3408-3_5

Abstract

The temperature dependence of structural parameters of orientational glasses of the halogenomethane family, Freon 112 ($(FCl_2C) - (CCl_2F)$) and Freon 112a ($(F_2ClC) - (CCl_3)$) are studied at short- (molecular) intermediate- (orientational correlations) and long-range (lattice parameters) scales by means of neutron diffraction. The two materials which are chemical isomers display strikingly different properties in their ordering patterns resulting from a shift in balance between electrostatic and excluded-volume interaction. The relevance of these findings to our understanding of glassy phenomena is discussed.

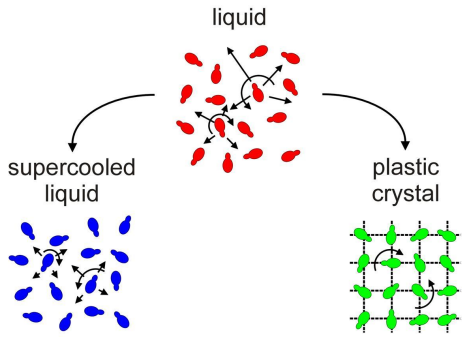

Figure 6.22: In a plastic crystal the molecular centres of mass are placed in a lattice but the molecules can rotate, more or less freely. [From Brand et al. [3].]

Introduction

Liquids are systems devoid of both long-range translational and orientational order whereas short-range order still remains at molecular scales resulting from the subtleties of forces acting on their constituent molecules. In turn, rotator-phase (plastic) crystals are liquid-like in the sense that molecules may rotate rapidly about the nodes of a crystal lattice defined by the molecular centres of mass. Rapid cooling of a liquid leads to a system where disorder is now of static nature, that is an amorphous material or a glass. Rather similar phenomena are found when cooling many plastic crystals, where the transition into a glassy state, now termed an orientational glass (OD), involves freezing the rotational degrees of freedom leading to a system with static orientational disorder (Figure 6.22) [1–3].

A glass transition may thus take place resulting from the dynamical arrest of one or more degrees of freedom due to the action of an external field such as a rapidly decreasing temperature or an increase in pressure. By convention it is considered that a glassy state has been achieved when the relevant relaxation time reaches a value of 10^2 s.

In addition to positional and orientational degrees of freedom

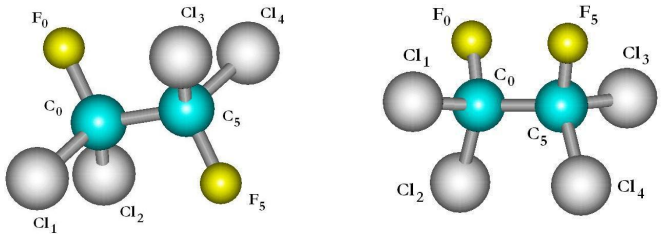

Figure 6.23: Freon 112, *trans* (left) and *gauche* (right) conformations.

characteristic of rigid-bodies further degrees of freedom need to be considered for materials composed of molecules having internal degrees of freedom with characteristic energy levels not too far above k_BT. These usually concern motions involving molecular internal rotation which lead to different molecular conformations and in this sense one terms "conformational glasses" to systems with conformational disorder.

Here we focus on the compound 1,1,2,2-tetrachloro-1,2-difluoroethane (Freon 112) which has a transition from a liquid to a bcc plastic phase at 299 K and an orientational glass transition at ca. 90 K, the transition to the completely ordered phase being extremely slow [4]. Freon 112 has two conformations energetically non-equivalent named *trans* and *gauche* (Figure 6.23). The *trans* conformation (with C2h symmetry) is somewhat more stable and has vanishing dipole moment while the *gauche* conformation (with C2 symmetry) does (0.26 D), the proportion between them being a function of temperature [5, 6].

Because a glass is defined by its dynamical properties, special attention must be drawn to them when characterizing it. The fragility, for instance, provides a measure of the temperature dependence of dynamical properties such as the relaxation time associated to the macroscopic viscosity [7]. In this respect, it turns out that most of the orientational glasses are rather strong, showing an exponential temperature dependence of their relaxation time, but Freon 112 is quite fragile. In fact, is the most fragile plastic crystal known so far

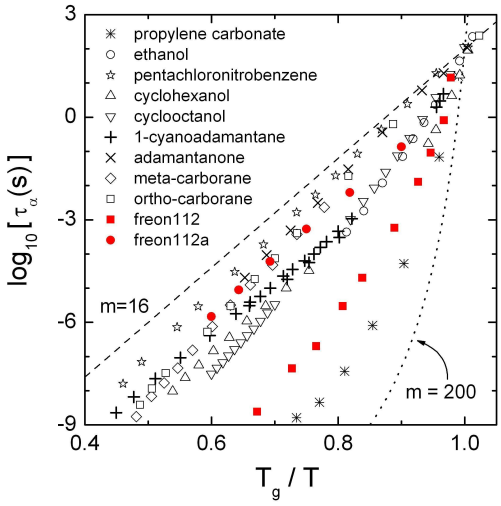

Figure 6.24: Angell plot of several orientational glasses, including Freon 112 and 112a, and a structural fragile glass (propylene carbonate) for comparison. Strong glasses are closer to an Arrhenius behaviour ($m = 16$) while fragile glasses depart from it. [From Pardo et al. [12].]

(Figure 3) [3, 8–12].

To ascertain the reasons leading to this extreme fragility, the study of the static, that is time-averaged, properties of Freon 112 is a must. To such an end, we have taken the endeavour of a full characterization of its structural properties, which apart from the intramolecular structure comprise the conformational disorder, as well as the short-, intermediate- and long-range order.

Neutron scattering is a powerful technique to get information from the structure as well as from the molecular dynamics. In particular, neutron diffraction has several advantages over other diffraction methods for studying liquid and amorphous structures which stem from the fact that neutrons interact mainly with atomic nuclei via the strong nuclear force (every isotope having a different scattering length that quantifies the strength of the interaction). As a result, the information contained in a diffraction pattern can be directly related

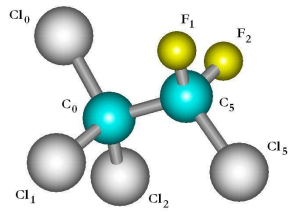

Figure 6.25: Freon 112a.

to the internuclear (or interatomic) structure of the system [13].

In this work we will also study the compound 1,1,1,2-tetrachloro-2,2-difluoroethane (Freon 112a), chemically very close to Freon 112 but with only one relevant conformation for temperatures of interest (Figure 6.25) and displaying a permanent dipole moment.

This substance also shows a transition from a liquid to a bcc plastic phase at 309 K but, unlike Freon 112, transits into a more stable ordered phase at 158 K and then a glass transition at 90 K [12], the same temperature as the transition of Freon 112. But, like most orientational glasses, it is rather strong [3, 12, 14, 15].

In what follows we will thus compare the properties and behaviour of Freon 112a to Freon 112, especially in liquid and bcc plastic phases, because its study may shed some light on the causes that bring about some of the peculiar characteristics of the latter.

Experiments and data reduction

The main objective of neutron diffraction is the determination of structure in terms of the radial distribution function, $g_{\alpha\beta}(\mathbf{r})$. This function is related to the probability of finding an atom β at position $\mathbf{r}$, relative to a reference atom α taken to be at the origin.

But what is measured in fact in neutron scattering is the differential scattering cross-section, $d\sigma/d\Omega(q)$, which is defined as the number of neutrons scattered per second towards a detector in a certain direction per incident beam flux and solid angle.

In the case of a liquid or a glass sample for which the average structure is isotropic, only the vector norms ($r = |\mathbf{r}|$ and $q = |\mathbf{q}|$) are

relevant.

The single differential scattering cross-section (1) can be split (in the static approximation) into its incoherent and coherent contributions [13].

$$\left[\frac{d\sigma}{d\Omega}(q)\right] = \left[\frac{d\sigma}{d\Omega}(q)\right]^{\text{incoh}} + \left[\frac{d\sigma}{d\Omega}(q)\right]^{\text{coh}} \tag{6.1}$$

The first term is independent of spatial correlation of the atomic sites and depends only on the distribution of scattering lengths present in the sample (2), leading to an isotropic (angle-independent).

$$\left[\frac{d\sigma}{d\Omega}(q)\right]^{\text{incoh}} = N_{\text{mol}} \sum_{i}^{m} b^2_{\text{incoh},i} \tag{6.2}$$

where N_{mol} is the number of molecules in the sample, i are the atomic positions within a single molecule and $b_{\text{incoh},i}$ is the incoherent scattering length of the chemical species.

The second term concerns diffraction from all atomic sites (including *self-scattering* from a single atom), but is independent from the distribution of scattering lengths, including only an average of them.

The coherent contribution can be further split into its self part (4), which does not give rise to any interference, and its distinct part (6), giving rise to interference due to the atoms within the same molecule and also from different molecules (5).

$$\left[\frac{d\sigma}{d\Omega}(q)\right]^{\text{coh}} = \left[\frac{d\sigma}{d\Omega}(q)\right]^{\text{coh}}_{\text{self}} + \left[\frac{d\sigma}{d\Omega}(q)\right]^{\text{coh}}_{\text{distinct}} \tag{6.3}$$

$$\left[\frac{d\sigma}{d\Omega}(q)\right]^{\text{coh}}_{\text{self}} = N_{\text{mol}} \sum_{i}^{m} b^2_{\text{coh},i} \tag{6.4}$$

where $b^2_{\text{coh},i}$ is the coherent scattering length of the chemical species at site i.

$$\left[\frac{d\sigma}{d\Omega}(q)\right]^{\text{coh}}_{\text{distinct}} = \left[\frac{d\sigma}{d\Omega}(q)\right]^{\text{coh}}_{\text{intra}} + \left[\frac{d\sigma}{d\Omega}(q)\right]^{\text{coh}}_{\text{inter}} \tag{6.5}$$

The distinct intramolecular and intermolecular contributions of the differential cross-section (5) are related to the sum of all partial structure factors, which is *essentially* proportional to the differential scattering cross-section, weighted by the respective coherent neutron scattering lengths (6).

$$\left[\frac{d\sigma}{d\Omega}(q)\right]^{\text{coh}}_{\text{distinct}} = \sum_{\alpha,\beta}^{n} b_{\text{coh},\alpha} b_{\text{coh},\beta} \left[S_{\alpha\beta}(q) - 1\right] = NF(q) \tag{6.6}$$

where n is the number of atoms within the molecules of the sample, N de total number of atoms and $F(q)$ is the total interference function.

Once the total interference function, corresponding to the weighted average on the summation (6) has been obtained, a simple Fourier transform of this reciprocal-space function will lead to the total pair-correlation function (7).

$$G(r) \equiv \frac{1}{2\pi^2 r \rho_0} \int_0^\infty qF(q) \sin(qr) dq \tag{6.7}$$

Experiments

To obtain precise information on the molecular correlations at atomic scales together with information about the crystal lattice parameters use is made of two neutron diffractometers, D1b and D4 at the Institut Laue-Langevin (Grenoble, France). The first instrument (D1b) employed thermal neutrons with $\lambda = 1.28$ Å chosen to determine with maximal precision the variation of the crystal lattice parameters by means of the positions of the main Bragg peaks. The second set (D4) was carried out using a diffractometer on a hot source with neutrons having a wavelength $\lambda = 0.502$ Å, shorter than the first, and thus with a broader momentum transfer range ($q_{\max} = 23$ Å^{-1}), then enabling the determination of the smaller distances corresponding to intramolecular structure and short range order of the compounds.

Corrections and data reduction

The normalization of the diffraction intensity pattern of a sample to an absolute cross section can be done through the comparison with

another sample of known cross-section and volume with respect to the first. In our case, a vanadium solid cylinder was also measured in the experiments for this purpose.

The computer code Correct [16] has been used to perform this normalization and also the background, multiple scattering and container attenuation corrections to the neutron diffraction data.

When the energy exchange between the neutron and the sample becomes comparable to the incident energy of the neutron, an inelastic correction becomes necessary due to the breakdown of the static approximation [13]. This is of greater magnitude with increasing q values (in a reactor source) and for lighter atoms, since a neutron striking an atom of small mass will transfer more energy.

A Placzek correction [17] to remove the inelastic effects has been performed by fitting a polynomial (9) to the higher range of q linearly weighting the data to account for the higher effect at higher values of q.

$$F(q) = p_0 + p_2 q^2 + p_4 q^4 + p_6 q^6 \tag{6.8}$$

Once the corrected total interference function was obtained, a Fourier transform had to be done to the experimental total interference function to obtain the total pair-correlation function.

Another difficulty with which we must deal with in diffraction experiments is that any instrumental setup has a maximum accessible momentum transfer, $q_{\max}$, and the Fourier transformation of that finite pattern leads to peak broadening in real space as well as to non-physical oscillations in $G(r)$ and its related functions. Since those ripples can be confused with the physical diffraction peaks, especially in the range of smaller distances, they must be avoided to obtain a reliable analysis.

A method commonly used to deal with that problem is to modulate the experimental total interference function by a damping window function before applying the Fourier transform [18] instead of just using the step function.

In this work the normalized *sinc* function (10) has been used for that purpose.

$$\operatorname{sinc}(x) \equiv \frac{\sin(\pi x)}{\pi x} \tag{6.9}$$

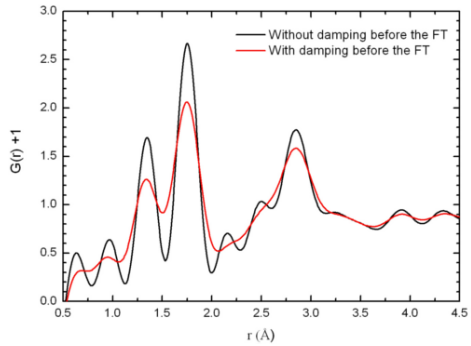

Figure 6.26: Comparison of the obtained total pair-correlation function of Freon 112a at 320 K when doing the FT with or without a sinc window function.

where $x = q/q_{\max}$.

Although the use of this function preserves the area of the peaks in the profile of the total pair-correlation function, one of the drawbacks of this method is that not only the unphysical ripples are damped but all the oscillations are, with the consequent loss of information (Figure 6.26).

An alternative method consists on Fourier-transforming the step function that describes the experimental q range and convolute it with the theoretical r-space functions before comparing or fitting them to the Fourier-transformed data [19].

Although this is a more accurate method is somewhat more sophisticated and time consuming and it was not considered necessary in the present work.

Results and Discussion

The first result coming out from the powder diffraction measurement carried out at D1B yields the temperature dependence of the molecular density of the compounds and is shown in Figures 6.27 and 6.28. The density is estimated within the bcc phase from the position of the main Bragg peaks in the diffraction pattern. The molecular densities for the liquid phase were previously measured by means of densito-

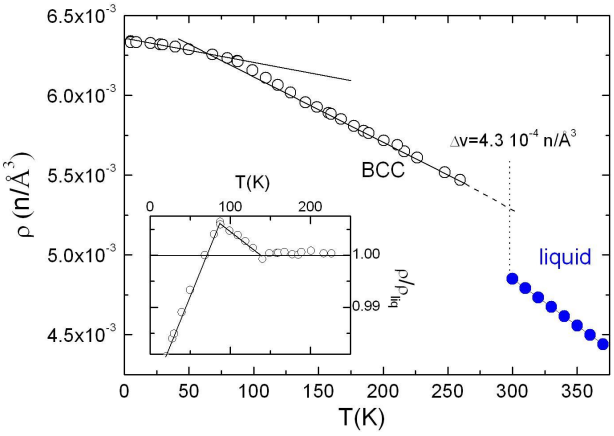

Figure 6.27: Molecular density of Freon 112.

metry.

In Freon 112 a clear change at 90 K in the slope of the molecular density yields a first signature of the main glass transition. A more subtle change in the tendency of the density is also found at 130 K. This change can be clearly seen in the inset of Figure 6.27 and it corresponds to the freezing of the *gauche-trans* conformational disorder as proposed by Kishimoto et al. [4] according to specific heat measurements.

The molecular density for the bcc phase is higher for Freon 112a (Figure 6.28) than for Freon 112. This fact can be thought of as due to a closer packing in the former thanks to an easier arrangement of molecules when there is only one conformation in respect to the case when there are several.

A series of molecular mechanics and ab initio calculations of an isolated single molecule have been performed with the Gaussian software package (using MM+ and STO-3G, 3-21G, 6-31G* and 6-31G** basis sets, respectively) to explore the expected positions of the peaks corresponding to intramolecular distances and also to determine the optimal procedure to find them.

Every calculation has been made using the results of the previous one as the initial conditions to reduce the computing time, except for

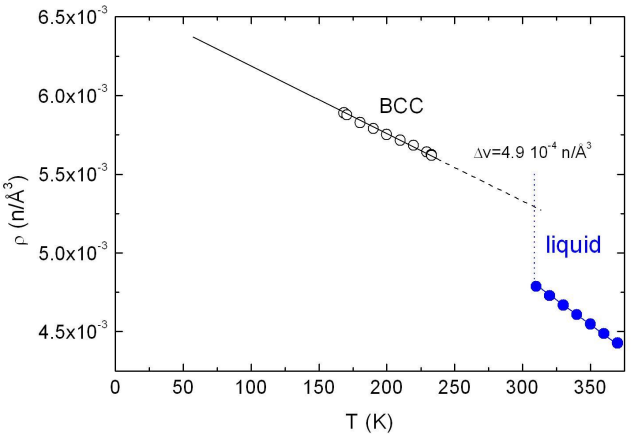

Figure 6.28: Molecular density of Freon 112a.

the last one (6-31G**) were the results from the MM+ calculation were also used to check the robustness of the method.

Since we have considered 0.01 Å as a lower bound for the minimum distance between peaks that we can resolve, we have concluded that in future works it is not worth it to increase the computing time using the larger basis set. Within the needed precision, the use of 6-31G* will yield the best result with an optimum computing time.

The experimental intramolecular part of the total pair-correlation function at different temperatures has been plotted together with the *ab initio* calculation to provide a visual aid for the intramolecular distances assignment to the $G(r)$ peaks for both Freon 112 and Freon 112a and is shown in Figure 6.29 and Figure 6.30 respectively.

The total pair-correlation function of Freon 112 contains contributions from both the *trans* and *gauche* conformations, and so we expect major changes in the shape of the peaks as the concentration of each conformation changes with temperature, as indeed is observed.

A closer look into the change of the position of certain peaks reveals a prominent variation of some relevant angles and distances within the molecule, occurring at the temperature of conformational freezing (Figure 6.31). The distances C-Cl and C-F, corresponding

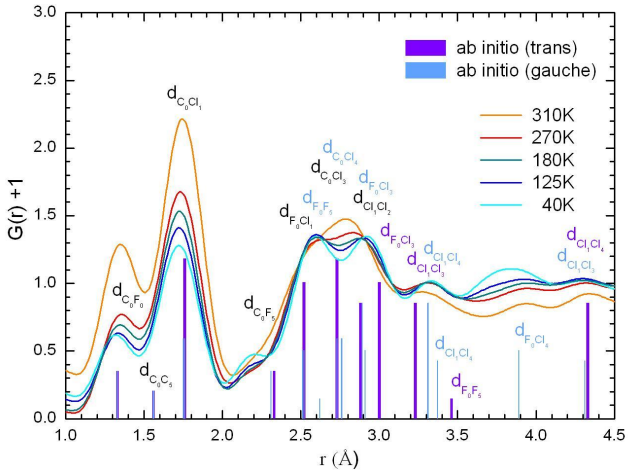

Figure 6.29: Total pair-correlation function for Freon 112 together with the *ab initio* calculation of intramolecular distances.

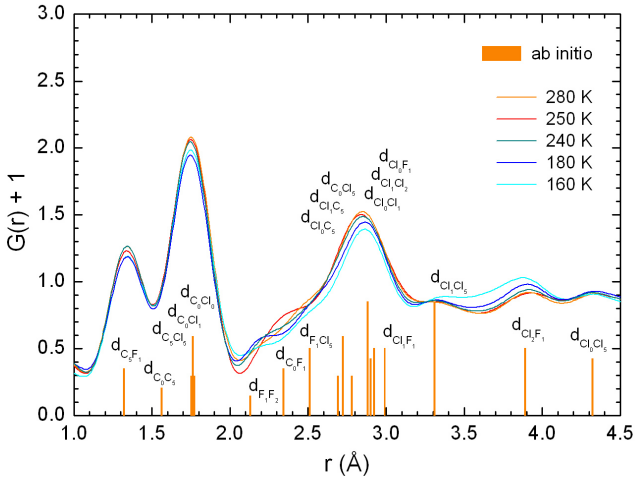

Figure 6.30: Total pair-correlation function for Freon 112a together with the *ab initio* calculation of intramolecular distances.

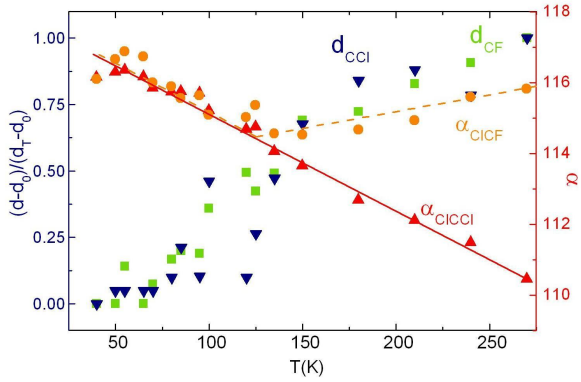

Figure 6.31: Reduced distances C-Cl and C-F and angles Cl-C-Cl and Cl-C-F (d_0 and d_T are the distances at 40 K and 275 K, respectively).

to directly bonded pairs, and the angle Cl-C-F, show this kind of behaviour, while the angle Cl-C-Cl does not seem to be sensitive to that particular temperature. The use of the relative distances within the crystalline bcc phase, $(d - d_0)/(d_T - d_0)$, instead of the plain distances, enables to scale the y-axis for an easier comparison.

The spatial extent of the total pair-correlation functions corresponding to purely intermolecular distances has also been plotted for Freon 112 and 112a to show the different short range order features and is shown in Figures 6.32 and 6.33, respectively.

Rather significant changes on the total pair-correlation function profile of Freon 112 can be observed for all the temperature range. The prominent shoulder of the main peak merges with the latter at 130 K where the *gauche-trans* freezing occurs; and there is a strong variation in the position of the peak around 9 Å, that has a change in the tendency precisely at 130 K, probably indicating substantial modifications in the short range order of the compound due to the conformational disorder (see the inset on Figure 6.32).

The high fragility of glasses is linked to the idea of a more complex energy landscape [20, 21]. The fact that orientational glasses are in a regular lattice (disorder being only of orientational character) usually accounts for the observation that most of them are rather strong.

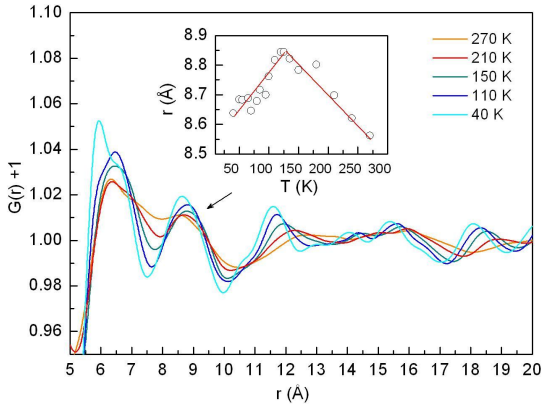

Figure 6.32: Total pair-correlation function for Freon 112 in the range of intermolecular distances. Temperature dependent position of the peak around 9 Å on the inset.

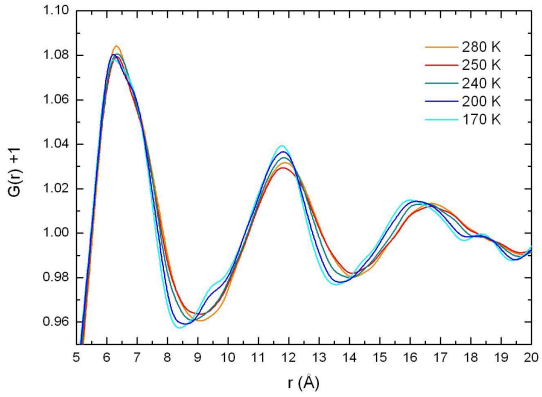

Figure 6.33: Total pair-correlation function for Freon 112a in the range of intermolecular distances.

The case of Freon 112 is quite different because the conformational disorder provides an additional source of intramolecular and intermolecular competing interactions, giving rise to a higher complexity that could explain its outstanding fragility among the orientational glasses.

In stark contrast, the changes with temperature of the short-range order pattern for Freon 112a are far milder. Its total pair-correlation function appears with well-defined peaks that change only slightly its position with temperature. Besides, there are bigger and less numerous peaks in the total pair-correlation function of Freon 112a which, altogether, denotes a simpler and rather unvarying features on its short-range order.

Conclusions

The structural changes observed for Freon 112 at all length scales provide some clues for a better understanding its outstanding properties. In particular, the main glass transition at 90 K of Freon 112 shows a clear signature in the temperature dependence of the molecular density arising from the reduced volume expansivity within the glassy state. On the other hand, the molecular density, short range order and molecular structure for Freon 112 show a sharp change at 130 K, the temperature at which the *gauche-trans* conformational freezing is taking place. In contrast, Freon 112a, with no conformational disorder, shows a mild variation of its structural properties with much more subtle changes. These results suggest that the conformational disorder of this compound plays a major role on explaining its complexity.

The differences in behaviour between the two compounds have to be ascribed to the presence in Freon 112a of relatively strong directional interactions due to its dipole moment as well as to the different molecular shapes of the two chemical isomers. These distinct behaviours unveil large differences between the potential energy surfaces of both isomers and thus exemplify how a shift in the balance between highly directional (electrostatic) and excluded-volume (vdW) interactions induced by a change in molecular topology gives

rise to a whole set of differences in structure and thermodynamics.

The present results constitute a step forward in our understanding of the microscopic details that may lead too disparate behaviour in macroscopic glassy properties such as the fragility and also come into line with results given in Reference [22] on a study of the isomeric effect concerning another glassy material.

In order to determine exactly which changes on short-range order are taking place and to determine structural molecular scenarios compatible with the experimental data, Monte Carlo and molecular dynamics simulations are being performed to try to reproduce some characteristics of its behaviour and to further understand the glass transition on this kind of materials.

Acknowledgements

This work was supported by grants from the Spanish Ministry of Science and Innovation (MICIN) (FIS2008-00837) and from the Generalitat de Catalunya (2005SGR-00535). One of us (MRE) acknowledges the PhD fellowship from MICINN.

References

All online references accessed on July 22, 2014.

[1] L. C. Pardo, N. Veglio, F. J. Bermejo, J. Ll. Tamarit, et al. *Phys. Rev. B* **72**, 014206 (2005).

[2] N. Veglio, F. J. Bermejo, L. C. Pardo, J. Ll. Tamarit, et al. *Phys. Rev. E* **72**(3), 031502 (2005).

[3] R. Brand, P. Lunkenheimer, and A. Loidl. *J. Chem. Phys.* **116**(23), 10386 (2002).

[4] K. Kishimoto, H. Suga, and S. Seki. *Bull. Chem. Soc. Jpn.* **51**(6), 1691 (1978).

[5] M. Iwasaki, S. Nagase, and R. Kojima. *Bull. Chem. Soc. Jpn.* **30**(3), 230 (1957).

[6] R. E. Kagarise and L. W. Daasch. *J. Chem. Phys.* **23**(1), 113 (1955).

[7] C. A. Angell. *J. Phys. Chem. Solids* **49**(8), 863 (1988).

[8] C. A. Angell, A. Dworkin, P. Figuiere, A. Fuchs, et al. *J. Chim. Phys.* **82**(7-8), 773 (1985).

[9] A. Drozd-Rzoska, S. J. Rzoska, S. Pawlus, et al. *Phys. Rev. B* **73**(22), 224205 (2006).

[10] A. Drozd-Rzoska, S. J. Rzoska, S. Pawlus, et al. *Phys. Rev. B* **74**(6), 064201 (2006).

[11] P. Mondal, P. Lunkenheimer, R. Böhmer, A. Loidl, et al. *J. Non-Cryst. Solids* **172**, 468 (1994).

[12] L. C. Pardo, P. Lunkenheimer, and A. Loidl. *J. Chem. Phys.* **124**(12), 124911 (2006).

[13] H. E. Fischer, A. C. Barnes, and P. S. Salmon. *Rep. Prog. Phys.* **69**(1), 233 (2006).

[14] R. Puertas, M. A. Rute, J. Salud, D. O. López, et al. *Phys. Rev. B* **69**(22), 224202 (2004).

[15] R. Puertas, J. Salud, D. O. López, M. A. Rute, et al. *Chem. Phys. Lett.* **401**(4-6), 368 (2005).

[16] M. Howe, R. McGreevy, and P. Zetterström. *Computer code CORRECT, correction program for neutron diffraction data* (1996). NFL Studsvik internal report.

[17] G. Placzek. *Phys. Rev.* **86**(3), 377 (1952).

[18] E. Lorch. *J. Phys. Part C Solid State Phys.* **2**(2), 229 (1969).

[19] I. Petri, P. S. Salmon, and H. E. Fischer. *Phys. Rev. Lett.* **84**(11), 2413 (2000).

[20] P. G. Debenedetti and F. H. Stillinger. *Nature* **410**(6825), 259 (2001).

[21] H. Shintani and H. Tanaka. *Nat. Phys.* **2**(3), 200 (2006).

[22] C. Talón, F. J. Bermejo, C. Cabrillo, G. J. Cuello, et al. *Phys. Rev. Lett.* **88**(11), 115506 (2002).

TOPIC 4: Interplay between intra- and intermolecular structures of 1,1,2,2-tetrachloro-1,2-difluoroethane

M. Rovira-Esteva,[1] A. Murugan,[1] L. C. Pardo,[1] S. Busch,[2] J. Ll. Tamarit,[1] Sz. Pothoczki,[1] G. J. Cuello,[3,4] and F. J. Bermejo[3,5]

[1]Grup de Caracterització de Materials, Departament de Física i Enginyeria Nuclear, ETSEIB, Universitat Politècnica de Catalunya, Diagonal 647, E-08028 Barcelona, Catalonia, Spain

[2]Physik Department E13 and Forschungs-Neutronenquelle Heinz Maier-Leibnitz (FRM II), Technische Universität München, Lichtenbergstr. 1, D-85748 Garching, Germany

[3]Facultad de Ciencia y Tecnología, Universidad del País Vasco / EHU, P. Box 644, E-48080 Bilbao, Spain

[4]Institut Laue Langevin, 6 Rue Jules Horowitz, BP. 156, F-38042 Grenoble Cedex 9, France

[5]Instituto de Estructura de la Materia, CSIC, Serrano 123, 28006 Madrid, Spain

Published: **Physical Review B 84, 064202 (August 2011).**
DOI: http://dx.doi.org/10.1103/PhysRevB.84.064202

Abstract

We report on the interplay between the short-range order of molecules in the liquid phase of 1,1,2,2-tetrachloro-1,2-difluoroethane and the possible molecular conformations, trans and gauche. Two complementary approaches have been used to get a comprehensive picture: analysis of neutron diffraction data by a Bayesian fit algorithm and a molecular dynamics simulation. The results of both show that the population of trans and gauche conformers in the liquid state can only correspond to the gauche conformer being more stable than the

trans. Distinct conformer geometries induce distinct molecular short range orders around them suggesting that a deep intra- and intermolecular interaction coupling is energetically favouring one of the conformers by reducing the total molecular free energy.

Introduction

The structure of molecular liquids has been extensively investigated by both, diffraction and simulation techniques in the last few decades. The evergreen question is the relation between the intra- and intermolecular parts of the structure. In this context, one of the most studied systems has been CCl_4, whose intramolecular structure has been well known for a long time [1, 2]. In a recent study, partial pair-distribution functions have shown that the intra- and intermolecular characteristic distances are well separated from each other [3]. However, such a clear decoupling occurs only in a minority of molecular systems; even for molecular liquids with one molecular centre, like $SbCl_5$ and WCl_6, the interplay between intra- and intermolecular contributions can be considerable [4]. The structure of liquid water, arguably the most important of all molecular liquids, has also been widely studied in this respect. Both the decoupled [5] and the coupled [6] approaches have been applied in structural modelling applications. In more complex systems, such as alcohols [7, 8], the intramolecular structure has been proven to have an effect on the intermolecular structure at short and even intermediate distances [9].

The determination of the intramolecular structure in the liquid or the solid phases is not an easy task. First because the diffraction experiments used for its determination allow the access to information only in reciprocal space, and second because any attempt of performing a fit has to deal with strong correlations between intramolecular parameters making it difficult to find the best fit to the data [9, 10]. These difficulties have been summarized in a recent work [11] where a modification of the Levenberg-Marquardt algorithm is presented. In this paper we present a different approach to the problem based on Bayes theorem [12] that helps making non linear fits less challenging [13].

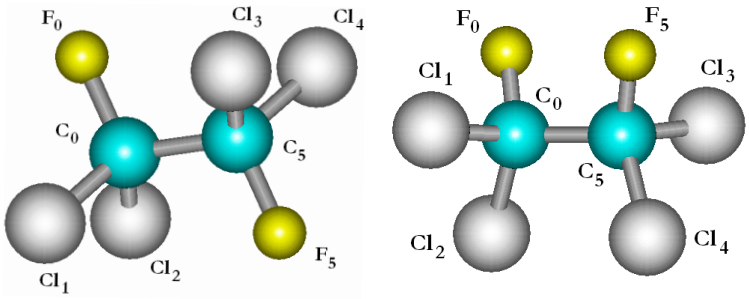

Figure 6.34: *Ab initio* calculation of the F-112 molecular structure in the gas phase for the trans (left) and gauche (right) conformers, together with the name convention of the atoms used in the present work.

The case of 1,1,2,2-tetrachloro-1,2-difluoroethane (hereafter F-112) is particularly interesting due to the fact that this compound has two rotamers and its liquid phase is a mixture of different intramolecular geometries. Figure 6.34 shows the intramolecular structure of the two possible F-112 conformers, trans and gauche. As there are two degenerate possibilities for a gauche conformation but only one for a trans conformation, the fraction of molecules in the gauche state would be 2/3 if there were no noticeable energy difference between the gauche and trans conformers. The structure has been determined at 0 K in the vacuum, i. e., without taking intermolecular interactions into account, through an *ab initio* calculation using the program HYPERCHEM[14] with the 6–31G** basis set (see Table 6.3). The atoms are arranged in staggered conformation and other dihedral angles exist only in transition states between the conformers. The *ab initio* calculation has yielded a very similar energy for both conformers with a difference $\Delta H = 0.006$ eV, being gauche slightly more stable.

The energy barrier (ΔH^*) and energy difference between the two conformers (ΔH) were experimentally determined using NMR, Raman and far infrared spectroscopy, and specific heat measurements, which yielded $\Delta H^* = 0.3$ eV $- 0.42$ eV and $\Delta H = 0.005 - 0.008$ eV [15–19]. This means that at 310 K ($RT \approx 0.027$ eV) hardly any molecule can be found in a transition state and that gauche and

Table 6.3: Comparison of the parameters obtained from the *ab initio* calculation of the F-112 molecule in the gas phase with the mean and standard deviation obtained from the normal distributions of the parameters found with the fits of the experimental measurements (gauche fraction c_g, interatomic dihedral angle α and distances r_{ij}, and vibrational parameters l_{ij}). Distances related to atomic bonds and atoms bonded to the same carbon have been considered common parameters to both conformers, and distances related to atoms bonded to different carbons have been separately fitted for each conformer, those corresponding exclusively to the gauche conformation have been labelled r^g. Lengths are given in Å, the angle α in degrees, and c_g is dimensionless.

Parameter	*Ab initio*	Fit values
c_g	0.67	0.68 ± 0.02
α	59.7	64 ± 2
$r_{C_0F_0}$	1.33	1.361 ± 0.001
$r_{C_0Cl_1}$	1.76	1.7446 ± 0.0006
$r_{C_0C_5}$	1.56	1.65 ± 0.02
$r_{F_0Cl_2}$	2.52	2.536 ± 0.009
$r_{Cl_1Cl_2}$	2.88	2.64 ± 0.02
$r_{C_5Cl_1}$	2.73	2.70 ± 0.01
$r^g_{C_5F_0}$	2.31	2.269 ± 0.006
$r^g_{C_5Cl_2}$	2.76	2.93 ± 0.02
$r^g_{C_5Cl_1}$	2.73	2.70 ± 0.01
$r^g_{Cl_1Cl_2}$	2.89	2.70 ± 0.04

Parameter	Fit values
l_{CF}	0.069 ± 0.001
l_{CCl}	0.0829 ± 0.0009
l_{CC}	0.27 ± 0.02
l_{ClF}	0.27 ± 0.01
l_{F1Cl}	0.290 ± 0.008
l_{C1Cl}	0.16 ± 0.01
l_{Cl1C}	0.19 ± 0.01
l_{F2Cl}	0.079 ± 0.003
l_{Cl2C}	0.13 ± 0.01
l_{F2F}	< 0.002
l_{Cl2C}	0.07 ± 0.01

trans conformers are nearly equally populated – with a slightly higher number of the lowest energy conformer.

Usually, gauche rotamers are less stable than trans because the atoms have a higher steric strain as they are closer to each other. Nonetheless, several compounds have been reported to display the opposite behaviour with gauche being more stable, which has been called "gauche-effect" [20, 21]. In particular, this effect has already been reported long time ago in some halogenoethanes [22, 23].

The F-112 NMR spectra were measured from a 33% and a 10% solution, and found the trans conformer to be at a lower energy than the gauche [15, 16]. However, energy differences between rotational isomers strongly depend on the dielectric constant of the medium due to interactions between the polar groups of the molecule and the solvent. Therefore, these results can not be simply applied to the case of the pure compound [24, 25]. Most references assume the trans rotamer to be the most stable conformer but a calculation of the intramolecular energy of the rotamer geometries, where the difference was $\Delta H = 0.003$ eV, returned a gauche conformer slightly more stable than the trans [23].

The intramolecular structure of F-112 has previously been assumed to be decoupled from the ordering of molecules at short distances, in some molecular dynamics simulations the molecules are even assumed to be rigid [26]. Nevertheless, studies on the structure at the inter- and intramolecular scale showed that the interplay of features at these two different length scales may explain the complex dynamics of F-112 [27–29].

The present work is focused on the determination of the molecular structure of F-112, its interplay with intermolecular ordering in the liquid phase, and a deep analysis of the short range order, and is organized as follows: after a short description of the experimental and simulation procedures, a fit method to obtain molecular parameters from the neutron diffraction data is presented. The molecular structure of F-112 will then be obtained from experimental data. Finally, in order to find out its relation with intermolecular length scale features, the short range ordering of molecules will be determined with molecular dynamics simulation results using flexible F-112 molecules.

In the appendix, it is explicitly explained how the errors are calculated when using the Fourier transform, the proposed method is validated by fitting artificially generated data of the structure of an ethene molecule, and the F-112 analysis is crosschecked by fitting the molecular dynamics results and comparing the intramolecular parameters with those obtained from the experimental fit.

Experimental and simulation details

6.2.0.4.1 Molecular dynamics simulation For the molecular dynamics simulations, the initial molecular geometry for F-112 was obtained by optimizing the molecular geometry at HF/6-31+G* level using the GAUSSIAN 03 program [30]. Because a generalized AMBER force field [31] was used in the simulation to describe the intra- and intermolecular interactions of F-112, which provides a completely flexible molecular model, the molecules could change between the trans and gauche conformers to reach the equilibrium population. After assuring that consistent results were obtained for the simulation irrespective of the initial molecular conformations, a gauche conformation was adopted as the initial molecular geometry for all the molecules in the simulation. The charges used in the simulation were obtained as best fit to the molecular electrostatic potential in a certain number of points around the molecule using the CHELPG procedure [32].

The simulations were carried out for liquid F-112 using the SANDER module in the AMBER8 software package [33]. The simulation box size was on average $78.5 \times 79.7 \times 77.02$ Å^3 containing 2345 molecules of F-112. The temperature of the isothermal-isobaric ensemble was maintained at 310 K and the pressure was set to 1 bar using the Nose-Hoover and the Parrinello-Rahman algorithms, respectively [34]. Once stabilization was reached, the density within the simulation box varied between 1.64 and 1.65 g/cm^3, very close to the experimental density which is 1.62 g/cm^3 [35]. The time step for integrating the equations of motion was 1 fs and the total time scale of the run was 10 ns.

6.2.0.4.2 Neutron diffraction experiments Diffraction patterns of a F-112 sample with 99% purity purchased from ABCR GmbH & Co. KG (Karlsruhe, Germany) were measured in the liquid phase at 310 K. Experiments were performed at the liquids and glasses neutron diffractometer D4c at the Institute Laue-Langevin (Grenoble, France) [36], using a wavelength of $\lambda = 0.5$ Å and an angular range for the detectors that yielded a scattering vector up to $q_{\max} \approx 23$ Å^{-1}. In order to correct and normalise the data, the empty cryostat, an empty sample holder, a boron powder sample and a vanadium rod were also measured, as in previous works [37, 38]. Absorption and multiple scattering corrections and normalization of the data were performed using the program CORRECT [39]. Additionally, inelastic corrections were also carried out by subtracting a polynomial expansion in powers of q^2 [40].

Evaluation of the diffraction data

6.2.0.4.3 Bayesian fit method Bayesian methods are routinely used in many branches of science [41]. Their use in condensed matter, although it has been proven to be very powerful, is still quite scarce [42, 43]. Among them, the atomic Reverse Monte Carlo method [44, 45] provides a maximum entropy solution to the problem of finding a molecular configuration that fits diffraction patterns within their errors. This method has been successfully used in the study of simple molecules such as water [6] or tetrahedral molecules [3, 37]. However, usually a careful preparation of the initial configuration is needed in order to be able to reproduce the experimental results. A preparation that, if not properly done, can be misleading in the case of complex molecules such as polyalcohols [7].

This problem of a strong dependence of the result on the initial choice of parameters is typical for fits with many parameters. In the case of Reverse Monte Carlo, the number of degrees of freedom of the system is extremely high because the description of the data is done by molecular configurations. To avoid this problem, we have developed an alternative Bayesian fit method to extract only the intramolecular structure from diffraction data. In this way, the amount

of parameters to describe a F-112 flexible molecule is reduced to only 23 (see below for the description of the parameters).

The classical approach to fit models to datasets is finding the parameters $\{P_i\}$ that minimizes the figure of merit χ^2. In contrast, Bayesian methods allow successive sets of parameters $\{P_i^{l+1}\}$, where l is a given step in the fit process, to be accepted with a probability

$$\mathcal{P}_{\text{accept}} = \exp\left[\frac{\chi^2\{P_i^{l+1}\} - \chi^2\{P_i^l\}}{2}\right] \quad . \tag{6.10}$$

This algorithm accepts parameters that do not decrease χ^2 if they are consistent with the data error bars.* From a geometrical point of view, the parameter values are allowed to go "uphill" in the $\chi^2\{P_i\}$ hypersurface. This method has two main consequences (i) The algorithm does not get stuck in local minima of the parameter space $\{P_i\}$ during the fit process. This is why the initial choice of the parameter values do not matter with this fit method [47]. ii) The results are described by means of probability distribution functions (PDF) that reflect all the complexity of the problem under study. This is because once the best fit is found, the program explores the whole parameter space compatible with the data and its errors. Note that in the following sections the word "parameter" will often be used instead of "parameter PDF" in a language abuse.

6.2.0.4.4 Fit function Independently from the choice of a Levenberg-Marquardt or a Bayesian approach to determine the best parameter set to describe the experimental data, a function has to be formulated that the algorithm should fit to the data. In our case, we have applied the Bayesian method to find molecular structures compatible with a diffraction pattern – simultaneously in reciprocal and in direct space.† This procedure helps to select the best set of parameters by optimizing the path used to approach the minimum in the χ^2 hypersurface.†

*See Appendix 6.2.0.4.4.

†See Appendix 6.2.0.4.5.

With respect to the first, in neutron diffraction of a molecular liquid the differential scattering cross section per atom can be separated into the q-dependent coherent contribution from different atomic sites and a constant term arising from other contributions [49]. Because the fit is intended to extract the intramolecular structure, in reciprocal space we will focus only on the intramolecular contribution of the aforementioned q-dependent term as performed previously [8–10, 50, 51],

$$\frac{1}{N}\left[\frac{d\sigma}{d\Omega}(q)\right]_{\text{coh}}^{\text{intra}} = \frac{1}{m}\sum_{i,j\neq i}^{m}\bar{b}_i\bar{b}_j^{*}\frac{\sin\left(qr_{ij}\right)}{\left(qr_{ij}\right)}\exp\left[-\left\langle\delta r_{ij}^2\right\rangle q^2/2\right] \quad , \quad (6.11)$$

where N is the total number of atoms in the sample, i and j are sites on the same molecule, m is the number of molecular sites, $\bar{b}_i$ is the coherent scattering length of the chemical species at site i, r_{ij} is the modulus of the mean separation between atoms i and j, and in the Debye-Waller term $\left\langle\delta r_{ij}^2\right\rangle = \left\langle u_i^2\right\rangle + \left\langle u_j^2\right\rangle$ where $\left\langle u_k^2\right\rangle$ $(k = i, j)$ is the mean squared vibrational amplitude for the atom at site k [49].

In the case of real space a radial distribution function, $\text{RDF}(r) \equiv 4\pi r^2\rho g(r)$, is used as defined in Ref. [49], derived from a Taylor series expansion of the distances through the quadratic terms of the displacements [52–56]. For distances compatible with those of the intramolecular structure [57],

$$\text{RDF}_{\text{calc}}(r) = P(r) + \frac{1}{B}\sum_{i,j\neq i}^{m}\bar{b}_i\bar{b}_j^{*}\frac{r}{r_{ij}}\frac{\exp\left[-\frac{1}{2}\frac{(r-r_{ij})^2}{\left\langle\delta r_{ij}^2\right\rangle}\right]}{\sqrt{2\pi\left\langle\delta r_{ij}^2\right\rangle}} \quad , \quad (6.12)$$

where $B = \frac{1}{m}\sum_{i,j\neq i}^{m}\bar{b}_i\bar{b}_j^{*}$ is a normalization constant, and $P(r)$ is a polynomial accounting for the density term $(4\pi\rho r^2)$ and any intermolecular contribution that is visible at the intramolecular length

scale. The introduction of this polynomial term is justified by the fact that the width of the first peak describing intermolecular structure (circa 2-3 Å) is at least an order of magnitude wider than those contributing to the intramolecular structure (between 0.01 Å and 0.1 Å), i.e., the peaks arising form the intramolecular structure are much sharper than the first one describing short range order (see for example Refs. [7, 37]).

Because changing the relative position of a single atom within the molecule will affect all interatomic distances r_{ij} related to that atom, those parameters have been reduced to a minimum set of independent variables, and since the fits are also performed taking into account molecular symmetries, the $m \cdot (m+1)$ parameters that would describe the molecular structure have been drastically diminished.

In order to obtain the experimental RDF from diffraction data, one needs to perform a Fourier transform of the measured scattering function (SF) to go from reciprocal space to real space. Unfortunately, the Fourier transformation of experimental data has two main well-known undesired effects in the RDF which are due to the finite experimentally available q-range: the peaks described by Eq. 6.12 are broadened, and a series of spurious peaks appears in addition to those defining molecular structure. The reason is that due to experimental limitations the recorded data is not only the SF but its product with $\Theta(q_{\max} - q)$, where Θ is the Heaviside step function representing the experimental window. Therefore, what is obtained in direct space is the convolution of the Fourier transformation of both functions [49]:

$$\mathrm{RDF}_{\mathrm{exp}}(r) = \mathrm{RDF}_{\mathrm{calc}}(r) \otimes \Theta'(r) \tag{6.13}$$

where $\Theta'(r) = [1 - \cos(q_{\max} r)]/r$ is the Fourier transform of $\Theta(q_{\max} - q)$.

The spurious peaks can be minimized (but not fully corrected) by previously applying a smoothing function to the SF that approaches zero for $q = q_{\max}$ but this solution has the drawback that the peaks are even more broadened in real space, smearing out intramolecular features [58]. Instead, we have carried out this convolution in real space to fully account for both effects (peak broadening and spurious peaks) of the limited reciprocal space accessible by the experiment [59, 60].†

The proposed algorithm to find the structure describing the data within their errors is implemented in the program FABADA [61], and it has already successfully been used to describe the dynamics from quasielastic neutron scattering experiments [62, 63] and from dielectric spectroscopy [64].

The intramolecular structure of F-112

The intramolecular structure of F-112 in the liquid phase has been determined by simultaneously fitting the experimental neutron diffraction SF and the RDF obtained from the Fourier transform of the data to assure the robustness of the best fit.[†,‡] For simplicity, the notation $l_{ij} \equiv \sqrt{\langle \delta r_{ij}^2 \rangle}$ has been used. The molecular parameters r_{ij} and l_{ij} follow the notation of the atoms in Fig. 6.34 and, since the two conformers have different molecular symmetries, the needed parameters are not the same. Distances related to atomic bonds and to atoms bonded to the same carbon have been considered common parameters to both conformers, and distances related to atoms bonded to different carbons have been separately fitted for each conformer (see Table 6.3).

Due to the symmetry of the trans conformer the dihedral angle between its atoms F–C–C–F has been assumed to be a distribution around 180°. The parameter α, shown in the inset of Fig. 6.35, has been used to fit the dihedral angle of the gauche conformer. In order to account for the fraction of the gauche and trans conformers in the liquid state, the parameter c_g has been introduced. It gives the gauche fraction (c_g) and the reciprocal fraction of trans ($1 - c_g$) in the liquid state. Thus, the total radial distribution function can be written as:

$$\mathrm{RDF}^{\mathrm{intra}} = (1 - c_g) \cdot \mathrm{RDF}_t^{\mathrm{intra}} + c_g \cdot \mathrm{RDF}_g^{\mathrm{intra}} \tag{6.14}$$

for the RDF, and correspondingly

$$\mathrm{SF}^{\mathrm{intra}} = (1 - c_g) \cdot \mathrm{SF}_t^{\mathrm{intra}} + c_g \cdot \mathrm{SF}_g^{\mathrm{intra}} \tag{6.15}$$

for the SF. It must be stressed that c_g and $1-c_g$ are in this equation, like all the parameters through the Bayesian method, probability distribution functions and not just scalars.†

Since we are interested in analysing the intramolecular part there is no interference between the scattering contributions of the distances between atoms in different molecules, therefore, a simple addition of each conformer contribution can be performed. However, this approach is based on the assumption that the molecules are either in the gauche or in the trans conformation and only a negligible amount is in a transition between the two. To address the point if the molecules are mainly present in the gauche or trans state, the probability $P_{\text{transition}}$ of finding a molecule in a transition state between the trans and gauche conformers at the highest point of the energy barrier, with respect to P_{conf}, the probability of finding it in a trans or gauche conformer, has been calculated: $P_{\text{transition}}/P_{\text{conf}} = \exp\left(\Delta H^*/k_B T\right) \approx 10^{-5} - 10^{-7}$ when taking the literature values for ΔH^*. We can therefore assess that molecules will be either in trans or gauche conformation.

This fact is also reflected in the molecular dynamics simulation, as can be clearly seen in Fig. 6.35 where only the dihedral angles corresponding to trans and gauche conformers are found. The weighting method to account for the contribution of each conformer to the RDF and to the SF has been tested using data from the simulation.‡

The values obtained from the *ab initio* simulation have been used as the initial parameters to fit simultaneously in direct and reciprocal space the composed diffraction functions (Eqs. 6.14 and 6.15). An excellent agreement with the experimental data is obtained for the whole experimental q-range (Fig. 6.36). The mean and standard deviations of the normal PDFs obtained from the fit of the diffraction data of the liquid phase together with the parameters obtained from *ab initio* calculations in the gas phase are compiled in Table 6.3. The molecular structure could be unambiguously determined from the experiment; of the dynamic parameters only the one related to the atomic vibrational amplitudes (l_{F2F}) could not. This is due to the

‡See Appendix 6.2.0.4.6.

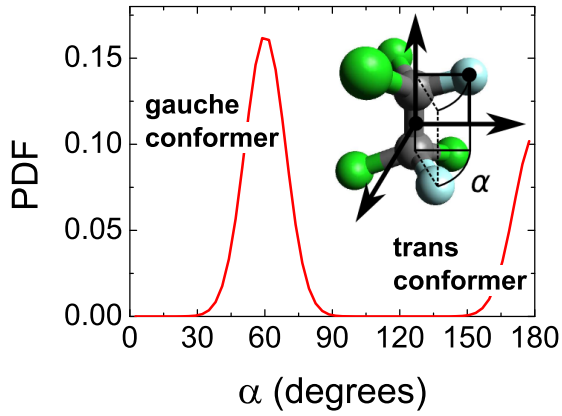

Figure 6.35: Probability distribution function (PDF) of the dihedral angle F–C–C–F of the F-112 molecule as extracted from the molecular dynamics simulation in the liquid state. Inset shows the definition of the dihedral angle α in a F-112 molecule.

small contribution that these atomic pairs have to the total intensity of the SF and the RDF.[†] Results summarized in Table 6.3 clearly show that the *ab initio* calculations (on vacuum) are substantially different.

One of the most remarkable result presented in Table 6.3 is that the obtained proportion of gauche conformer is (68±2)%. Taking into account the energy differences between trans and gauche conformers determined by previous experiments, this fraction should be between 60% and 62% at 310 K if the trans rotamer is assumed to be the most stable. Conversely, Fig. 6.37 shows that the c_g PDF is clearly peaked at 68%. In addition, this value is even higher than 2/3 which is the maximal value that could theoretically be reached at high temperatures if this were the case. On the other hand, if the gauche rotamer is assumed to have the lowest energy, the gauche fraction should be between 71% and 73%, and 2/3 would become the minimum theoretical value that could be reached at high temperatures, slightly below the actual observed value of the PDF peak.

Another way to lend further support to the hypothesis H_{free} of

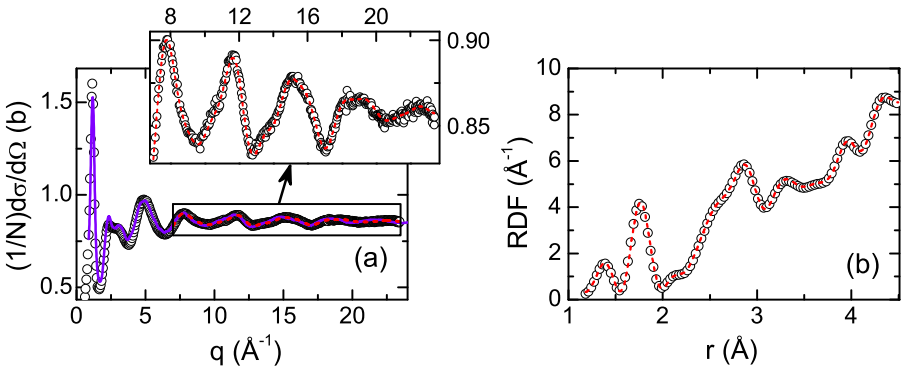

Figure 6.36: (a) Experimental SF of F-112 (circles) with its best fit (dashed orange line) in the range of higher q-values (here $7 - 23$ Å), where the intermolecular contribution is not significant, and the SF obtained by the molecular dynamics simulation (solid violet line). The inset zooms into the fitted portion of the experimental SF which is shown together with the best fit. (b) Experimental RDF (circles) with its best fit (dashed orange line) in the intramolecular distances domain. Note that the experimental RDF is the Fourier transform of the experimental SF and the fit is the calculated RDF convolved with Θ'.

having an additional parameter with any concentration PDF over the hypothesis $H_{2/3}$ of having a fixed gauche fraction of 2/3, is to compare the χ^2 PDFs of these two models [62]. As it can be seen in the inset of Fig. 6.37, the H_{free} model is preferred to the model $H_{2/3}$, because the χ^2 PDF has its peak at a smaller value.

This analysis provides strong indication that gauche is the more stable conformer in the F-112 liquid phase. Deviations of the gauche population from the expected values can be ascribed to possible differences in the short range order seen by trans and gauche molecules, that could energetically favour one or the other conformer. This being analogous to the effect produced on the energy difference of the conformers by different mixtures of solvents with a distinct dielectric constant, thus coupling its intramolecular structure with the surrounding intermolecular interactions [24, 25].

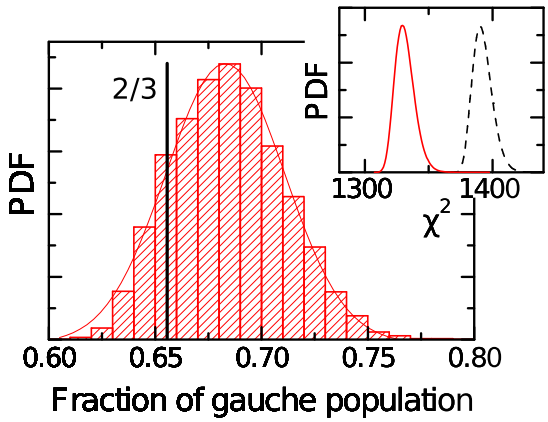

Figure 6.37: The probability density function (PDF) associated with the fraction of gauche conformer population in the sample c_g obtained from the fit to the experimental data. Inset shows the χ^2 PDF of hypothesis $H_{2/3}$ (dashed black line) and H_{free} (solid red line).

In order to ascertain the validity of the previously stated assumption concerning the proportion of the gauche conformer due to differences in the molecular ordering, a molecular dynamics simulation using flexible molecules was performed. The simulation yields the same result that is obtained by fitting experimental data: a large fraction of gauche conformer. The value of the gauche population obtained in the simulations is 74%, even higher than the one obtained experimentally, thus supporting the conclusion that gauche is the most stable conformer in the liquid phase. Last but not least, the agreement between experimental results and the simulations confers a reliable proof of the validity of the used method.‡

The intermolecular short range ordering of F-112

The first step to analyse the short range order of F-112 is to determine the number of molecules in the first coordination shell. The molecular coordination number was obtained through the integration of the RDF of the distances between the centres of mass (with respect to a

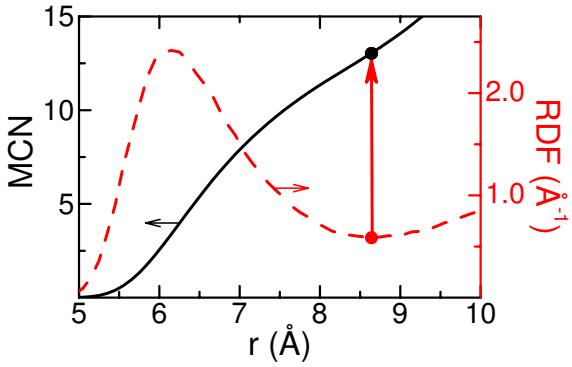

Figure 6.38: Radial distribution function (RDF) of the molecular centres of mass (dashed red line) together with the molecular coordination number (MCN) (solid black line) of F-112 from the molecular dynamics simulation. An upward arrow indicates the MCN value that corresponds to the RDF minimum, which was used to define the first neighbour shell. The corresponding MCN (black point) is 13.

central one). The number of molecules within the first coordination shell is 13 as can be seen in Fig. 6.38.

We analyze the differences between the relative positions of F-112 molecules in the first coordination shell around trans and gauche molecules. Figure 6.39 displays a scheme to define the angle ϕ used to analyse the short range order around each conformer. For both conformers ϕ is the equatorial molecular angle defined as the one between the reference molecule plane (defined by the C–C axis and a fluorine atom) and the neighbour molecule position plane (defined by the C–C axis of the reference molecule and the central point of the C–C axis in the neighbour molecule). This angle gives direct information about the arrangement of molecules. Roughly speaking, $\phi = 0°$ corresponds to configurations where neighbour molecules are in the direction of one of the fluorine atoms.

The PDF associated to the equatorial angle ϕ only for the first neighbour around trans and gauche conformers is depicted in Fig. 6.40. The ordering of the molecules is different around trans and gauche conformers as can be directly seen in the figure. Closest

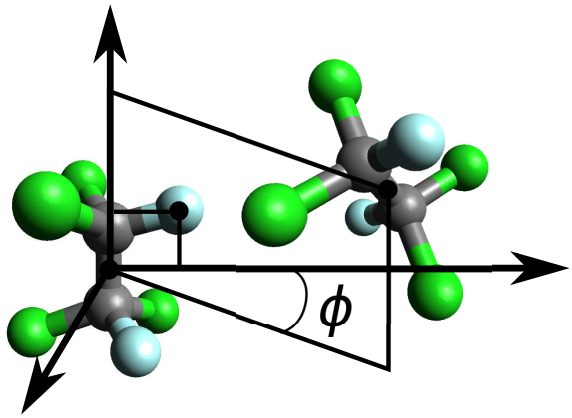

Figure 6.39: Scheme of the definition of the equatorial angle ϕ between the reference molecule plane and the position plane of the neighbour molecule in F-112. For both conformers the reference molecule plane is defined by the C–C axis and a fluorine atom, and the position plane of the neighbour molecule is defined by the C–C axis of the reference molecule and the central point of the C–C axis of the neighbour molecule. In the case of the trans conformer, the plane containing the other fluorine atom will be located at $\phi_F = 180°$ while, in the case of the gauche conformer, this plane will be located at an angle $\phi_F = \alpha$.

neighbours align preferably in the direction of the fluorine atoms, hence, due to the different geometries of both conformers, molecules tend to locate at $\phi = 0°$ and 180° around trans conformers, and at $\phi = 0 - 60°$ around gauche conformers (in the direction of the small region between the fluorine atoms). Both profiles reflect the symmetry of its conformer geometry, which is the plane going through the C–C axis with $\phi = 0°$ and 180° for the trans, and the plane going through the C–C axis with $\phi = 30°$ and 210° for the gauche.

It is now clear that there is a difference in the ordering of the first neighbouring molecules around a central trans or gauche conformer. How far does this difference reach? Figure 6.40 shows the probability density of finding a neighbour molecule at a certain angle ϕ around

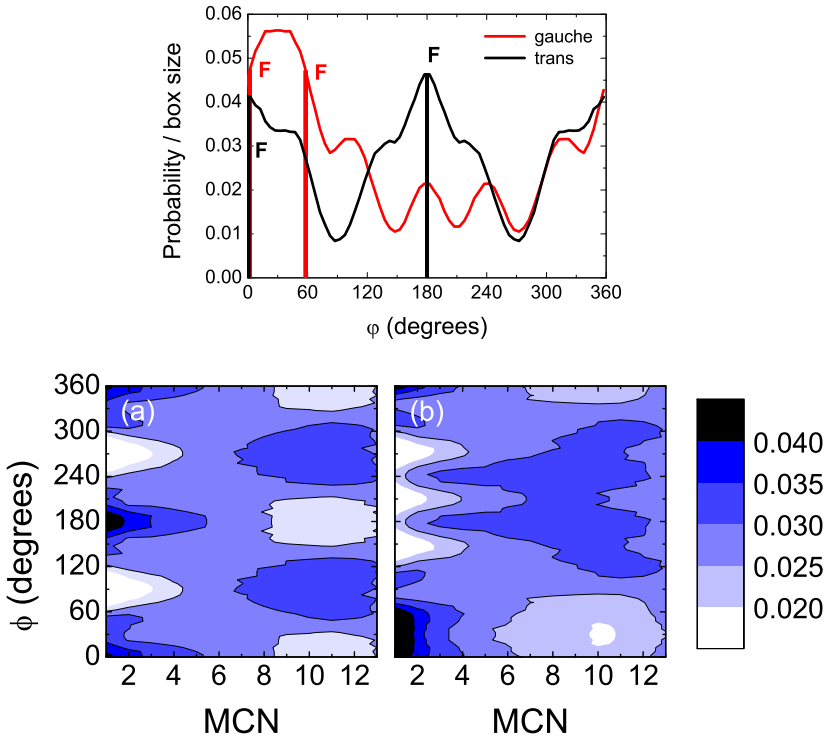

Figure 6.40: Top: Probability density of the equatorial angle of the central point ϕ of the first neighbour molecule (MCN = 1) surrounding trans (black lines) and gauche (red lines) conformers, extracted from the molecular dynamics simulation in the liquid state. Vertical lines show the direction in which the fluorine atoms are found for each conformer. Bottom: The same probability density as a function of MCN surrounding trans (a) and gauche (b) conformers (darker shade means higher probability).

a trans or a gauche reference molecule as a function of the molecular coordination number. This representation provides information at a first glance about the angular distribution of neighbouring molecules when moving away from the reference molecule, and thus gives a picture of the short range order inside the whole first coordination shell. A look to this figure readily tells us that the relative position of molecules is different for each conformer even at rather long distances from the reference molecule. As expected, at longer distances the molecular ordering starts to smear out but, even then, trans and gauche molecules try to fill the gaps that the closest neighbours left empty, so a difference in the molecular arrangement is still maintained, a phenomenon observed as well in carbon tetrachloride [37]. A complete characterization of the short range order of F-112 using this kind of bivariate analysis [66, 67] is being carried out, and additional differences in the relative orientation of molecules have already been found.

Concluding remarks

Concerning the intramolecular structure of F-112, it has been possible to show that within the liquid phase the gauche conformer represents $(68 \pm 2)\%$ of the molecular population, which supports the conclusion that it is the most stable conformer in the liquid phase.

The model with a distribution of an adjustable gauche conformer fraction is preferred over the model with a fixed fraction of 2/3, which is a reflection that the intra- and intermolecular degrees of freedom are deeply interwined in F-112. Thus, it is essential to use flexible molecular models that allow conformation population variability to get true insight on the behaviour of this compound.

Departure from the expected conformer population has been tentatively attributed to the difference in the short range order around trans and gauche molecules, that energetically favours one of the conformers, coupling intra- and intermolecular interactions. It has been shown through the analysis of molecular dynamics simulations that the first neighbour molecules tend to locate in the direction of the fluorine atoms, therefore a different molecular short range order-

ing around trans and gauche molecules is induced by each conformer geometry. Angular distribution differentiates trans and gauche rotamers up to relatively long distances because, even when defined positions start to blur, since F-112 molecules fill the gaps that the closest neighbours did not occupy, a contrast is still preserved.

Successful use of this Bayesian analysis based method to determine the molecular structure from diffraction data, through the fit of not only the experimentally obtained SF in the reciprocal space, but also simultaneously the RDF in the real space obtained through Fourier transformation, will help to pave the way to understanding the molecular structures and the short range order in complex disordered systems.

Acknowledgments

This work was supported by the Spanish Ministry of Science and Innovation (FIS2008-00837) and by the Government of Catalonia (2009SGR-1251).

We would like to thank one of the reviewers for his/her suggestions, that significantly increased the accessibility of the article, and for the additional validation tests proposed, which assured a stronger robustness of the fitting method introduced in this work.

Appendix: Calculating the error in Fourier transformations

Errors associated with the data play a major role in the proposed fit scheme to obtain molecular structure parameters because they regulate the capability of the program to go uphill in the $\chi^2\{P_i\}$ hypersurface.

Because the method is optimized by the simultaneous fit of the functions in both the reciprocal and the direct space, it is not enough to know the experimental error from the measured SF, it is also necessary to calculate the errors of the RDF obtained after Fourier transforming the experimental data and convolving with Θ'. And since this is not an obvious calculation, it is explained in detail in this Appendix.

Errors have been calculated following two alternative approaches: by error propagation of the discretised Fourier transform and by using a Monte Carlo method [68].

The discretised version of the Fourier transform that has been applied to the experimental SF to obtain the RDF is

$$\mathrm{RDF}_{\mathrm{exp}}(r) = 4\pi\rho r^2 + \frac{2r}{\pi}\sum_{k=1}^{n} q_k F_{\mathrm{exp}}(q_k)\sin(q_k r)\Delta q \tag{6.16}$$

where $k = 1, \ldots, n$ are the experimental points, Δq is the sampling interval and F_{exp} is the differential scattering cross section per atom subtracted by the constant term $\overline{\sigma}_{\mathrm{scatt}}/4\pi$, the average scattering cross section $\overline{\sigma}_{\mathrm{scatt}}$. If the theory of error propagation is applied to Eq. 6.16 and it is assumed that errors are normally distributed, a relationship is obtained between the errors of the SF and the RDF:

$$\varepsilon_{\mathrm{RDF}(r)} = \varepsilon_{F(q)}\sum_{k=1}^{n}\frac{2}{\pi}(q_k r)\sin(q_k r)\Delta q \quad . \tag{6.17}$$

Errors in the RDF calculated in this way have been plotted in Fig. 6.41(b) and are essentially linear with respect to r (the slight sinusoidal modulation can barely be seen).

The Monte Carlo method to calculate errors consists in Fourier transforming SFs generated with normally distributed random points and obtain the PDFs of the points in real space as a function of r after a number of SFs have been generated and Fourier transformed in this manner. A single example of such a SF and several RDFs corresponding to Fourier transformation of different SF are shown in Figs. 6.41(a) and (b), respectively. The PDFs of the points have been calculated in this case after Fourier transformation of 1000 random SFs. As it can be seen in the inset of Fig. 6.41(b), normal distributions for the data were obtained in real space as well allowing thus to calculate errors using Eq. 6.17. The error at each point has been obtained from the standard deviation of its normal distribution and they have been plotted in Fig. 6.41(b) together with the errors calculated from error propagation. As we can see in the figure, both methods lead to the

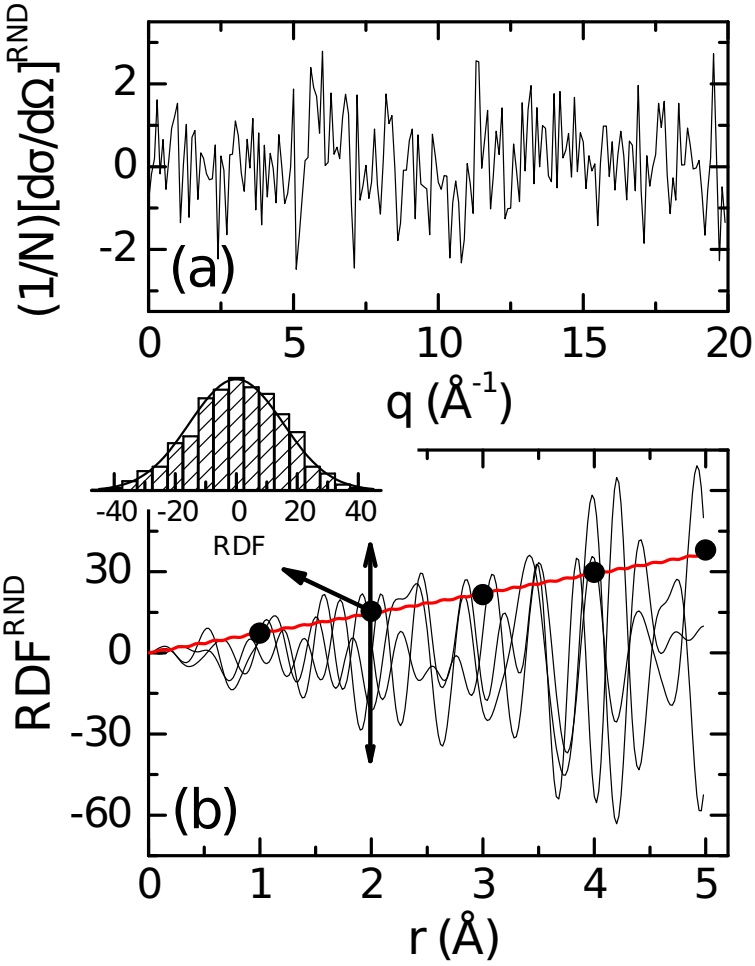

Figure 6.41: (a) Scattering function S^{RND} generated as normally distributed data points. (b) Several $\mathrm{RDF}^{\mathrm{RND}}$ obtained from Fourier transforming different S^{RND} like the one in (a) (thin black lines), errors calculated by Monte Carlo simulation (points) and by error propagation (thick red line). The inset represents the distribution of $\mathrm{RDF}^{\mathrm{RND}}$ values at a single point obtained by Fourier transforming 1000 S^{RND}, showing that data are also normally distributed in real space.

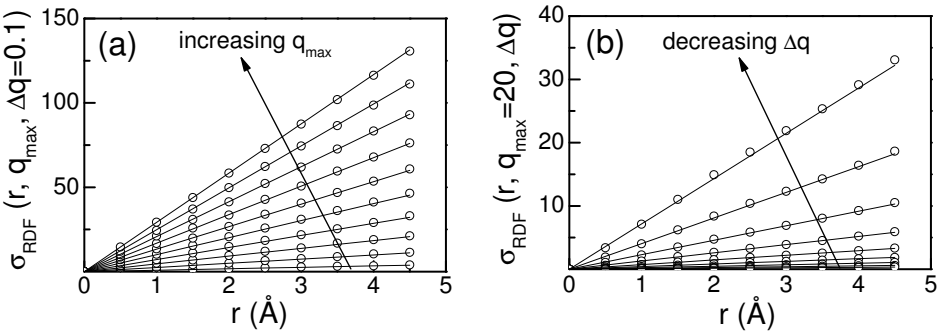

Figure 6.42: Calculation of RDF errors after Fourier transformation of the SF using error propagation of random data with a normal distribution (dots) and convenient estimation of these errors through Eq. 6.18 (lines). Errors have been calculated as a function of q_{max} with Δq fixed (a) and vice versa (b).

same result (points from Monte Carlo calculation lie on top of the curve from error propagation) despite the fact that the Monte Carlo method needs a considerably greater computational effort.

Using the error propagation method, a grid of the RDF error as a function of r, Δq, and q_{max} has been calculated. Figure 6.42 shows two series of error calculations: for fixed Δq and for fixed q_{max} (points in Figs. 6.42(a) and 6.42(b), respectively).

From the calculated $\varepsilon(r, \Delta q, q_{max})$ at different $q_{\max}$ and Δq, the following relationship has been obtained:

$$\varepsilon_{\mathrm{RDF}}(r) = m(q_{\max}, \Delta q) \cdot r \tag{6.18}$$

where the value of the slope $m(q_{\max}, \Delta q)$ satisfies the empirical equation $\log_{10} m = 1.5341 \cdot \log_{10} q_{\max} + 0.495 \cdot \log_{10} \Delta q - 0.646$. The advantage of using this equation is that since $q_{\max}$ and Δq are usually constant parameters in diffraction experiments, $m(q_{\max}, \Delta q)$ has to be computed only once.

The errors obtained using the proposed relationship have also been plotted in Fig. 6.42 as straight lines. Excellent agreement between both validates the proposed relationship as a convenient way

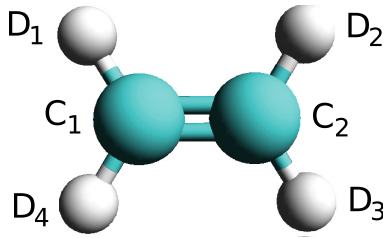

Figure 6.43: Structure of the ethene molecule used to validate the proposed algorithm, together with the name convention used in Table 6.4.

to estimate errors of RDFs obtained through the Fourier transform of experimental SFs.

Appendix: Bayesian fit method validation

In order to attest the validity and robustness of the proposed fit method to obtain molecular structure parameters from diffraction data, the whole process will be performed to two known samples so that the outcome of the fit can be compared to the real values.

6.2.0.4.5 Fitting a synthetic test molecule The sample used for this test consists on a generated SF dataset corresponding to a deuterated ethene molecule (see Fig. 6.43) with a known geometry. The SF has been generated using Eq. 6.11 without the polynomial term $P(r)$ and adding normally distributed random numbers to those values so that the error associated with the generated experimental dataset is $\sigma = 0.002$. The geometric parameters used to build the molecule, listed in Table 6.4, do not exactly correspond to the empirical ones. Once the distance between carbon atoms r_{CC} and between carbon and deuterium atoms r_{CD}, and the angle between two deuterium atoms bonded to the same carbon α_{DCD} are known, the structure of this molecule can be fully determined. Furthermore, as far as the vibrational parameters l_{ij} are concerned, only six have been considered independent after taking into account the molecular symmetry.

Table 6.4: Comparison of the parameters used to generate the ethene molecular data (interatomic distances r_{ij} and angle α_{ijk}, and vibrational parameters l_{ij}) with the mean and standard deviation of the normal distributions of the parameters obtained from the fits. Lengths are in Å and angles in degrees.

Parameter	Seed values	Fit values
$r_{C_1C_2}$	1.3	1.294 ± 0.004
$r_{C_1D_1}$	1.1	1.100 ± 0.001
α_{DCD}	117.0	116.9 ± 0.4
$l_{C_1C_2}$	0.05	see Fig. 6.46
$l_{C_1D_1}$	0.1	0.103 ± 0.001
$l_{C_1D_2}$	0.1	0.098 ± 0.003
$l_{D_1D_4}$	0.1	0.107 ± 0.005
$l_{D_1D_2}$	0.2	0.200 ± 0.010
$l_{D_1D_3}$	0.2	0.200 ± 0.015

In Fig. 6.44 we show the RDF of ethene obtained by Fourier transformation of the constructed experimental SF and the RDF obtained directly from the model (calculated using the seed parameters of Table 6.4 in Eq. 6.12) after convolving the model with Θ'. Good agreement of the latter (see inset in Fig. 6.44) supports the validity of both, the Taylor approximation in Eq. 6.12, and the method accounting for the truncation effects in the SF.

Two ways of fitting the generated data have been undertaken to check the suitability of the proposed method: using only the SF, and using both the SF and the RDF. As it can be seen in Fig. 6.45(a), although both methods are able to describe the data within experimental error, the second method leads to a smaller χ^2 value for the SF (inset in this figure). In order to clarify why fitting in both direct and reciprocal space is more desirable than just in reciprocal space, we have plotted in Fig. 6.45(b) the RDFs obtained with the fit of only the SF and the fit where direct and reciprocal space were simultaneously used. As it can readily be seen in this figure, very similar

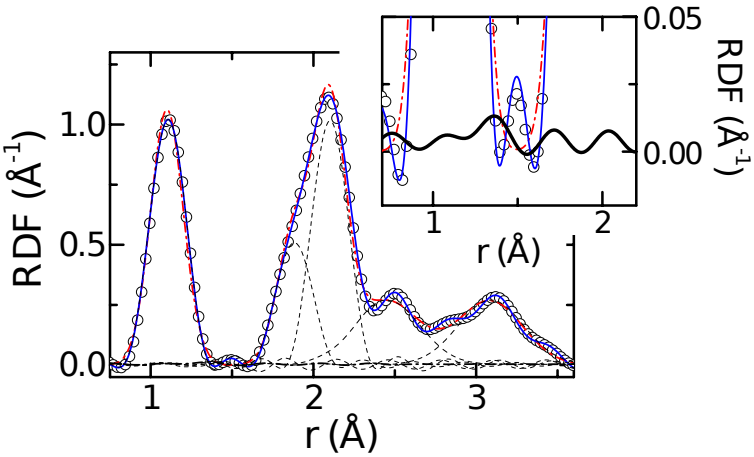

Figure 6.44: RDF of ethene obtained by Fourier transformation of the generated SF (circles), RDF calculated directly using the model (dash-dot red line), and RDF obtained through the convolution of the model with Θ' (solid blue line). Dashed black lines are individual contributions from the different atomic pairs (also convolved with Θ'). Inset zooms the part of the RDF where the small r_{CC} contribution is located (solid black line).

functions in reciprocal space (both of them fit the SF data within the error) may be completely different in real space, leading in some extreme cases as this one to results devoid of physical meaning. That is because the profile of the $\chi^2\{P_i\}$ hypersurface is different in reciprocal and direct space, and since the parameters we are using for the fit are natural real space magnitudes their minima appear better defined in real space. Fitting in both spaces at the same time helps thus to select the sets of parameters that are more likely to yield a closer description to the real system. Consequently, fits were performed hereafter in this way.

Figure 6.46 shows the PDFs as a function of rescaled parameters (r_{CC}, r_{CD}, α_{DCD}) with respect to their maximum probability values. Figure 6.46(a) clearly evidences that PDFs are well described by normal distributions. Errors were calculated as usual in these PDFs, i.e.,

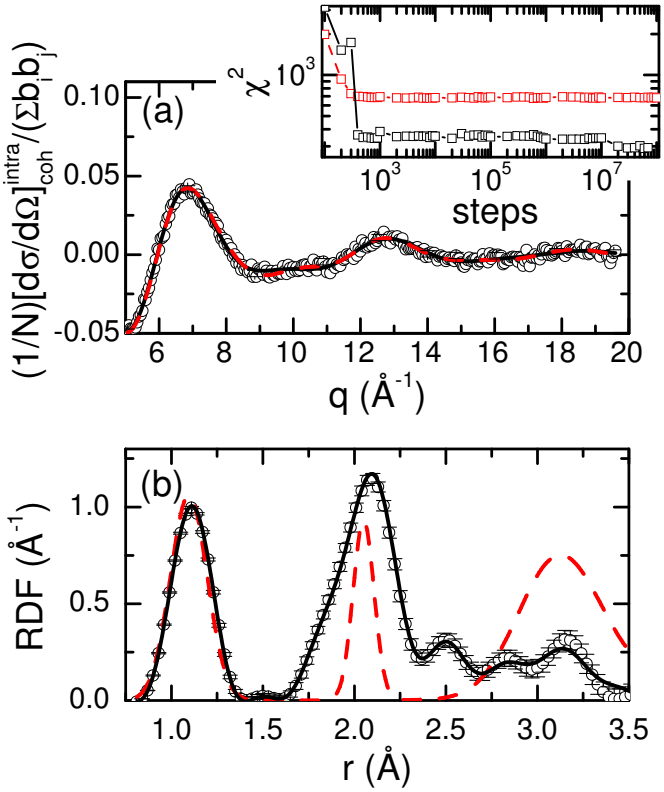

Figure 6.45: Best fits of the generated molecular structure of ethene (black circles) using only the SF (dashed red line) or using both the SF and the RDF (solid black line) of the generated dataset. Normalized SFs are shown in (a) and RDFs in (b). Inset shows in semilogarithmic scale the χ^2 evolution of the SF through the fit process using one or both functions.

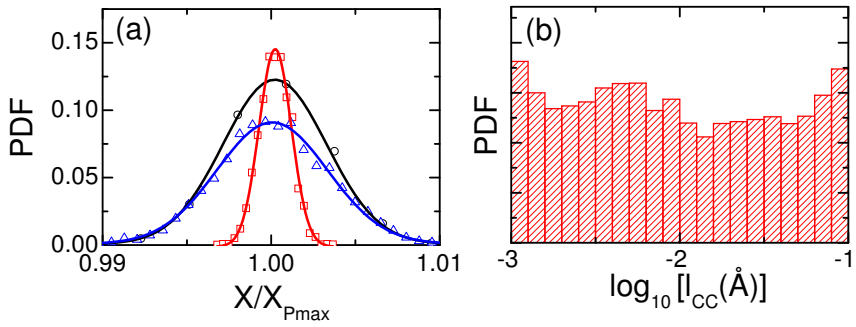

Figure 6.46: (a) PDFs obtained for the structural parameters of ethene, x-axis rescaled by the most probable value of each parameter (r_{CD} red squares, r_{CC} black circles and α_{DCD} blue triangles). (b) PDF obtained for l_{CC}, the vibrational parameter of the two carbon atoms of ethene.

one standard deviation from the mean of the PDF containing 68% of values.

The same conclusion (not shown) has been obtained for the vibrational l_{ij} parameters (Table 6.4), except l_{CC}, which could not be described at all by a normal distribution. Because not even the length scale of l_{CC} could be determined, a maximum ignorance prior distribution in logarithmic scale, or Jeffreys prior [69], has been used to calculate its PDF, which is shown in Fig. 6.46(b). From the figure it is clear that it makes no sense to give a value to this parameter, because any l_{CC} will be able to fit both the SF and RDF equally well within the error. In order to further understand this fact, a zoom of the area in the RDF where this peak is located has been displayed in the inset of Fig. 6.44. The contribution of the carbon-carbon term is so small that the peak can barely be distinguished in this figure, that is the reason why l_{CC} can not be determined. Nevertheless, we would like to point out that, even if this peak is not visible, since the fit is performed taking into account the whole molecular geometry and differences in the distance between carbon atoms induce changes in the positions of many other peaks, it has been possible to accurately determine the parameter r_{CC} concerning the peak position of

the distance between carbon atoms contribution.

6.2.0.4.6 Fitting the intramolecular parameters from a molecular dynamics simulation The mathematical procedure, i. e., the fit method and the way it has into account termination effects of experimental data, has been already tested in the preceding section using a synthetic dataset generated from a reasonably simple known molecular geometry. Nevertheless, it would be useful to test the validity of the method from a dataset, not directly obtained from a mathematical description of a known geometry, but from a situation much closer to the experiment.

In this test the known sample will be the SF and RDF datasets obtained from the F-112 molecular dynamics simulation. The molecular structure obtained from the SF fit will be compared to the molecular parameters that have been used in the simulation. Special attention has been devoted to test if the fit procedure is able to obtain the parameter accounting for the concentration of gauche conformer c_g. That is to say, whether the existence of two conformers with two different geometries can be accounted by generating a function weighted by that concentration PDF (see Eqs. 6.14 and 6.15), in Fig. 6.47(a) we show the excellent agreement between the SF obtained from the simulation and its best fit obtained using the proposed algorithm. The intramolecular parameters used in the simulation and those obtained from the fit procedure are in all cases compatible with the errors.

To quantify the discrepancies between the original intramolecular structure and the parameters obtained from the fit, we introduce the relative error calculated as $(P_{\mathrm{MD}} - P_{\mathrm{fit}})/P_{\mathrm{MD}}$, where P_{MD} are the parameters that have been used in the molecular dynamics simulation, and P_{fit} are the parameters obtained from the fit of the SF produced by the simulation. This relative error ranges from 0.03% to 0.5% for the intramolecular distances, and from 0.6% to 13% for the vibrational parameters. As discussed in the previous section, vibrational parameters are in first approximation uncorrelated for every atomic pair, and are thus subjected to a greater error. This error is greatly increased, even to the extreme of avoiding its determination, if the

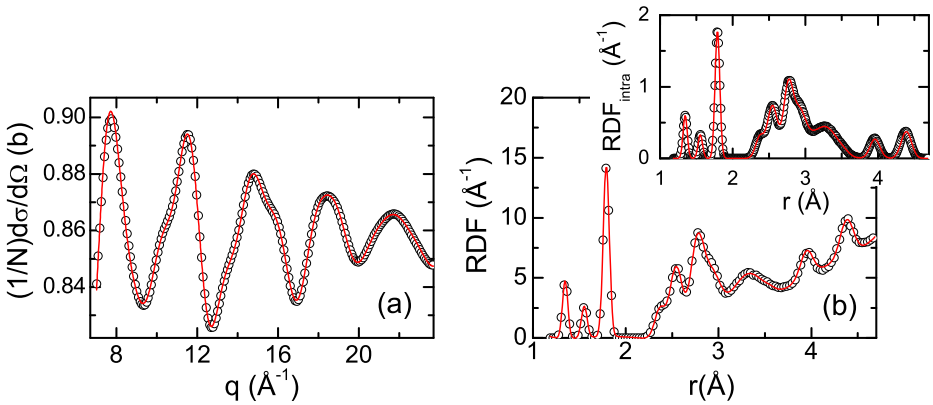

Figure 6.47: Scattering function (a) and Radial distribution function (b) obtained from the molecular dynamics simulation (black circles) together with the best SF fit obtained through the proposed algorithm (red line). The inset shows the RDF intramolecular contribution of the simulation, together with the RDF calculated from the parameters of the SF best fit.

atomic pair contribution to the total SF is small. Concerning the gauche conformer concentration, the determination from the fit has a relative error of 2%, a value which lays within the c_g error given by its resolved PDF. Therefore we conclude that Eq. 6.11 correctly describes the data, and that the fit procedure is able to reproduce the original values used in the molecular dynamics simulation, including the gauche conformer fraction.

In order to verify whether Eq. 6.12 is a valid approximation, we have also calculated the intramolecular RDF shown in the inset of Fig. 6.47 using the parameters that have been obtained through the fit of the SF. The resemblance between the intramolecular RDF calculated from the simulation and the one calculated from the SF fit is virtually perfect, thus evidencing that the approximation in Eq. 6.12 used to describe the RDF is appropriate. Moreover, we have also tested which is the effect of modelling the intermolecular contribution as a polynomial, as it is performed in our work with the real data. The fit obtained using this approximation is extremely good,

as it can be seen in Fig. 6.47(b). The parameters determined from this fit are again close to those used in the simulation. In this case, the relative errors of the distances range from 0.1% to 3%, errors from the vibrational parameters range from 0.6% to 7%, and error in the gauche concentration is about 2%, all of them within the error bars of the fit determination.

6.2.0.4.7 Validation summary The tests performed using a generated ethene SF and RDF datasets, and that performed on molecular dynamics data, allow to conclude the following:

- We properly accounted for finite information effects of experimental data (termination effects of the SF).
- The approximation used to describe the RDF derived from a Taylor series expansion of the distances through the quadratic terms of the displacements is valid.
- The fit procedure is robust both determining intramolecular distances and rotamer concentrations, due to the fact that these parameters are strongly interrelated. Even distances whose contribution can not be observed neither in the SF nor the RDF can be determined due to their dependence on the remaining intramolecular distances.
- Vibrational parameters may be determined only if their contribution is significant enough. But in any case, the obtained PDFs using the proposed method allow, at least, to limit their values.
- A polynomial can be used to model the intermolecular contribution to the RDF, with the drawback of slightly increasing the associated errors of the intramolecular parameters. Concerning the particular case of F-112, the modelling carried out to have into account the rotamer population in the calculation of the SF and the RDF has been successfully established by weighting each conformer contribution by its concentration.

References

All online references accessed on July 22, 2014.

[1] A. H. Narten, M. D. Danford, and H. A. Levy, J. Chem. Phys., **46**, 4875 (1967).

[2] P. A. Egelstaff, D. I. Page, and J. G. Powles, Mol. Phys., **20**, 881 (1971).

[3] Sz. Pothoczki, L. Temleitner, P. Jovari, S. Kohara, and L. Pusztai, J. Chem. Phys., **130**, 064503 (2009).

[4] L. Pusztai and R. L. McGreevy, J. Chem. Phys., **125**, 044508 (2006).

[5] A. K. Soper, J. Phys.-Condens. Mat., **22**, 404210 (2010).

[6] L. Pusztai, Phys. Rev. B, **60**, 11851 (1999).

[7] A. Vrhovsek, O. Gereben, Sz. Pothoczki, M. Tomsic, A. Jamnik, S. Kohara, and L. Pusztai, J. Phys.-Condens. Mat., **22**, 404214 (2010).

[8] A. Adya, L. Bianchi, and C. Wormald, J. Chem. Phys., **112**, 4231 (2000).

[9] C. Talón, F. J. Bermejo, C. Cabrillo, G. J. Cuello, M. A. González, J. W. Richardson, A. Criado, M. Ramos, S. Vieira, F. L. Cumbrera, and L. M. González, Phys. Rev. Lett., **88**, 115506 (2002).

[10] G. Venturi, F. Formisano, G. J. Cuello, M. R. Johnson, E. Pellegrini, U. Bafile, and E. Guarini, J. Chem. Phys., **131**, 034508 (2009).

[11] M. K. Transtrum, B. B. Machta, and J. P. Sethna, Phys. Rev. Lett., **104**, 060201 (2010).

[12] T. Bayes and R. Price, Philos. T., **53**, 370 (1763).

[13] L. C. Pardo, M. Rovira-Esteva, S. Busch, M. D. Ruiz-Martín, J. Ll. Tamarit, and T. Unruh, (2009), arXiv: 0907.3711v3 [physics.data-an] .

[14] "Hyperchem Professional 7.51," Hypercube, Inc., 1115 NW 4th

Street, Gainesville, Florida 32601, USA.

[15] R. A. Newmark and C. H. Sederhol, J. Chem. Phys., **43**, 602 (1965).

[16] R. A. Newmark and R. E. Graves, J. Phys. Chem., **72**, 4299 (1968).

[17] R. E. Kagarise and L. W. Daasch, J. Chem. Phys., **23**, 113 (1955).

[18] R. A. Pethrick and E. Wynjones, J. Chem. Soc. A, 54 (1971).

[19] K. Kishimoto, H. Suga, and S. Seki, Bull. Chem. Soc. Jpn., **51**, 1691 (1978).

[20] S. Wolfe, Acc. Chem. Res., **5**, 102 (1972).

[21] R. C. Bingham, J. Am. Chem. Soc., **98**, 535 (1976).

[22] J. R. Durig, J. Liu, T. S. Little, and V. F. Kalasinsky, J. Phys. Chem., **96**, 8224 (1992).

[23] R. J. Abraham and K. Parry, J. Chem. Soc. B, 539 (1970).

[24] R. J. Abraham and M. A. Cooper, Chem. Commun., 588 (1966).

[25] R. J. Abraham and M. A. Cooper, J. Chem. Soc. B, 202 (1967).

[26] F. Affouard, E. Cochin, F. Danede, R. Decressain, M. Descamps, and W. Haeussler, J. Chem. Phys., **123**, 084501 (2005).

[27] L. C. Pardo, P. Lunkenheimer, and A. Loidl, J. Chem. Phys., **124**, 124911 (2006).

[28] L. C. Pardo, F. J. Bermejo, J. Ll. Tamarit, G. J. Cuello, P. Lunkenheimer, and A. Loidl, J. Non-Cryst. Solids, **353**, 999 (2007).

[29] M. Rovira-Esteva, L. C. Pardo, J. Ll. Tamarit, and F. J. Bermejo, in *Metastable Systems under Pressure*, NATO Science for peace and Security Series: A. Chemistry and Biology, edited by S. J. Rzoska, A. Drozd-Rzoska, and V. Mazur (Springer Netherlands, 2009) pp. 63–77.

[30] M. J. Frisch, G. W. Trucks, H. B. Schlegel, G. E. Scuseria, M. A. Robb, et al, "Gaussian 03, Revision B.05," Gaussian, Inc., Pitts-

burgh, PA, 2003.

[31] J. M. Wang, R. M. Wolf, J. W. Caldwell, P. A. Kollman, and D. A. Case, J. Comput. Chem., **25**, 1157 (2004).

[32] C. M. Breneman and K. B. Wiberg, J. Comput. Chem., **11**, 361 (1990).

[33] D. A. Case, I. T. E. Cheatham, C. L. Simmerling, J. Wang, R. E. Duke, et al, *AMBER 8*, University of California, San Francisco, CA (2004).

[34] P. M and R. A, Phys. Rev. Lett., **45**, 1196 (1980).

[35] F. Hovorka and F. E. Geiger, J. Am. Chem. Soc., **55**, 4759 (1933).

[36] H. E. Fischer, G. J. Cuello, P. Palleau, D. Feltin, A. C. Barnes, Y. S. Badyal, and J. M. Simonson, Appl. Phys. A: Mater. Sci. Process., **74**, S160 (2002).

[37] L. C. Pardo, J. Ll. Tamarit, N. Veglio, F. J. Bermejo, and G. J. Cuello, Phys. Rev. B, **76**, 134203 (2007).

[38] G. J. Cuello, J. Phys.-Condens. Mat., **20**, 244109 (2008).

[39] M. Howe, R. McGreevy, and P. Zetterström, *Computer code CORRECT, correction program for neutron diffraction data* (1996), NFL Studsvik internal report.

[40] G. Placzek, Phys. Rev., **86**, 377 (1952).

[41] R. Trotta, Contemp. Phys., **49**, 71 (2008).

[42] D. S. Sivia, C. J. Carlile, W. S. Howells, and S. Konig, Physica B, **182**, 341 (1992), International Workshop On Quasielastic Neutron Scattering, Windsor, England, Apr 06-07, 1992.

[43] S. Bacallado, J. D. Chodera, and V. Pande, J. Chem. Phys., **131**, 045106 (2009).

[44] R. L. McGreevy, J. Phys.-Condens. Mat., **13**, R877 (2001).

[45] R. L. McGreevy and L. Pusztai, Mol. Sim., **1**, 359 (1988).

[46] See Appendix 6.2.0.4.4.

[47] L. C. Pardo, M. Rovira-Esteva, S. Busch, J.-F. Moulin, and

J. Ll. Tamarit, Phys. Rev. E, **84**, 046711 (2011).

[48] See Appendix 6.2.0.4.5.

[49] H. E. Fischer, A. C. Barnes, and P. S. Salmon, Rep. Prog. Phys., **69**, 233 (2006).

[50] F. Leclerq, P. Damay, M. Founaki, P. Chieux, M. C. Bellissent-Funel, A. Rassat, and C. Fabre, Phys. Rev. B, **48**, 2748 (1993).

[51] M. Kreitmeir, G. Heusel, H. Bertagnolli, K. Todheide, C. J. Mundy, and G. J. Cuello, J. Chem. Phys., **122**, 154511 (2005).

[52] R. James, Phys. Z., **33**, 737 (1932).

[53] M. Iwasaki, S. Nagase, and R. Kojima, Bull. Chem. Soc. Jpn., **30**, 230 (1957).

[54] J. Karle, *Diffraction studies on non-crystalline substances*, edited by I. Hargittai and W. J. Orville-Thomas (Elsevier, Amsterdam, and Akadémiai Kiadó, Budapest, 1981) pp. 243–267.

[55] M. Alvarez, F. J. Bermejo, P. Chieux, E. Enciso, J. Alonso, and N. Garcia, J. Phys.-Condens. Mat., **1**, 8595 (1989).

[56] P. Rozier, A. Burian, and G. J. Cuello, J. Non-Cryst. Solids, **351**, 632 (2005).

[57] K. A. Johnson and W. S. Howells, J. Phys.-Condens. Mat., **11**, 9239 (1999).

[58] E. Lorch, J. Phys. Part C Solid, **2**, 229 (1969).

[59] I. Petri, P. S. Salmon, and H. E. Fischer, Phys. Rev. Lett., **84**, 2413 (2000).

[60] J. Waser and V. Schomaker, Rev. Mod. Phys., **25**, 671 (1953).

[61] L. C. Pardo, http://gcm.upc.edu/members/luis-carlos/bayesiano *FABADA (Fitting Algorithm for Bayesian Analysis of DAta)* (2009).

[62] S. Busch, C. Smuda, L. C. Pardo, and T. Unruh, J. Am. Chem. Soc., **132**, 3232 (2010).

[63] M. Rovira-Esteva, A. Murugan, L. C. Pardo, S. Busch, M. D. Ruiz-Martin, M. S. Appavou, J. Ll. Tamarit, C. Smuda, T. Un-

ruh, F. J. Bermejo, G. J. Cuello, and S. J. Rzoska, Phys. Rev. B, **81**, 092202 (2010).

[64] J. C. Martinez-Garcia, J. Ll. Tamarit, L. C. Pardo, M. Barrio, S. J. Rzoska, and A. Droz-Rzoska, J. Phys. Chem. B, **114**, 6099 (2010).

[65] See Appendix 6.2.0.4.6.

[66] L. C. Pardo, M. Rovira-Esteva, J. Ll. Tamarit, N. Veglio, F. J. Bermejo, and G. J. Cuello, in *Metastable Systems under Pressure*, NATO Science for peace and Security Series: A. Chemistry and Biology, edited by S. J. Rzoska, A. Drozd-Rzoska, and V. Mazur (Springer Netherlands, 2009) pp. 79–91.

[67] P. Jedlovszky, A. Vincze, and G. Horvai, Phys. Chem. Chem. Phys., **6**, 1874 (2004), 81st International Bunsen Discussion Meeting on Interfacial Water in Chemistry and Biology, Velen, Germany, Sep 19-23, 2003.

[68] J. M. Fornies-Marquina, J. Letosa, M. Garcia-Gracia, and J. M. Artacho, IEEE T. Magn., **33**, 1456 (1997).

[69] H. Jeffreys, *Theory of Probability* (Clarendon Press, Oxford, 1939).

6.3 Fits and model selection with a Bayesian approach

The frequentist approach to fits is extensively used in all fields of science but it has a series of limitations: a) It assumes experimental data errors with a normal distribution, parameters with symmetric errors, a quadratic functional dependence with χ^2, and a unique solution (never multimodal distributions). b) The iterative Levenberg-Marquardt algorithm can only find the local minimum in the region where its initialization values are located, thus, the choice of those values is critical to find the global minimum, and often involves non-trivial guessing. c) Parameter correlations evaluated through the covariance matrix are often overlooked, resulting in underestimated errors.

The purpose of this research was to develop a fit method and quantitative model selection scheme that allowed to express the whole complexity of the scientific problems, and that took into account the experimental limitations of the data, using the minimum number of assumptions possible. The developed method based on the Bayesian approach overcomes the aforementioned limitations and yields results in the form of probability distribution functions, which are able to reflect this complexity. No assumptions are needed, but they can be included in the analysis if desired. Additionally, quantitative model selection is inbuilt within the algorithm.

Results were presented in several conferences, and published mainly in the articles: L. C. Pardo, M. Rovira-Esteva, S. Busch, M. D. Ruiz-Martín, et al., Bayesian Analysis of QENS data: From parameter determination to model selection, arXiv:0907.3711v3 [physics.data-an] (2009); L. C. Pardo, M. Rovira-Esteva, S. Busch, M. D. Ruiz-Martín, et al, J. Phys.: Conf. Ser. **325**, 012006 (2011); and L. C. Pardo, M. Rovira-Esteva, S. Busch, J.-F. Moulin, et al, Phys. Rev. E **84**, 046711 (2011).

TOPIC 5: Bayesian Analysis of QENS data: From parameter determination to model selection

L. C. Pardo,[1] M. Rovira-Esteva,[1] S. Busch,[2] M. D. Ruiz-Martín,[1] J. Ll. Tamarit,[1] and T. Unruh,[2]

[1]Grup de Caracterització de Materials, Departament de Física i Enginyeria Nuclear, ETSEIB, Universitat Politècnica de Catalunya, Diagonal 647, E-08028 Barcelona, Catalonia, Spain

[2]Physik Department E13 and Forschungs-Neutronenquelle Heinz Maier-Leibnitz (FRM II), Technische Universität München, Lichtenbergstr. 1, D-85748 Garching, Germany

Eprint: **arXiv: 0907.3711v3 [physics.data-an]**
URL: http://arxiv.org/abs/0907.3711v3

Abstract

The extraction of any physical information from quasielastic neutron scattering spectra is generally done by fitting a model to the data by means of χ^2 minimization procedure. However, as pointed out by the pioneering work of D.S. Sivia et al. [1], also another probabilistic approach based on Bayes theorem [2] can be employed. In a nutshell, the main difference between the classical χ^2 minimization and the Bayesian approach is the way of expressing the final results: In the first case, the result is a set of values of parameters with a symmetric error $(P_i \pm \varepsilon_i)$ and a figure of merit such as χ^2, whereas in the second case the results are presented as probability distribution functions (PDF) of both, parameters and merit figure. In this contribution, we demonstrate how final PDFs are obtained by exploring all possible combinations of parameters that are compatible with the experimental error. This is achieved by allowing the fitting procedure to wander in the parameter space with a probability of visiting a certain point

$P = \exp(-\chi^2/2)$, the so called Gibbs sampling. Three advantages of this method will be emphasized: First, correlations between parameters are automatically taken into account, which implies, for example, that parameter errors are correctly calculated, correlations show up in a natural way and ill defined parameters (i. e., parameters for which data only support the calculation of lower or upper bounds) are immediately recognized from their PDF. Second, it is possible to calculate the likelihood of a determined physical model, and therefore to select the one among many that fits the data best with a minimal number of parameters, in a correctly defined probabilistic way. Finally, in the case of a low count rate where the Gaussian approximation to the Poisson statistics fails, this method can also be used by simply redefining χ^2.

Introduction

Science is based on the success of an hypothesis to describe experimental results, i. e., is based on the amount of "truth" and "falsity" of an hypothesis when contrasted with experimental results [3]. In order to find a quantitative method to determine this "amount of truth", hypotheses in science should at the end be reduced to a mathematical expression depending on a set of parameters with some physical meaning. The "amount of truth" is then determined by fitting the mathematical model to some experimental data. The general method to do so is to minimize the squared distance between experimental data and the points generated by the mathematical model. Furthermore, taking also into account the error associated with experimental data, a figure of merit χ^2 can be defined

$$\chi^2 = \sum_{k=1}^{n} \frac{(H_k\{P_i\} - D_k)^2}{\sigma_k^2} \tag{6.19}$$

where n is the number of experimental points and m is the number of parameters, D_k $(k = 1, \ldots n)$ are the experimental data, $H_k\{P_i\}$ $(k = 1, \ldots n)$ are the values obtained from our hypothesis (the mathematical model) using the $\{P_i\}$ $(i = 1, \ldots m)$ set of parameters contained in the model, and σ_k $(k = 1, \ldots n)$ are the experimental errors

associated with the respective D_k. Therefore, the fitting procedure has a twofold goal: first, to find the set of parameters $\{P_i\}$ which describes the experimental data best, and second, using this set of parameters, to define a figure of merit which quantifies the "amount of truth" of the proposed hypothesis. In order to be able to compare different hypotheses with different numbers of parameters it is reasonable to define a figure of merit which penalizes additional parameters such as the *reduced* χ^2 defined as:

$$\chi^2_\nu = \frac{\chi^2}{n-m} \tag{6.20}$$

where n is the number of experimental points and m is the number of parameters, so $n-m$ is the number of degrees of freedom. The aforementioned way to quantify how good experimental data are described by a hypothesis is based on what is called a "frequentist" approximation to the problem* and has many drawbacks associated with both the fitting procedure and the way to quantify the correctness of the hypothesis describing experimental data.

Data fits are usually done by minimizing the aforementioned χ^2 (Equation 6.19) using the Levenberg-Marquardt algorithm, which aims to find the minimum of the $\chi^2\{P_i\}$ hypersurface. Unfortunately, usually local minima make the algorithm unable to find the absolute minimum. For this reason, this method can find a final solution only when the algorithm is initialized with parameters near the global minimum. The final solution is then characterized by a set of parameters with an associated error $(P_k \pm \varepsilon_k)$ and the figure of merit χ^2_ν. This way of quantifying the best fit to the data is based on the supposition that there is only one minimum in the $\chi^2(P_k)$ hypersurface compatible with data error, and that the functional dependence of $\chi^2(P_k)$ is quadratic on each parameter (i. e., one can stop at the second term of a Taylor expansion of the obtained minimum), and thus allowing only symmetric errors. Moreover, errors are usually calculated disre-

* The "frequentist" description defines probability of a certain event A, $P(A)$, as the limiting frequency with which the event A is observed when a great number of events A is taken into account.

garding possible correlations between them† and are thus generally underestimated.

We present in this work a method both to perform fits and to analyse results based exclusively on probability by using what is called Bayesian inference. The main difference with the previously exposed frequentist method is the absence of *any* supposition on the $\chi^2\{P_i\}$ landscape which will rather be explored using the probabilities determined from experimental data. The method results in a different way to express fitted parameters and the figure of merit showing all the complexity of the final solution: they become Probability Distribution Functions (PDFs) obtained directly from exploring the $\chi^2\{P_k\}$ hypersurface.

The paper will be organized as follows: first the ubiquitous χ^2 will be defined using exclusively probability theory, and on this basis a method to sample the $\chi^2\{P_k\}$ hypersurface will be presented: the Gibbs sampling. We will then refer on how both the frequentist and Bayesian methods select an hypotheses among others, stressing the advantages of using the second approach. Finally the presented method implemented in the FABADA package [4] will be applied to three real cases related to neutron scattering each stressing different aspects of the proposed method. In the first example, the importance of letting parameters free or fixed in the fitting process will be stressed. The second example will focus on the PDF obtained from a set of data fitted simultaneously, and model selection will be addressed in the third example.

What is behind the ubiquitous χ^2?

The objective of the so called *Bayesian methods* [1, 2] is to find the probability that a hypothesis is true given some experimental *evidence*. This is done taking into account both our *prior* state of

† In fact it is possible to calculate errors taking into account the correlation between parameters using the frequentist approach (still supposing a parabolic dependence of parameters on $\chi^2\{P_i\}$). This could be done diagonalizing the covariant matrix. This procedure is nevertheless not usually found in the literature resulting in an underestimation of errors.

knowledge concerning the hypothesis, and the *likelihood* that the data is described by the proposed hypothesis. Using probability notation, and only considering the case that the experiment consists of a series of data D_k and that the hypothesis is represented by H_k, we can relate the aforementioned probabilities using the Bayes theorem [5]:

$$P(H_k \mid D_k) = \frac{P(D_k \mid H_k)P(H_k)}{P(D_k)} \tag{6.21}$$

where $P(H_k \mid D_k)$ is called the *posterior*, the probability that the hypothesis is in fact describing the data. $P(D_k \mid H_k)$ is named the *likelihood*, the probability that our data is well described by our hypothesis. $P(H_k)$ is called the *prior*, the knowledge we have beforehand about the hypothesis, and $P(D_k)$ is a normalization factor to assure that the integrated posterior probability is unity. In the method here presented we will assume no prior knowledge (maximum ignorance prior [2]), and in this special case Bayes theorem takes the simple form:

$$P(H_k \mid D_k) \propto P(D_k \mid H_k) \equiv L \tag{6.22}$$

where L is a short notation for likelihood.

We need first to find the likelihood that one data point D_k is described by the mathematically modelled hypothesis H_k. In a counting experiment such as those related to neutron scattering this probability follows a Poisson distribution

$$P(D_k \mid H_k) = \frac{{H_k}^{D_k}\, e^{-H_k}}{D_k!}. \tag{6.23}$$

Nevertheless, for a high enough number of counts, the Poisson PDF can be well approximated by a Gaussian one with $\sigma = \sqrt{D_k}$ as it is shown in Figure 6.48, and hence the likelihood that the set of data points D_k is correctly described by the hypothesis H_k can be written as

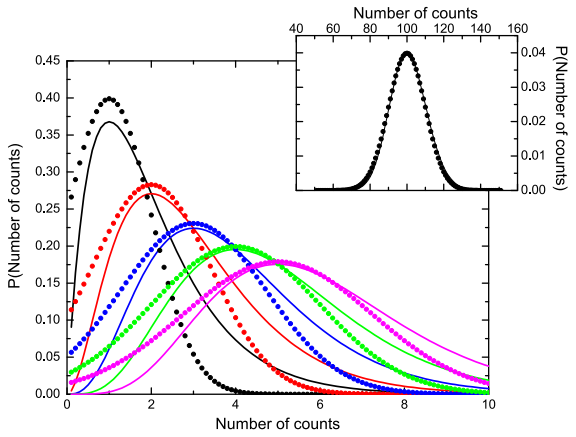

Figure 6.48: Poisson statistics followed by a counting experiment such as a neutron scattering experiment (lines). For an increasing number of counts, the Poisson distribution can be approximated by a Gaussian function (points) with $\sigma = \sqrt{n}$, being n the number of counts.

$$L \propto \prod_{k=1}^{n} \exp\left[-\frac{1}{2}\left(\frac{H_k - D_k}{\sigma_k}\right)^2\right]$$
$$= \exp\left[-\frac{1}{2}\sum_{k=1}^{n}\left(\frac{H_k - D_k}{\sigma_k}\right)^2\right] = \exp\left(-\frac{\chi^2}{2}\right).$$

Therefore, we have found the meaning of the ubiquitous χ^2 based only on probabilistic grounds: it is related to the probability that a certain set of data is well described by an hypothesis, and hence the goal of minimizing χ^2 is finding a set of parameters that maximizes the likelihood associated with the proposed mathematical model. The probability theory behind χ^2 allows therefore also to deal with the case of experiments with only few counts where the Gaussian approximation is not valid any more and the Poisson distribution must be

employed simply by redefining χ^2 as

$$\chi^2 = -2\sum_{k=1}^{n} \ln\left[\frac{{H_k}^{D_k} e^{-H_k}}{D_k!}\right] \tag{6.24}$$

The Bayesian method: Gibbs sampling of parameter space

The probabilistic understanding of χ^2 makes it possible to define a unique method, first to fit the experimental data, and then to analyse the obtained results, using a Markov Chain Monte Carlo (MCMC) technique. A set of parameters ${P_i}^{\text{new}}$ is generated from an old set ${P_i}^{\text{old}}$ by randomly changing one of the parameters.‡ The probability to accept the new set of parameters is given by

$$\frac{P(H({P_i}^{\text{new}}) \mid D_k)}{P(H({P_i}^{\text{old}}) \mid D_k)} = \exp\left(-\frac{\chi^2_{\text{new}} - \chi^2_{\text{old}}}{2}\right) \tag{6.25}$$

where χ^2_{new} and χ^2_{old} correspond to the χ^2 (as defined in Equation 6.19) for the new and old set of parameters. This way of exploring the parameter space (called Gibbs sampling) is similar to the way used to find the possible molecular configurations of a determined system at a given temperature using the classical Monte Carlo method: the values of physical constants such as the potential energy will in fact be a PDF related to all the configurations explored by the Monte Carlo method. It is therefore possible to relate energy to $\sum(H_k - D_k)^2$, the magnitude giving information about the fit quality of the hypothesis with respect to the data, and temperature to the error associated with the data ($T \sim \sigma^2$). This way of exploring the parameter space has two main advantages:

- In the fitting process, the Bayesian method is able to accept a new set of parameters that do not decrease χ^2, if this change is compatible with the experimental error and therefore does

‡ Parameters are changed randomly, but their maximum change is restricted. A new parameter is therefore generated following $P_i^{\text{new}} = P_i^{\text{old}} + (\text{RND} - 0.5) \cdot 2P_i^{\max}$ where RND is a random number between 0 and 1, and $P_i^{\max}$ is the maximum change allowed.

not get stuck in local minima as the Levenberg-Marquardt algorithm. In other words, the presented method is able to go "uphill" in the $\chi^2\{P_i\}$ hypersurface if the barrier is compatible with the error. Nevertheless, in order to avoid the presented algorithm to get stuck even in the case when barriers are greater than those associated to experimental error a simulated annealing can be used. This algorithm calculates a fictitious $\chi^2 = \sum_{k=1}^{n} \frac{(H_k - D_k)^2}{T\sigma^2}$ where T is a constant defined to artificially increase the experimental error, and by similitude with classical Montecarlo simulation is named as "temperature". Fits are then started at high temperature, and the system is relaxed by lowering the temperature up to T=1.

- Concerning the analysis of the results obtained by the fit, the exploration of the whole parameter space compatible with data using the MCMC method allows both to find the PDF associated with the likelihood directly related the figure of merit χ^2 (see Equation 6.24), and the parameters, taking into account possible correlations between them, or minima not describable by a quadratic approximation.

Model selection

Data can usually be described by more than one hypothesis, each implying a different physical mechanism to explain experimental results. Albeit the importance to perform model selection accurately, vague arguments are usually given to prefer a model among others and usually no quantitative arguments are given to justify why an hypothesis is preferred, although it is possible to do so using both the frequentist and Bayesian methods. Model selection can be performed using the frequentist approach by using the χ^2_ν figure of merit (see Equation 6.20) which takes into account the addition of parameters to a model by dividing χ^2 by the degrees of freedom. Therefore, if two models fit the data with equal success, i. e., with the same χ^2, the model with less parameters (with the smallest χ^2_ν) will be favoured. In some sense this is nothing but quantifying the Ockham's razor princi-

ple: it is necessary to shave away unnecessary assumptions (parameters). Model selection performed by using χ^2_ν has the same drawbacks as the determination of parameter errors: we suppose that there is a single minimum in $\chi^2\{P_i\}$, that this minimum parabolic depends on all parameters and that there are no correlations between parameters. In fact, if these three suppositions are accomplished, then the PDF of the χ^2 reads [2]

$$P(\chi^2) \propto (\chi^2)^{N/2-1} \exp\left(-\chi^2/2\right) \tag{6.26}$$

N is, in this simple case, the number of parameters. In Figure 6.49 the chi-square distribution for increasing degrees of freedom (number of parameters) is shown. As can be seen in the inset from Figure 6.49, this distribution has a term which is independent from the number of parameters, $\exp\left(-\chi^2/2\right)$, and that decreases together with the quality of the fit, or when the error associated with the experimental data σ_k increases. The term $(\chi^2)^{N/2-1}$, depending on the number of degrees of freedom, increases exponentially with the number of parameters, displacing the maximum of the χ^2 distribution to higher values. Therefore, even using the frequentist approach, the aforementioned preference for models that fit equally well the data with the minimum number of parameters is based on probability theory: those models with the maximum in the χ^2 distribution placed at lower values will be preferred. The Bayesian method finds in a natural way the PDF of χ^2 by exploring the parameter space without the suppositions made in the frequentist approximation, hence the obtained PDF will in general not follow the χ^2 distribution described by Equation 6.26.

Examples

Determining the intramolecular structure of CCl_4 Molecular structure can be calculated from diffraction experiments by fitting the high q-range of the scattering function $S(q)$ to the following equation (see Reference [6]):

$$S(q) = h \sum_{i,j}^{m} b_i^{\text{coh}}\, b_j^{\text{coh}}\, \frac{\sin(qr_{ij})}{qr_{ij}}\, \exp\left[-\frac{1}{2}\left(l_{ij}q\right)^2\right] \tag{6.27}$$

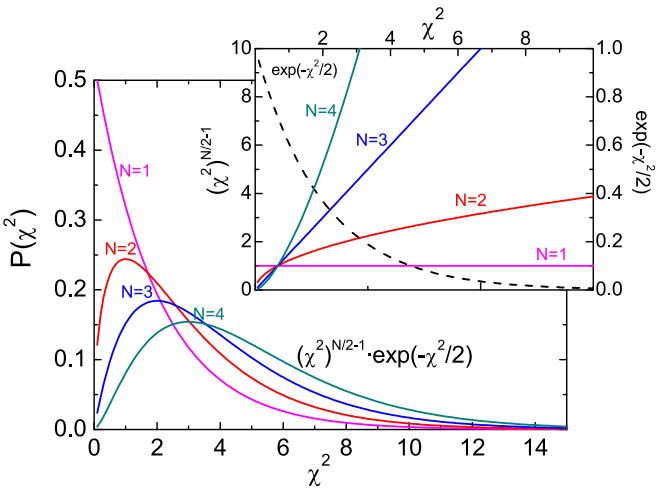

Figure 6.49: χ^2 distribution ($(\chi^2)^{N/2-1} \exp(-\chi^2/2)$) for an increasing number of fit parameters N. The inset shows the terms associated to the quality of the fit $\exp(-\chi^2/2)$ together with the one depending on the number of parameters of the model $(\chi^2)^{N/2-1}$.

where b_i^{coh} are the coherent cross sections for each element, r_{ij} are the intramolecular distances and $l^2 = \langle u_{ij}^2 \rangle$ are the vibrational Mean Square Displacements (MSD) between elements i and j, and h is a scaling factor.

In the proposed example, our objective is to calculate the intramolecular structure of carbon tetrachloride (one of the first molecular liquids studied by diffraction methods). The determination of its molecular structure implies to obtain the distance between carbon and chlorine atoms, the Cl-Cl distance is fixed by the tetrahedral symmetry, and the MSD between chlorine atoms and carbon and chlorine atoms.

Experiments were performed at the diffractometer D1b in the Institute Laue Langevin (Grenoble, France) using a wavelength of $\lambda = 2.52$ Å (see [7]). Figure 6.50a shows a good agreement between experimental data and two fits of Equation 6.27, one with a fixed scale factor h, and the other with h as a free parameter. Figures 6.50b and c show the PDF from parameters r_{CCl} and l_{CCl} obtained

through the two aforementioned fits. Concerning the r_{CCl} PDF, we can immediately see that its determination is robust since both fixed and free scale factor h lead to the same PDF. On the contrary, the PDF associated with l_{CCl} is sensible to the way we have performed the fit: if the scale factor is fixed we obtain a most probable value for this parameter ($l_{\mathrm{CCl}} = 0.066$ Å), but for a free scale factor h only a maximum value for l_{CCl} can be obtained due to the correlation between both parameters (h and l_{CCl}). Defining the upper limit as that for which the integrated probability is 0.682 (as errors are usually defined in the frequentist approach [§]) the upper limit $l_{\mathrm{CCl}} = 0.02$ Å can be determined from the cumulative distribution function (see Figure 6.50).

This example shows the main difference compared to the frequentist approximation: the results are presented as PDF. This has the advantage that, as it happens with the determination of l_{CCl} leaving h free, the result to our parameter determination can be expressed as a limit for the parameter, which is impossible with the frequentist approximation.

Parameter estimation: isotropic rotation Quasi Elastic Neutron Scattering (QENS) is perfectly suited to determine the molecular dynamics in the liquid phase. Usually this dynamics is studied by splitting the spectra into diffusion and rotation contributions

$$S(q,\omega) = S(q,\omega)_{\mathrm{trans}} \otimes S(q,\omega)_{\mathrm{rot}} \tag{6.29}$$

where $S(q,\omega)_{\mathrm{trans}}$ is the translational contribution and $S(q,\omega)_{\mathrm{rot}}$ is associated with the rotation of the molecule, assuming that both movements are independent from each other. If we assume that the translation is described by a diffusion mechanism and, therefore, de-

[§] Errors are defined supposing that parameter PDFs follow a Gaussian distribution:

$$P(\text{parameter}) = \frac{1}{\sigma\sqrt{2\pi}} exp\left(-\frac{x^2}{2\sigma^2}\right). \tag{6.28}$$

The probability that a parameter is within the interval $\pm\sigma$ is 0.683.

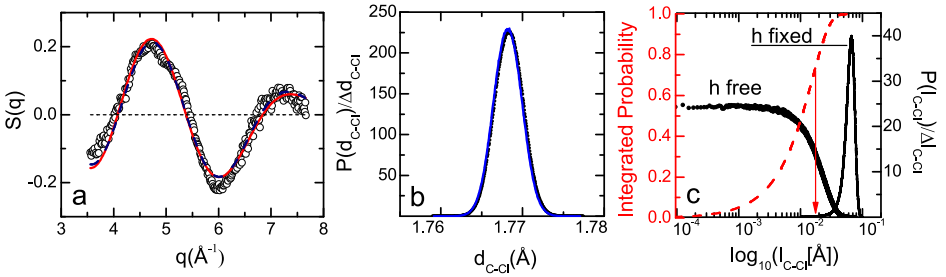

Figure 6.50: (a) High momentum transfer scattering function for CCl_4, where the main contribution to S(q) is that related to the molecular structure. Lines are the best fits to S(q) setting the scale factor fixed and free in the fitting procedure. (b) Probability distribution functions obtained for the distances between carbon and chlorine atoms r_{CCl}, and Mean Square Displacement between carbon and chlorine atom (l_{CCl}) for both cases (fixed h, points, and free h, line). $PDF(l_{CCl})$ has been represented in logarithmic scale to show the different length scales explored by the Bayesian method. In addition, for l_{CCl} using a h free fit the integrated probability is shown, arrow points an integrated probability of 0.68 following the standard definition of errors in the frequentist approximation.[§]

scribed by the Fick Equation, and that rotation is isotropic [8]:

$$S(q,\omega)_{\text{trans}} = \frac{1}{\pi}\,\frac{Dq^2}{\omega^2 + (Dq^2)^2} \tag{6.30}$$

$$S(q,\omega)_{\text{rot}} = A_0(q\cdot R)\,\delta(\omega) + \sum_{l=1}^{\infty} A_l(q\cdot R)\frac{1}{\pi}\,\frac{l(l+1)D_r}{\omega^2 + [l(l+1)D_r]^2} \tag{6.31}$$

where D and D_r are the translational and rotational diffusion coefficients, $A_l(q\cdot R)$ are spherical Bessel functions and R is the radius of rotation. We have performed QENS experiments at the TOFTOF spectrometer [9, 10] at the FRM II reactor (Munich) in order to determine the dynamics of 1,2-trans-dichloroethylene. The data were corrected for self-absorption using the program FRIDA [11]. A series of fits for each temperature with the model described by Equations 6.29,

6.30 and 6.31. Usually, each q value is fitted separately, obtaining the diffusion coefficient from a second linear fit to the q^2 dependence of the broadening of the central Lorentzian $\Gamma_{\text{trans}}(q^2) = Dq^2$, and the radius of rotation from the obtained $A_0(q \cdot R) = \sin(qR)/qR$ or eventually by independently fitting all spectra using Equation 6.29 to each $S(q = q_i, \omega)$. However, our hypothesis is described by the whole set of the aforementioned Equations 6.29, 6.30 and 6.31, and thus errors arising from the two-step fitting procedure can be minimized by simply fitting the spectra $S(q, \omega)$ for all q values, i. e., fitting the complete q-dependent data set with only D, D_r and R as physical parameters. The results for the radius of rotation are shown in Figure 6.51 using the presented Bayesian method together with those obtained using a Levenberg-Marquardt algorithm for each q-value. First of all, because fits were performed by the frequentist approximation separately for each q-value (see Figure 6.51b), the radius of rotation has a q-dependence which is not present in the Bayesian fit (see Figure 6.51a), consequently stressing the importance of fitting the whole data set together. A fit using the Bayesian algorithm has also been performed to a spectrum for $q = 0.4$ Å^{-1} and $T = 300$ K in order to compare the error bars obtained by both methods. The error bar using the Bayesian approach was calculated by obtaining the PDF for the radius of rotation and then fitting a Gaussian function with $\sigma = \varepsilon$, being ε the frequentist parameter error. This error bar is plotted in Figure 6.51b, together with that determined by the frequentist method. As it can be seen in the Figure the error obtained by the presented method is much bigger that that estimated by the frequentist method. The presented Bayesian method is therefore able to deal with simultaneous fits of various curves, obtaining the PDF of physical parameters as a function of temperature (see Figures 6.51c, d, and e).

Model selection: Diffusion in phospholipid membranes Phospholipids are the main component of cell walls and can also be used in technological applications as for example drug delivery or food industry. Their dynamics is studied on many time- and length-scales

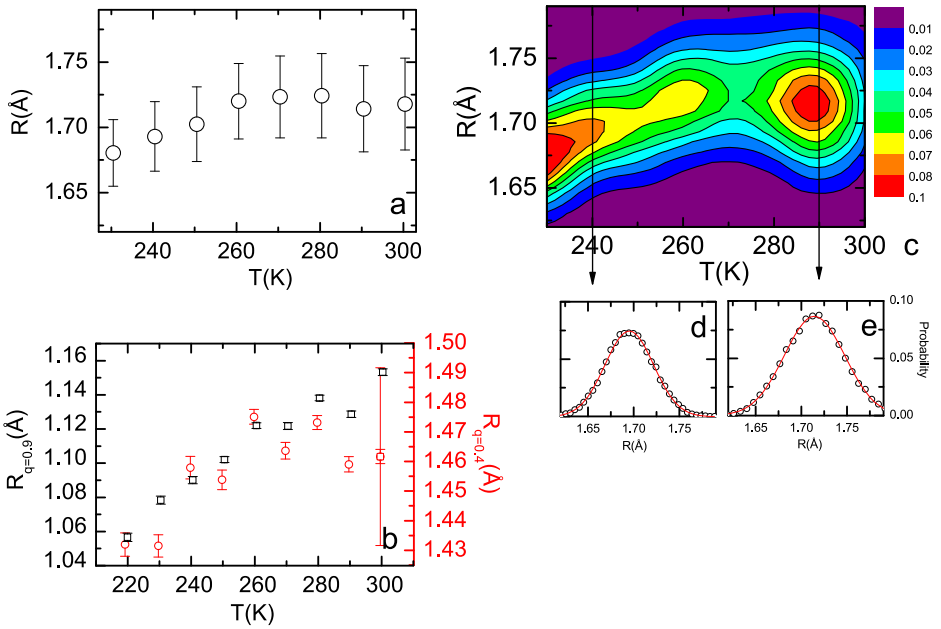

Figure 6.51: Radius of rotation obtained (a) from the Bayesian fitting procedure applied to all $S(q,\omega)$ spectra and (b) from the frequentist fit to each q-value individually (here only $q = 0.4$ Å and $q = 0.9$ Å values are shown). An error bar obtained from the Bayesian method is plotted in (b) for $S(q = 0.4, \omega)$ at $T = 300$ K. In (c) the PDF for the radius of rotation is also shown as a function of the temperature ($P(R,T)$) with two cuts ($P(R)$) for $T = 240$ K and $T = 290$ K.

with different techniques, among them quasielastic time-of-flight neutron scattering which probes the motions that dominate on times of about 100 ps.

As will be discussed in detail elsewhere [12], the question arose from previous neutron scattering experiments [13, 14] whether the long-range motion of phospholipids is visible on these times or if the motion appears rather localized, trapped in a cage of neighbours. This difference can be seen in the line shape of $S(q,\omega)$: Motions that are localized during the observation time cause a central line that is not broadened beyond the resolution of the instrument but cause a

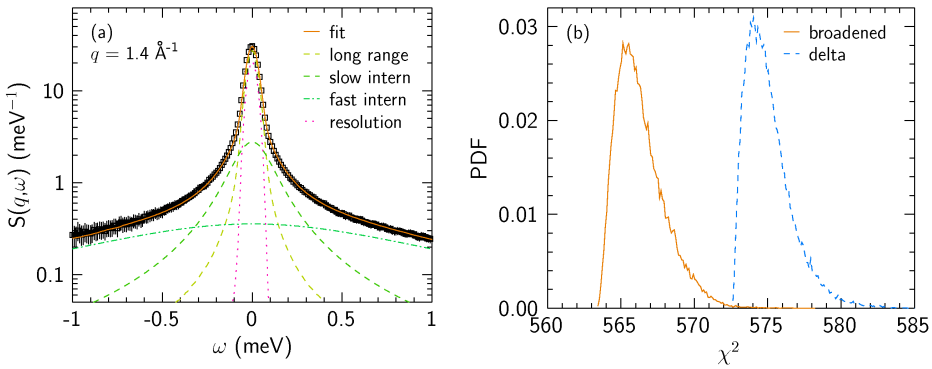

Figure 6.52: (a) Spectra of the hydrated phospholipid DMPC together with a fit and the instrumental resolution. Internal motions were approximated with two Lorentzians, the long-range motion was either assumed to be invisible (delta-shaped central line, not shown) or visible (broadened central line, shown here). (b) The χ^2 PDF associated with both the broadened central line and a delta function, showing that for any combination of parameters the broadened model is preferable compared to the delta model: The data justify the assumption that the long-range motion is visible.

foot in the spectrum. In contrast, long-range motions do broaden the central line.

The neutron scattering experiments were performed with the phospholipid DMPC (1,2-Dimyristoyl-sn-Glycero-3-Phosphocholine) in a liquid crystal fully hydrated with D_2O at the neutron time-of-flight spectrometer TOFTOF at the FRM II (Munich). A typical spectrum is shown in Figure 6.52a after standard corrections including self absorption and subtraction of the D_2O spectra, obtained with the program FRIDA [11]. It is possible to fit the data "satisfactorily" with both, a broadened and a delta-shaped central line.

As stated before, Bayesian analysis is able to quantify how "satisfactory" the fits are, taking into account the whole $\chi^2\{P_i\}$ landscape and avoiding assumptions about it. In Figure 6.52b, the PDFs associated with χ^2 for the two models are displayed. The normal

Levenberg-Marquardt algorithm would simply return the parameters at the minimal reachable value of χ^2 together with this quantity. It is obvious that introducing an additional parameter, the nonzero width of the central line, reduces the χ^2. The question that needs to be answered is if this reduction is significant enough to justify the additional parameter.

The χ^2_ν gives this answer, however relying on the assumptions discussed above. Employing the Bayesian Analysis, no assumptions are made as the $\chi^2\{P_i\}$ landscape is rendered explicitly. One can see in Figure 6.52b that the model incorporating a broadened central line does not only yield the smaller χ^2 minimum but also the PDF associated with χ^2 is for any combination of parameters smaller than the one of the delta model.

Therefore, the model comparison between the two possibilities of broadened and non-broadened central line favours the model with a broadened line.

Summary

We have proposed a general Bayesian method to fit data, analyse results from the fit, and from these results to perform model selection between competing hypotheses. In contrast to the classical frequentist approach, where some assumptions are done concerning the χ^2 landscape (there is only a minimum of $\chi^2\{P_i\}$ able to describe data within its error, this minimum has a square dependence on the parameters, and parameters are not correlated), the proposed method samples the parameter space with the only guide of probability, thus having the following advantages:

- In the fitting procedure, the Bayesian method will not get stuck in local minima if its barrier is smaller than the error associated with the experimental data set.
- Parameters are obtained as PDFs and, because the whole parameter space is sampled, correlations between parameters are naturally taken into account. Moreover, a natural way to define errors based on the PDF of parameters is obtained within this

method, which following the frequentist approximations would be the 68% confidence interval around the most probable parameter value, i. e., the parameter is inside these limits with a probability $P = 0.68$. PDFs may take an arbitrary form, for example indicating that only a superior limit to the parameter can be extracted from the experimental data.

- The likelihood (which as we have seen is directly related to χ^2) obtained with this method is also a PDF hence revealing the whole complexity of the parameter landscape. Model selection is then performed taking into account all parameter combinations compatible with the experiment.

- The presented method is flexible enough to deal with low counts experiments where the Poissson distribution cannot be approximated by a Gaussian function, by simply redefining χ^2 in the Gibbs sampling algorithm.

This work was supported by the Spanish Ministry of Science and Technology (FIS2008-00837) and by the Government of Catalonia (2005SGR-00535).

References

All online references accessed on July 22, 2014.

[1] D. S. Sivia, C. J. Carlile, W. S. Howells, and S. Konig. *Physica B* **182**(4), 341 (1992). International Workshop On Quasielastic Neutron Scattering, Windsor, England, Apr 06-07, 1992.

[2] D. Sivia and J. Skilling. *Data Analysis: A Bayesian Tutorial*. Oxford University Press (2006).

[3] K. R. Popper. *Conjectures and Refutations: The Growth of Scientific Knowledge*. Routledge (1963).

[4] L. C. Pardo. *FABADA (Fitting Algortihm for Bayesian Analysis of DAta)* (2009). URL http://gcm.upc.edu/members/luis-carlos/bayesiano.

[5] T. Bayes and R. Price. *Philos. T.* **53**, 370 (1763).

[6] H. E. Fischer, A. C. Barnes, and P. S. Salmon. *Rep. Prog. Phys.* **69**(1), 233 (2006).

[7] L. C. Pardo, J. Ll. Tamarit, N. Veglio, F. J. Bermejo, et al. *Phys. Rev. B* **76**(13), 134203 (2007).

[8] M. Bée. *Quasielastic Neutron Scattering. Principles and Applications in Solid State Chemistry, Biology and Materials Science.* Adam Hilger, Bristol (1988).

[9] T. Unruh, J. Neuhaus, and W. Petry. *Nucl. Instr. and Meth. A* **580**(3), 1414 (2007).

[10] T. Unruh, J. Neuhaus, and W. Petry. *Nucl. Instr. and Meth. A* **585**(3), 201 (2008).

[11] J. Wuttke. *FRIDA (Fast Reliable Interactive Data Analysis)* (2006). URL http://sourceforge.net/projects/frida/.

[12] S. Busch, C. Smuda, L. C. Pardo, and T. Unruh. *J. Am. Chem. Soc.* **132**(10), 3232 (2010).

[13] S. König, W. Pfeiffer, T. Bayerl, D. Richter, et al. *J. Phys. II France* **2**(8), 1589 (1992).

[14] J. Tabony and B. Perly. *Biochim. Biophys. Acta, Biomembr.* **1063**(1), 67 (1991).

TOPIC 6: FABADA: a Fitting Algorithm for Bayesian Analysis of DAta

L. C. Pardo,[1] M. Rovira-Esteva,[1] S. Busch,[2] M. D. Ruiz-Martín,[1] and J. Ll. Tamarit,[1]

[1]Grup de Caracterització de Materials, Departament de Física i Enginyeria Nuclear, ETSEIB, Universitat Politècnica de Catalunya, Diagonal 647, E-08028 Barcelona, Catalonia, Spain

[2]Physik Department E13 and Forschungs-Neutronenquelle Heinz Maier-Leibnitz (FRM II), Technische Universität München, Lichtenbergstr. 1, D-85748 Garching, Germany

Published: **Journal of Physics: Conference Series 325, 012006 (January 2011).**

DOI: **http://dx.doi.org/10.1088/1742-6596/325/1/012006**

Abstract

The fit of data using a mathematical model is the standard way to know if the model describes data correctly and to obtain parameters that describe the physical processes hidden behind the experimental results. This is usually done by means of a χ^2 minimization procedure. Although this procedure is fast and quite reliable for simple models, it has many drawbacks when dealing with complicated problems such as models with many or correlated parameters. We present here a Bayesian method to explore the parameter space guided only by the probability laws underlying the χ^2 figure of merit. The presented method does not get stuck in local minima of the χ^2 landscape as it usually happens with classical minimization procedures. Moreover correlation between parameters are taken into account in a natural way. Finally, parameters are obtained as probability distri-

bution functions so that all the complexity of the parameter space is shown.

Introduction

Science is based on the success of an hypothesis to describe experimental results, i. e., is based on the amount of "truth" and "falsity" of an hypothesis when contrasted with experimental results [1]. In order to find a quantitative method to determine this "amount of truth", hypotheses in science should at the end be reduced to a mathematical expression depending on a set of parameters with some physical meaning. The "amount of truth" is then determined by fitting the mathematical model to some experimental data. To quantify that, a figure of merit χ^2 can be defined as

$$\chi^2 = \sum_{k=1}^{n} \frac{(H_k\{P_i\} - D_k)^2}{\sigma_k^2} \tag{6.32}$$

where n is the number of experimental points, D_k $(k = 1, \ldots, n)$ are the experimental data, $H_k\{P_i\}$ $(k = 1, \ldots, n)$ are the values obtained from our hypothesis (the mathematical model) using the $\{P_i\}$ $(i = 1, \ldots, m)$ set of parameters contained in the model, m is the number of parameters, and σ_k $(k = 1, \ldots, n)$ are the experimental errors associated with the respective measured points D_k.

Data fitting is usually done by minimizing χ^2 (Equation 6.32) using the Levenberg-Marquardt algorithm, which aims to find the minimum of the $\chi^2\{P_i\}$ hypersurface. This fit procedure has a twofold goal: first, to find the set of parameters $\{P_i\}$ which best describes the experimental data within their errors, and second, using this set of parameters, to define a figure of merit which quantifies the "amount of truth" of the proposed hypothesis, taking into account how well it describes the data. In order to be able to compare different hypotheses with different numbers of parameters, it is reasonable to define a figure of merit which penalizes the addition of parameters such as the *reduced* χ^2, defined as $\chi^2_\nu = \frac{\chi^2}{n-m}$. In this equation, n is the number of experimental points and m is the number of parameters, so $n - m$ is the number of degrees of freedom.

This way to quantify how well experimental data are described by a hypothesis is based on what is called a frequentist approximation of the problem,* and has many drawbacks associated with both the fit procedure (it usually gets stuck in local minima of the χ^2 hypersurface when the model is complex) and the way to quantify the correctness of the hypothesis describing experimental data. The final result using this method is characterized by a set of parameters with an associated error $(P_k \pm \varepsilon_k)$ and the figure of merit χ^2_ν. This way of quantifying the best fit to the data is based on the supposition that there is only one minimum in the $\chi^2\{P_i\}$ hypersurface within the data error, and that the functional dependence of $\chi^2\{P_i\}$ is quadratic on each parameter i (i. e., one can stop at the second term of a Taylor expansion of the obtained minimum), and thus allowing only symmetric errors. Moreover, errors are usually calculated disregarding possible correlations between parameters and are thus generally underestimated.

The main difference of Bayesian inference from the previously exposed frequentist method is the absence of *any* supposition on the $\chi^2\{P_i\}$ landscape which will rather be explicitly explored taking into account experimental data. The method results in a different way to express fitted parameters and the figure of merit showing all the complexity of the final solution: they become Probability Distribution Functions (PDFs) obtained directly from exploring the $\chi^2\{P_i\}$ hypersurface. Although Bayesian methods are widely used in astronomy or biology [2–5], they are scarcely used in condensed matter and usually for very specific tasks such as in the analysis of QENS data [6], and the analysis of diffraction data [7–10]. We present in this work a general method to perform fittings and to analyse results based exclusively on probability by using Bayesian inference.

Although the presented Bayesian method is general, it is specially useful in three situations. Firstly, when the classical fitting procedure gets stuck in a local minimum of the chi squared hypersurface, i.e, when the present parameter set does not correspond to the best obtainable fit but any small parameter value change even decreases the

*The frequentist description defines probability of a certain event A $(P(A))$ as the limiting frequency with which the event A is observed when a great number of events A is taken into account.

fit quality. This may happen for example when fitting the intramolecular structure to diffraction data [11, 12] but is a well known problem in basically every fit normally surpassed by a careful choice of the initial parameter values. Secondly when an intricate model selection shall be performed, such as in the case of models that describe molecular motions using QENS [13] or dielectric data [14]. Finally when the model is ill defined and more than one combination of parameters is able to describe data, or when data only allows to limit the range of parameters but not to obtain a best fitting value [15].

Data analysis using the Bayesian method

What is behind the ubiquitous χ^2? The objective of the so called *Bayesian methods* [6, 16] is to find the probability that a hypothesis is true given some experimental evidence. This is done by taking into account both our prior state of knowledge concerning the hypothesis, and the likelihood that the data is described by the proposed hypothesis. Using probability notation, and considering the case that the experiment consists of a series of data D_k and that the hypothesis is represented by H_k, we can relate the aforementioned probabilities using the Bayes theorem [16, 17]:

$$P(H_k \,|\, D_k) = \frac{P(D_k \,|\, H_k) P(H_k)}{P(D_k)} \tag{6.33}$$

where $P(H_k \,|\, D_k)$ is called the *posterior*, the probability that the hypothesis is in fact describing the data. $P(D_k \,|\, H_k)$ is the likelihood, the probability that our data is well described by our hypothesis. $P(H_k)$ is called the prior, the PDF summarizing the knowledge we have beforehand about the hypothesis, and $P(D_k)$ is a normalization factor to assure that the integrated posterior probability is unity. In the following, we will assume no prior knowledge (maximum ignorance prior [16]), and in this special case Bayes theorem takes the simple form $P(H_k \,|\, D_k) \propto P(D_k \,|\, H_k) \equiv L$, where L is a short notation for likelihood.

In order to quantify the Bayes theorem, we need first to find the likelihood that one data point D_k is described by the mathematically

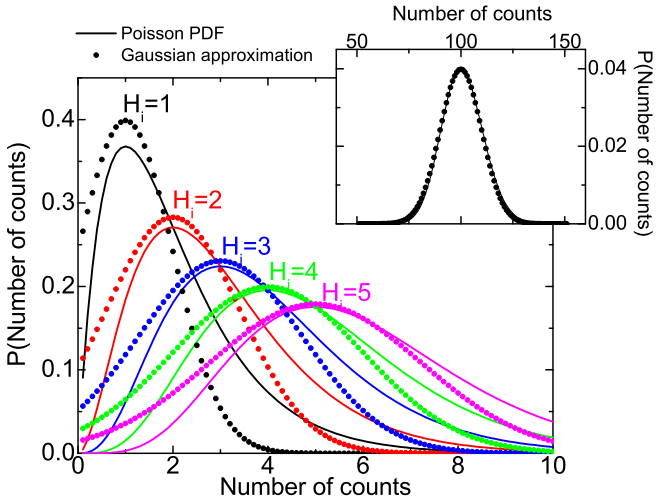

Figure 6.53: Poisson statistics followed by data in a counting experiment such as a scattering one (lines), and its usual Gaussian approximation (points) for an increasing number of expected counts. For an increasing number of counts, the Poisson distribution (line) can be approximated by a Gaussian function (points) with $\sigma = \sqrt{n}$, being the number of counts n. The inset shows that for a number of counts as great as 100 the approximation works quite well.

modelled hypothesis H_k. In a counting experiment, this probability follows a Poisson distribution. It can be well approximated by a Gaussian distribution with $\sigma = \sqrt{D_k}$ (see also [16]) if the number of counts is high enough as it is shown in Figure 6.53. Therefore for *one* experimental point ($k = i$, $i = 1, \ldots, n$):

$$P(D_{k=i} \,|\, H_{k=i}) = \frac{{H_k}^{D_k}\, e^{-H_k}}{D_k!} \approx \frac{1}{\sigma\sqrt{2\pi}} \exp\left[-\frac{1}{2}\left(\frac{H_k - D_k}{\sigma_k}\right)^2\right] \tag{6.34}$$

Where on the right hand side of the expression it is not explicitly written that the equation is related to a single experimental point $i = k$ for simplicity. The likelihood that the set of data points D_k is

correctly described by the hypothesis H_k can be therefore written as

$$P(D_k \,|\, H_k) \propto \prod_{k=1}^{n} \exp\left[-\frac{1}{2}\left(\frac{H_k - D_k}{\sigma_k}\right)^2\right] = \exp\left[-\frac{1}{2}\sum_{k=1}^{n}\left(\frac{H_k - D_k}{\sigma_k}\right)^2\right] = \exp\left(-\frac{\chi 2}{2}\right) \quad . \quad (6.35)$$

The figure of merit χ^2 is therefore related to the likelihood that the data is well described by the hypothesis H_k. The probability theory behind χ^2 also allows to deal with the case of experiments with only few counts where the Gaussian approximation, for which $\chi^2 = -2 \ln L$, is not valid any more and the Poisson distribution must be employed, simply by redefining χ^2 [16] as

$$\chi^2 = -2 \sum_{k=1}^{n} \ln\left[\frac{{H_k}^{D_k} e^{-H_k}}{D_k!}\right] \quad (6.36)$$

The Bayesian method The probabilistic understanding of χ^2 makes it possible to define a unique method, first to fit the experimental data, and then to analyse the obtained results, using a Markov Chain Monte Carlo (MCMC) technique where a set of parameters P_i^{new} is generated from an old set P_i^{old} by randomly changing one of the parameters, i. e., $P_i^{\text{new}} = P_i^{\text{old}} + (\text{RND} - 0.5)\, 2\Delta P_i^{\max}$. In the last equation, $\Delta P_i^{\max}$ is the maximum change allowed for the parameter and will be called parameter jump for short, and RND is a random number between 0 and 1. The probability to accept the new set of parameters is given by

$$\frac{P(H(P_i^{\text{new}}) \,|\, D_k)}{P(H(P_i^{\text{old}}) \,|\, D_k)} = \exp\left(-\frac{\chi^2_{\text{new}} - \chi^2_{\text{old}}}{2}\right) \quad (6.37)$$

where χ^2_{new} and χ^2_{old} correspond to the χ^2 (as defined in Equation 6.32) for the new and old set of parameters. Both fitting and analysis consist therefore in the successive generation of parameter sets $\{P_i\}$ (Markov Chains) with the successive acceptances ruled by Equation 6.37.

Two academic examples

Fitting a Gaussian In order to test the fit algorithm, a standard function such as a Gaussian

$$y(x) = \frac{a}{\sqrt{2\pi w}} \exp\left[-\frac{(x - x_c)^2}{2w^2}\right] + b \tag{6.38}$$

was generated with the parameter set $\{a, w, x_c\} = \{10.0, 1.0, 5.0\}$ and being b fixed to zero. The data were generated with a normally distributed error associated with each point of 0.05 and subsequently fitted by the presented algorithm using the same formula (with $b = 0$).

The calculated PDFs associated with each parameter P_i are shown in the top row of Figure 6.54 together with the χ^2 dependence on this parameter, calculated by varying only the parameter P_i and leaving the others fixed, i. e., making a cut of the hypersurface $\chi^2\{a, w, x_c\}$. As one may expect, the minimum of χ^2 coincides with the maximum probability of each parameter PDF.

The most probable parameter *values* – the ones where the PDF is maximal – coincide very nicely with the original values as can be seen in the top row of Figure 6.54. In the following, the discussion will focus on the determination of the parameter *errors*. There are two ways to determine the parameter errors: (i) the commonly used definition of the error as the value of the parameter that increases χ^2 by one unit ($\Delta P = |P(\chi^2_{\text{min}}) - P(\chi^2_{\text{min}} + 1)|$) and (ii) the width of the Gaussian associated with the PDF (the width of the Gaussian at $y = e^{-0.5} \cdot y^{\text{max}}$).

The obtained PDFs can be well described by a Gaussian function in the present examples (solid line in the PDFs shown in Figure 6.54). This proves that in this simple case the minimum of $\chi^2\{P_i\}$ is quadratic in each parameter, and therefore the frequentist definitions of errors can be used – the two measures of the parameter errors should coincide. The error is the defined in such a way that P_i has a 68% probability to be within $P_i - \sigma_{P_i}$ and $P_i + \sigma_{P_i}$ (see [18]).

In Figure 6.54 it can be seen that errors calculated from the PDFs are equal (for x_c) or larger (for a and w) than those calculated using the method of incrementing χ^2. This discrepancy can be explained by parameter correlations seen in the contour plots of the

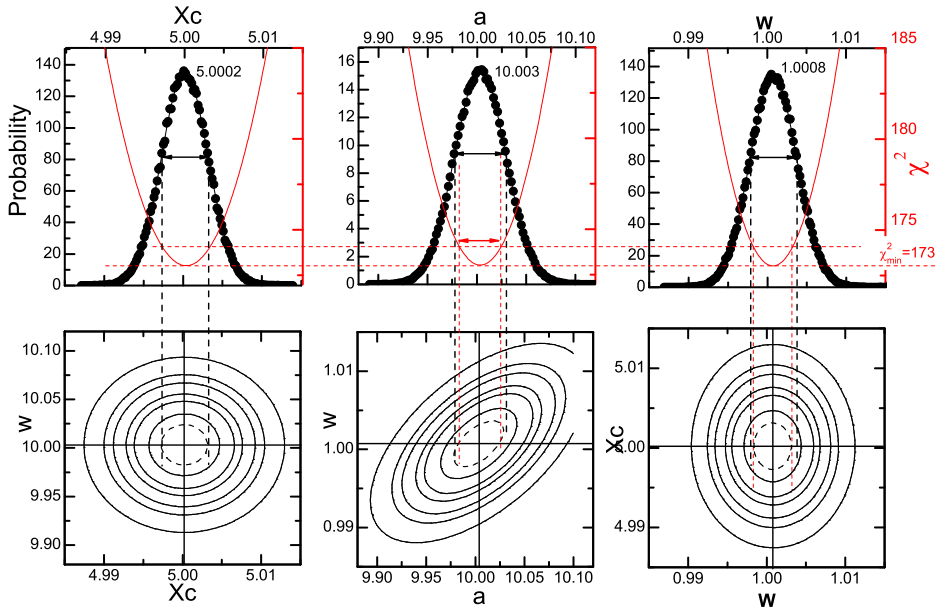

Figure 6.54: Upper row: PDFs associated with the centre x_c, amplitude a and width w of a Gaussian function (solid circles) together with the $\chi^2(P_i)$ around its minimum value, fixing all parameters except P_i (lines). Bottom row: $\chi^2(P_i, P_j)$ plots showing the correlation between parameters, the contour lines have a distance of $\Delta\chi^2 = 1$.

two-dimensional cuts through the $\chi^2(P_i, P_j)$ hypersurface shown in the bottom row of Figure 6.54: from the symmetry of the contours involving x_c it can be concluded that x_c is independent from both, a and w, whereas these two parameters are correlated, causing the main axis of the contour ellipsoids to be not parallel to the parameter axes. For the parameters a and w, the error calculated from the PDF coincides with the limits of the contour $\chi^2 = \chi^2_{\text{min}} + 1$. The error calculated from χ^2 coincides with the intersection of the contour with the x axis, thus underestimating its value.

Although this fact is well known in the frequentist approximation [18], to take correlation between parameters into account would involve diagonalizing the covariant matrix. That is scarcely done

and in any case is useful only in simple cases as the one presented when errors are symmetric, i. e., when $\chi^2\{P_i\}$ is quadratic in P_i. The Bayesian approach takes in a natural way any correlation between parameters into account, and can also treat non-Gaussian PDFs, being much more powerful than the frequentist approximation.

Fitting with Poisson statistics The standard way of fitting data using the minimization of χ^2 (as defined in Equation 6.35) is no longer valid when the number of counts is low. However, as we have seen, simply by redefining χ^2 using Equation 6.36, we can perform the fits when the number of counts is arbitrarily low.

To test our algorithm we have generated a series of random numbers D_K following a Poisson distribution around different fixed values H_K. We have then fitted these series of randomly generated points using the usual definition of χ^2, Equation 6.35, therefore wrongly assuming that the numbers were generated following a Gaussian PDF (see Figure 6.53) and with the definition given in Equation 6.36, that is, correctly assuming that D_K follows a Poisson PDF around H_K.

In Figure 6.55 we show the relative discrepancy between the fitted value and the value H_K used to generate the series of points using both methods as a function of the value H_K on a logarithmic scale. As expected, for H_K greater than about 10^3 both methods yield the same result. On the contrary for smaller values the discrepancy increases, reaching 30% for $H_K = 1$.

It is therefore important to take into account that in the limit of low counts the usual approximation between Poisson and Gaussian statistics should not be used. In Figure 6.55 it is displayed the fit of a Gaussian function (Equation 6.38) with parameters $\{a, w, x_c, b\} = \{20, 5, 1, 2\}$ each point D_K being generated following a Poisson distribution. The fit using Poisson statistics is closer to the generated function, i. e., unaffected by the error, as it can be seen in the figure, proving that the proposed algorithm is also useful to fit in the case of low count rates.

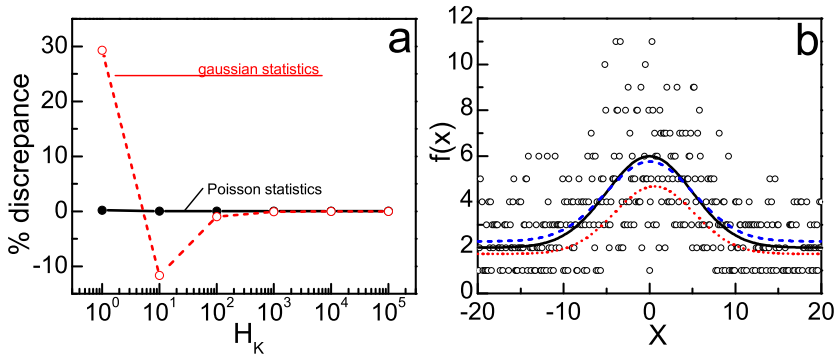

Figure 6.55: (a) Discrepancy between the fits to a constant value H_K set to 10^i, $i = 0, 1, \ldots, 5$ using a Gaussian (empty circles) and a Poisson statistic (full circles), being D_K values generated using a Poisson statistics. (b) Gaussian function generated assuming a low-count experiment (circles), i. e., assuming a Poisson statistics for each point. The solid line is the generated function unaffected by the error, and the dashed line the fitted function. Dotted line is the fit assuming a normal distribution of errors.

Conclusions

We have proposed a general Bayesian method to fit data and analyse results from the fit [19]. The classical frequentist approach makes some assumptions concerning the χ^2 landscape: there is only a minimum of $\chi^2\{P_i\}$ able to describe data within its error, this minimum has a quadratic dependence on the parameters, and the parameters are not correlated. The here proposed method avoids such problems, sampling the parameter space only with the guide of probability rules. This method has already been successfully used to analyse experiments coming from diffraction experiments [20], quasielastic neutron scattering [13, 15, 21] and dielectric spectroscopy [14]. We finally summarize the main advantages of the proposed method:

- The Bayesian method will not get stuck in local minima of the χ^2 hypersurface during the fit procedure if its barrier is smaller than the error associated with the experimental data set [20].

- Parameters are obtained as PDFs and, because the whole parameter space is sampled, correlations between parameters are taken into account. Moreover, a natural way to define errors based on the PDF of parameters is obtained within this method [14, 15, 21].
- The likelihood (which as we have seen is directly related to χ^2) obtained by this method is also a PDF hence revealing the whole complexity of the parameter landscape. Model selection is then performed taking into account all parameter combinations compatible with the experiment [13].

Acknowledgements

This work was supported by the Spanish *Ministerio de Ciencia e Inovación* (FIS2008-00837) and by the Catalonia government (2009SGR-1251). We would also like to thank helpful comments on the manuscript made from K. Kretschmer, T. Unruh, and I. Pereyra.

References

All online references accessed on July 22, 2014.

[1] K. R. Popper. *Conjectures and Refutations: The Growth of Scientific Knowledge*. Routledge (1963).

[2] R. Trotta. *Contemp. Phys.* **49**(2), 71 (2008).

[3] J. P. Huelsenbeck, F. Ronquist, R. Nielsen, and J. P. Bollback. *Science* **294**, 5550 (2001).

[4] G. A. T. McVean, S. R. Myers, H. S, P. Deloukas, et al. *Science* **304**, 5670 (2004).

[5] R. Diehl, H. Halloin, K. Kretschmer, A. W. Strong, et al. *A&A* **449**(3), 1025 (2006).

[6] D. S. Sivia, C. J. Carlile, W. S. Howells, and S. Konig. *Physica B* **182**(4), 341 (1992). International Workshop On Quasielastic Neutron Scattering, Windsor, England, Apr 06-07, 1992.

[7] F. J. Bermejo, J. Santoro, F. J. Mompean, and J. C. Dore. *Nucl. Instrum. Meth. Phys. Res. B* **34**, 505 (1988).

[8] S. Bacallado, J. D. Chodera, and V. Pande. *J. Chem. Phys.* **131**(4), 45106 (2009).

[9] O. Gereben, P. Jóvári, L. Temleitner, and L. Pusztai. *J. Optoelectron. Adv. Mater.* **9**(10), 3021 (2007).

[10] S. Pothoczki, L. Temleitner, P. Jóvári, S. Kohara, et al. *J. Chem. Phys.* **130**, 064503 (2009).

[11] A. K. Adyaa and L. Bianchi. *J. Chem. Phys.* **112**(9), 4231 (2000).

[12] F. Leclercq, P. Damay, M. Foukani, P. Chieux, et al. *Phys. Rev. B* **48**(4), 2748 (1993).

[13] S. Busch, C. Smuda, L. C. Pardo, and T. Unruh. *J. Am. Chem. Soc.* **132**(10), 3232 (2010).

[14] J. C. Martinez-Garcia, J. o. Tamarit, L. C. Pardo, M. Barrio, et al. *J. Phys. Chem. B* **114**, 6099 (2010).

[15] L. C. Pardo, M. Rovira-Esteva, S. Busch, M. D. Ruiz-Martín, et al. (2009). arXiv:0907.3711v3[physics.data-an].

[16] D. Sivia and J. Skilling. *Data Analysis: A Bayesian Tutorial*. Oxford University Press (2006).

[17] T. Bayes and R. Price. *Philos. T.* **53**, 370 (1763).

[18] W. H. Press, S. A. Teukolsky, W. T. Vetterling, and B. P. Flannery. *Numerical Recipes in Fortran 77: the art of scientific computing*. Cambridge University Press, 2nd edition (1992).

[19] L. C. Pardo. *FABADA (Fitting Algortihm for Bayesian Analysis of DAta)* (2009). URL http://gcm.upc.edu/members/luis-carlos/bayesiano.

[20] M. Rovira-Esteva, N. A. Murugan, L. C. Pardo, S. Busch, et al. *Phys. Rev. B* **84**, 064202 (2011).

[21] M. Rovira-Esteva, A. Murugan, L. C. Pardo, S. Busch, et al. *Phys. Rev. B* **81**(9), 092202 (2010).

TOPIC 7: Fitting in a complex χ^2 landscape using an optimized hypersurface sampling

L. C. Pardo,[1] M. Rovira-Esteva,[1] S. Busch,[2] J.-F. Moulin,[3] and J. Ll. Tamarit,[1]

[1]Grup de Caracterització de Materials, Departament de Física i Enginyeria Nuclear, ETSEIB, Universitat Politècnica de Catalunya, Diagonal 647, E-08028 Barcelona, Catalonia, Spain

[2]Physik Department E13 and Forschungs-Neutronenquelle Heinz Maier-Leibnitz (FRM II), Technische Universität München, Lichtenbergstr. 1, D-85748 Garching, Germany

[3]Helmholtz-Zentrum Geesthacht, Institut für Werkstoffforschung, Abteilung WPN, Instrument REFSANS, Forschungs-Neutronenquelle Heinz Maier-Leibnitz (FRM II), Lichtenbergstr. 1, D-85748 Garching, Germany

Published: **Physical Review E 84, 046711 (October 2011).**
DOI: **http://dx.doi.org/10.1103/PhysRevE.84.046711**

Abstract

Fitting a data set with a parametrized model can be seen geometrically as finding the global minimum of the χ^2 hypersurface, depending on a set of parameters $\{P_i\}$. This is usually done using the Levenberg-Marquardt algorithm. The main drawback of this algorithm is that despite of its fast convergence, it can get stuck if the parameters are not initialized close to the final solution. We propose a modification of the Metropolis algorithm introducing a parameter step tuning that optimizes the sampling of parameter space. The ability of the parameter tuning algorithm together with simulated annealing to find

the global χ^2 hypersurface minimum, jumping across $\chi^2\{P_i\}$ barriers when necessary, is demonstrated with synthetic functions and with real data.

Introduction

Fitting a parametrized model to experimental results is the most usual way to obtain the physics hidden behind data. However, as nicely reported by Transtrum et al. [1], this can be quite challenging and it usually takes "weeks of human guidance to find a good starting point". Geometrically, the problem of finding a best fit corresponds to finding the global minimum of the χ^2 hypersurface. As this hypersurface is often full of fissures, local minima prohibit an efficient search. The human guidance consists usually of a set of tricks (depending on every particular problem) that allow to choose the starting point in this landscape such that the first minimum found is indeed the global minimum.

This problem is usually due to the mechanism that is behind classical fit algorithms such as Levenberg-Marquardt (LM) [2]: a set of parameters $\{P_i\}$ is optimized by varying the parameters and accepting the modified parameter set as a starting point for the next iteration only if this new set reduces the value of a cost or merit function such as χ^2. From a geometrical point of view, those algorithms allow only downhill movements in the $\chi^2\{P_i\}$ hypersurface. Therefore they can get stuck in local minima or get lost in flat regions of the χ^2 landscape [1]. This means that they are only able to find an optimal solution if they are initialized around the absolute minimum of the χ^2 hypersurface.

The challenge of finding the global minimum can be alternatively tackled by Bayesian methods [3, 4] as demonstrated in different fields such as astronomy or biology [5–9], solid state physics [10–12], quasielastic neutron scattering data analysis [13], and Reverse Monte Carlo methods [14–18]. We follow a Bayesian approach to the fit problem in this contribution. This method is based on another mechanism to wander around in parameter space: instead of allowing only downhill movements, parameter changes that increase χ^2 can also be

accepted if the change in χ^2 is compatible with the data errors.

To do that, a Markov Chain Monte Carlo (MCMC) method is used, where the Markov Chains are generated by the Metropolis algorithm [19, 20]. However, while in the case of the LM algorithm the initialization of parameters is critical to the convergence of the algorithm, it is here the tuning of the maximum parameter change allowed at each step (called parameter jumps hereafter) that will decide the success of the algorithm to find the global $\chi^2\{P_i\}$ minimum in an efficient way.

If the parameter jumps are chosen too small, the algorithm will always accept any parameter change, getting lost in irrelevant details of the $\chi^2\{P_i\}$ landscape. If chosen too large, the parameters will hardly be accepted and the algorithm will get stuck every now and then. Moreover, in the case of models defined by more than one parameter, when parameter jumps are not properly chosen, the parameter space can be over-explored in the direction of those parameters with too small jump lengths, in other words, the model would be insensitive to the proposed change of these parameters. On the other hand, some other parameters can be associated to a jump so big that changes are hardly ever accepted.

Different schemes have been proposed in order to change parameter jumps to explore the target distribution efficiently using Markov Chains under the generic name of adaptive MCMC [21]. Using the framework of the Stochastic Approximation [22] we present in this work an algorithm belonging to the group of "Controlled Markov Chains" [23, 24] where the calculation of new parameter jumps takes the history of the Markov Chain and previous parameter jumps into account.

Two main approaches are known which take the Markov Chain history into account: Adaptive Metropolis (AM) algorithms[25] (implemented for example in PyMC [26]) and algorithms that use rules following Robbins-Monro update [24, 27, 28]. In the first case, parameter jumps are tuned using the covariance matrix at every step, so that once the adaptation is finished the algorithm should be wandering with a parameter jump close to the "error" of the parameter (defined as the variance of the posterior parameter PDF). In some

cases, this kind of algorithm [21] can get stuck if the acceptance ratio of a parameter is too high or too low. In this case the Markov Chain stops learning from the past history, thus the optimization is stopped with suboptimal parameter jumps. This problem is overcome by Robbins-Monro update rules that change parameter jumps so that they are accepted with an optimal ratio.

The main danger of optimized Metropolis algorithms is that adaptation might cause the Markov Chain to not converge to the target distribution any more. In other words, the Markov Chain might lose its ergodicity. For example in the case of AM algorithms, the generated chain is not Markovian since it depends on the history of the chain. However, as demonstrated by Haario et al. [25], the chain is able to reproduce the target distribution, i. e., is ergodic. In the second type of algorithms, the Robbins-Monro type, ergodicity properties must be assured by updating only at regeneration times [28]. In any case, as pointed out by Andrieu et al. [21] the convergence to the target distribution is assured if optimization vanishes. In other words, if parameter jumps oscillate around a fixed value the ergodic property of the Markov Chain is assured.

The presented algorithm is based on the stochastic approach of Robbins-Monro with an updating rule inspired by the one of Gilks et al. [28]. Optimization of parameter jumps is therefore performed with two goals in mind:

- To calculate them in such a way that all parameters are accepted with the same ratio. Adjusting parameter jumps so that all parameter changes will have the same acceptance ratio is important to explore the $\chi^2\{P_i\}$ landscape with the same efficiency in all parameter directions.

- To adjust parameter jumps to a value tailored to the stage of the fit. This will turn out to be important when exploring the $\chi^2\{P_i\}$ hypersurface using the simulated annealing technique [29], since this allows the parameter jumps to be optimized to explore $\chi^2\{P_i\}$ (see subsection fitting in a complex χ^2 landscape): at the beginning of the fit process the algorithm will set parameter jumps to a large value to explore large portions of

the χ^2 landscape, and at the final stages these parameter jumps will be set to small values by the same algorithm in order to find its absolute minimum.

Geometrically, we can interpret the algorithm as setting the parameter step sizes to a value related to the hypersurface landscape. First, it modifies the parameter jump to take into account the shape of the hypersurface along a parameter direction. If $\chi^2\{P_k\}$ (the cut along a parameter k) is flat (the parameter direction is "sloppy" following Sethna's nomenclature [30]), the parameter step size is set to a larger value, and parameters will move faster in this sloppy direction. On the contrary, in the directions where the $\chi^2\{P_k\}$ has a larger slope (the "stiff" direction following Sethna's nomenclature), parameter steps will be set to a smaller value so that they are accepted with the same as the previous ones. Second, it modifies the parameter jumps to take the shape of the global χ^2 landscape into account when the simulated annealing is used. At the beginning of the fit parameter jumps will be set to a large value so that details of $\chi^2\{P_k\}$, i. e., local minima, will be smeared out, making it easier to find the global minimum. However, during the last steps of the fitting process, parameter steps will be set to a small value by the algorithm so that the system will be allowed to relax inside the minimum.

The present work gives a detailed description on how the algorithm works, and will be organized as follows: We first recall briefly on the Metropolis method applied to generate Markov Chains. In the next section, the proposed algorithm to optimize the parameter step size is introduced. Afterwards, we check its robustness to find optimized parameter jumps using a simple test function; and finally we test the ability of the regenerative algorithm combined with the simulated annealing technique to find the global minimum of χ^2, even with poor initialization values, using a simple function with a complex $\chi^2\{P_i\}$ landscape. The algorithm presented in this work has been implemented in the program FABADA [31].

The fit method

Fitting with the Bayesian ansatz Fitting data using the Metropolis algorithm is based on an iterative process where successively proposed parameter sets are accepted according to the probability that these parameters describe the actual data, given all available evidence. Hence this method makes use of our knowledge of the error bars of the data.

We now briefly recall how this can be done using a Metropolis algorithm, to proceed in the next section with the algorithm to adjust parameter jumps.

We should first start with the probabilistic bases behind the χ^2 definition. The probability $\mathbb{P}(H \mid D)$ that an hypothesis H is correctly describing an experimental result D is related to the likelihood $\mathbb{P}(D \mid H)$ that experimental data D_k $(k = 1, \ldots, n)$ are correctly described by a model or hypothesis H_k $(k = 1, \ldots, n)$; using Bayes theorem [3, 4],

$$\mathbb{P}(H_k \mid D_k) = \frac{\mathbb{P}(D_k \mid H_k)\, \mathbb{P}(H_k)}{\mathbb{P}(D_k)} \tag{6.39}$$

where $\mathbb{P}(H_k \mid D_k)$ is called the *posterior*, the probability that the hypothesis is in fact describing the data. $\mathbb{P}(D_k \mid H_k)$ is the *likelihood*, the probability that the description of the data by the hypothesis is good. $\mathbb{P}(H_k)$ is called the *prior*, the probability density function (PDF) summarizing the knowledge we have about the hypothesis before looking at the data. $\mathbb{P}(D_k)$ is a normalization factor to assure that the integrated posterior probability is unity.

In the following we will assume no prior knowledge (maximum ignorance prior [4]), in this special case Bayes theorem takes the simple form

$$\mathbb{P}(H_k \mid D_k) \propto \mathbb{P}(D_k \mid H_k) \equiv L \tag{6.40}$$

where L is a short notation for likelihood.

Although this is by no means a prerequisite, we will assume in the following that the likelihood that every single data point D_k described by the model or hypothesis H_k follows a Gaussian distribution. The case of a Poisson distribution was discussed previously [32, 33]. For

data with a Gaussian distributed uncertainty with width σ, the likelihood for each individual data point takes the form

$$\mathbb{P}(D_k \mid H_k) = \frac{1}{\sigma\sqrt{2\pi}} \exp\left[-\frac{1}{2}\left(\frac{H_k - D_k}{\sigma_k}\right)^2\right] \tag{6.41}$$

and correspondingly, the likelihood that *the whole* data set is described by this hypothesis is

$$\begin{aligned} \mathbb{P}(D_k \mid H_k) &\propto \prod_{k=1}^{n} \exp\left[-\frac{1}{2}\left(\frac{H_k - D_k}{\sigma_k}\right)^2\right] \\ &= \exp\left[-\frac{1}{2}\sum_{k=1}^{n}\left(\frac{H_k - D_k}{\sigma_k}\right)^2\right] \\ &= \exp\left(-\frac{\chi^2}{2}\right) \quad . \end{aligned} \tag{6.42}$$

The Metropolis algorithm will in this special case consist on the proposition of successive sets of parameters $\{P_i\}$. A new set of parameters is generated changing one parameter at a time using the rule

$$P_i^{\text{new}} = P_i^{\text{old}} + r \cdot \Delta P_i^{\max} \tag{6.43}$$

where $\Delta P_i^{\max}$ is the maximum change allowed to the parameter or parameter jump and r is a random number between -1.0 and 1.0. The new set of parameters will always be accepted if it lowers the value of χ^2, or, if the opposite happens it will be accepted with a probability

$$\frac{\mathbb{P}(H\{P_i^{\mathrm{l}+1}\} \mid D_k)}{\mathbb{P}(H\{P_i^{\mathrm{l}}\} \mid D_k)} = \exp\left(-\frac{\chi^2_{\mathrm{l}+1} - \chi^2_{\mathrm{l}}}{2}\right) \tag{6.44}$$

where $\chi^2_{\mathrm{l}+1}$ and χ^2_{l} correspond to the χ^2 for the proposed new set of parameters and the old one, respectively. Otherwise, this new parameter value will be rejected and the fit function does not change during this step.

The Metropolis algorithm described here is very similar to the one used in statistical physics to find the possible molecular configurations (microstates) at a given temperature. In that case the

algorithm minimizes the energy of the system while allowing changes in molecular positions that yield an increase of the energy if it is compatible with the temperature.

Inspired by the similarities between fitting data using a Bayesian approach and molecular modelling using Monte Carlo methods, a simulated annealing procedure proposed by Kirkpatrick [29] might optionally be used (see for example [10, 34]). Following the idea of that work, the χ^2 landscape might be compared with an energy landscape used to describe glassy phenomena [35]. What we do is to start at high temperatures, i. e., in the liquid phase, where details of the energy landscape are not so important. By lowering the temperature fast enough the system might fall into a local minima, i. e., in the glassy phase. In that case the system is quenched as it is normally done by standard fitting methods. The presented algorithm aims to avoid being trapped in local minima using an "annealing schedule" as suggested by Kirkpatrick. This is done by artificially increasing the errors of the data to be fitted and letting the errors slowly relax until they reach their true values. Because this is very similar to what is performed in molecular modelling, the parameter favouring the uphill movements in Equation 6.45 is usually called *temperature*, yielding the acceptance rule

$$\frac{\mathbb{P}(H(P_i^{\mathrm{l}+1}) \mid D_k)}{\mathbb{P}(H(P_i^{\mathrm{l}}) \mid D_k)} = \exp\left(-\frac{\chi^2_{\mathrm{l}+1} - \chi^2_{\mathrm{l}}}{2\,T}\right) \quad . \tag{6.45}$$

As it happens with Monte Carlo simulations, increasing the temperature will increase the acceptance of parameter sets that increase χ^2, thus making the jump over χ^2 barriers between minima easier.

Adjusting the parameter step size The objective of tuning the parameter step size is to choose a proper value for $\Delta P_i^{\max}$ in Equation 6.43 to optimize the parameter space exploration.

Given the total number of algorithm steps N and the number of steps that yield a change in χ^2, i. e., the number of successful attempts, K, the ratio R of steps yielding a χ^2 change is $R = K/N$. R_{desired} is defined as the ratio with which *some parameter* should

be accepted in a step. As we want every parameter to be changed with the same ratio, $R_{i,\text{desired}} = R_{\text{desired}}/m$ where m is the number of parameters.

The algorithm is initialized with a first guess for the parameter step sizes. This first guess, as will be seen shortly, is not important due to the fast convergence of the algorithm to the optimized values. The calculation of a new $\Delta P_i^{\max}$, i. e., the regeneration of the Markov Chain, is done after N steps, i. e., at regeneration times, through the equation

$$\Delta P_i^{\max,\text{new}} = \Delta P_i^{\max,\text{old}} \frac{R_i}{R_{i,\text{desired}}} \tag{6.46}$$

where R_i is the actual acceptance ratio of parameter i. Following the previous equation, if the calculated ratio $R_i/R_{i,\text{desired}}$ is equal to one, i. e., if all parameters are changing with the same predefined ratio, $\Delta P_i^{\max}$ will not be changed.

If during the fit process a change of parameter P_i is too often accepted, the parameter space is being over explored with regard to parameter i. The algorithm will then make $\Delta P_i^{\max}$ larger in order to reduce its acceptance. The contrary happens if the acceptance is too low for a parameter: the algorithm makes $\Delta P_i^{\max}$ smaller to increase its acceptance ratio. This will set different step sizes for each parameter, making the exploration of all of them equally efficient.

Demonstrations of fitting functions

Fitting in a well-behaved χ^2 landscape The optimization of the parameter step size is shown using the Gaussian function

$$y(x) = \frac{A}{W\sqrt{2\pi}} \exp\left[-\frac{(x-C)^2}{2W^2}\right] \tag{6.47}$$

where A is the amplitude, W is the width and C is the centre of the Gaussian. A function has been generated with the parameter set $\{A, W, C\} = \{10, 1, 5\}$ and a normally distributed error with $\sigma = 0.1$ was added. A series of tests with different initial values for parameter jumps and different desired acceptance ratios have been carried out (see below for details). The initial parameters for the fit were

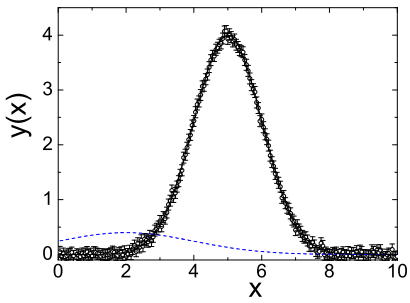

Figure 6.56: Circles: Generated Gaussian function to test the algorithm with the parameters $\{A, W, C\} = \{10, 1, 5\}$. Dashed line: starting point for all performed tests ($\{A, W, C\} = \{2, 2, 2\}$). Solid line: best fit, i. e., minimum χ^2 fit, of the Gaussian function.

$\{A, W, C\} = \{2, 2, 2\}$. In all cases the algorithm was able to fit the data as can be seen in Figure 6.56.

The parameter step size was adjusted every 1000 steps. Three cases are shown in Figure 6.57: an initial $\Delta P_i^{\max}$ of 10 (a very large jump compared to the parameter values, nearly always resulting in a rejection of the new parameters) and an R_{desired} of 66%, the same $\Delta P_i^{\max}$ with an R_{desired} of 9% and finally a $\Delta P_i^{\max}$ of 10^{-4} (a very small jump compared to the parameter values, resulting in a slow exploration of the parameter space) and an R_{desired} of 9%. It can be seen that the algorithm manages in all these extreme cases to adapt the jump size quickly and reliably in order to make R equal to R_{desired}.

In Figure 6.58 we show the three individual acceptance ratios R_i for the different parameters as a function of the fit steps for different initialization values of the parameter jumps ΔP_i, for different values of R_{desired}, and setting the number of steps to recalculate parameter jumps N to 1000. When the total acceptance ratio is set to $R_{\text{desired}} = 66\%$ (solid line), the algorithm is able to change all parameter jumps (see Figure 6.58(b)), making the acceptance ratio R_i of every parameter equal to $R_{\text{desired}}/m = 22\%$ and thus the total acceptance ratio R to 66%. The same happens if the acceptance is set

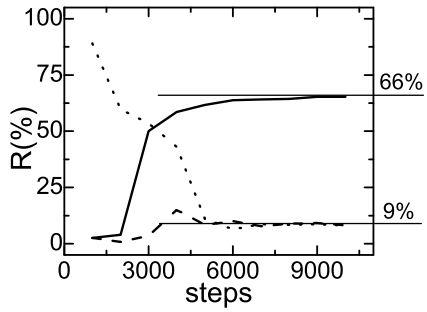

Figure 6.57: Total acceptance ratio R as a function of the number of steps when R_{desired} is set to 66% and 9% (solid and dashed or dotted lines). In the second case ($R_{\text{desired}} = 9\%$), dashed and dotted lines represent the values of R as a function of algorithm step for two different parameter step size initializations ($\Delta P_i^{\max} = 10$ and $\Delta P_i^{\max} = 10^{-4}$, respectively)

to 9%: the algorithm finds the parameter step sizes (see dashed line in Fig. 6.58(b)) which yield a total acceptance ratio of 9% within the first 5000 steps, no matter how the parameter step sizes were initialized.

To explicitly show how this is linked with the geometrical features of the χ^2 landscape, the inset of Figure 6.58(b) shows a cut of the χ^2 hypersurface along parameters A and C, leaving parameter W fixed to its best fit value W_{BF}. As can readily be seen, the $\chi^2\{A, C, W = W_{\text{BF}}\}$ hypersurface is sloppy in the direction of parameter A and stiff in the direction of parameter C. The algorithm has thus correctly calculated a parameter step size which is larger for A than for C, along whose direction the χ^2 well is narrower. This fact makes the final parameter step sizes proportional to the errors of each parameter – if the global minimum is not multimodal, is quadratic in all parameters, and those are not correlated.

In order to show the robustness of the algorithm, we have also made disparate initial guesses for parameter step sizes $\Delta P_i^{\max}$ about three decades below the correct acceptance ratio, setting $R_{\text{desired}} =$

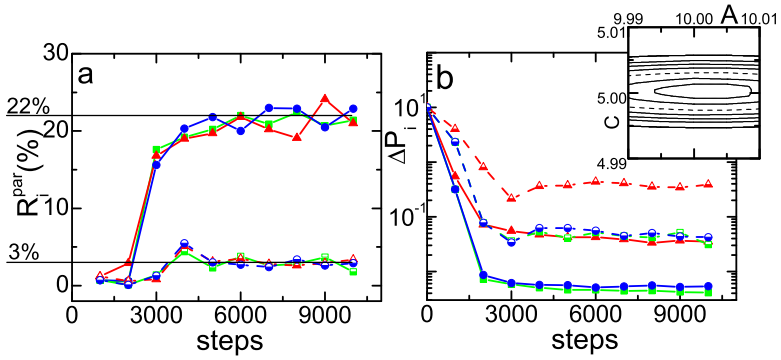

Figure 6.58: a) Acceptance ratio R_i for parameters A, W, C involved in the fit of the Gaussian following Equation 6.47 (red triangles, green squares and blue circles respectively) when R_{desired} is set to 66% and 9% (solid and dashed lines). b) Parameter step size as a function of the number of steps (line and symbols code as in figure a). The inset shows a cut through the χ^2 hypersurface along A and C directions fixing W to the best fit value.

9%. As displayed in Figure 6.58, after about 5000 steps the acceptance ratio R (N is again 1000 steps) has already reached the desired value. It can be seen in Figure 6.59(a) that the acceptance ratio for each parameter reaches again the value $R_{\text{desired}}/m = 3\%$ and parameter step sizes are virtually equal to those obtained previously as shown in Figure 6.59(b).

To stress the relevance of the aforementioned algorithm to explore the parameter space correctly, thus assuring its convergence, we have calculated the normalized $\Delta\chi^2$PDF in all tested cases. As can be seen in Figure 6.60, the $\Delta\chi^2$ PDF after 10^5 steps matches the chi-square distribution

$$\mathbb{P}(\Delta\chi^2) \propto \left(\Delta\chi^2\right)^{\left(\frac{m}{2}-1\right)} \exp\left(-\frac{\Delta\chi^2}{2}\right) \tag{6.48}$$

with $m = 3$ as expected [2]. In Figure 6.60 we show the $\Delta\chi^2$ PDF

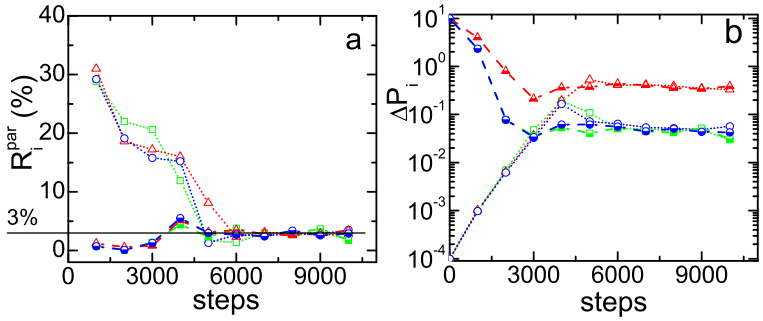

Figure 6.59: a) Acceptance ratio R_i for parameters A (triangles), W (squares), C (circles) involved in the fit of the Gaussian following Equation 6.47 when initial parameter step sizes are set to $\Delta P_i = 10$ (dashed line) and $\Delta P_i = 10^{-4}$ (dotted line). b) Parameter step size as a function of the number of steps (lines and symbols as in figure a).

obtained after 10^4 steps for different cases: first setting $\Delta P_i^{\max}$ equal to the value calculated by the algorithm and second setting $\Delta P_i^{\max}$ equal to the initial guess and finally to a value, calculated a posteriori, which is proportional to the best fit parameters $\Delta P_i^{\max} = 0.1\, P_i$ (inset of Figure 6.60)

As can be seen in Figure 6.60, when $\Delta P_i^{\max}$ is set much higher than the optimal step sizes, the Metropolis algorithm scans the whole parameter space $\{P_i\}$, but jumping between disparate regions with very different values of χ^2, therefore with a low acceptance rate of new parameter sets (dashed line in Figure 6.60). This causes a poor exploration of parameter space. In contrast, a small value over-explores only a restricted portion of $\{P_i\}$, falling very often in local minima of the parameter space (dotted line in the same figure). Also choosing parameter jumps proportional to the final parameters leads to a poor exploration of parameter space (solid line in the same figure). Finally, after the same number of steps, when using the optimized parameter

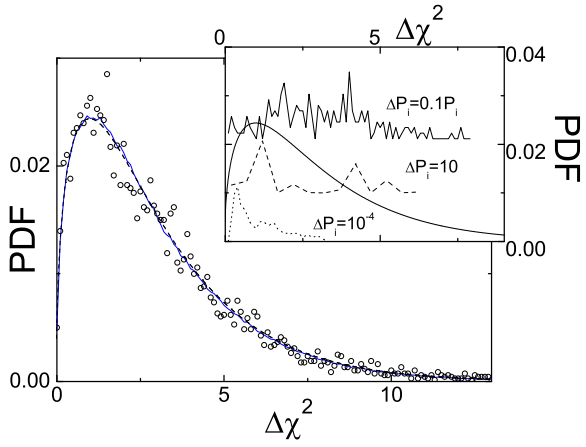

Figure 6.60: The dashed line represents a chi-square distribution for three parameters, i. e., $m = 3$ (see text for details). Solid line is the obtained PDF associated to $\Delta\chi^2$ when calculated for 10^5 steps. Circles represent the same distribution when calculated using only 10^4 steps. The inset shows the χ^2 PDFs when calculated with parameters allowed to change with $\Delta P_i = 10^{-4}$, $\Delta P_i = 10$, $\Delta P = 0.1\, P_i$. Successive PDFs are displaced on the ordinate axis for clarity of the figure.

step sizes obtained by the algorithm the χ^2 PDF follows the theoretical expectation, meaning that the parameter space is correctly sampled.

Fitting in a complex χ^2 landscape As pointed out before, one of the main problems when dealing with data fitting using the LM algorithm is to find a proper set of initial parameters close enough to the global minimum of the $\chi^2\{P_i\}$ hypersurface. As an example we show in Figure 6.61 the function $\sin(x/W)$ for $W = 5$ affected by a normal distributed error with $\sigma = 0.1$. In Figure 6.62(a) we show the $\chi^2\{W\}$ landscape associated to the generated function. As it can be seen, the $\chi^2\{W\}$ landscape for this function has a great number of

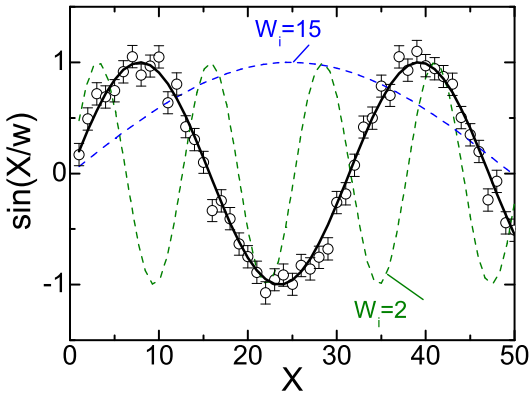

Figure 6.61: Synthetic $\sin(x/5)$ function (circles) together with the best fit using parameter step sizes tuning together with simulated annealing (line). Dashed lines are the fits using the LM algorithm with starting parameters $W_i = 2$ and $W_i = 15$.

local minima and a global minimum at $W = 5$. We have fitted the function using the LM algorithm and initializing the parameter at $W_i = 2$ and $W_i = 15$ (see Figure 6.61). As expected, both fits were not able to find the global minimum that fits the function. In fact only if the LM algorithm is initialized between $W = 3.6$ and $W = 9.0$ it is able to succeed in fitting the data.

We now test the ability of our algorithm to jump across χ^2 barriers delimiting successive local minima to find the global one. For this task we have used the simulated annealing method, decreasing the temperature one decade every 3000 steps from $T = 1000$ to $T = 1$. The parameter jump calculation has been performed every $N = 1000$ steps. While the initial temperature allows to explore wide regions of the parameter space, the last temperature will let the acceptance be determined only by the real errors of the data.

In Figure 6.62(b) we show the parameter W as a function of al-

gorithm step for the two aforementioned initializations together with the χ^2 landscape (a). Parameter step sizes were initialized after a first run of optimization of 2000 steps. As can be seen in this figure, after 3000 steps both runs have already reached the absolute χ^2 minimum. Successive steps just relax the system to the final temperature $T = 1$.

As it can be seen in Figure 6.62, the way the minimum is reached depends on the parameter initialization. Parameter step sizes are larger for the run started with $W_i = 15$ with a flat local minimum. The contrary happens with the run initialized at $W_i = 2$, parameter step sizes are set small due to the narrow wells of the χ^2 landscape in this region. However, both runs are able to avoid getting stuck in local minima, jumping over rather high χ^2 barriers and successfully reaching the best fit.

Conclusion

Classical fit schemes are known to fail when the parameters are not initialized close enough to the final solution. We have proposed in this work to use an Adaptive Markov Chain Monte Carlo Through Regeneration scheme, adapted from that of Gilks et al. [28], combined with a simulated annealing procedure to avoid this problem.

The proposed algorithm tunes the parameter step size in order to assure that all of them are accepted in the same proportion. Geometrically the parameter step size is set large when a cut of $\chi^2\{P_i\}$ along this parameter is flat, i. e., when the change of the $\chi^2\{P_i\}$ hypersurface along this parameter is sloppy. Similarly the parameter step size is set small if $\chi^2\{P_i\}$ wells are narrow.

Moreover, the step sizes can be modulated by a temperature added to the acceptance equation that makes jumps across χ^2 barriers easier, i. e., using a simulated annealing method [29]. From a geometric point of view, a high temperature makes the $\chi^2\{P_i\}$ wells artificially broader, smearing out details of local minima. This is important at the first stages of a fit process. At final stages of the fitting, temperature is decreased, making parameter jumps smaller, and thus allowing the system to relax, once it is inside the global

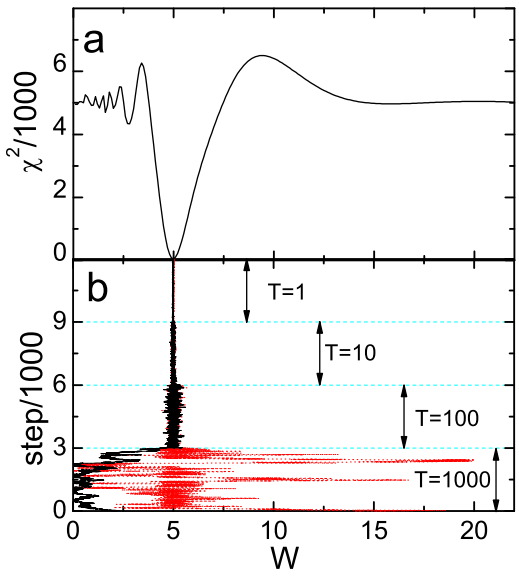

Figure 6.62: (a) $\chi^2\{W\}$ landscape obtained for the function $\sin(x/W)$ with a normal error associated of $\sigma = 0.1$ (see Figure 6.61). (b) Algorithm steps for two different initializations , black solid line for $W_i = 2$ and red dashed line for $W_i = 15$, as a function of parameter W

minimum.

By fitting simulated data including statistical errors we verified that our algorithm actually fulfils the requirements of ergodicity (it converges to the target distribution), robustness (the ability to reach the χ^2 minimum independent of the choice of starting parameters), ability to escape local minima and to explore efficiently the χ^2 landscape, and guarantee that it will self tune to converge to the global minimum avoiding an infinite search with large steps.

More complex problems have already successfully been studied with this algorithm such as model selection using Quasielastic Neutron Scattering data [36, 37], non-functional fits in the case of dielec-

tric spectroscopy [38] or finding the molecular structure from diffraction data with a model defined by as many as 27 parameters [39]. In the last case, the proper initialization of parameters to use a LM algorithm would have been a difficult task, made easy by the use of the presented algorithm.

Acknowledgments

This work was supported by the Spanish Ministry of Science and Technology (FIS2008-00837) and by the Catalonia government (2009SGR-1251). We would also like to thank helpful comments and discussions on the manuscript made from K. Kretschmer, Anand Patil, Christopher Fonnesbeck, and A. Font.

References

All online references accessed on July 22, 2014.

[1] M. K. Transtrum, B. B. Machta, and J. P. Sethna. *Phys. Rev. Lett.* **104**(1), 060201 (2010).

[2] W. H. Press, S. A. Teukolsky, W. T. Vetterling, and B. P. Flannery. *Numerical Recipes in Fortran 77: the art of scientific computing*. Cambridge University Press, 2nd edition (1992).

[3] T. Bayes and R. Price. *Philos. T.* **53**, 370 (1763).

[4] D. Sivia and J. Skilling. *Data Analysis: A Bayesian Tutorial*. Oxford University Press (2006).

[5] R. Trotta. *Contemp. Phys.* **49**(2), 71 (2008).

[6] J. P. Huelsenbeck, F. Ronquist, R. Nielsen, and J. P. Bollback. *Science* **294**, 5550 (2001).

[7] G. A. T. McVean, S. R. Myers, H. S, P. Deloukas, et al. *Science* **304**, 5670 (2004).

[8] R. Diehl, H. Halloin, K. Kretschmer, A. W. Strong, et al. *A&A* **449**(3), 1025 (2006).

[9] A. N. Naganathan, R. Perez-Jimenez, V. M. noz, , et al. *Phys. Chem. Chem. Phys.* **13**, 17064 (2011).

[10] J. J. Mortensen, K. Kaasbjerg, S. L. Frederiksen, J. K. N. rskov, et al. *Phys. Rev. Lett.* **95**, 216401 (2005).

[11] F. J. Bermejo, J. Santoro, F. J. Mompean, and J. C. Dore. *Nucl. Instrum. Meth. Phys. Res. B* **34**, 505 (1988).

[12] S. Bacallado, J. D. Chodera, and V. Pande. *J. Chem. Phys.* **131**(4), 45106 (2009).

[13] D. S. Sivia, C. J. Carlile, W. S. Howells, and S. Konig. *Physica B* **182**(4), 341 (1992). International Workshop On Quasielastic Neutron Scattering, Windsor, England, Apr 06-07, 1992.

[14] R. L. McGreevy and L. Pusztai. *Molec. Simul.* **1**, 359 (1988).

[15] L. Pusztai. *J. Non-Cryst. Sol.* **227-230**(1), 88 (1998).

[16] R. L. McGreevy. *J. Phys.: Cond. Matter* **13**, R877 (2001).

[17] G. Evrard and L. Pusztai. *J. Phys.: Cond. Matter* **17**, S1 (2005).

[18] O. Gereben, P. Jóvári, L. Temleitner, and L. Pusztai. *J. Optoelectron. Adv. Mater.* **9**(10), 3021 (2007).

[19] N. Metropolis, A. Rosenbluth, M. Rosenbluth, A. Teller, et al. *J. Chem. Phys.* **21**, 1087 (1953).

[20] W. K. Hastings. *Biometrika* **57**(1), 97 (1970).

[21] C. Andrieu and J. Thoms. *Stat. Comput.* **18**, 343 (2008).

[22] A. Benveniste, M. Métivier, and P. Priouret. *Adaptive Algorithms and Stochastic Approximations*. Springer, Berlin (1990).

[23] V. S. Borkar. *Topics in Controlled Markov Chains*. Longman, Harlow (1990).

[24] C. Andrieu and C. P. Robert. *Controlled MCMC for optimal sampling*, volume 0125 of *Cahiers de Math'ematiques du Ceremade*. Universit'e Paris-Dauphine (2001).

[25] H. Haario, E. Saksman, and J. Tammien. *Bernouilli* **7**(2), 223 (2001).

[26] A. Patil, D. Huard, and J. F. Christopher. *J. Stat. Soft.* **35**, 1 (2001).

[27] H. Robbins and S. Monro. *Math. Stat.* **22**, 400 (1951).

[28] W. R. Gilks, G. O. Roberts, and S. K. Sahu. *J. Am. Stat. Assoc.* **93**, 1045 (1998).

[29] S. Kirkpatrick. *J. Stat. Phys.* **34**, 347 (1984).

[30] J. J. Waterfall, F. P. Casey, R. N. Gutenkunst, K. S. Brown, et al. *Phys. Rev. Lett.* **104**, 060201 (2010).

[31] L. C. Pardo. *FABADA (Fitting Algortihm for Bayesian Analysis of DAta)* (2009). URL http://gcm.upc.edu/members/luis-carlos/bayesiano.

[32] L. C. Pardo, M. Rovira-Esteva, S. Busch, M. D. Ruiz-Martín, et al. .

[33] L. C. Pardo, M. Rovira-Esteva, S. Busch, M. D. Ruiz-Martín, et al. (2009). arXiv:0907.3711v3[physics.data-an].

[34] J. Schulte. *Phys. Rev. E* **53**, R1348 (1996).

[35] P. G. Debenedetti and F. H. Stillinger. *Nature* **410**, 259 (2001).

[36] M. Rovira-Esteva, A. Murugan, L. C. Pardo, S. Busch, et al. *Phys. Rev. B* **81**(9), 092202 (2010).

[37] S. Busch, C. Smuda, L. C. Pardo, and T. Unruh. *J. Am. Chem. Soc.* **132**(10), 3232 (2010).

[38] J. C. Martinez-Garcia, J. Ll. Tamarit, L. C. Pardo, M. Barrio, et al. *J. Phys. Chem. B* **114**, 6099 (2010).

[39] M. Rovira-Esteva, N. A. Murugan, L. C. Pardo, S. Busch, et al. *Phys. Rev. B* **84**, 064202 (2011).

6.4 Solution to the local density paradox in carbon tetrachloride (CCl_4)

In molecular liquids both the position and the orientation of the molecules are highly disordered. In plastic crystals molecules can rotate more or less freely but their centres of mass are located in a regular lattice, this results in a structure that displays long range positional order but keeps the orientational disorder of the molecules.

Carbon tetrachloride shows both phases and its disordered structure was one of the first and most extensively studied. The goal of this research was to determine the short range order of this compound at each phase to solve the local density paradox, that is, the reason why the density of the liquid is lower than in the plastic phase although molecules are located closer in the first case.

On the one hand, a Bayesian method was used for the fit to the experimental data and to obtain the parameters regarding its intramolecular geometry and, on the other hand, molecular dynamics simulations as well as reverse Monte Carlo modelling was used to study its intermolecular structure.

The analysis showed that although the configuration preferred by molecules in the liquid allows them to sit closer to each other, it does not allow them to stack properly, which results in a mixture of configurations that prevents the molecules from attaining long range order, yielding a poorer global packing and thus a lower density.

Results were presented in several conferences, and partially published in the article: L. C. Pardo, M. Rovira-Esteva, J. Ll. Tamarit, N. Veglio, et al., A procedure to quantify the short range order of disordered phases, *Metastable Systems under Pressure*, pp. 79-91 (book chapter) (2009).

TOPIC 8: A procedure to determine the short range order of disordered phases

L. C. Pardo,[1] M. Rovira-Esteva,[1] J. Ll. Tamarit,[1], N. Veglio,[1] F. J. Bermejo,[2] and G. J. Cuello[3]

[1]Grup de Caracterització de Materials, Departament de Física i Enginyeria Nuclear, ETSEIB, Universitat Politècnica de Catalunya, Diagonal 647, E-08028 Barcelona, Catalonia, Spain

[2]CSIC–Department Electricity and Electronics, UPV/EHU, Box 644, 4880 Bilbao, Spain

[3]Institut Laue Langevin, 6 Rue Jules Horowitz, BP. 156, F-38042 Grenoble Cedex 9, France

Book: **Metastable Systems under Pressure, p. 79, Springer Verlag (November 2009).**
Collection: **NATO Science for Peace and Security Series A - Chemistry and Biology**
Editors: **S. Rzoska, A. Drozd-Rzoska, and V. Mazur**
ISBN: **978-90-481-3406-9**
DOI: **http://dx.doi.org/10.1007/978-90-481-3408-3_6**

Abstract

Determination of the short- and intermediate-range structure of disordered materials is a necessary step to fully understand their properties. Despite of this, no generally accepted procedure exists to date to extract structural information from diffraction data. In this paper we describe a method which enables determination of the short-range structure of disordered molecular phases. This general method is applied to one of the first studied molecular liquids, carbon tetrachloride, and to its plastic phase being able to unravel the so called local density paradox: although molecules are closer in the liquid than in

the plastic phase, the density of the former is lower than that of the later. The analysis of the short range order in both phases shows that although the minimal energy configuration allows a closer approach of molecules, it hinders the formation of the face centred cubic long range ordered lattice due to the difficulty of molecules to form stacked structures.

Introduction

Crystallography is a well established science that allows, among other things, to extract structural information of an ordered arrangement of atoms from a diffraction experiment. In fact, the knowledge of its structure is fundamental in order to characterize a crystalline phase and this helps in the comprehension of a large amount of physical data, from dynamics to thermodynamics. This is done by means of well established procedures (as Rietveld refinement) supported by a huge amount of software. Astonishingly enough this is not the case for disordered phases such as liquids or plastic phases (a phase where, although the centres of mass of the molecules are in long range ordered positions, the molecules rotate more or less freely) and their non-ergodic associated states, or in other words, their glasses. In these cases physical data is usually interpreted not taking into account the Short Range Order (SRO) structure, probably simply due to the lack of a well established procedure to determine their structures.

In this chapter we offer a method to fully determine the structure of disordered phases, from the molecular structure to the SRO, and we apply it to the determination of the structure of one of the first molecular liquids studied ever, carbon tetrachloride, and its not so well studied plastic phase. Concerning the SRO of the liquid phase, regarded as the most probable dimmer configuration between two "close" molecules, no consensus exists so far. Considering the CCl_4 molecule as a tetrahedron, where the chlorine atoms are sitting in its corners and the central carbon atom is equidistant to those corners, we find in the literature the configurations face to face [1, 2], corner to face (also called Apollo) [3], corner to corner [4], and edge to edge

or interlocked [5]. However a recent work of Rey [6], where for the first time a clear quantitative definition of the aforementioned configurations is presented, demonstrates that although the edge to edge (or interlocked) configuration (as defined there) clearly dominates, other configurations such as face to face are also possible at very short distances between molecules. Concerning the plastic phase, all the members of the methyl-halogenomethane family $(CCl_n(CH_3)_{(4-n)}$ with $n = 0, 1, 2, 3, 4$; including CCl_4 ($n = 4$) has a phase transition from the liquid phase to a plastic phase with a high-symmetry lattice (cubic or rhombohedral) [7, 8], which in the case of CCl_4 is Face Centred Cubic (FCC) [9–11].

Experiments and data treatment

A series of neutron diffraction experiments were carried out using the D1b diffractometer at the Institute Laue Langevin, Grenoble, France. The instrument is a general purpose powder diffractometer which uses a banana-shaped detector covering a wide angular range. The measurements were performed using a wavelength $\lambda = 1.2805$ Å which, combined with data acquisition at two different detector positions, allowed us to cover a q-range up to 8 $Å^{-1}$ large enough to study the structure factor, account made of the small intermolecular distances. Details concerning the instrument settings and data correction procedures (inelastic contributions, multiple scattering, detector efficiency, self absorption, and normalization to a known vanadium sample) are given elsewhere [12, 13]. Concerning the plastic phase phase, the growth of a polycrystalline FCC phase was ascertained by the emergence of a set of crystalline Bragg peaks as described previously [12, 13]. Experimental results for the liquid phase are shown in Figure 6.63a, as well as the total radial distribution function for the FCC phase (calculated as $G(r) = 1 + \rho_0^{-1} (2\pi)^{-3} \mathcal{FT}[S(q) - 1]$, where $\mathcal{FT}$ means Fourier Transform). For a description of data treatment see in this series the paper entitled "Neutron diffraction as a tool to explore the free energy landscape in orientationally disordered phases" or Reference [14–16].

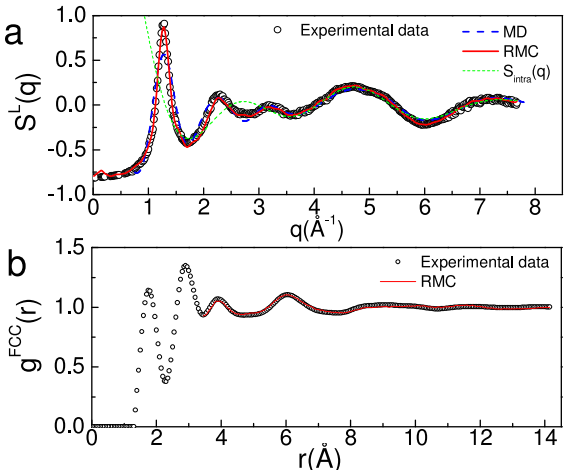

Figure 6.63: a) Scattering function for liquid Carbon Tetrachloride together with its determination by means of molecular dynamics and Reverse Monte Carlo (RMC). With dotted lines we show the determination of the intramolecular structural parameters determined by the Bayesian method described in the text. b) Total radial distribution function for the FCC phase, together with the results of RMC.

Extracting the molecular structure from data

Total scattering function $S(q)$ has two terms corresponding to distances between atoms at two different length scales: a long scale contribution from intermolecular distances that is the most important contribution in the low-q region of $S(q)$, and a short scale contribution which will mainly contribute in the high-q region of the scattering function. A common method to determine the molecular structure is to fit the scattering function using the expression:

$$S(q) = \sum_{i,j}^{m} b_i b_j \frac{\sin(qr_{ij})}{qr_{ij}} \mathrm{e}^{-\frac{1}{2}\left(u_{ij}^2 q^2\right)} \tag{6.49}$$

where r_{ij} are the intramolecular distances and u_{ij}^2 are the mean square displacements between i and j atoms (the Debye-Waller term, see Reference [14–16]).

In order to fit experimental data, a standard Levenberg-Marquardt (LM) method for minimizing χ^2 is usually performed. This method has two main drawbacks: it can get stuck in local minima of the χ^2-parameter space and therefore must be initialized using values close enough to the final parameters somehow inferred beforehand. In addition the method supposes that there is only one minimum in the χ^2-parameter space (i.e., the solution is not multimodal) and that this minimum must have a quadratic form on all parameters involved. The first problem can be avoided using a "shake" algorithm, i.e., once the LM procedure is stopped at some point, the fitting is repeated from a close set of parameters in order to assure the robustness of the result. The second problem is unavoidable using a minimum χ^2 approach. It implies that LM can only deal with symmetric errors around the highest probable value of parameters, and that the correlation between parameters can only be lineal. Moreover, even if the χ^2 minimum is in fact quadratic, the procedure makes very difficult to take into consideration the correlation between parameters. To obtain them the covariant matrix should be diagonalized, being the eigenvalues the real error of the parameters along the eigenvectors defined by linear combinations of parameters. This implies that in many works errors are calculated under the hypothesis that parameters are independent, and for this reason are underestimated.

An alternative way to reach the minimum of χ^2 is the use of the Bayesian approach, which deals with the direct determination of the Probability Distribution Function (PDF) for the final parameters. This method has the advantage that all the parameter space compatible with the experimental error is explored and therefore correlation between parameters and multimodal minima in the χ^2-parameter space are naturally taken into account. For a review on Bayesian methods the reader is refereed to the excellent monograph of Sivia et al. (Reference [17]), while in this work we will only briefly explain the method used for our specific problem.

In order to obtain the PDF for the parameters, we have used a Markov Chain Monte Carlo method to explore the parameter space. This method is similar to a classical Monte Carlo simulation where the distance between calculated and experimental data ($(y_{\mathrm{calc}}-y_{\mathrm{exp}})^2$)

plays the role of energy, and the experimental error (σ) plays the role of temperature. The method (as employed in this work) is based on the hypothesis that experimental data have a Gaussian distribution around the real value. This is true for a counting experiment with large enough amount of counts, because in this case a Poisson distribution can be approximated by a Gaussian one. Therefore the probability that a function with given fitting parameters (D_k) (what is called the "Hypothesis" in Bayes theorem) is describing your n experimental data points (x_k) with an error σ_k (i.e., data x_k supposed to be normally distributed around D_k with a standard deviation of σ_k) can be expressed as:

$$L \propto P(x_k|D_k) = \prod_k^n e^{-\frac{1}{2}\left(\frac{x_k - D_k}{\sigma_k}\right)^2} \tag{6.50}$$

$$= e^{-\frac{1}{2}\sum_k^n \left(\frac{x_k - D_k}{\sigma_k}\right)^2} = e^{-\frac{\chi^2}{2}} \tag{6.51}$$

This is usually called the likelihood of the hypothesis, or in other words the probability that the fitted function with a given set of parameters is describing the data within the experimental error. In regard to the previous expression, it is easy to see that in fact minimizing χ^2 is just maximizing the likelihood ($\log L \propto -\chi^2/2$) when a Gaussian distribution is assumed for the data. However, the previous method for fitting functions is more general because other distributions than Gaussian can also be used, as in the case of an experiment with a low count rate where the Gaussian approximation to the Poisson distribution is no more applicable.

In order to obtain the PDFs, starting from a set of parameters that minimizes χ^2, we generate randomly a new set of them, being the change between the new and old accepted having in to account the likelihoods of the two parameter sets

$$\frac{P\left(x_k|D_k^{\text{new}}\right)}{P\left(x_k|D_k^{\text{old}}\right)} = e^{-\frac{1}{2}(\chi^2_{\text{new}} - \chi^2_{\text{old}})} \tag{6.52}$$

where $D_k^{\text{new (old)}}$ are the points generated using the new (old) set of parameters.

In Figure 6.64 we show the PDFs obtained for the parameters fitted to the intramolecular structure of CCl_4 using equation (6.49): the distance between the carbon and chlorine atom, and the mean square displacement between the C-Cl and Cl-Cl atom pairs (Cl-Cl distance can be calculated form the tetrahedral geometry of the molecule). In Figure 6.63a we show the fitted function together with experimental data, taking the highest probable parameters obtained by the proposed Bayesian method: $d_{\mathrm{CCl}} = 1.768 \pm 0.004$ Å; $u_{\mathrm{ClCl}} = 0.18 \pm 0.01$ Å^2 and $u_{\mathrm{CCl}} = 0.06 \pm 0.02$ Å^2. Having a careful look at the last parameter u_{CCl} depicted in Figure 6.64 we can see that the probability distribution is not symmetric, being more probable for this parameter to be smaller than larger with respect to the highest probable one. In the case of the simple molecule studied in this work, the proposed method gives the real error of parameters and improves the robustness of their determination in comparison with the standard minimum χ^2 method, but will give the same final parameters as the LM algorithm. We have seen however that for more complicated molecules only the Bayesian method exposed in this work is able to give reasonable results, avoiding the aforementioned danger of LM algorithm being stuck at a local minimum (as the ones studied in the article "Neutron diffraction as a tool to explore the free energy landscape in orientationally disordered phases" in this series, and Reference [18]).

Extracting the short range order from data

In order to extract the configurations to be analysed in the next section, we have both taken the results obtained in a previous Molecular Dynamics (MD) simulation (details on the simulation are given elsewhere [5], and also performed a Reverse Monte Carlo (RMC) analysis of the obtained data on both phases, liquid and ODIC [12, 13]. It should be kept in mind that the two methods are from first principles completely different, needing the first one (MD) a priori information about the intermolecular interaction potentials. In the case of RMC no initial information is needed (except from macroscopic density), and only the experimental result is driving the algorithm to find a

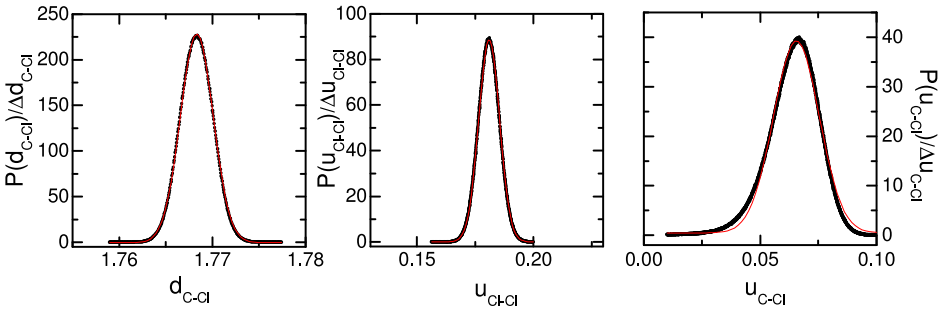

Figure 6.64: Normalized PDFs for the intramolecular structural parameters, together with the fitting of a Gaussian function. The maximum of each PDF, i.e., the most probable parameter value, has been used to calculate the intramolecular structure function of Figure 6.63.

final configuration compatible with the experimental data [19, 20]. It should also be pointed out that a third way combining the advantages of the two methods is possible, the so called Empirical Potential Structure Refinement (EPSR) [21], but this method has not been used in the present work. Flexible molecules have been used in both cases (MD and RMC), being their initial geometry determined by ab initio calculations [12, 13]. The total structure factor for the liquid at 298 K was analysed by RMC method using a simulation box composed by 1000 molecules, with dimensions set to reproduce the experimental density of the liquid ($L = 54.34$ Å). As it has been shown in Figure 6.63, the agreement between the spectra simulated from the RMC and MD configurations and the experimental $S(q)$ is excellent. In what concerns the ODIC phase, a RMC simulation at 240 K has been performed using a box containing 6x6x6 cells, with a length extracted from the Bragg peaks appearing in the spectra ($L = 50$ Å). In this case, the fit was performed using the total radial distribution function as in Reference [22]. The RMC fitting has been performed allowing only small-amplitude motions of the molecular centres about the lattice sites defined by the Bragg peaks, and changing the orientations of the molecules. The agreement between fitted and experimental data can be seen in Figure 6.63b (for further

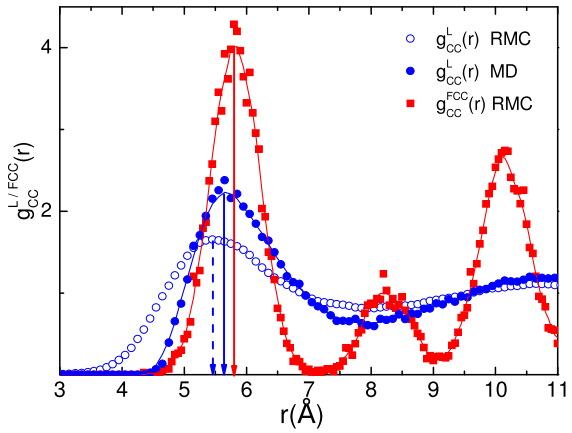

Figure 6.65: Molecular Coordination Number (MCN) as a function of the distance, for the liquid phase (filled circles MD, empty circles RMC) and the FCC phase (squares). Arrows show the maxima of MCN for the aforementioned phases, i.e., the maximum of local density.

details, see Reference [12, 13]).

Analysis of final configurations

Positional ordering In Figure 6.65 we have plotted the Partial Radial Distribution Function (PRDF) $g_{\mathrm{CC}}(r)$ for the molecular centres ($\rho g_{\alpha\beta}(r)\mathrm{d}r$ is defined as the probability of finding a molecule β within the shell $r\mathrm{d}r$ surrounding an atom α, being ρ the macroscopic density). Astonishingly enough, although the macroscopic density is larger in the FCC plastic phase than in the liquid phase, molecules are closer in the second phase. Moreover, the maximum of the PRDF is located at higher distances independently of the used method to obtain the molecular centres PRDF. This "local density paradox" adds new interest in studying the SRO of the two disordered phases, and only a careful method taking into account the 3D SRO would lead to a correct answer.

To obtain the SRO, we have taken the idea of the bivariate analysis, used to study the molecular ordering at interfaces between liquids

and vapors [23], and we have applied it to the study of liquid and plastic phases of CCl_4. In order to locate the position of a second molecule from a central one, three orthogonal axis must be defined in relation with the molecular structure. In our case the z-axis is set along the direction of a C-Cl bond, being another C-Cl bond in the zy-plane (see Figure 6.66). Using this convention we can calculate the azimuthal angle θ as the scalar product between the unit vector along the intramolecular C-Cl bond defined as the z-axis and the intermolecular C-C distance joining the molecular centres of two molecules.

$$\theta = \vec{r}_{C_1-Cl_{1i}} \cdot \vec{r}_{C_1-C_2} \tag{6.53}$$

being C_i $(i = 1, 2)$ the carbon atom from the reference molecule or from the molecule the position of which is to be calculated respectively, and Cl_{ij} $(i = 1, 2,\ j = 1, 4)$ one of the four $i(j)$ chlorine atoms of molecule $i(j)$.

In the same way we can define the equatorial angle φ as the scalar product between the unit vectors perpendicular to two planes: the zy-plane defined by two different intramolecular C-Cl vectors and the plane defined by the z-axis and the intermolecular C-C vector:

$$\phi = \vec{r}_{C_1-Cl_{1i}} \times \vec{r}_{C_1-Cl_{1j}} \cdot \vec{r}_{C_1-Cl_{1i}} \times \vec{r}_{C_1-C_2} \tag{6.54}$$

In Figure 6.67 we show the probability of finding a molecule at a position determined by the equatorial and azimuthal angles (ϕ,cos(θ)) for the first four neighbours (a,c) and therefore molecular distances r_{CC} less than 5.73 Å and 5.63 Å for MD and RMC configurations respectively. The same is depicted in Figures 6.67b and 6.67d also for MD and RMC but in this case for the next four-molecule shell ($5.63 < r_{CC} < 6.5$ Å and $5.63 < r_{CC} < 6.6$ Å). As it can be immediately appreciated, although RMC gives a much more disordered distributions of molecules, for the first molecules the SRO obtained using the two methods is the same, being both completely independent. Unfortunately, because RMC method is a Maximum Entropy method, i.e., it gives the most disordered solution compatible with experiment and therefore the most probable, no clear SRO is appre-

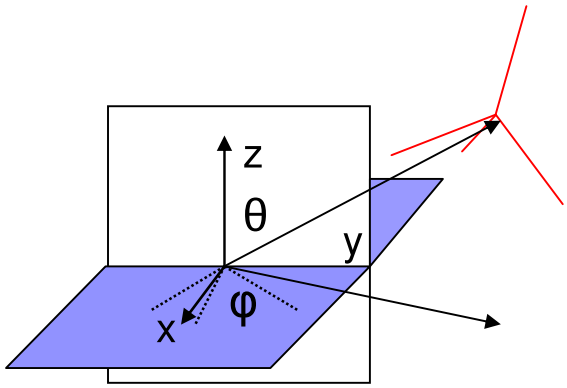

Figure 6.66: Chosen axis in order to calculate the positional ordering of two CCl_4 molecules.

ciated for long distances, and therefore for the liquid phase the discussion will be focused on the MD configurations (see Figure 6.68). On the contrary, in the case of the FCC phase, because a positional ordering already exists, the SRO is clearly determined by the RMC method (see Figure 6.68c).

We define the First Molecular Coordination Shell (FMCS) as the molecules within the first peak of the C-C PRDF, i.e., for distances $r_{CC} < 7.5$ Å (see Figure 6.64). In Figure 6.68 we have depicted the probability of finding a molecule at a position $(\phi, \cos(\theta))$ for successive shells surrounding a central molecule within the FMCS containing only four molecules each: in Figure 6.68a we have therefore the positional ordering for the first four molecules, in Figure 6.68b for the next four molecules and in Figure 6.68c for the last four molecules inside the FMCS. A glance to Figure 6.68 clearly reveals that the distribution of molecules changes as a function of their distance to the central molecule even inside the FMCS. Moreover, molecules in a shell tend to fill the gaps left by the molecules in a shell closer to the central molecule. Taking into account the tetrahedral symmetry of the molecule, the first four neighbours are sitting in the faces of the central molecule (Figure 6.68a), the next four neighbours in the edges and a small fraction in the corners (Figs. 6a,b), and the

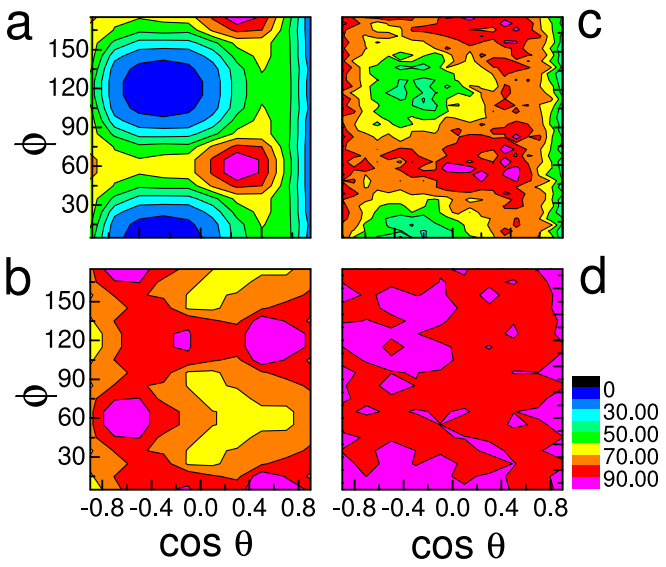

Figure 6.67: Comparison of the ordering obtained for the liquid phase by means of MD (a,b) and RMC (c,d) for the first four molecules surrounding a central one (a MD,c RMC), and for the next four molecules (b MD, d RMC). The color scale represents the normalized probability of finding the molecule at a given position ($P(\phi, \cos(\theta))/P_{\max}$).

last four neighbours in the corners of the central molecule (Figure 6.68c). On the other hand, for the FCC phase, due to its positional ordered nature, we must consider the 12 closer molecules at a distance $r \approx a/\sqrt{2}$. In fact what is represented in Figure 6.68c is the relative orientation of the molecule with respect to the lattice axes, since the positional ordering of molecular centres is fixed in the FCC lattice. Our results are in complete agreement with previous MD simulations [3, 10, 11, 24] where it is asserted that C-Cl vectors lie along [110] and [100] directions. To make this point clear, we can see in Figure 6.68c spots at $(\cos\theta, \phi) = (-0.33, 0°)$ and $(0.33, 60°)$, which means that molecules are placed in the corners and faces with respect of the first neighbours, which lie in the [110] directions. Molecules oriented along the [100] directions are represented at the spots $(0.7, 0°)$ and $(-0.7, 60°)$ and would correspond to the molecules placed in the edge

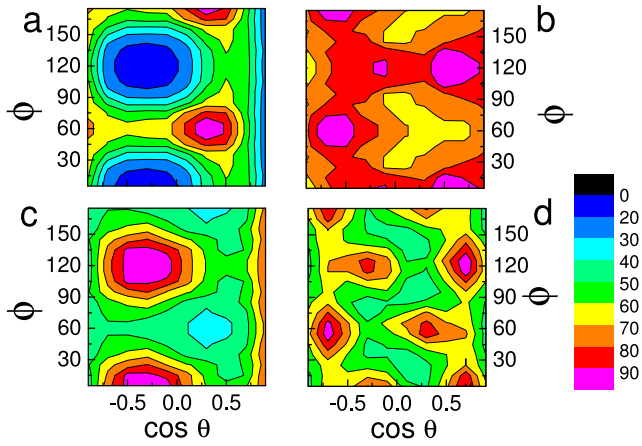

Figure 6.68: Comparison of the positional ordering obtained for the liquid phase (a,b,c) and for the FCC phase (d) by means of MD simulation. Colour scale is defined as in Figure 6.67.

of the molecules in the liquid phase represented by the large spots at about $(0.58, 0°)$ and $(-0.58, 60°)$.

Orientational ordering In order to extract the maximum quantitative information about the relative orientation of molecules we have calculated an histogram of the angle between all possible combinations of C-Cl vectors of two different molecules

$$\alpha = \vec{r}_{\mathrm{C_1-Cl_{1i}}} \cdot \vec{r}_{\mathrm{C_2-Cl_{2j}}} \tag{6.55}$$

Nevertheless if only the probability $P(\alpha)$ of finding an angle α between two C-Cl vectors is studied, the information about the position of molecules is lost, and therefore we would add orientational information for molecules that are placed at different points. For this reason in Figure 6.69 we have plotted the probability $P(\alpha)$ as a function of the cosine of their azimuthal angle $P(\cos\theta, \cos\alpha)$, and therefore we would be eventually able to distinguish between different orientations of molecules sitting in different places. Nevertheless that is not the case as it can be seen in Figure 6.69, where the spots found in the $\cos\alpha$ are independent of that found in the $\cos\theta$, that is,

the position. Lets now define molecules that are "parallel" oriented as those with C-Cl vectors of different molecules pointing in the same direction (therefore $\cos\alpha = 1$), and "antiparallel" as those with C-Cl vectors pointing in opposite directions (therefore $\cos\alpha = -1$). Then the first four molecules surrounding the central one are antiparallel oriented, the next four parallel, and the last four molecules within the FMCS are again antiparallel oriented, standing for the spots at $\cos\alpha = -1$, $\cos\alpha = 1$ and $\cos\alpha = -1$, respectively. For the case of the FCC phase, molecules are parallel oriented irrespective of their position, as can be seen in Figure 6.69d.

Regarding the previous works carried out on CCl_4 in which different or even contradictory molecular arrangements are proposed, and taking into account the present analysis, we can understand the origins of the controversy on the molecular arrangement of this simple molecular liquid. First, the structure of the liquid is distance-dependent and an analysis of the whole first FMCS will lead to wrong results, and second, a bivariate analysis, or any other analysis taking into account the three spatial degrees of freedom of the SRO, must be performed to obtain SRO and must avoid collapsing information in 1-D representations. Joining the aforementioned results obtained for positional and orientational ordering of CCl_4 molecules in the liquid phase we can tentatively assign some configurations found in the literature to molecular arrangements although, as pointed out by Rey [5] only a quantitative definition of those molecular arrangements makes fully sense. Then we can characterize the molecular arrangement of the first four molecules in the liquid as the face to face configuration [1, 2], the next four molecules would be in an Apollo [3] or edge to edge configuration (interlocked of Reference [5]), and the last four molecules of the FMCS in a corner to corner configuration [4]. On the contrary, for the case of the plastic phase, no matter how molecules are positionally arranged, C-Cl vectors are parallel giving rise to Apollo or edge to edge like configurations. This fact provides us a hint to solve the aforementioned "local density paradox". The minimum energy dimmer arrangement is so that faces of the tetrahedra are touching each other (face to face arrangement), but such an arrangement avoids the possibility of a long range ordered lattice. On

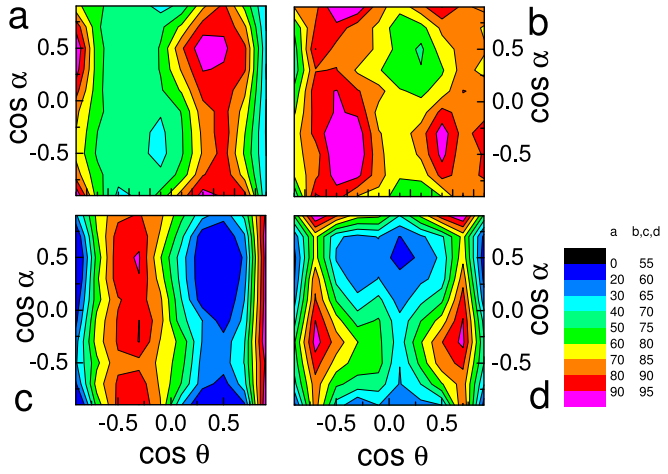

Figure 6.69: Comparison of the orientational ordering obtained for the liquid phase (a,b,c) and for the FCC phase (d) by means of MD simulation. Colour scale is defined as in Figure 6.67.

the contrary for the FCC phase, although closest molecules are not arranged in a minimum energy configuration, they are in all cases arranged in a parallel way, allowing therefore the formation of molecular stacking. It must be borne in mind that this ordering is dynamic in nature, but favouring the aforementioned parallel orientation of molecules.

Conclusions

In this paper we have described a method to fully characterize the SRO in disordered phases. The Bayesian method exposed in the first part of this work allows a robust determination of molecular parameters, and a clearly defined calculation of the errors on the basis of probability theory. In addition we offer an easy method to extract from molecular configurations the SRO (positional and orientational). Using these two methods we have been able to unravel the structure of the liquid phase for carbon tetrachloride, which has been revealed to be richer than previously thought within the first molecular coordination shell. In this phase positional and orienta-

tional short range ordering of molecules simply tries to minimize the energy, the molecules filling the gaps left by successive shells of molecules, and therefore changing the molecular arrangement along shell distance. The situation is different for the plastic phase, for which not only minimizing the energy plays a role in the SRO, but also the possibility of forming molecular stacking, and therefore allowing the formation of a positional long range ordered structure.

Acknowledgements

We would like to acknowledge R. Rey for instructive discussions, and also to allowing us to use the MD configurations obtained in ref. 4. This work was supported by grants from the Spanish Ministry of Science and Innovation (MICINN) (FIS2008-00837) and from the Generalitat de Catalunya (2005SGR-00535). One of us (MRE) acknowledges the PhD fellowship from MICINN. NATO Collaborative Linkage Grant CBP NUKR. CLG 982312 is also acknowledged. We thank ILL and Spanish CRG-D1B for allocating neutron beam time.

References

All online references accessed on July 22, 2014.

[1] L. J. Lowden and D. Chandler. *J. Chem. Phys.* **61**(12), 5228 (1974).

[2] P. Jedlovszky. *J. Chem. Phys.* **107**(18), 7433 (1997).

[3] I. McDonald, D. G. Bounds, and M. L. Klein. *Mol. Phys.* **45**(3), 521 (1982).

[4] P. Jovari, G. Meszaros, L. Pusztai, and E. Svab. *J. Chem. Phys.* **114**, 8082 (2001).

[5] R. Rey, L. Pardo, E. Llanta, K. Ando, et al. *J. Chem. Phys.* **112**(17), 7505 (2001).

[6] R. Rey. *J. Chem. Phys.* **126**(16), 164506 (2007).

[7] L. C. Pardo, M. Barrio, J. Ll. Tamarit, D. O. López, et al. *Chem. Mater.* **17**, 6146 (2005).

[8] L. C. Pardo, M. Barrio, J. Ll. Tamarit, D. O. López, et al. *J. Phys. Chem.* **105**, 10326 (2001).

[9] I. McDonald, D. G. Bounds, and M. L. Klein. *Mol. Phys.* **45**, 521 (1982).

[10] W. Breymann and R. M. Pick. *J. Chem. Phys.* **91**, 3119 (1989).

[11] M. More, H. B. Lefebvre, J. and, B. M. Powell, and C. M. E. Zeyen. *J. Phys. C* **13**, 2833 (1980).

[12] N. Veglio, F. J. Bermejo, L. C. Pardo, J. Ll. Tamarit, et al. *Phys. Rev. E* **72**, 031502 (2005).

[13] L. C. Pardo, N. Veglio, F. J. Bermejo, J. Ll. Tamarit, et al. *Phys. Rev. B* **72**, 014206 (2005).

[14] G. J. Cuello. *J. Phys.-Condens. Mat.* **20**(24), 244109 (2008). URL http://stacks.iop.org/0953-8984/20/i=24/a=244109.

[15] H. E. Fischer, A. C. Barnes, and P. S. Salmon. *Rep. Prog. Phys.* **69**(1), 233 (2006).

[16] C. Talón, F. J. Bermejo, C. Cabrillo, G. J. Cuello, et al. *Phys. Rev. Lett.* **88**(11), 115506 (2002).

[17] D. Sivia and J. Skilling. *Data Analysis: A Bayesian Tutorial*. Oxford University Press (2006).

[18] L. C. Pardo, F. J. Bermejo, J. Ll. Tamarit, G. J. Cuello, et al. *J. Non-Cryst. Solids* **353**(8-10), 999 (2007).

[19] R. L. McGreevy. *J. Phys.: Cond. Matter* **13**, R877 (2001).

[20] G. Evrard and L. Pusztai. *J. Phys.: Cond. Matter* **17**, S1 (2005).

[21] URL http://www.isis.rl.ac.uk/Disordered/DMGroup/DM_epsr.htm. See this link and references therein.

[22] L. Karlsson and R. L. McGreevy. *Physica B* **100**, 234 (1997).

[23] P. Jedlovszky, A. Vincze, and G. Horvai. *Phys. Chem. Chem. Phys.* **6**, 1874 (2004).

[24] R. Rey. *J. Phys. Chem. B* **112**(2), 344 (2008).

6.5 Steric and electrostatic influences in trichlorobromomethane ($CBrCl_3$) and dibromodichloromethane (CBr_2Cl_2)

The structure of the liquid of the carbon tetrachloride tetrahedral molecule (CCl_4), which does not have a dipole moment, has been one of the most extensively studied. Other molecules of the form $CBr_xCl_{(4-x)}$ ($x = 0, 1, 2, 3$) essentially retain this tetrahedral geometry except for minor distortions, but the magnitude and direction of their molecular dipole varies greatly due to differences between Br and Cl electronegativities.

The aim of this work was to study the effect on the short range order of quasitetrahedral molecules of the steric and electrostatic interactions. Trichlorobromomethane ($CBrCl_3$) and dibromodichloromethane (CBr_2Cl_2) are suitable model systems because the dipole of the first is in the direction of the bromine atom, located in one of the tetrahedron vertices, and the dipole of the second is between the two bromine atoms, midway on one of the edges, but they both display a similar magnitude.

The short range order analysis of the two liquids was carried out through reverse Monte Carlo modelling of the experimental data as well as molecular dynamics simulations. Two sets of simulations, one where the atoms had their partial charges and another where they did not, allowed to single out the electrostatic contribution from the structural changes. Comparison was carried out with previous CCl_4 studies, which provided an ideal reference system.

The relative position of the centres of mass of the neighbour molecules in $CBrCl_3$ and CBr_2Cl_2 were shown to be the same as in CCl_4.

The relative orientation of the closest molecules in $CBrCl_3$ favours an antiparallel configuration of their dipoles. No difference can be observed when electrostatic effects are taken into account.

In CBr_2Cl_2, when no electrostatic interactions are included in the simulation, the molecules above the equatorial plane of the reference

molecule dipole prefer a parallel configuration of the dipoles while the ones below the equatorial plane prefer an antiparallel configuration. This is solely due to the steric effects induced by the more bulky bromine atoms of the reference molecule, which are located above the equatorial plane. Since electrostatic interactions favour an antiparallel configuration of the dipoles, when they are included in the simulation they increase the antiparallel configuration where it was already predominant and counteract the parallel configuration elsewhere.

Results were presented in several conferences, and mainly published in the article: Sz. Pothoczki, A. Ottochian, M. Rovira-Esteva, L. C. Pardo, et al., Phys. Rev. B **85**, 014202 (2012).

TOPIC 9: Role of steric and electrostatic effects in the short-range order of quasitetrahedral molecular liquids

Sz. Pothoczki,[1] A. Ottochian,[1] M. Rovira-Esteva,[1] L. C. Pardo,[1] J. Ll. Tamarit,[1], and G. J. Cuello[2]

[1]Grup de Caracterització de Materials, Departament de Física i Enginyeria Nuclear, ETSEIB, Universitat Politècnica de Catalunya, Diagonal 647, E-08028 Barcelona, Catalonia, Spain

[2]Institut Laue Langevin, 6 Rue Jules Horowitz, BP. 156, F-38042 Grenoble Cedex 9, France

Published: **Physical Review B 85, 014202 (January 2012).**

DOI: http://dx.doi.org/10.1103/PhysRevB.85.014202

Abstract

The study of how both steric and electrostatic interactions affect the structure of liquids formed by quasitetrahedral molecules has been undertaken in this work. We have studied trichlorobromomethane ($CBrCl_3$) and dibromodichloromethane (CBr_2Cl_2), both displaying a dipole along their C_{3v} and C_{2v} molecular symmetry axes, respectively. The short-range order of the liquid state has been determined using neutron diffraction experiments that were modelled through the reverse Monte Carlo (RMC) technique. To study changes in steric effects due to the distortion of the tetrahedral symmetry, we have compared our results with a previous RMC modelling of carbon tetrachloride (CCl_4). The subtle effects of the dipole in the structure of the liquid have been determined using a set of molecular dynamics simulations with and without atomic partial charges, being the force field validated via comparison with the diffraction data. In a first approximation, neither steric nor electrostatic interactions are able

to modify the molecular ordering of a fully tetrahedral liquid such as CCl_4. A more detailed analysis indicates that, although the interaction between dipoles does not have appreciable effects when aligned along the C_{3v} molecular axes, as for the $CBrCl_3$, it enhances the antiparallel orientation of dipoles when it is oriented along the C_{2v} axes, as in the case of CBr_2Cl_2.

Introduction

Molecular disordered systems such as liquids are devoid of ordering only at long length scales. Locally, each molecule tends to minimize the configuration energy relative to its neighbours, giving rise to a short-range ordered structure. This local ordering that does not minimize the energy of the system as a whole but, only locally, has been identified as one of the reasons for the existence of glasses [1, 2]. Quantifying the local ordering of a polyatomic molecular liquid from diffraction experiments is not a simple task. The basic problem is that, due to the isotropy of the liquid, diffraction experiments give an average of the distance between molecules. In other words: the subtle spatial short-range order (SRO) of the liquid is collapsed into a one-dimensional pattern or, at best, when enough isotopic substitutions are possible, into as many patterns as contributions from atomic pairs. In any case, molecular orientations must be inferred somehow from a histogram of distances measured in the reciprocal space. To overcome such a problem, two types of computational methods are mainly proposed to study the liquid structure: molecular dynamics (MD) simulations and reverse Monte Carlo (RMC) methods.

In MD simulations, after a force field between the molecules is set, the equations of motion of the system are integrated along a microcanonical path. The information on the structure is calculated by averaging uncorrelated configurations collected along this path. The correctness of the force field is then tested by comparing the obtained structure factor $S(q)$ with the experimental one. The main advantage of this method is that the system by itself reaches the single structure compatible with the given force field and the thermodynamic conditions. The great drawback is that the force field must be known

beforehand to describe real data [3].

The RMC method [4, 5] and the empirical potential structure refinement (EPSR) [6, 7] are inverse methods that produce structures in real space consistent with experimental data measured in the reciprocal space. Then the structure is analysed only from the configurations that match the experimental diffraction pattern within its error. The considerable advantage of RMC modelling for molecular liquids is that no knowledge of the system is required beforehand (apart from the density and a reasonable initial molecular structure that will be refined during the process).

In this paper, we have used both self-contained MD and RMC techniques for two reasons, first, because if the short-range order obtained from both of them is the same, it will reinforce the conclusions obtained from the present work and, second, because a lack of a direct comparison between the two methods is found in the literature.

Concerning the intermolecular structure in disordered phases, different methods to characterize the relative orientations of molecules can be found in the literature [8–13]. In this paper, the local molecular ordering is studied with an extensive up-to-date analysis by means of 2D distribution maps already used in previous works [14–17].

The molecular structure of the halogenomethane derivatives formed by a central carbon atom and a combination of four chlorine and bromine atoms, $CCl_xBr_{(4-x)}$ ($x = 0, \ldots, 4$), is close to a perfect tetrahedron. Moreover, their quasiglobular shape results in a similar phase behaviour. They display, on cooling from the liquid, a plastic phase where the molecules can rotate almost freely, but the centres of mass are unable to diffuse away from the equilibrium points of a regular lattice. On further cooling, all of them form also a low-temperature ordered monoclinic phase with the same structure [18–20]. The choice in this work of the trichlorobromomethane $CBrCl_3$ (TCl) and dibromodichloromethane CBr_2Cl_2 (DBr) substances is based on the symmetry properties of their dipolar moments, which are quite similar in magnitude [21] but aligned along their C_{3v} and C_{2v} axes, respectively. These facts make these systems especially suited to study the effects of both steric and electrostatic interactions in tetrahedral molecular liquids.

In order to disentangle the features of the molecular ordering arising from the steric effects or from the electrostatic interaction, two different strategies exploiting the advantages of the two aforementioned methods (MD and RMC) have been adopted. Firstly, we have compared our results with the well-known CCl_4 molecular liquid [22–27]. Due to the fact that the latter has a perfect tetrahedral symmetry, it can be used as a reference system to study the steric effects that arise from the symmetry breaking in the distorted tetrahedral molecules TCl and DBr. Afterwards, the influence of the electrostatic effects is analysed by a series of two MD simulations: one without electrostatic interactions, the other adding partial charges to the atoms.

The paper is organized as follows: in Section 6.5, the details of the neutron diffraction experiments, RMC and MD simulations, and their consistence are exposed. In Section 6.5, the SRO analyses for TCl, DBr, and their comparison with the reference system (CCl_4) are conducted using a bivariate angular analysis. We will first analyse the relative position of two molecules and then their relative orientations. Finally, we summarize the main results comparing the two compounds with the reference system.

Experimental and computational details

Experimental details Samples of TCl ($CBrCl_3$) and DBr (CBr_2Cl_2) were obtained from Sigma-Aldrich (St. Louis, USA) and Acros Organics (Geel, Belgium) with a purity of 99+% and 99%, respectively. Since the measured melting points agreed well with the ones reported in the bibliography, no further purification was performed. Experiments were carried out at the Institute Laue Langevin (Grenoble, France). In the case of DBr, the D4C diffractometer was used with a wavelength of $\lambda = 0.5$ Å, and for TCl, the D1B diffractometer with $\lambda = 1.28$ Å. Empty cryostat, empty sample holder, and an absorbing sample were also measured to perform corrections on the data due to the sample environment contributions to the pattern, and a cylindrical vanadium rod was also measured in order to normalize data and correct the detector efficiency. Self-absorption corrections were performed using the Paalman and Pings approach. As in

previous works [15–17], all the aforementioned effects, together with multiple scattering corrections, were performed using the software CORRECT [28], and inelastic corrections were additionally carried out by subtracting a polynomial expansion in powers of q^2.

Reverse Monte Carlo modeling: computational details Neutron diffraction experiments were interpreted by means of RMC computer modelling, which constructs large structural models that are consistent with experimental results within the experimental errors. The total scattering structure factor was modelled considering both intra- and intermolecular parts. A detailed description of RMC modelling can be found in References [4], [5], [29], and [30], and, therefore, we provide here only the relevant points.

The initial configurations contained 2000 randomly oriented molecules in cubic boxes with periodic boundary conditions. The box lengths were 68.998 Å for TCl and 69.282 Å for DBr, corresponding to atomic densities of 0.03044 $Å^{-3}$ for TCl and 0.03007 $Å^{-3}$ for DBr, chosen according to the experimental densities [18, 20]. The molecular units are held together by fixed neighbour constraints (*fnc*), which allow bond lengths to fluctuate within predefined tolerances. This approach proved to be very useful for other molecular liquids [31, 32]. The basic parameters of the simulations such as *fnc* limits and intermolecular minimum atom-atom (cutoff) distances can be found in Table 6.5.

All calculations were run for several million accepted moves, where the ratio of accepted/rejected moves varied between 1:3 and 1:10, i.e., typically several thousand moves were accepted per atom. The RMC modelling of CCl_4 has been taken from previous work [25, 27].

Molecular dynamics simulations: computational details In the MD simulations, we considered for both TCl and DBr liquids models without and with atomic partial charges. We studied therefore four liquid systems of $N = 864$ molecules (256 when the electrostatic interaction is included for TCl) enclosed in a cubic box with periodic boundary conditions. The box dimensions are chosen in

	TCl ($CBrCl_3$)		DBr (CBr_2Cl_2)	
	fnc (Å)	r_{cutoff} (Å)	*fnc* (Å)	r_{cutoff} (Å)
C-C		3.5		3.5
C-Br	1.83 – 2.07	2.5	1.83 – 2.03	2.5
C-Cl	1.63 – 1.90	2.5	1.65 – 1.85	2.5
Br-Br		3.0	3.083 – 3.283	3.0
Cl-Br	2.89 – 3.17	2.9	2.87 – 3.07	2.9
Cl-Cl	2.77 – 3.03	2.7	2.8 – 3.1	2.7
	Angle (°)		Angle (°)	
Cl-C-Cl	110 ± 8		112.5 ± 0.5	
Br-C-Cl	110 ± 8		107.5 ± 0.5	
Br-C-Br			112.5 ± 0.5	

Table 6.5: Characteristics of the molecular computer models used in the RMC modelling (*fnc*: fixed neighbour constraints corresponding to the tolerances of intramolecular bond lengths; r_{cutoff}: intermolecular closest approaches between atoms).

order to reproduce the same density of the experimental samples. Since for the moment we neglect internal motions, the models consist of rigid molecules. The bonds and the intramolecular angles, detailed in Table 6.6, were provided by fitting the high-q region of the total scattering structure factor of the neutron diffraction using a Bayesian fit scheme [16, 33, 34]. This ensures the best coincidence of the structure function $S(q)$ at high q between the MD model and the experiments; in other words, it ensures the molecular geometry is realistic. The matching between the values that provides a good description of the data using the RMC modelling (Table 6.5) and those arising from the high-q fit (Table 6.6) is excellent. Moreover, with regard to the molecular geometry, the obtained values for the angles yield that TCl and DBr are indeed quasitetrahedral molecules (tetrahedral angle is around 109.5°).

The corresponding geometrical constraints were satisfied with the

	TCl ($CBrCl_3$)	DBr (CBr_2Cl_2)
C-Br	1.949Å	1.953Å
C-Cl	1.760Å	1.775Å
Cl-C-Cl	108.5°	109.2°
Br-C-Cl	110.4°	109.2°
Br-C-Br		111.0°

Table 6.6: Bond lengths and angles for the rigid molecule model of TCl and DBr obtained by the high-q fit of the diffractogram.

SHAKE algorithm [35] with a relative accuracy of 10^{-6}. For the intermolecular interaction, the Optimized Potentials for Liquid Simulations parameters were used, and a spherical truncation scheme between molecular centres was taken with a cutoff value of 12 Å. When electrostatic forces are introduced, the Ewald summation method has been used, with the convergence parameter $\alpha \sim 13/L$ and $k_{\max} = 14$. The equations of motion have been integrated with the Leapfrog algorithm and a time step of 1 fs. Molecules were initially placed in an Face-centred cubic lattice with random orientation for all systems, and then the system was equilibrated at 450 K in the NVT ensemble. Then successive NVT equilibrations using Berendsen method with a relaxation time of $t = 0.01$ ps were applied for a time of 20 ps at 300 and 273 K for TCl and DBr, respectively. A production run was performed in order to obtain at least 25 independent configurations. We considered independent two configurations if the elapsed time between them is 0.1τ, where τ is the relaxation time of the orientational self-correlation function.

Consistency with experiments Figure 6.70 shows the total scattering structure factors of TCl and DBr obtained from the experiment together with those obtained from RMC and MD techniques. The agreement with the experiment is nearly perfect for both liquids and both techniques, especially for the RMC modelling. In the high-q region, the good agreement of RMC simulation suggests that the

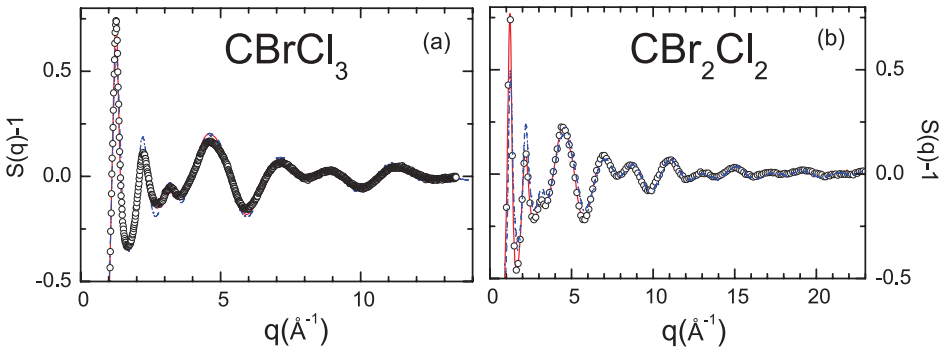

Figure 6.70: Total scattering structure factors for (a) liquid TCl and (b) DBr. Circles: experimental data; red solid lines: RMC; blue dashed lines: MD simulation.

molecular structures defined by the *fncs* are appropriate for these liquids. Concerning the intramolecular structure, the tetrahedral angles arising from RMC (Table 6.5) and MD (Table 6.6) do not differ significantly from each other. This ascertains the quasitetrahedral geometry of the molecules that can be seen in Figure 6.72, where the molecules have been depicted following the intramolecular parameters of Table 6.6.

Results and discussions

Positional ordering The local ordering analysis of the molecules in the liquid phase of TCl and DBr has been restricted to the closest molecules because, as shown in Reference [15], they fully determine the position and orientation of successive molecular shells. However, as it will be seen, due to the quasitetrahedral symmetry of the molecules, it will be possible to find this first molecule at four different positions. In other words, the first molecule might be placed in any of the four positions imposed by the quasitetrahedral symmetry of the molecules with a probability $P = 0.25$. We consider therefore only the molecules up to a distance r_1 defined by the following condition:

$$\mathrm{MCN_{CC}} = 4\pi\rho_0 \int_0^{r_1} g_{\mathrm{CC}}(r) r^2 \mathrm{d}r = 1 \tag{6.56}$$

where $\mathrm{MCN_{CC}}$ is the carbon-carbon molecular coordination number, ρ_0 is the molecular number density (in $\mathrm{\AA}^{-3}$ units), and $g_{\mathrm{CC}}(r)$ is the carbon-carbon radial distribution function. As seen in Figure 6.71, the $g_{\mathrm{CC}}(r)$ values obtained for TCl, DBr, and CCl_4 using the RMC technique are very similar. No big changes with respect to CCl_4 are thus expected to arise in the short-range molecular order from the tetrahedral symmetry breaking in TCl and DBr. Concerning the $g_{\mathrm{CC}}(r)$ obtained by MD [Figure 6.71(b) and 6.71(c)], the electrostatic effects seem to be negligible for TCl since no significant change is seen adding or not partial charges to the molecules in the simulation. On the contrary, atomic partial charges in DBr impose a more marked structure in $g_{\mathrm{CC}}(r)$ with higher peaks and a slightly different packing distance. Its origin will be explained later together with the orientational ordering features.

The probability of the relative position between two molecules can be fully determined by the 3D function $g_{\mathrm{CC}}[r, \cos(\theta), \varphi]$, where r is the distance between carbon atoms of the molecules, φ is the equatorial angle, and θ is the azimuthal angle of the vector joining two carbon atoms. In order to define the azimuthal θ and equatorial φ angles for a given reference molecule, a polar frame must be set taking into account the molecular symmetry [14, 16, 17].

For TCl, the Z axis lies along the C_{3v} symmetry axis, i.e., the C-Br vector, which is parallel to its dipolar moment, while the origin of angle φ lies in one of the Br-C-Cl molecular planes [see Figure 6.72(a)]. Similarly, for the DBr molecule, the Z axis is set along its C_{2v} symmetry axis, i.e., parallel to the bisecting vector between the two C-Br vectors which, as in TCl, is also parallel to the dipolar moment of the molecule. The φ equatorial angle origin is set in this case in the Br-C-Br plane [see Figure 6.72(b)]. For the sake of comparison between the three molecular liquids, the CCl_4 reference system has been defined both along its C_{3v} axis, as in TCl, and along its C_{2v} axis, as in DBr.

The positional molecular ordering for each system is described

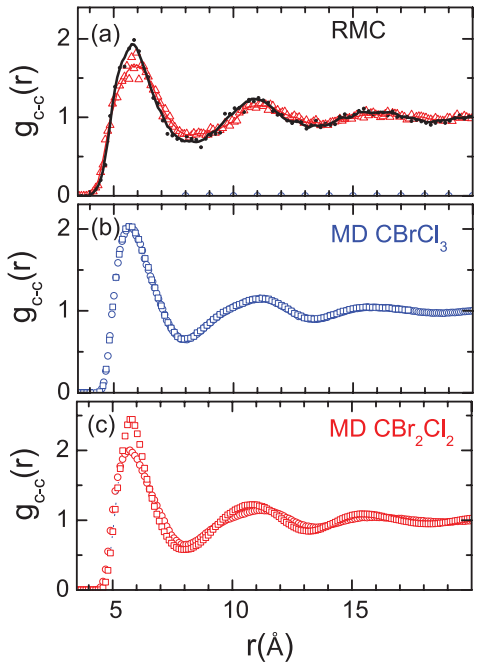

Figure 6.71: (a) Carbon-carbon partial radial distribu- tion function for TCl (circles), for DBr (triangles), and for CCl_4 (solid line) from the analysis of RMC configurations. The results from MD simulation switching on (squares) and off (circles) the electrostatic interaction, respectively, are also shown in (b) for TCl and (c) for DBr.

through a 2D probability map (Figures 6.73 and 6.74) given by the bivariate analysis of φ and $\cos(\theta)$. The probability related to the azimuthal angle θ is calculated using the cosine of the angle instead of the angle. To meet the requirement that an isotropic distribution should lead to a flat probability map, P has been normalized to the map area. Four calculations have been performed for each compound (TCl and DBr): (a) reference system CCl_4 obtained from RMC modelling using the symmetry axis of the molecule studied: C_{3v} in the case of TCl and C_{2v} in the case of DBr, (b) RMC modelling of the studied system, (c) MD simulation without partial charges, and (d) MD simulation with partial charges. As it is seen in Figures 6.73 and

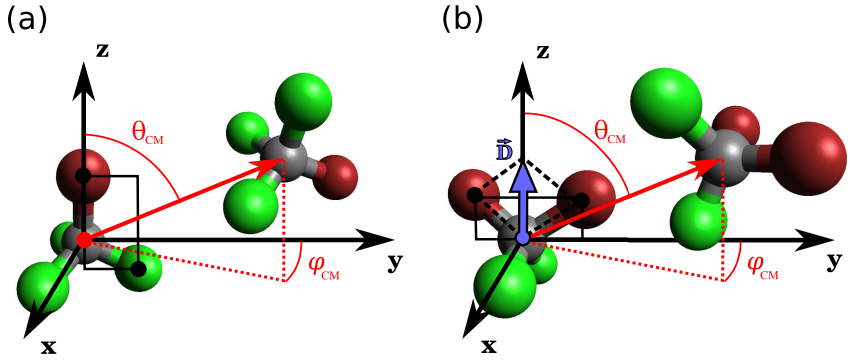

Figure 6.72: Arbitrary arrangements of two (a) TCl and (b) DBr molecules showing the axes and θ and φ angle definitions used to determine the molecular position. Green (light gray), red (dark gray), and gray spheres represent the Cl, Br, and C atoms, respectively.

6.74, results arising from the RMC model (b) and the MD simulation (d) are virtually the same, thus assuring the robustness of the obtained positional orderings.

In order to analyse the positional maps of Figures 6.73 and 6.74, we present in Table 6.7 the coordinates where the spots arising from the relative positions $[\varphi, \cos(\theta)]$ should appear, assuming that the carbon atom of the neighbour molecule sits in front of the tetrahedral faces of the reference one and that the molecule has full tetrahedral symmetry as in CCl_4, i.e., that there is a carbon atom in front of all four tetrahedron faces. The calculations were performed using the two axes definitions of Figure 6.72, thus setting the Z axis along the C_{3v} and C_{2v} symmetry axes of the tetrahedron. In the first case, a carbon atom of a neighbour molecule placed in front of the bottom face of the tetrahedron [see Figure 6.72(a)], that is $\theta = 180°$, would give a contribution to the 2D positional map at $\cos(\theta) = -1$, and φ would be undetermined because it corresponds to the pole of the coordinate system. Molecular symmetry, however, imposes that the neighbour molecules are also found in front of the three upper faces of the tetrahedron, with an azimuthal angle of $\theta = 70.5°$. These are the positions corresponding to the $[\varphi, \cos(\theta)]$ pairs $(60°, 0.33)$,

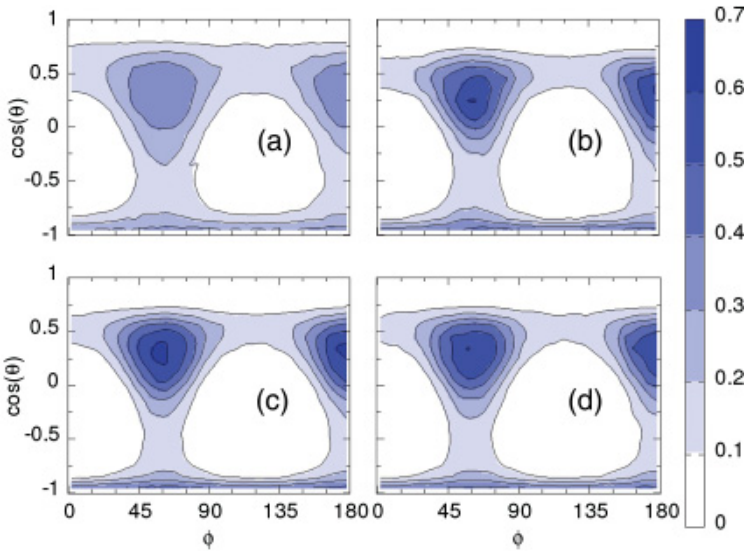

Figure 6.73: Positional ordering for studied liquids (TCl) with C_{3v} symmetry. (a) Reference system (RMC modelling of CCl_4), (b) RMC modelling, (c) MD simulation without charges, and (d) MD simulation with charges.

$(180°, 0.33)$, and $(300°, 0.33)$, the last being equivalent to $(60°, 0.33)$ in the probability map due to XZ symmetry.

The $[\varphi, \cos(\theta)]$ pairs obtained by placing the Z vector in the C_{2v} molecular axis are calculated in a similar way. In this case, the spots appear at the $[\varphi, \cos(\theta)]$ pairs $(0°, -0.58)$ and $(180°, -0.58)$ and also at $(90°, +0.58)$, equivalent to $(270°, +0.58)$ due to the XZ symmetry. The first two pairs correspond to neighbour molecules located at $\theta = 125.3°$ in front of the lower faces formed by two Cl and one Br atoms, and the last two correspond to molecules located at $\theta = 54.7°$ in front of the upper faces formed by one Cl and two Br atoms. Note that changing the frame of reference in CCl_4 changes the position and the shape of the probability spots in the positional maps, but not their meaning. In the case of TCl, the change of the spot shape is extreme because molecules sitting in the lower face of the molecule are to be seen as a large spot without a well-defined equatorial angle (in fact,

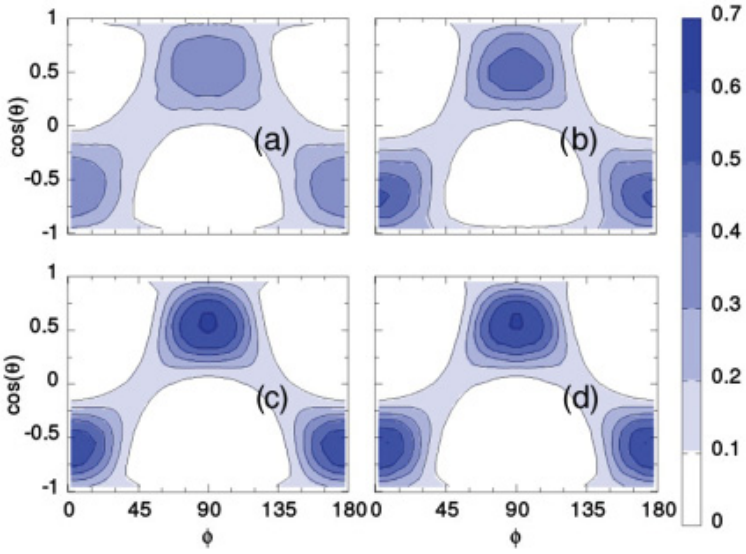

Figure 6.74: Positional ordering for studied liquids (DBr) with C_{2v} symmetry. (a) Reference system (RMC modelling of CCl_4), (b) RMC model, (c) MD simulation without charges, and (d) MD simulation with charges.

this happens whenever trying to perform a projection from spherical coordinates into a 2D map).

Concerning CCl_4, since only the spots calculated in Table 6.7 appear in Figures 6.73(a) and 6.74(a), we conclude that the preferred relative positions of the two closest molecules are the neighbouring molecules being arranged in front of the respective tetrahedron faces of the reference molecule (see Table 6.7) in concordance with previous works [15].

In order to study how the distortion of the tetrahedral symmetry affects the liquid structure of TCl and DBr, RMC results for both liquids [Figures 6.73(b) and 6.74(b)] have been compared with the reference system CCl_4 [Figures 6.73(a) and 6.74(a)]. It can be seen that this distortion seems to have no effect in the relative position of two neighbour molecules, given the similarity of the maps. In other words, TCl and DBr behave as fully tetrahedral liquids concerning the rela-

Symmetry	φ	$\cos(\theta)$	θ
C_{3v}	Undetermined	-1	180.0°
(Figure 6.73)	60°, 180°, 300°	$+0.33$	70.5°
C_{2v}	0°, 180°	-0.58	125.3°
(Figure 6.74)	90°, 270°	$+0.58$	54.7°

Table 6.7: Coordinates of the spots expected to appear in the 2D probability maps describing the relative position of two molecules, if carbon atoms of a neighbour molecule sit on the face of the tetrahedron of a reference molecule. Calculations have been performed in the frames of reference parallel to both the C_{3v} and C_{2v} axes of the tetrahedron (see Figure 3). For molecules located in the poles, the φ coordinate is undetermined.

tive position of two neighbouring molecules. Moreover, the positional maps of TCl and DBr obtained from the MD simulations performed without and with partial charges [Figures 6.73(c) and 6.74(c), and Figures 6.73(d) and 6.74(d), respectively] both yield a high similarity to that obtained for the CCl_4 [Figures 6.73(a) and 6.74(a)]. This shows that the electrostatic interaction plays no relevant role in the relative position of neighbour molecules, neither in TCl nor in DBr, and indicates also that the differences between the $g_{CC}(r)$ from the two MD simulations for DBr [see Figure 6.72(a)] arise not from the positional ordering but from their relative orientation (see next section).

Orientational ordering The orientational ordering is usually studied simply taking into account an angle between two characteristic vectors of a reference molecule and its first neighbours. Typically, only the probability distribution of the cosine of that angle is calculated in the literature. However, this unidimensional distribution hides the fact that molecules in different positions might have different orientations. In order to identify the position of the molecules with a given orientation, the probability distribution has been calcu-

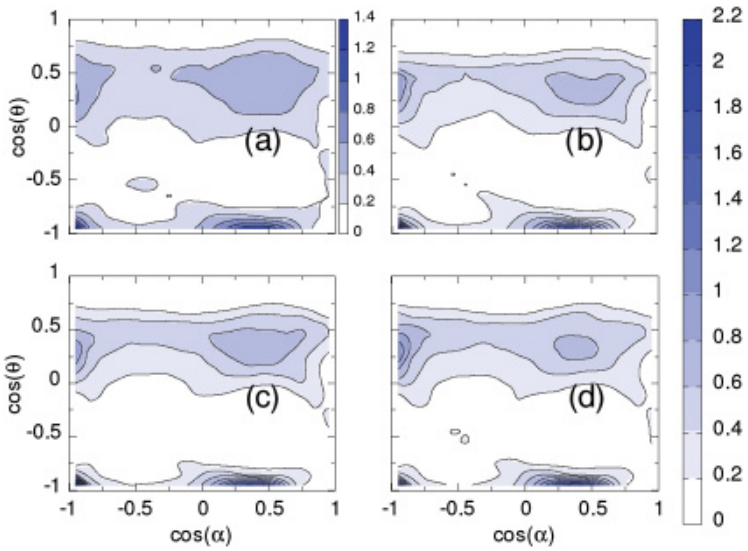

Figure 6.75: Orientational ordering for studied liquids with C_{3v} (TCl) symmetry. (a) Reference system (RMC modelling of CCl_4), (b) RMC model, (c) MD simulation without charges, and (d) MD simulation with charges.

lated as a function of an angle characterizing molecular orientation, α, and an angle related to the relative position, the azimuthal angle θ, thus generating a 2D probability map [10] (Figures 6.75 and 6.76). As explained before, probabilities are calculated using the cosines of the angles when necessary so that isotropic distributions lead to flat probability maps. As in the case of the molecular position determination, four types of calculations have been performed for each liquid (TCl and DBr): (a) reference system CCl_4, obtained with the same method as in Figures 6.73 and 6.74, (b) RMC modeling of the studied system, (c) MD simulation without partial charges, and (d) MD simulation with partial charges. It is worth pointing out that the good agreement between the RMC [Figures 6.75(b) and 6.76(b)] and the MD simulations [Figures 6.75(c) and 6.76(c), and Figures 6.75(d) and 6.76(d)] ascertains that also the orientational ordering analysis for both TCl and DBr is grounded on a solid base.

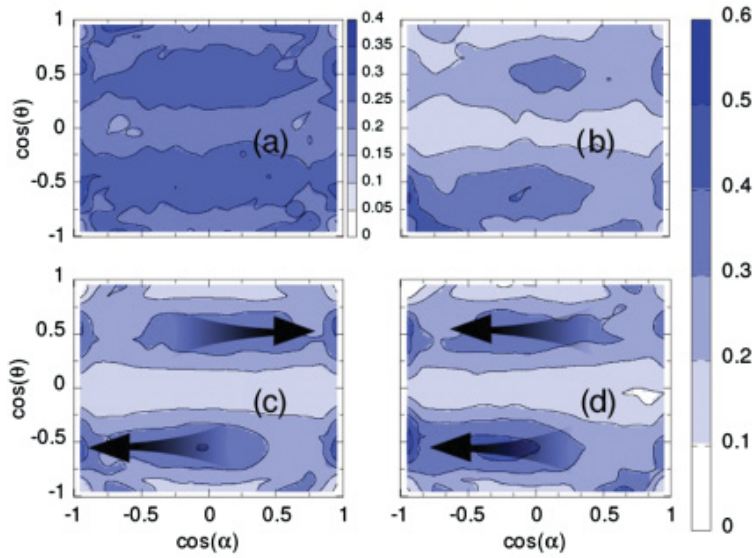

Figure 6.76: Orientational ordering for studied liquids with C_{2v} (DBr) symmetry. (a) Reference system (RMC modelling of CCl_4), (b) RMC model, (c) MD simulation without charges, and (d) MD simulation with charges. Arrows in (c) and (d) indicate, respectively, the steric and the steric plus electrostatic effect on the molecular ordering.

First of all, we should recall that the x and y axes are related to relative orientation and position of two molecules, respectively. Therefore, concerning the position, the lower horizontal bands in Figure 6.75 in the probability maps correspond to orientations of the neighbour molecule located in front of the bottom face of the tetrahedron, and the upper bands correspond to the orientations of neighbours located in front of the three upper faces. On the other hand, Figure 6.76 shows in the higher bands the orientation of the neighbours in front of the two upper faces of the tetrahedron and in the bottom bands of the molecules located in front of the two bottom faces.

At a first stage, we will only focus on two relative molecular orientations to simplify our discussion: the parallel configuration and the antiparallel one. The orientation of two molecules is parallel when

the characteristic vectors chosen to describe the relative orientation of two molecules (the C_{3v} and C_{2v} symmetry axis for CCl_4 and the dipolar moment for molecules DBr and TCl) are parallel, giving a trivial contribution at $\cos(\alpha) = 1$ (spots appearing at the right edge of the graphs in Figures 6.75 and 6.76). In the case of an antiparallel ordering, the spot in the probability map should be located at $\cos(\alpha) = -1$ (at the left edge of the same graphs). However, due to molecular symmetry and the degeneration of the reference frame definition, additional orientational spots can appear for the same position of a neighbour molecule, i.e., for the same value of $\cos(\theta)$.

In the case of two fully tetrahedral CCl_4 molecules with one C-Cl vector (the C_{3v} molecular axis) oriented antiparallel to each other, the trivial contribution will be found at $\cos(\alpha) = -1$ in Figure 6.75(a). The contributions at $\cos(\alpha) = 0.33$ are given by the angles between the remaining three C-Cl vectors of each molecule that, for symmetry reasons, are the only compatible with the closest packing of a tetrahedral molecule. On the other hand, if the same molecular ordering is evaluated, taking into account a C_{2v} molecular axis as in Figure 6.76(a) in addition to the contribution at $\cos(\alpha) = -1$, nontrivial spots will appear at $\cos(\alpha) = 1$ and $\cos(\alpha) = 0$. The calculations for the pairs $[\cos(\alpha), \cos(\theta)]$, taking into account the orientations using the C_{2v} and C_{3v} tetrahedron axes, are gathered in Table 6.8. As it can be seen, these spots are not enough to distinguish between parallel and antiparallel configurations in the case of C_{2v} symmetry. However, the calculated spots in Table 6.8 are compatible with the antiparallel configuration [see Figures 6.75(a) and 6.76(a)], in agreement with previous results on CCl_4 [15]. Concerning TCl and DBr, the orientational map also corresponds to the antiparallel configuration, regardless of whether they are distorted tetrahedra and do not possess the C_{3v} or C_{2v} symmetry axes, respectively. This yields to the conclusion that, in a first approximation, neither steric nor electrostatic effects substantially change the short-range ordering of the DBr and TCl nearly tetrahedral molecules, neither the position nor the orientation of neighbouring molecules.

In Figure 6.77, we have depicted the most probable configuration of the first neighbour for both liquids TCl and DBr obtained from

Symmetry	Orientation	$(\cos\alpha, \cos\theta)$	(α, θ)
C_{3v}	Parallel	$(1, -1)$ $(1, -0.33)$	$(0°, 180°)$ $(0°, 109.5°)$
(Figure 6.75)	Antiparallel	$(-0.33, -1)$ $(-0.33, 0.33)$	$(109.5°, 180°)$ $(-70.5°, 70.5°)$
		$(-1, -1)$ $(-1, -0.33)$	$(180°, 180°)$ $(180°, 109.5°)$
		$(0.33, -1)$ $(0.33, 0.33)$	$(70.5°, 180°)$ $(70.5°, 70.5°)$
C_{2v}	Parallel	$(1, \pm 0.58)$	$(0°, 125.3°)$ $(0°, 54.7°)$
(Figure 6.76)	Antiparallel	$(0, \pm 0.58)$	$(90°, 125.3°)$ $(90°, 54.7°)$
		$(-1, \pm 0.58)$	$(180°, 125.3°)$ $(180°, 54.7°)$
		$(-1, \pm 0.58)$	$(180°, 125.3°)$ $(180°, 54.7)$
		$(0, \pm 0.58)$	$(90°, 125.3°)$ $(90°, 54.7°)$
		$(1, \pm 0.58)$	$(0°, 125.3°)$ $(0°, 54.7°)$

Table 6.8: Spots expected to appear in the probability map $P(\cos\alpha, \cos\theta)$ when the parallel or antiparallel orientation is assumed, being the molecules located in front of the faces of the reference molecule. In addition to the trivial $\cos\alpha = \pm 1$ contributions, the spots that would appear just due to assuming a fully tetrahedral symmetry, as in the case of CCl_4, have also been calculated.

the information of the probability maps in Figures 6.73–6.76. Reference molecules have been oriented along their C_{3v} and C_{2v} axes, respectively, as in Figure 6.72. As seen in Figures 6.73 and 6.74, first neighbours can be in front of any of the four faces of the tetrahedron, but for the sake of clarity, only the molecule in front of one of the faces has been depicted. Concerning the orientation, we show in Figure 6.77 only the configuration corresponding to the spots at $\cos(\alpha) = -1$ in Figures 6.75 and 6.76 because this probability is slightly higher for DBr. The other configurations can be obtained from successive rotations around the axes of their associated tetrahedra, generating the large spots at $\cos(\alpha) \approx 0$.

A more detailed analysis of the relative molecular orientation in TCl and DBr can be carried out, taking into account that the obtained probability maps constitute a quantitative way to determine molecular orientation. Molecules with an unlikely arrangement will hardly be observed and will prefer to have the relative position and orientation associated to high-probability regions. Therefore, the low-

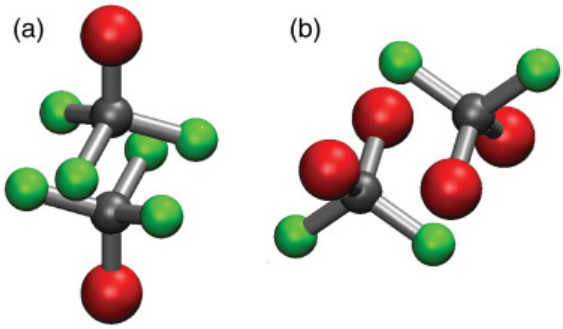

Figure 6.77: Most probable configuration for (a) TCl and (b) DBr molecular pairs obtained from the probability maps of Figures 6.73, 6.74, 6.75, and 6.76. TCl and DBr molecules are oriented along their C_{3v} and C_{2v} axes according to the axis definition of Figure 6.72.

probability regions might be seen as barriers between the molecular configurations described by the high-probability regions. The maximum probability value in each map, P_{max}, is thus related with the height of such barriers and will give us information about how strong a certain molecular ordering is defined. As it can be seen in Figures 6.75 and 6.76, the P_{max} value of CCl_4 is smaller than that of TCl and DBr, respectively. Since this difference is the same for all MD simulations, regardless of whether partial charges are added or not to the atoms, this fact has to be related with the steric effects produced by the loss of tetrahedral symmetry that imposes a more restricted orientation of the neighbour molecules.

Taking into account this relation between a high value of P_{max} and a more defined orientation of a neighbouring molecule, some general features concerning the molecular reorientation based on Figures 6.75 and 6.76 should be highlighted. In the foregoing discussion, we will assume that both TCl and DBr are perfect tetrahedra. For example, when referring to a rotation about the C_{3v} symmetry axis of DBr, it will implicitly mean that we assume for that molecule a perfect tetrahedral symmetry and that the rotation is done around a vector going from the central carbon to a Cl or Br atom. When calculations are made taking into account C_{2v} symmetry as in Figure 6.76, the proba-

bility map appears more smeared out than the one calculated for the C_{3v} molecular symmetry (see Figure 6.75). As aforementioned, this feature might be quantified by the maximum of the color scale P_{max}. For the CCl_4 molecule, P_{max} decreases from 1.4 in Figure 6.75 to 0.4 in Figure 6.76, this decrease is more extreme when TCl ($P_{max} = 2.2$) is compared with DBr ($P_{max} = 0.6$). It clearly emerges then that, by modifying the frame of reference from a C_{3v}- to a C_{2v}-oriented axis [Figures 6.72(a) and 6.72(b), respectively], the height of the orientational barrier that a molecule must overcome to change the relative orientation with respect to the neighbour molecule around the axes is decreased, thus the C_{3v} axis being stiffer than the C_{2v} axis.

To explain this fact, it should be noted that rotations that leave the C_{3v} axis unchanged are precisely those around the C_{3v} axis, and these rotations will be responsible for changes in the orientation of the C_{2v} molecular axis. Therefore, the higher value of P_{max} of the orientational map calculated using the C_{3v} axis (Figure 6.75), compared to that obtained using the C_{2v} axis (Figure 6.76), evidences that the molecular reorientations around the C_{3v} axis (which leave this axis unchanged) are more probable than those around a C_{2v} axis. Moreover, since the probability scale in Figures 6.75 and 6.76 is unchanged by adding or not partial charges, we conclude that the stiffness of the C_{3v} axis is mainly determined by steric effects.

To prove this statement, a simple calculation of the configuration energy profile is shown in Figure 6.78 for two neighbouring molecules: the first fixed and the other rotating along its C_{3v} and C_{2v} axes, assuming as aforementioned a fully tetrahedral symmetry for the molecules. For both TCl and DBr, the starting relative orientation is energetically the most stable. For both compounds, the energy barriers are much higher for rotations around the C_{2v} axes, which imply a displacement of the C_{3v} axes, than for those around the C_{3v} axes, which leave these axes unchanged, as it is revealed by Figure 6.78, in agreement with the conclusion obtained directly from the orientational maps.

Concerning the influence of electrostatic forces in the molecular ordering of TCl, we have compared the orientational maps without and with electrostatic interactions [Figures 6.75(c) and 6.75(d), re-

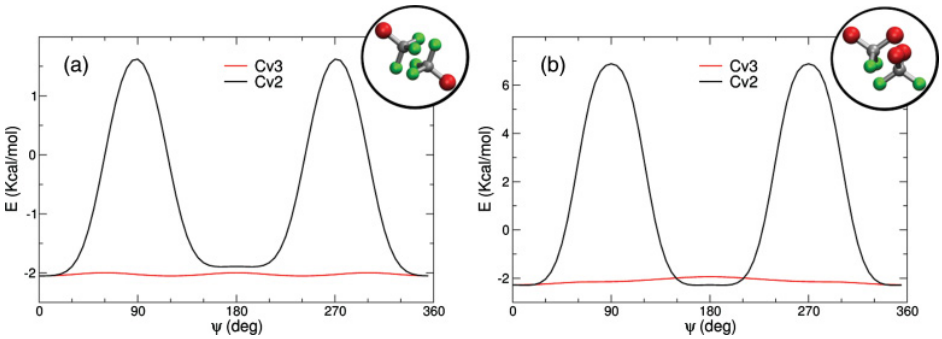

Figure 6.78: Energy for a dimer formed by the two closest molecules of (a) TCl and (b) DBr as a function of the angle rotated around their C_{2v} axes and around their C_{3v} axes, assuming that both molecules are perfect tetrahedra. Insets show the most stable configuration, chosen as starting configuration for the rotation along C_{3v} and C_{2v} axes, respectively.

spectively]. Since the probability maps are almost identical for TCl, we conclude that electrostatic effects do not affect the molecular ordering in this compound. On the other hand, the DBr case is slightly different. The central spots around $[\cos(\alpha), \cos(\theta)] = (0, \pm 0.58)$ are symmetric for CCl_4, whereas in DBr, they become slightly asymmetric. If no partial charges are added to the molecule, a neighbour at positive $\cos(\theta)$ prefers to orient the dipole toward positive values of $\cos(\alpha)$, and at negative $\cos(\theta)$ towards negative values of $\cos(\alpha)$ [see the arrows in Figure 6.76(c)]. The reason why changes on the dipole orientation are seen in DBr and not in TCl is because, in the first case, the dipole is oriented along the C_{2v} axis that is more mobile than the dipole of TCl oriented along its C_{3v} axis.

To understand this point, we must recall some geometrical facts. The distance from the central carbon to the chlorine atom, $d_{CCl} = 1.775$ Å, is smaller than that to the bromine atom, $d_{CBr} = 1.953$ Å. Therefore, since the Z axis is oriented towards the bromine atoms, the molecule is bulkier upwards ($\cos(\theta) > 0$) than downwards ($\cos(\theta) < 0$). The molecular shape of DBr induces thus the neighbours to move in such a direction that the empty space between

molecules is minimized. To accomplish this requirement, molecules in the upper part tilt aside of the molecular z axis, and those in the lower tilt inside the z axis. This is seen in Figure 6.76(c) as a displacement of the central spot located around $\cos(\theta) = 0.58$ towards larger values of $\cos(\alpha)$ and in the opposite direction for spots located around $\cos(\theta) = -0.58$ [see the arrows in Figure 6.76(c)]. So in DBr, the steric effect promotes the parallel or the antiparallel orientation of the C_{2v} axis depending on the relative position of the neighbour molecule.

The electrostatic interaction, on the contrary, tends to orient dipoles in an antiparallel direction to minimize the electrostatic energy. This can be seen when comparing the maps obtained using the MD simulations without and with the partial charges of the molecule [cf. Figures 6.76(c) and 6.76(d), respectively], where the large central spots tend to move towards negative values of $\cos(\alpha)$, irrespective of their position, i.e., irrespective of the sign of $\cos(\theta)$ [see arrows in Figure 6.76(d)], when the electrostatic interaction is added. The orientation of two molecules in DBr depends therefore on both steric and electrostatic effect, and their effects are balanced or reinforced depending on the molecular position.

Conclusions

Reverse Monte Carlo modelling of neutron diffraction measurements has been performed to investigate the intermolecular structure of $CBrCl_3$ and CBr_2Cl_2 liquids composed by slightly distorted tetrahedral molecules. Simultaneously, molecular dynamics simulations have been carried out to study the role of electrostatic interactions in these systems. We provide a comparison with a reference system (CCl_4) to highlight the influence of the steric effects in the short-range order. Our results concerning both mutual position and orientation of molecules are validated by the excellent agreement between the measurements and the simulations (using RMC and MD). Once the robustness of the obtained short-range ordering of molecules is assessed, three sets of conclusions concerning relative position and orientation of molecules and concerning molecular reorientations re-

sult.

First of all, as seen when TCl and DBr molecular arrangements in the liquid phase are compared with that of CCl_4, neither steric nor electrostatic interactions produce a change of the relative position of two neighbouring molecules with respect to the reference tetrahedral molecule CCl_4 (see Figures 6.73 and 6.74). This statement is supported by the fact that switching on and off the electrostatic forces in the MD simulations of the liquid TCl and DBr does not change their position distributions with respect to liquid CCl_4.

Concerning the relative orientation of two molecules (Figures 6.75 and 6.76), all the spots present on CCl_4 appear as well on both polar molecules, DBr and TCl. Therefore, steric and electrostatic effects are not able to avoid any of the molecular orientations present in CCl_4. A more detailed analysis, though, allows us to detect some differences between TCl and DBr: In the case of TCl, no appreciable change in any of the studied cases has been seen in comparison with CCl_4. Together with the previous result on the relative position, we can conclude that, in TCl, none of the effects, steric or electrostatic, change the short-range order from that of a fully tetrahedral molecule such as CCl_4.

In contrast, the relative orientation of two molecules shows some differences in the case of DBr. For this compound, the balance between two competing effects determines the molecular ordering. Steric effects force neighbours to reorient, optimizing the molecular packing. This reorientation takes place in opposite directions for each molecule depending on its position due to the molecular asymmetry [see the arrows in Figure 6.76(c)]. The electrostatic interactions, on the other hand, tend to orient the molecular dipoles antiparallel, irrespective of their position [see the arrows on Figure 6.76(d)]. Therefore, electrostatic and steric effects either reinforce each other or compete depending on the relative molecular position, thus determining the molecular orientation. Finally, the probability maps related to the molecular orientation (Figures 6.75 and 6.76) yield the conclusion that, due to steric effects, movement of the C_{3v} axis in quasitetrahedral molecules is more restricted than the movement of the C_{2v} axis. Two consequences can be drawn from this fact. First

of all, the higher mobility of C_{2v} axis causes that electrostatic effects are clearer when the dipole is oriented parallel to this axis, as it happens in DBr. On the other hand, since movements of the C_{3v} axis are more constrained than those of C_{2v} , rotations are more probable around the C_{3v} axis. This conclusion is confirmed by a calculation of the energy barriers that molecules must overcome when rotating around these two molecular axes.

Acknowledgments

This article was supported by the Spanish Ministry of Science and Innovation (MICINN) Grant FIS2008-00837 and by the Government of Catalonia (2008SGR-1251). Two of the authors (A. O. and Sz. P.) acknowledge the postdoctoral fellowships of the Departament de Física i Enginyeria Nuclear and the Universitat Politècnica de Catalunya, respectively.

References

All online references accessed on July 22, 2014.

[1] H. Tanaka. *J. Chem. Phys.* **111**, 3163 (1999).

[2] H. Tanaka. *Phys. Rev. E* **62**, 6968 (2000).

[3] M. P. Allen and D. Tildesley. *Computer Simulation of Liquids*. Clarendon Press, Oxford (1987).

[4] R. L. McGreevy and L. Pusztai. *Mol. Simul.* **1**, 359 (1988).

[5] R. L. McGreevy. *J. Phys. Cond. Matter* **13**, R877 (2001).

[6] A. K. Soper. *Chem. Phys.* **202**, 295 (1996).

[7] A. K. Soper. *Phys. Rev. B* **72**, 104204 (2005).

[8] I. M. Svishchev and P. G. Kusalik. *Physica A* **192**, 628 (1993).

[9] I. M. Svishchev and P. G. Kusalik. *J. Chem. Phys.* **99**, 3049 (1993).

[10] P. Jedlovszky, A. Vincze, and G. Horvai. *Phys. Chem. Chem. Phys.* **6**, 1874 (2004).

[11] R. Rey. *J. Chem. Phys.* **129**, 224509 (2008).

[12] L. Temleitner, L. Pusztai, Y. Akahama, H. Kawamura, et al. *Phys. Rev. B* **78**, 014205 (2008).

[13] S. Imberti and D. T. Bowron. *J. Phys. Condens. Matter* **22**, 404212 (2010).

[14] L. C. Pardo, M. Rovira-Esteva, J. Ll. Tamarit, N. Veglio, et al. In S. J. Rzoska, A. Drozd-Rzoska, and V. Mazur, editors, *Metastable Systems under Pressure*, NATO Science for Peace and Security Series: A. Chemistry and Biology, pages 79–91. Springer Netherlands (2009).

[15] L. C. Pardo, J. Ll. Tamarit, N. Veglio, F. J. Bermejo, et al. *Phys. Rev. B* **76**(13), 134203 (2007).

[16] M. Rovira-Esteva, N. A. Murugan, L. C. Pardo, S. Busch, et al. *Phys. Rev. B* **84**(6), 064202 (2011).

[17] M. Rovira-Esteva, A. Murugan, L. C. Pardo, S. Busch, et al. *Phys. Rev. B* **81**(9), 092202 (2010).

[18] B. Parat, L. C. Pardo, M. Barrio, J. Ll. Tamarit, et al. *Chem. Mater.* **17**, 3359 (2005).

[19] L. C. Pardo, M. Barrio, J. Ll. Tamarit, D. O. López, et al. *Chem. Mater.* **17**, 6146 (2005).

[20] M. Barrio, J. Ll. Tamarit, P. Negrier, L. C. Pardo, et al. *New J. Chem.* **32**, 232 (2008).

[21] M. Barrio, P. Negrier, J. Ll. Tamarit, L. C. Pardo, et al. *J. Phys. Chem. B* **111**, 8899 (2007).

[22] A. H. Narten, M. D. Danford, and H. A. Levy. *J. Chem. Phys.* **46**, 4875 (1967).

[23] P. A. Egelstaff, D. I. Page, , and J. G. Powles. *Mol. Phys.* **20**, 881 (1971).

[24] P. Jedlovszky. *J. Chem. Phys.* **107**(18), 7433 (1997).

[25] P. Jóvári, G. Mészáros, L. Pusztai, and E. Sváb. *J. Chem. Phys.* **114**(18), 8082 (2001).

[26] R. Rey. *J. Chem. Phys.* **126**(16), 164506 (2007).

[27] Sz. Pothoczki, L. Temleitner, P. Jóvári, S. Kohara, et al. *J. Chem. Phys.* **130**(6), 064503 (2009).

[28] M. Howe, R. McGreevy, and P. Zetterström. *Computer code CORRECT, correction program for neutron diffraction data* (1996). NFL Studsvik internal report.

[29] G. Evrard and L. Pusztai. *J. Phys.: Cond. Matter* **17**, S1 (2005).

[30] O. Gereben, P. Jóvári, L. Temleitner, and L. Pusztai. *Journal of Optoelectronics and Advanced Materials* **9**(10), 3021 (2007). 3rd International conference on Amorphous and Nanostructured Chalcogenides, Brasov, Romania, 2007.

[31] L. Pusztai and R. L. McGreevy. *J. Chem. Phys.* **125**(4), 044508 (2006).

[32] L. Temleitner and L. Pusztai. *Phys. Rev. B* **81**, 134101 (2010).

[33] L. C. Pardo, M. Rovira-Esteva, S. Busch, M. D. Ruiz-Martín, et al. *J. Phys.: Conf. Ser.* **325**, 012006 (2011).

[34] L. C. Pardo, M. Rovira-Esteva, S. Busch, J.-F. Moulin, et al. *Phys. Rev. E* **84**, 046711 (2011).

[35] J. P. Ryckaert, G. Ciccotti, and H. J. C. Berendsen. *J. Comput. Phys.* **23**, 327 (1977).

Chapter 7

Conclusions

The knowledge of the intramolecular geometry and short range order of disordered systems is essential to understand their behaviour. This kind of insight is a great help to unravel the significant interactions at play in complex systems, simply because the resulting structure has been shaped by them.

However, their study involves many difficulties, partly due to disordered systems being intrinsically more complex, but also because measurements are usually an average of all possible 1D projections of the 3D structure, so there is not a unique solution and a great number of assumptions have to be made.

Motivated by the scientific problems, several analysis methods have been developed, tested, and put to use throughout this work.

The Bayesian approach to obtain molecular structure from experimental data has shown to be very robust to determine its geometry, allowing to make less assumptions than with other methods, naturally taking into account parameter correlations, and providing the full complexity of the fit in the solution.

This is quite crucial because intramolecular structure is usually needed to tackle the analysis of intermolecular structure. Techniques such as reverse Monte Carlo and molecular dynamics simulations often require input parameters in their models which account for the molecular structure, and they may be very sensitive to them.

Extensive use of bivariant analysis has been successfully applied to

the simulation and modelling configurations, and multiple approaches have been explored to obtain the maximum amount of information from the data.

Limiting the analysis to convenient distance intervals from the reference molecule, probability density functions of the molecular arrangements were calculated as a function of two positional angles, one positional and one orientational angle, or two orientational angles. This last case showed to be specially interesting because it gives the most popular relative orientations of the molecular pairs.

It was possible to select a small range of molecular-pair orientations to analyse their relative location separately from the rest of molecules in the simulation, which could also be done vice versa. And a powerful quantitative analysis was carried out through integration of the probability density functions in certain positional and orientational ranges of interest.

Using these and other methods several compounds were studied. Here, work on trans-1,2-dichloroethene (HClC=CClH), 1,1,2,2-tetrachloro-1,2-difluoroethane ($Cl_2FC-CCl_2F$), 1,1,1,2-tetrachloro-1,1-difluoroethane ($Cl_3C-CClF_2$), carbon tetrachloride (CCl_4), trichlorobromomethane ($CBrCl_3$), and dibromodichloromethane (CBr_2Cl_2) has been presented.

Trans-1,2-dichloroethene structural and dynamic anomalies between its high and low density liquids were shown to be related to a strongly correlated molecular ordering at lower temperatures that allows a better packing, yielding the higher than expected density and the highly cooperative motions. Therefore, regardless of whether the anomalies correspond to a first order liquid-liquid phase transition or not (continuous versus discontinuous changes), it has been shown that this liquid has different properties and displays different short range order structures depending on the external conditions.

The gauche conformation of 1,1,2,2-tetrachloro-1,2-difluoroethane was shown to be more stable in the liquid than the trans conformation, contrary to most compounds, due to a coupling between intra- and intermolecular interactions that favours it. A coupling which stems mainly from its conformational disorder. The exceptional fragility of this compound could be then explained through

the complexity of its energy landscape.

1,1,1,2-tetrachloro-1,1-difluoroethane, a similar compound which is rather strong, does not have this conformational disorder and showed a much more simple short range order.

The local density paradox between the liquid and plastic phase of carbon tetrachloride was made clear through comparison of the intermolecular structure in both phases. Even if the liquid favours configurations where molecules can sit closer to each other, these particular configurations do not allow proper stacking, such as in the plastic phase, which results in worse molecular packing and globally yields a lower density.

The quasi-tetrahedral molecule trichlorobromomethane did not show any significant deviation with respect to the short range order of carbon tetrachloride. It was shown that, although its molecules have dipolar moments that display antiparallel arrangements and, hence, electrostatic interactions are at play, they fit into the steric symmetry of the molecule leaving it mainly undisturbed.

Dibromodichloromethane, also a quasi-tetrahedral molecule, did show some differences in the relative orientation of the neighbours with respect to carbon tetrachloride, although not in the position. Without electrostatic interactions, steric interactions favour neighbours near the bromine side of the molecule to arrange in parallel configuration and those near the chlorine side to arrange in antiparallel configuration. Electrostatic interactions favour antiparallel configurations everywhere, thus cooperating or competing with the steric interactions depending on the relative position of the molecules considered.

Some general conclusions can be drawn:

- When comparing different phases of the same molecule or compounds of the same family, often the relative position of the center of mass of molecules is essentially the same, and the differences in their relative orientation are what really determines the packing and the behaviour of the compound.

- A lack of long range order indicates that the aggregated interactions strongly affect at a short range but quickly lose their

intensity with distance. Therefore, arrangement of the closest molecules is strongly determined but farther neighbours simply fill the available gaps that are left.

- There is a strong influence of the intramolecular structure of the molecule on the short range order, and vice versa, with many competing interactions. Thus, both structures must be studied together in order to provide a comprehensible full picture of the problem, specially when the molecule is not completely rigid and has several degrees of freedom. In particular, different intramolecular structures may display diverse dipole moments, which can radically change the role of the electrostatic interactions and alter the delicate equilibrium.

- In disordered systems, a delicate equilibrium between the contributions of different interactions often exists, and thus a qualitative description may be not enough to understand the behaviour of the system, and a quantitative analysis must be performed. In particular regarding the population of each type of arrangement, either intramolecular or intermolecular.

- In glassy systems that have frozen degrees of freedom and are out-of-equilibrium, taking into account thermal history is very important because different states may be achieved through different paths. To be able to reproduce the experiment and to understand the physics of the compounds, it is crucial that the dynamics of the process are accounted for.

Several methods and procedures have been detailed in this work that can be used to elucidate the structure of disordered systems. Although much work remains to be done understanding the behaviour of many other compounds, this contribution will help to provide some insight in the behaviour of those systems, to devise and test future theories that fully explain them.

References

All online references accessed on July 22, 2014.

[1] J. M. Ziman. *Models of disorder: the theoretical physics of homogeneously disordered systems*. Cambridge University Press, Cambridge, 1979.

[2] J. A. Barker and D. Henderson. What is "liquid"? Understanding the states of matter. *Rev. Mod. Phys.*, 45(4):587, 1976.

[3] G. Niklasson. *Physics of disordered structures (Lecture notes)*. Uppsala University, Uppsala, 2011. Available online at http://www.teknik.uu.se/ftf/education/Disordered_materials/forelasningdo.html.

[4] H. E. Fischer, A. C. Barnes, and P. S. Salmon. Neutron and x-ray diffraction studies of liquids and glasses. *Rep. Prog. Phys.*, 69(1):233–299, 2006.

[5] E. A. Guggenheim. *Thermodynamics: An advanced treatment for chemists and physicists*. North Holland Publishing, Amsterdam, fifth edition, 1967.

[6] M. A. Meyers, P.-Y. Chen, A. Y.-M. Lin, and Y. Seki. Biological materials: Structure and mechanical properties. *Prog. Mater. Sci.*, 53(1):1, 2008.

[7] J. Ubbink, A. Burbidge, and R. Mezzenga. Food structure and functionality: a soft matter perspective. *Soft Matter*, 4:1569, 2008.

[8] Y. H. Roos. Glass Transition Temperature and Its Relevance in Food Processing. *Annu. Rev. Food Sci. Technol.*, 1:469, 2010.

[9] G. Akovali, editor. *Polymers in construction*. Rapra Technology Limited, Shawbury, UK, 2005.

[10] B. Zberg, P. J. Uggowitzer, and J. F. Löffler. MgZnCa glasses without clinically observable hydrogen evolution for biodegradable implants. *Nature Mater.*, 8, 2009.

[11] P. A. Egelstaff. *An Introduction to the Liquid State*. Academic Press, London, 1967.

[12] A. Cavagna. Supercooled liquids for pedestrians. *Phys. Rep.*, 476:51, 2009.

[13] G. Jackson. *Statistical Mechanics of Liquids and Complex Fluids*. University of Oxford, 2012.

[14] H.-D. Jakubke and H. Jeschkeit, editors. *Concise Encyclopedia Chemistry*. Walter de Gruyter & Co., Berlin, 1994.

[15] C.N. Likos. Effective interactions in soft condensed matter physics. *Phys. Rep.*, 348:267, 2001.

[16] R. Brand, P. Lunkenheimer, and A. Loidl. Relaxation dynamics in plastic crystals. *J. Chem. Phys.*, 116:10386, 2002.

[17] P. Gibbs. Is glass liquid or solid?, 1996. Available online at http://math.ucr.edu/home/baez/physics/General/Glass/glass.html.

[18] P. G. Debenedetti and F. H. Stillinger. Supercooled liquids and the glass transition. *Nature*, 410:259, 2001.

[19] W. Kob and H. C. Andersen. Testing mode-coupling theory for a supercooled binary Lennard-Jones mixture I: The van Hove correlation function. *Phys. Rev. E*, 51(5):4626, 1995.

[20] W. Kob and H. C. Andersen. Testing mode-coupling theory for a supercooled binary Lennard-Jones mixture I. intermediate scattering function and dynamic susceptibility. *Phys. Rev. E*, 52(4):4134, 1995.

[21] C. A. Angell, K. L. Ngai, G. B. McKenna, P. F. McMillan, and S. W. Martin. Relaxation in glassforming liquids and amorphous solids. *J. Appl. Phys.*, 88(6):3113, 2000.

[22] N. T. Kovalenko and I. Z. Fisher. Method of integral equations in statistical theory of liquids. *Soviet Physics Uspekhi*, 15(5): 592, 1973.

[23] G. L. Squires. *Introduction to the Theory of Thermal Neutron Scattering*. Dover Publications, New York, 1978.

[24] Y. Rosenfeld and N. W. Ashcroft. Theory of simple classical fluids: Universality in the short-range structure. *Phys. Rev. A*, 20(3):1208, 1979.

[25] S. Kawanishi, T. Sasuga, and M. Takehisa. A novel liquid state of trans-1,2-dichloroethylene. *J. Phys. Soc. Jpn.*, 51:1579, 1982.

[26] J. Ziolo S. Rzoska, J. Ll. Tamarit A. Drozd-Rzoska, and N. Veglio. New evidence for a liquid-liquid transition in a one-component liquid. *J. Phys.: Condens. Matter*, 20:244124, 2008.

[27] K. Merkel, A. Kocot, R. Wrzalik, and J. Ziolo. Origin of the liquid-liquid phase transition for trans-1,2-dichloroethylene observed by ir spectroscopy. *J. Chem. Phys.*, 129:074503, 2008.

[28] K. Kishimoto, H. Suga, and S. Seki. Calorimetric study of the glassy state. XIV. calorimetric study on unusual glass transition phenomena in cfcl2-cfcl2. *Bull. Chem. Soc. Jpn.*, 51(6):1691–1696, 1978.

[29] L. C. Pardo, P. Lunkenheimer, and A. Loidl. α and β relaxation dynamics of a fragile plastic crystal. *J. Chem. Phys.*, 124: 124911, 2006.

[30] J. Baruchel, J. L. Hodeau, M. S. Lehmann, J. R. Regnard, and C. Schlenker, editors. *Neutron and Synchrotron Radiation for Condensed Matter Studies - Theory, Instruments and Methods*, volume 1 of *HERCULES Series (Higher European Research Course for Users of Large Experimental Systems)*. Les Editions de Physique, Les Ulis (France), 1993.

[31] F. Hippert, E. Geissler, J. L. Hodeau, E. Lelièvre-Berna, and J. R. Regnard, editors. *Neutron and Synchrotron Radiation for Condensed Matter Studies - Neutron and X-ray Spectroscopy*, volume 5 of *HERCULES Series (Higher European Research*

Course for Users of Large Experimental Systems). Springer, Dordrecht (Netherlands), 2006.

[32] P. Bandyopadhyay and C. U. Segre. MuCal: Calculation of atomic properties for X-rays, 2013. Available online at http://www.csrri.iit.edu/periodic-table.html. Cross section data used for their calculations have been taken by the authors from *Compilation of X-ray Cross Sections* by W. H. McMaster, et al. (available online at http://cars9.uchicago.edu/mcbook/).

[33] V. F. Sears. Neutron scattering lengths and cross sections. *Neutron News*, 3(3):26, 1992. Data available online at http://www.ncnr.nist.gov/resources/n-lengths/.

[34] C. L. Tang. *Fundamentals of Quantum Mechanics for Solid State Electronics and Optics*. Cambridge University Press, Cambridge, 2005. Available online at http://lib.org.by/info/P_Physics/PQm_Quantum%20mechanics/Tang%20C.%20Fundamentals%20of%20Quantum%20Mechanics,%20for%20solid%20state%20electronics%20and%20optics%20%28CUP,%202005%29%28222s%29_PQm_.pdf.

[35] N. F. Mott. *Elements of Wave Mechanics*. Cambridge University Press, London, 1952. Available online at http://archive.org/details/elementsofwaveme031632mbp.

[36] S. W. Lovesey. *Theory of Neutron Scattering from Condensed Matter*. Oxford University Press, Oxford, 1984.

[37] P. G. Radaelli. *Crystal Structure and Dynamics (Lecture notes)*. University of Oxford, Oxford, 2013. Available online at http://www2.physics.ox.ac.uk/students/course-materials/c3-condensed-matter-major-option.

[38] R. Pynn. *Neutron Scattering – A Non-destructive Microscope for Seeing Inside Matter*. Springer, New York, 2009.

[39] C. N. Booth. *Particle Physics (Lecture notes)*. The University of Sheffield, Sheffield, 2013. Available online at http://www.cbooth.staff.shef.ac.uk/phy304/.

[40] V. F. Sears. Neutron scattering lengths and cross sections. *Neutron News*, 3(3):26–28, 1992.

[41] P. M. Rinard. *Neutron Interactions with Matter*. U. S. Nuclear Regulatory Comission, Washington, DC, 1991.

[42] J. G. Powles. The structure of molecular liquids by neutron scattering. *Advances in Physics*, 22(1):1, 1973.

[43] D. Thirumalai, R. D. Mountain, and T. R. Kirkpatrick. Ergodic behavior in supercooled liquids and in glasses. *Phys. Rev. A*, 39(7):3563–3574, 1989.

[44] F. J. Bermejo, A. Criado, R. Fayos, R. Fernandez-Perea, H. E. Fischer, E. Suard, A. Guelylah, and J. Zuniga. Structural correlations in disordered matter: An experimental separation of orientational and positional contributions. *Phys. Rev. B*, 56 (18):11536–11545, 1997.

[45] K. A. Johnson and W. S. Howells. The liquid-state structure of octafluoropropane and decafluoro-n-butane as determined by neutron diffraction. *J. Phys.-Condens. Mat.*, 11(47):9239–9248, 1999.

[46] NMI3. Neutron methods and techniques for research, 2012. Available online at http://nmi3.eu/neutron-research/techniques-for-.html.

[47] Department of Energy Training Coordination Program (Eg&G Idaho, Inc). *Nuclear Physics and Reactor Theory*. DOE Fundamentals Handbook. U. S. Department of Energy, Washington, DC, 1993.

[48] R. Pynn. Neutron scattering. A primer. *Los Alamos Science*, 19:1, 1990.

[49] Institut Laue-Langevin. *The Yellow Book 2008 - Guide to Neutron Research Facilities*. Institut Laue-Langevin, Grenoble (France), 2008.

[50] ISIS Science & Technology Facilities Council. Vesuvio science, 2012. Available online at http://www.isis.stfc.ac.uk/instruments/vesuvio/science/vesuvio-

science4846.html.

[51] M. Arai and K. Crawford. *Chapter 2, Neutron Sources and Facilities*. Springer, New York, 2009.

[52] H. E. Fischer, G. J. Cuello, P. Palleau, D. Feltin, A. C. Barnes, Y. S. Badyal, and J. M. Simonson. D4c: A very high precision diffractometer for disordered materials. *Appl. Phys. A: Mater. Sci. Process.*, 74(Part 1 Suppl. S):S160–S162, 2002.

[53] I. Anderson, H. Börner, J. Brown, C. J. Carlile, R. Cubitt, R. Currat, A. J. Dianoux, R. B. von Dreele, D. Dubbers, R. S. Eccleston, B. Farago, A. W. Hewat, M. Johnson, J. Kulda, G. Lander, E. Lelièvre-Berna, G. J. McIntyre, S. A. Mason, R. P. May, A. Oed, H. Rauch, J. R. Stewart, F. Tasset, J. Tribolet, W. Waschkowski, and C. C. Wilson. *Neutron Data Booklet*. Institut Laue-Langevin, Grenoble (France), second edition, 2003.

[54] Institut Laue-Langevin. *Rapport transparence et sécurité nucléaire. Réacteur Haut Flux*. Institut Laue-Langevin, Grenoble (France), 2010.

[55] P. K. Willendrup, E. Knudsen, K. Lefmann, and E. Farhi. *Component Manual for the Neutron Ray-Tracing Package McStas, Version 1.12*. Risø DTU, Roskilde (Denmark), 2011.

[56] Institut Laue-Langevin. Orange cryostat instruction manual, 2012. Available online at http://www.ill.eu/html/instruments-support/sample-environment/equipment/low-temperatures/cryostats/instruction-manual/.

[57] Birkbeck College. Advanced certificate in powder diffraction on the web, 2012. Available online at http://pd.chem.ucl.ac.uk/pdnn/inst3/samples.htm.

[58] H. E. Fischer. Recent developments in the D4C diffractometer project. *ILL Annual Report 97*, 1997. URL http://www.ill.eu/fileadmin/users_files/Annual_Report/AR-97/page/29inst.htm.

[59] A. K. Adya. *Neutron Scattering. Technique and Applications*

to Molten salts., volume 52 of *NATO Science Series*. Kluwer Academic Publishers, Dordrecht (Netherlands), 2002.

[60] D. A. Shea and D. Morgan. The helium-3 shortage: Supply, demand, and options for Congress. *Congressional Research Service Reports*, R41419, 2010.

[61] Institut Laue-Langevin. CRG two-axis diffractometer D1B, 2012. Available online at http://www.ill.eu/instruments-support/instruments-groups/instruments/d1b/.

[62] C.-H. Lee, M.-K. Moon, V. T. Em, Y.-N. Choi, H.-S. Oh, and U.-W. Nam. High-resolution and high-intensity neutron diffractometer with linear position-sensitive detector. *Nuclear Instruments and Methods in Physics Research A*, 2003. http://144.206.159.178/ft/787/183944/4699945.pdf.

[63] T. C. Hansen, P. F. Henry, H. E. Fischer, J. Torregrossa, and P. Convert. The D20 instrument at the ILL: a versatile high-intensity two-axis neutron diffractometer. *Meas. Sci. Technol.*, 19:034001, 2008.

[64] J. Bouillot and J. Torregrossa. A radial oscillating collimator for small position sensitive detectors. *Revue Phys. Appl.*, 19: 799, 1984.

[65] W. F. Kuhs and T. C. Hansen. Time resolved neutron diffraction studies with emphasis on water ices and gas hydrates, 2006. Presentation available online at http://www.minsocam.org/msa/rim/rim63_ch_08_kuhs.pdf.

[66] T. Gutberlet. JCNS - Forschungszentrum Jülich, 2009. ACCESS Activity - General Assembly in Villigen (Switzerland), March 31, 2009.

[67] T. Unruh, J. Neuhaus, and W. Petry. The high-resolution time-of-flight spectrometer TOFTOF. *Nuclear Instruments and Methods in Physics Research Section A: Accelerators, Spectrometers, Detectors and Associated Equipment*, 580(3):1414–1422, 2007.

[68] Technische Universität München. TOFTOF - Cold neutron

time-of-flight spectrometer, 2014. Available online at http://www.mlz-garching.de/toftof.

[69] J. R. D. Copley and T. J. Udovic. Neutron time-of-flight spectroscopy. *J. Res. Natl. Inst. Stand. Technol.*, 98(1):71, 1993.

[70] NMI3. Time-of-flight spectroscopy overview, 2014. Available online at http://nmi3.eu/neutron-research/techniques-for-/dynamics/time-of-flight-spectroscopy.html.

[71] Helmholtz Zentrum Berlin. Neutron time-of-flight spectroscopy: how does it work and why do we need it?, 2014. Available online at https://www.helmholtz-berlin.de/forschung/oe/funkma/soft-matter/forschung/laufzeit/index_de.html.

[72] Institut Laue-Langevin. D4CREG, 2012. Available online at http://www.ill.eu/en/html/instruments-support/instruments-groups/instruments/d4/more/manual/d4creg/.

[73] G. F. Knoll. *Radiation Detection and Measurement*. John Wiley & Sons, Inc., New York, third edition, 2000.

[74] Astrophysics Research Institute (Liverpool John Moores University). Astro fundamentals: Light and its detection, 2012. Available online at http://www.astro.ljmu.ac.uk/courses/phys134/scopes.html.

[75] M. A. Howe, R. L. McGreevy, and P. Zetterström. CORRECT*: A correction program for neutron diffraction data*, 1996. NFL Studsvik internal report.

[76] V. F. Sears. Dynamical theory of neutron diffraction. *Can. J. Phys.*, 56(10):1261–1288, 1978.

[77] G. J. Cuello. Determination of amorphous structures by neutron diffraction (tutorial HERCULES 2008), 2008.

[78] H. H. Paalman and C. J. Pings. Numerical evaluation of x-ray absorption factors for cylindrical samples and annular sample cells. *J. Appl. Phys.*, 33(8):2635–&, 1962.

[79] A. K. Soper and P. A. Egelstaff. Multiple scattering and attenu-

ation of neutrons in concentric cylinders: I. Isotropic first scattering. *Nuclear Instruments and Methods*, 178(2-3):415, 1980.

[80] I. A. Blech and B. L. Averbach. Multiple scattering of neutrons in vanadium and copper. *Phys. Rev.*, 137:A1113–A1116, 1965.

[81] V. F. Sears. Slow-neutron multiple scattering. *Adv. Phys.*, 24 (1):1–45, 1975.

[82] L. A. Rodríguez Palomino, J. Dawidowski, J. J. Blostein, and G. J. Cuello. Data processing method for neutron diffraction experiments. *Nuclear Instruments and Methods in Physics Research Section B: Beam Interactions with Materials and Atoms*, 258(2):453, 2007.

[83] T. Bausenwein, H. Bertagnolli, K. Tödheide, and P. Chieux. Multiple scattering and self-absorption correction for high-pressure neutron diffraction with cylindrical cells. *Nuclear Instruments and Methods in Physics Research Section B: Beam Interactions with Materials and Atoms*, 61(4):527, 1991.

[84] J. Dawidowski and G. J. Cuello. Experimental corrections in neutron diffraction of ambient water using H/D isotopic substitution. *J. Phys.: Conf. Ser.*, 340(1):012004, 2012.

[85] G. Placzek. The scattering of neutrons by systems of heavy nuclei. *Phys. Rev.*, 86(3):377–388, May 1952. doi: 10.1103/PhysRev.86.377.

[86] G. C. Wick. The scattering of neutrons by systems containing light nuclei. *Phys. Rev.*, 94(5):1228, 1954.

[87] E. Guarini. The neutron double differential cross-section of simple molecular fluids: Refined computing models and nowadays applications. *J. Phys.: Condens. Matter*, 15(19):R775, 2003.

[88] J. L. Yarnell, M. J. Katz, R. G. Wenzel, and S. H. Koenig. Structure factor and radial distribution function for liquid argon at 85 K. *Phys. Rev. A*, 7(6), 1973.

[89] I. Petri, P. S. Salmon, and H. E. Fischer. Defects in a disordered world: The structure of glassy $gese_2$. *Phys. Rev. Lett.*, 84(11): 2413–2416, Mar 2000. doi: 10.1103/PhysRevLett.84.2413.

[90] J. Waser and V. Schomaker. The Fourier inversion of diffraction data. *Rev. Mod. Phys.*, 25(3):671–690, 1953.

[91] J. M. Fornies-Marquina, J. Letosa, M. Garcia-Gracia, and J. M. Artacho. Error propagation for the transformation of time domain into frequency domain. *IEEE T. Magn.*, 33(2, Part 2): 1456–1459, 1997.

[92] M. Rovira-Esteva, N. A. Murugan, L. C. Pardo, S. Busch, J. Ll. Tamarit, Sz. Pothoczki, G. J. Cuello, and F. J. Bermejo. Interplay between intramolecular and intermolecular structures of 1,1,2,2-tetrachloro-1,2-difluoroethane. *Phys. Rev. B*, 84:064202, 2011.

[93] J. Letosa, M. Garcia-Gracia, J. M. Fornies-Marquina, and J. M. Artacho. Performance limits in TDR technique by Monte Carlo Simulation. *IEEE T. Magn.*, 32(3, Part 1):958–961, 1996.

[94] K. R. Popper. *Conjectures and Refutations: The Growth of Scientific Knowledge*. Routledge Classics, London, 2002.

[95] W. H. Press, S. A. Teukolsky, W. T. Vetterling, and B. P. Flannery. *Numerical Recipes in C: The Art of Scientific Computing*. Cambridge University Press, second edition, 1992. Available online at http://apps.nrbook.com/c/index.html.

[96] M. K. Transtrum, B. B. Machta, and J. P. Sethna. Why are nonlinear fits to data so challenging? *Phys. Rev. Lett.*, 104: 060201, 2010.

[97] D. Sivia and J. Skilling. *Data Analysis: A Bayesian Tutorial*. Oxford University Press, New York, 2006.

[98] T. Bayes and R. Price. An Essay towards Solving a Problem in the Doctrine of Chances. By the Late Rev. Mr. Bayes, F. R. S. Communicated by Mr. Price, in a Letter to John Canton, A. M. F. R. S. *Philos. T.*, 53:370–418, 1763.

[99] G. Sala, F. Haberl, J. José, A. Parikh, R. Longland, L. C. Pardo, and M. Andersen. Constraints on the mass and radius of the accreting neutron star in the rapid burster. *Astrophys. J.*, 752(2):158, 2012.

[100] L. C. Pardo. *FABADA (Fitting Algortihm for Bayesian Analysis of DAta)*, 2009. http://gcm.upc.edu/members/luis-carlos/bayesiano.

[101] W. K. Hastings. Monte carlo sampling methods using markov chains and their applications. *Biometrika*, 57(1):97, 1970.

[102] W. R. Gilks, G. O. Roberts, and S. K. Sahu. Adaptive Markov chain Monte Carlo through regeneration. *J. Am. Stat. Assoc.*, 93:1045, 1998.

[103] S. Kirkpatrick, Jr. C. D. Gelatt, and M. P. Vecchi. Optimization by simulated annealing. *Science*, 220:671, 1983.

[104] M. Rovira-Esteva, A. Murugan, L. C. Pardo, S. Busch, M. D. Ruiz-Martin, M. S. Appavou, J. Ll. Tamarit, C. Smuda, T. Unruh, F. J. Bermejo, G. J. Cuello, and S. J. Rzoska. Microscopic structures and dynamics of high- and low-density liquid trans-1,2-dichloroethylene. *Phys. Rev. B*, 81(9):092202, MAR 1 2010.

[105] L. C. Pardo, M. Rovira-Esteva, S. Busch, M. D. Ruiz-Martín, J. Ll. Tamarit, and T. Unruh. Bayesian analysis of QENS data: From parameter determination to model selection. 2009.

[106] S. Busch, C. Smuda, L. C. Pardo, and T. Unruh. Molecular mechanism of long-range diffusion in phospholipid membranes studied by quasielastic neutron scattering. *J. Am. Chem. Soc.*, 132(10):3232–3233, 2010. doi: 10.1021/ja907581s.

[107] J. C. Martinez-Garcia, J. Ll. Tamarit, L. C. Pardo, M. Barrio, S. J. Rzoska, and A. Droz-Rzoska. Disentangling the secondary relaxations in the orientationally disordered mixed crystals: cycloheptanol + cyclooctanol two-component system. *J. Phys. Chem. B*, 114:6099, 2010.